FAILURE OF GRAPHITE/EPOXY INDUCED BY DELAMINATION

by

JOHN CHARLES BREWER

S.B. MASSACHUSETTS INSTITUTE OF TECHNOLOGY (1983)
S.M. MASSACHUSETTS INSTITUTE OF TECHNOLOGY (1985)

SUBMITTED TO THE DEPARTMENT OF AERONAUTICS
AND ASTRONAUTICS IN PARTIAL FULFILLMENT OF
THE REQUIREMENTS FOR THE DEGREE OF

DOCTOR OF PHILOSOPHY

AT THE

MASSACHUSETTS INSTITUTE OF TECHNOLOGY

MAY 1988

© Massachusetts Institute of Technology 1988

Signature of Author ______________________
Department of Aeronautics and Astronautics
May 19, 1988

Certified by ______________________
Professor Paul A. Lagace
Thesis Supervisor
Department of Aeronautics and Astronautics

Certified by ______________________
Professor James W. Mar
Thesis Supervisor
Department of Aeronautics and Astronautics

Certified by ______________________
Dr. John F. Mandell
Thesis Supervisor
Department of Materials Science and Engineering

Accepted by ______________________
Professor Harold Y. Wachman
Chairman, Department Graduate Committee

MASSACHUSETTS INSTITUTE OF TECHNOLOGY
MAY 24 1988
LIBRARIES
Aero

WITHDRAWN
M.I.T.
LIBRARIES

FAILURE OF GRAPHITE/EPOXY INDUCED BY DELAMINATION

by

JOHN CHARLES BREWER

Submitted to the Department of Aeronautics and Astronautics on May 19, 1988 in partial fulfillment of the requirements for the Degree of Doctor of Philosophy in Aeronautics and Astronautics.

ABSTRACT

The progression of delamination damage in graphite/epoxy laminates was investigated. Delamination initiation of specimens with fabric and unidirectional plies was explored. The lamination sequences yielded high thermally- and mechanically-induced interlaminar normal stresses. The Quadratic Delamination Criterion was shown to accurately correlate the initiation when thermally-induced stresses were included. In the remaining experiments, delamination size was monitored with dye penetrant-enhanced x-radiography after each test to a predetermined load. Specimen width was varied for $[\pm 15_3]_s$ specimens and failure stress was found to be independent of specimen width. Lamination sequence and effective ply thickness were varied using $[\pm 15_n/0_n]_s$ and $[0_n/\pm 15_n]_s$ specimens (n=1,2,3,5,8). No critical delamination size was found for any specimen type. In all cases, delamination initiation was a necessary prerequisite to delamination growth. Final failure was controlled by in-plane strength considerations of the delaminated sublaminates. Constraints of intact sublaminates on damaged sublaminates can affect delamination growth and final failure. The effect of placing primarily warp fibers ($\pm 20°$) or fill fibers ($\pm 70°$) at the critical delamination interface of fabric $[\pm 20_F]_s$ laminates was studied. There were discernable effects of interface character on delamination growth and final failure. $[0_3/\pm 15_3]_s$ specimens with implanted delaminations and angle ply splits demonstrated that delaminations strongly interact with damage in neighboring plies such as splits. A strain energy release rate analysis was modified to include several aspects of the three-dimensional nature of observed damage as well as the effects of finite specimen dimensions. Nonetheless, the model was unable to yield a constant value of strain energy release rate, as calculated from the data, as would be expected. A full three-dimensional model including the details of sublaminate constraint and the interaction of the delamination and angle ply split is warranted.

Thesis Supervisor: Professor Paul A. Lagace

Title: Associate Professor of Aeronautics and Astronautics

ACKNOWLEDGEMENTS

Completing a thesis such as this requires the understanding and assistance of a great many people. I cannot hope to name all the individuals who have assisted me along the way, but I would like to express my gratitude publicly to as many as possible without doubling the length of this document.

The first group which must be given credit is my doctoral thesis committee. It was chaired by my hard working friend Paul Lagace. I could not and would not be in this position today without Paul's help and encouragement. Professor James W. Mar has been an inspiration to me and the rest of the laboratory. We are all grateful to him. Dr. John F. Mandell of the Materials Science and Engineering Department was invaluable with his observations and input.

I would like to acknowledge the contribution of the faculty and staff of the Department of Aeronautics and Astronautics and the Technology Laboratory for Advanced Composites. Most especially, I owe a debt of gratitude to Al Supple who encouraged me over the years and mediated my disputes with inanimate objects. I would also like to thank Professor John Dugundji, Ping, Carl, Bonnie, Al Shaw, and all the rest.

There is no room to recognize the more than one hundred TELAC members I have worked with over the last 8½ years, but I do appreciate their help. A special thanks goes out to those who have helped me with my graduate work, including Mary, Rich, Gail, and Doug. The hundreds of tests in the ear-splitting racket of the testing room would have been intolerable without them. I know the Gods of Graphite will watch over them. I would also like to thank Pierre Minguet for his help with the finite element model and Christos Kassapoglou for teaching me the intracacies of interlaminar stresses.

The people I have lived with during my time at MIT have made life much more bearable. I would like to thank the members of J Entry at MacGregor House, the residents of Conner 5 over the past three years, and, of course, the resident and non-resident members of MIE.

I know am truly blessed to have a wonderful family like mine. I have met many people with unpleasant home lives. I want to express my appreciation to my parents, brothers, sisters, nieces, and nephews for being the type that people envy. I would also like to acknowledge all my in-laws for being supportive during this effort.

I could not conclude these acknowledgements without recognizing the two most important people in my life: my wife, Katy, and my daughter, Maggie. I know their sacrifices have been great during the terrible last months of thesis writing. I will make it up to them soon. They have been wonderful and I love them for it.

When I mention my daughter, I know it is no secret that she has had serious medical problems. I would like to take this opportunity to express my sincerest appreciation to everyone who showed concern (and especially those who gave their blood) during her hospitalizations. I must also thank the staff of the Children's Hospital Medical Center and the Harvard Community Health Plan for their outstanding work. In particular, the efforts of Dr. Herbert "Herbie the Heart Doctor" Cohn, Dr. Richard Jonas, Dr. Mary VanderVelde, Dr. Judy Becker, and Mary Czezot, R.N. made a very long ordeal bearable for Katy and me and have helped Maggie to become the relatively healthy normal child she is today. With this kind of care, I have no doubt that she will grow strong and tall and live a long, full life. It is for this that I am most grateful.

This work was performed in the Technology Laboratory for Advanced Composites (TELAC) of the Department of Aeronautics and Astronautics at the Massachusetts Institute of Technology. This work was sponsored by the Boeing Aircraft Company under contract number BMAC PO AA0045 and the United States Air Force Office of Scientific Research under grant number AFOSR-85-0206.

DEDICATION

To my dear wife, Katy

TABLE OF CONTENTS

TABLE OF CONTENTS (Continued)

TABLE OF CONTENTS (Continued)

TABLE OF CONTENTS (Continued)

LIST OF FIGURES

LIST OF FIGURES (Continued)

LIST OF FIGURES (Continued)

LIST OF FIGURES (Continued)

LIST OF FIGURES (Continued)

LIST OF FIGURES (Continued)

LIST OF TABLES

LIST OF TABLES (Continued)

NOMENCLATURE

a	delamination length in a two-dimensional analysis
A_{del}	area of delaminated region
b	specimen test section halfwidth
E	modulus
E_{lam}	longitudinal modulus of the completely laminated specimen
E_{loc}	local longitudinal modulus of a differentially thin cross-section of the specimen
E^*	weighted average longitudinal modulus of the sublaminates of a delaminated specimen
F	coefficient in a general tensor criterion
G	strain energy release rate
$\hat{G}$	strain energy release rate determined from the two-dimensional finite element analysis
GPa	Gigapascal (= 10^9 Pascals)
l	specimen test section halflength
mm	millimeter
MPa	Megapascal (= 10^6 Pascals)
n	normalized effective ply thickness
psia	pounds per square inch of absolute pressure
psig	pounds per square inch of gage pressure (pressure above atmospheric)
S	in-plane shear strength of the unidirectional composite
T	temperature
t	laminate thickness
t_{ply}	ply thickness
u, v, w	displacements in the x_1, x_2, and x_3 directions, respectively

U	internal energy
$\bar{U}$	internal energy per unit length
x	distance from a reference point, such as the free edge
x_{avg}	averaging dimension in the Quadratic Delamination Criterion
Y^t	in-plane transverse strength
Z^c	compressive interlaminar normal strength
Z^t	tensile interlaminar normal strength
Z^{s1}	interlaminar shear strength for σ_{1z}
Z^{s2}	interlaminar shear strength for σ_{2z}
α	coefficient of thermal expansion
β	ratio of the local strain level to the average strain level over the specimen length
δ	total longitudinal displacement for the test section
ε	strain level
ε^*	average strain level over the specimen length
μstrain	microstrain (microinch/inch of strain)
σ	stress
$\bar{\sigma}$	component of stress averaged over a distance x_{avg} from the free edge
σ_o	far-field stress
θ	lamination angle
°C	degrees Celsius

SUBSCRIPTS

c	critical value for delamination
del	delaminated
F	fabric graphite/epoxy composite

I	mode I (opening) component
II	mode II (sliding) component
III	mode III (tearing) component
lam	laminated
loc	local
L, 1	longitudinal or 0° direction
T, 2	transverse or 90° direction
U	unidirectional graphite/epoxy composite
z, 3	through-the-thickness direction

SUPERSCRIPTS

c	only compressive values considered
t	only tensile values considered

CHAPTER 1

INTRODUCTION

Advanced composite materials have made significant advances in aerospace engineering possible. All aspects of the industry have found applications for these light, stiff materials. Although material and processing costs are presently high, these are often offset by reduced material waste and life cycle fuel savings.

One aircraft which employs advanced composites extensively is the Voyager. This experimental craft was able to fly non-stop around the world without aerial refueling. This enterprise demonstrated to the world the potential of advanced composites as structural materials.

An example of the use of composites in production aircraft is the Beechcraft Starship 1. This fuel efficient business jet recently became the first aircraft with a primary structure composed entirely of advanced composites to obtain structural certification from the Federal Aviation Administration. The certification of the Starship marks the beginning of an era when the use of advanced composites in aircraft structural design will be routine.

The success of the Voyager and the Starship would not have been possible without the groundbreaking application of composites on other aircraft. The Boeing 757 and 767 aircraft were designed primarily for fuel efficiency and as such used advanced composites extensively in secondary structures.

Advanced composites have many uses in military aircraft. They offer ease of fabrication of the complex configurations necessary for reducing radar cross-section. The potential weight savings allows the designer to increase range, payload, and/or maneuverability. Only the weight savings from advanced composites makes the AV-8B vertical takeoff and landing (VTOL) fighter possible in its present configuration.

The inherent anisotropy of fibrous composites gives them the potential to be "tailored" in useful ways. An example of the ambitious use of aeroelastic tailoring is the Grumman/DARPA X-29 forward swept wing aircraft. By adjusting the lamination angles of the plies in the wing skins, the wings can be swept forward while inhibiting aeroelastic instabilities such as divergence.

Advanced composites are important in the field of astronautics. In an industry where launch costs are measured in thousands of dollars per pound, the ability to replace structural weight with functioning electronics is extremely valuable. The material and fabrication costs are essentially negligible.

The largest examples of an application of advanced composites in a spacecraft are the payload bay doors on the space shuttle orbiter. Another example is the filament wound solid rocket booster case designed for the space shuttle. These cases have far less mass than their D6ac steel counterparts (32200 kg versus 46000 kg for each booster case). Although the Challenger disaster has put plans to use filament wound cases on hold, they could be used to achieve polar orbit on space shuttle launches from Vandenburg Air Force Base or to significantly increase payload to orbit.

Despite recent progress, advanced composites still have a great deal of untapped potential. At present, the design safety factors are quite high. Even the primary structure of the Starship is more lightly loaded than some of the composite secondary structures on the larger commercial jets. As researchers learn more about the complex behavior of composites, engineers can more confidently use them to a fuller extent.

An issue of utmost importance to engineers is the understanding of all possible failure modes. One of the most puzzling to date is delamination. In this mode, the layers or "plies" of the composite separate from each other in the out-of-plane direction even when the loading is in-plane [e.g. 1]. Delamination has been determined to result from the out-of-plane failure of a thin interply matrix layer [2]. This failure results from a full three-dimensional state of stress that arises in multi-directional composite plates [e.g. 3]. These stresses are significant in regions near free edges, cutouts, and ply dropoffs. Once a delamination has initiated, it can propagate across a part causing an immediate loss of strength and stiffness and, often, failure.

The primary objective of this work is to determine the damage sequence which leads to "premature" failure of general graphite/epoxy laminates induced by delamination. Investigations in the literature have generally focused on either delamination initiation [e.g. 4] or growth [e.g. 5]. Wang and Crossman [6] recognized that there are three phases of delamination: initiation, growth, and final failure. In this thesis, each phase will be investigated both experimentally and analytically.

A secondary objective is to develop analytical models which can correlate data and serve as a basis for prediction of the various damage stages. Such models can aid in the preliminary design process by allowing designers to compare larger numbers of candidate laminates on the basis of their propensity to fail via delamination.

Chapter 2 of this thesis is a review of the literature regarding interlaminar stresses, delamination initiation, growth, and final failure in laminated composites. The approach taken to achieve the objectives of this investigation are discussed in Chapter 3. The general manufacturing procedures are detailed in Chapter 4. A series of experiments undertaken to investigate delamination initiation in laminates dominated by thermally-induced interlaminar normal stresses are described in Chapter 5. Four sets of experiments undertaken to ascertain the stages of damage progression and evaluate their interaction are discussed in Chapter 6. In Chapter 7, modifications to existing models of delamination growth are proposed in order to better approximate the observed damage. The investigation is summarized in

Chapter 8. The significance of the experimental results is ascertained and the applicability of the analytical model is evaluated. The relevant conclusions of this work are summarized in Chapter 9 along with recommendations for further research into the subject of the ultimate strength of composite laminates prone to delamination failure.

CHAPTER 2

SUMMARY OF PREVIOUS WORK

A great deal of research has been conducted on advanced composite materials. In this chapter, the literature which deals with out-of-plane or "interlaminar" stresses will be reviewed. Subsequently, literature concerning each of the three phases of delamination of graphite/epoxy composites (initiation, growth, and final failure) will be discussed.

2.1 Interlaminar Stresses and Delamination

Researchers have investigated delamination of advanced composites for some time. Delamination has been determined to result from the out-of-plane failure of a thin interply matrix layer [2]. Interlaminar stresses are responsible for the initiation of this damage. These stresses have high gradients and are significant only in regions near free edges, notches, and ply dropoffs.

Classical Laminated Plate Theory [e.g. 7] describes the behavior of a laminated set of plies or "laminate" by imposing continuity of in-plane strain throughout the laminate thickness. For reference, the coordinate system used in this investigation is depicted in Figure 2.1. The elastic properties of a ply (e.g. modulus, Poisson's ratio, coefficient of mutual influence) are functions of the angular orientation of its fibers. Hence, there will in general be a

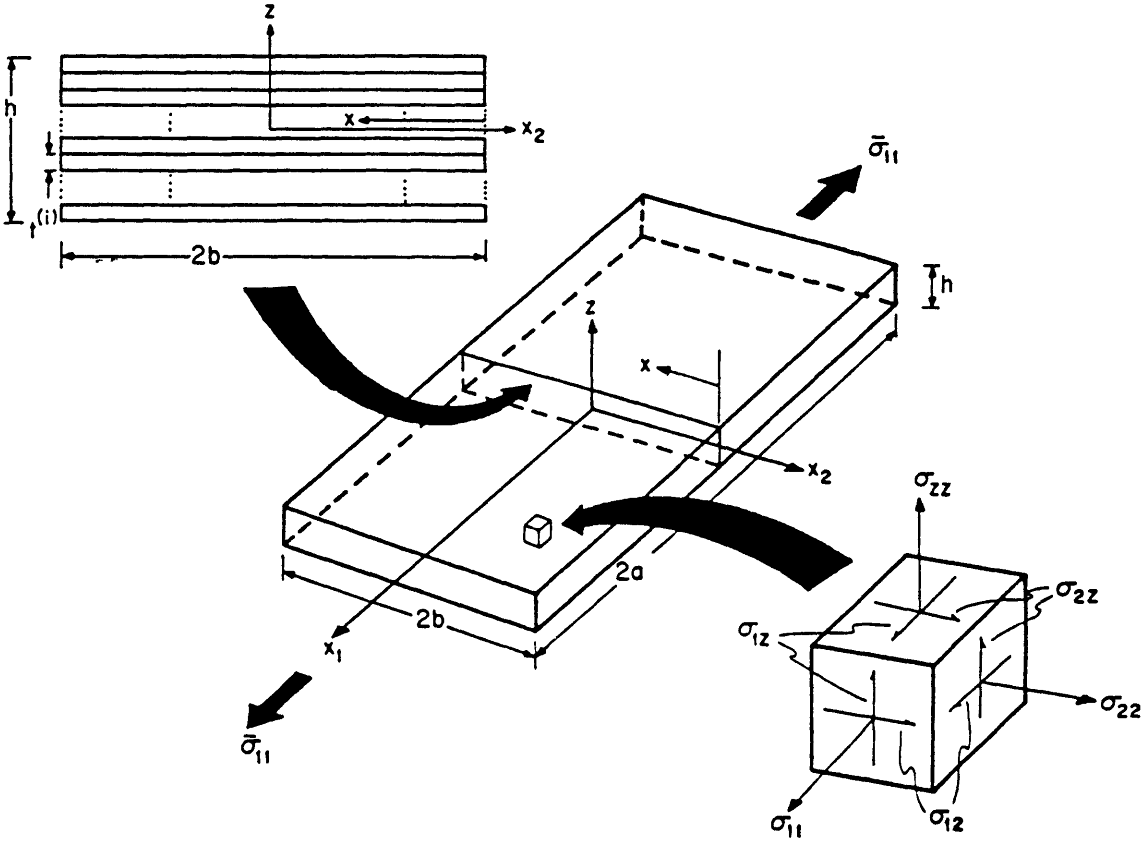

FIGURE 2.1 GEOMETRY FOR THE PROBLEM OF A LAMINATED PLATE UNDER UNIAXIAL LOAD

mismatch between the elastic properties of neighboring plies. The effect of the difference in elastic properties is that each ply has its own in-plane stress state (σ_{11}, σ_{22}, and σ_{12}). For example, if the Poisson's ratio is not identical in all plies, the Classical Laminated Plate Theory solution will predict non-zero transverse stress (σ_{22}) that will vary from ply to ply for the case of uniaxial loading. This solution will satisfy the stress-free boundary conditions at the free edge of a specimen only in an average sense. The boundary conditions and equilibrium requirements will result in a full three-dimensional state of stress in the region near the free edge.

The calculation of interlaminar stresses has been an important research topic. Numerical methods such as finite elements [e.g. 8,9] and finite difference [10] have been used. Early analytical approaches focused on one component at a time. Pagano and Pipes [11] derived a rough approximation for interlaminar normal stress (σ_{zz}) by assuming a stress distribution and enforcing force and moment equilibrium at the free edge. Puppo and Evensen [12] calculated the interlaminar shear stress σ_{1z} by modeling the interlaminar matrix layers as isotropic shear layers. Pipes and Pagano [13] attempted a Fourier series approach. They found, however, that the derivative of displacement with respect to location through the thickness diverged with the addition of terms. Hsu and Herakovich [14] used a perturbation solution and obtained good agreement with finite difference solutions. They also found some instabilities in σ_{zz} and a dependence of the distribution shape on specimen width and applied strain.

Pagano and Soni [15] recognized that actual composite parts contain a substantial number of layers. An associated finite element model would be computationally intensive and unwieldy. They believed the problem would require a more sophisticated approach. They developed a variational method specialized to the interlaminar stress problem. The method divides the part into "global" and "local" domains. The local domain is the region of interest. The remainder of the part is in the global domain. Most characteristics of the global domain are smeared together. The approach is akin to substructuring in the general finite element method.

Kassapoglou and Lagace [16] approached the evaluation of interlaminar stresses by assuming stress distributions which satisfied the boundary conditions and differential and integral equilibrium. The complementary energy of the system is evaluated symbolically and made stationary. When actual stresses and elastic parameters are considered, the parameters needed to describe the interlaminar stress distributions can be solved for iteratively. This method was shown to require far less computational effort than the finite element method while showing excellent agreement with solutions in the literature. Any significant differences could be traced to the solution in the literature not satisfying the boundary conditions or equilibrium. The method has been evaluated for some special cases [17] and extended to thermally-induced loading [18].

Wang and Choi [19] have suggested that there is a stress singularity at the free edge of composite laminates. This singularity, however, may only be important over regions so small that the underlying assumptions of smeared homogeneity of ply properties may break down and fiber and matrix properties may have to be considered explicitly. The theoretical existence of the singularity may therefore have only limited practical importance.

There are several options in evaluating interlaminar stresses. The method of Kassapoglou and Lagace will be used in this investigation because it is efficient and accurate. It does not include a singularity in its present form, but this does not appear to be an important factor in the present investigation.

2.2 Delamination Initiation

The interlaminar stress state is instrumental in initiating delamination. Nonetheless, how to incorporate knowledge of the interlaminar stress state into the prediction of delamination initiation has been a subject of debate. Two basic methodologies have been explored: the mechanics of materials approach and the strain energy release rate approach.

2.2.1 Initial Qualitative Approaches

Early attempts to correlate delamination initiation with the interlaminar stress state were essentially qualitative. Pipes et al. [3] studied $[\pm\theta]_s$ laminates. These laminates have no mismatch of Poisson's ratio from ply to ply. Classical Laminated Plate Theory therefore predicts no transverse stress (σ_{22}). Interlaminar stress calculations [e.g. 17] show that the interlaminar normal stress (σ_{zz}) is negligible. The conclusion reached was that the interlaminar shear stress σ_{1z} was primarily responsible for delamination in these laminates. Herakovich [20] also investigated laminates containing no Poisson's mismatch. He compared $[\pm\theta_2]_s$ ("clustered") laminates with $[(\pm\theta)_2]_s$ ("alternating") laminates. The essential differences between these laminates are the layer thickness and the resulting interlaminar shear stresses. The magnitude of the interlaminar shear stresses σ_{1z} at the interfaces of interest is greater in the clustered laminates. Herakovich found that the clustered laminates failed at significantly lower stresses. This indicates earlier delamination initiation. He concluded that "the differences are explained analytically through consideration of the influence of layer thickness on the magnitude of the interlaminar shear stress."

Rodini and Eisenmann [1] attempted a quantitative approach by trying to correlate delamination with the volume integral of the interlaminar normal stress (σ_{zz}). They only integrated over that volume of the laminate between the free edge and the point where σ_{zz} changed sign. They proposed that the propensity for delamination could be determined with a Weibull distribution of the value of this integral. They used the approximate solution of Pagano and Pipes [11] to determine σ_{zz}. This approach predicts that delamination strength is a strong function of specimen length. They achieved "reasonable correlation of analysis and tests" although they did not specifically test the effect of specimen length.

Lagace [21] also considered the effect of σ_{zz}. Instead of integrating over the entire volume, however, he rated the propensity of various interfaces to delaminate on the basis of the integral of σ_{zz} from the free edge to the point where it changed sign. Specimen length was not considered. Specimen thickness was only accounted for indirectly in that it changed the distribution of σ_{zz} on each interface. He believed that higher tensile values of this integral was a good indication of a greater propensity for delamination.

These early approaches often achieved good qualitative agreement with the data generated for the special cases and conditions in the individual references. None of them, however, was general enough to be used in all cases for general laminates.

2.2.2 Strain Energy Release Rate Approaches

Delaminations can be regarded as interlaminar cracks.

This prompted some researchers to look at delamination onset and growth in terms of fracture mechanics methodologies. The most popular approach is the strain energy release rate. Rybicki et al. [5] reasoned that methods developed for crack growth in isotropic metals could be extended to the delamination of laminated composites. The strain energy release rate approach can be applied in terms of the energy per unit area of crack growth available from released strain energy (strain energy release rate curves) and the energy per unit area needed to create the new surface area (delamination resistance curve or "R-curve").

Rybicki et al. [5] determined the strain energy released during incremental crack growth using a two-dimensional finite element model of a laminate cross-section. To evaluate the change in energy, they released an additional node at the crack tip, and reevaluated the finite element model. They could approximate the change in energy by closing the node with the nodal forces observed when that node was closed. The energy was the integral of the product of virtual force and virtual displacement. This is the "virtual crack closure" method. Data they obtained suggested that "the strain energy release rate appears to warrant further investigation as a way of predicting initiation" of delamination in composites.

Wang and Crossman [6] engaged in further work with the strain energy release rate approach and the virtual crack closure method. They specifically noted that the three components of force and displacement could be integrated separately to obtain the mode I (opening), mode II (sliding), and mode III (tearing) contributions to strain energy release rate. They assumed that a small interlaminar crack does exist. They approximated the R-curve as starting at zero at the initial crack size and rising quickly to an asymptotic value for all larger crack sizes. The strain energy release rate curve they obtained from their finite element analysis contained a slight hump for a small delamination size. When the strain level was such that this hump approximated the R-curve as illustrated in Figure 2.2, the conditions were said to be acceptable for "pop-in" of a delamination initiation. They obtained data for some cases. They tested $[\pm 25/90_n]_s$ with n ranging from one half to eight [22,23]. They found good correlation for delamination initiation for the thinner laminates (n less than or equal to three) despite the fact that transverse cracks in the 90° layer appeared before delamination initiation for laminates with n greater than or equal to two. For all thicker laminates, the observed delamination initiation strain was significantly below the predicted value. Their results for some quasi-isotropic laminates showed good agreement [24]. Their analysis for these cases led them to believe that pop-in delaminations are on the order of one to three ply thicknesses in size.

Kim and Hong [25] applied this methodology to angle ply laminates. They obtained good agreement with their data. They determined that mode III dominates the interlaminar failure of angle ply laminates. This is not surprising given

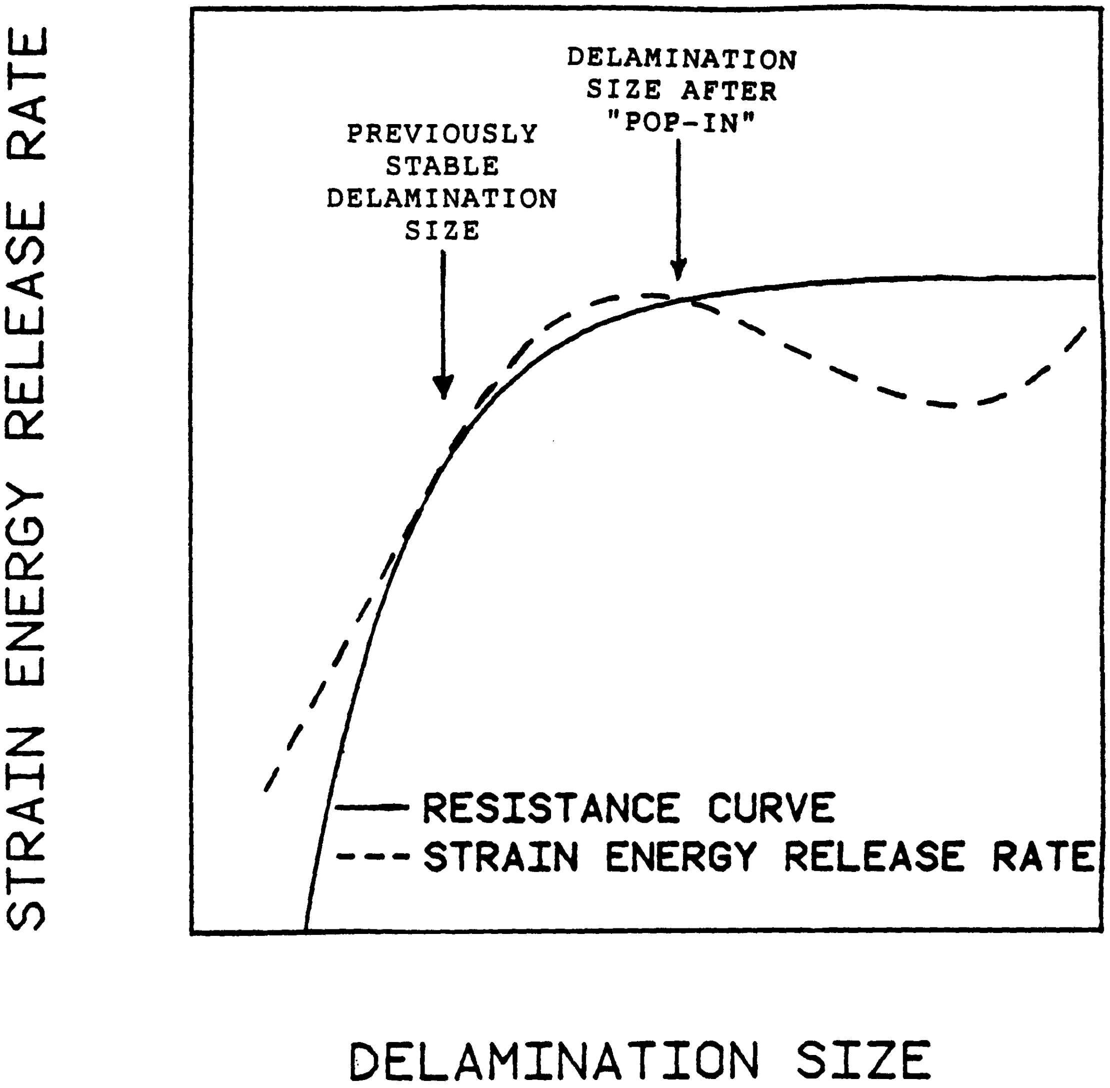

FIGURE 2.2 SCHEMATIC OF THE STRAIN ENERGY RELEASE RATE CURVE AND THE CRACK GROWTH RESISTANCE CURVE AT "POP-IN" OF THE DELAMINATION INITIATION

that the predicted interlaminar normal stress σ_{zz} and interlaminar shear stress σ_{2z} at the free edge of virgin angle ply laminates are zero [17].

O'Brien [26] derived a simpler method of obtaining an approximate value for the strain energy release rate. He modeled the delaminations as strips along the free edge of a specimen. The selection of this geometry assumes nothing changes with respect to longitudinal position, including delamination width and strain level. He calculated the energy in the laminated and delaminated regions in terms of the longitudinal modulus, the laminate dimensions, and the strain level. He used a rule of mixtures approach to calculate the modulus of the delaminated region from the moduli of the sublaminates. He obtained the following expression for strain energy release rate:

$$G = \frac{t\varepsilon^2}{2}\left(E_{lam} - E^*\right) \tag{2.1}$$

where: G = strain energy release rate
t = laminate thickness
ε = strain level
E_{lam} = modulus of the laminated region
E^* = weighted average modulus of delaminated region.

The factor t embodies the general principle that the energy available is proportional to the laminate thickness and, therefore, the ply thickness. The factor ε^2 shows that the available energy is proportional to the square of the strain level. O'Brien concedes that this equation only gives a value for total energy released. An approach such as virtual crack closure is necessary to determine the relative contribution of the various modes. He includes no provisions for any more general delamination geometry and makes no attempt to account for the effects of the interlaminar stress boundary region.

O'Brien's equation can be applied to the delamination initiation in a laminate if it is assumed that there is one critical value of strain energy release rate, G_c, for delamination initiation. In cases in which the effective ply thickness is varied by stacking plies of the same angular orientation together, it predicts that initiation stress will be inversely proportional to the square root of the effective ply thickness. He was able to get reasonable agreement for his data for delamination initiation of $[+45_n/-45_n/0_n/90_n]_s$ specimens. He concluded that this method was "sufficient" for the purposes of preliminary design.

In a subsequent paper, O'Brien et al. [27] compared the utility of a width tapered double cantilever beam (WTDCB) specimen with a $[\pm30/\pm30/90/\overline{90}]_s$ "edge delamination specimen" to measure the critical value of strain energy release rate. They computed G_c for the edge delamination specimen using equation 2.1 and the delamination initiation onset strain. They determined the mode I component of strain energy release rate, G_I, in the edge delamination case using the virtual crack closure method. They found it was significantly lower than the critical value, G_{Ic}, determined from the WTDCB specimen data and that data from both types of tests are necessary to quantify a material's "interlaminar fracture toughness".

O'Brien [28] then attempted to quantify the effect of mode I contribution to strain energy release rate on the critical value of total strain energy release rate. He varied lamination sequences so that the total strain energy release rate remained constant while the mode I contribution varied. He concluded that for brittle resin systems under static loading, the criterion for onset of delamination was that G_I reach a critical value. Further experiments by O'Brien et al. [29] indicated that "toughened" resins had lower critical values of G_I when the mode I contributions constituted a smaller percentage of total strain energy release rate.

The strain energy release rate approach is based on a sound principle: events can only occur if they are energetically feasible. Nonetheless, the proposed forms have some problems. Both the virtual crack closure method and the O'Brien equation assume simplified geometry and a constant strain level with respect to longitudinal position. This will most likely not be the case for a delamination in a general laminate. Additionally, data can only be correlated with the O'Brien equation if G_c is taken to be a function of the mode I contribution to the strain energy release rate. At present, this requires finite element modeling and a large data base. This nullifies the benefits gained from having a simple approach.

Of the papers dealing with strain energy release rate as a method for predicting or correlating delamination initiation [5,6,22-29], only Wang and Crossman [6] mention preexisting delaminations in their derivation. Nonetheless, fracture mechanics methodologies are derived in terms of crack tip stress fields. The virtual crack closure results show that the strain energy release rate approaches zero for such small delaminations. This brings into question the applicability of fracture mechanics methodologies to delamination initiation. If no crack of sufficient size and proper orientation exists at the free edge, then there may not be sufficient concentration of stresses to bring about crack extension. Broek [30] has stated, "The energy criterion is a necessary criterion for crack extension. It need not be a sufficient criterion." Hence, delamination may have to initiate via some other mechanism before fracture mechanics methodologies can apply. Once the delamination has initiated, however, this delamination may itself serve as a crack of sufficient size for fracture mechanics methodologies to apply.

2.2.3 Average Stress Mechanics of Materials Approaches

Wang and Choi [19] suggested the existence of a stress singularity at the free edge. Although the region over which this effect is important may be extremely small in most cases, a singularity brings into question the applicability of straightforward mechanics of materials approaches. The free edge is an example of a small region of high stress and high stress gradients. In one sense, it is akin to the stress concentration at the edge of a hole. In the case of a hole in a composite specimen, data suggests the stress at the edge of the hole far exceeds the in-plane strength of the laminate. To deal with this effect in holes, Whitney and Nuismer [31] introduced the "average stress" concept. They averaged the theoretical longitudinal stress (σ_{11}) over a distance from the edge of the hole. The general equation for an average stress is:

$$\bar{\sigma}_{ij} = \frac{1}{x_{avg}} \int_0^{x_{avg}} \sigma_{ij} \, dx \tag{2.2}$$

where: σ_{ij} = stress component
$\bar{\sigma}_{ij}$ = average stress component
x = distance from a reference edge
x_{avg} = averaging dimension.

They predicted failure when this stress reached a critical value.

In an analagous fashion, the theoretical values of interlaminar shear and normal stresses far exceed reasonable strength parameters before delamination initiation is observed. Kim and Soni [4] thus attempted to correlate delamination initiation with an average value of interlaminar normal stress. They averaged the stress over one nominal ply thickness and approximated the interlaminar normal strength by the transverse strength of the unidirectional composite. The resulting criterion was therefore that delamination initiates when:

$$\bar{\sigma}_{zz} = Y^t \tag{2.3}$$

where: Y^t = in-plane transverse strength of the unidirectional composite.

They only considered tensile interlaminar normal stress capable of initiating delamination. Their results demonstrated that the theoretical value of the interlaminar normal stress far exceeded the estimated strength.

In a subsequent investigation, Kim and Soni [32] analyzed the effect of the interlaminar shear stress σ_{1z}. They averaged this shear component over one nominal ply thickness and estimated the interlaminar shear strength as the in-plane shear strength of the unidirectional composite. The resulting criterion was that delamination initiates when the absolute magnitude of the average interlaminar shear stress reached the estimated shear strength:

$$\left|\bar{\sigma}_{1z}\right| = S \tag{2.4}$$

where: S = in-plane shear strength of the unidirectional composite.

Reasonable agreement was obtained. They did not discuss which interlaminar stress component was more important or how to choose between the two criteria they proposed.

Kim and Soni [33] then proposed a general criterion which included the effects of all interlaminar stress components. The criterion stated that delamination would initiate when:

$$F_{zz}\bar{\sigma}_{zz}^2 + F_{tt}\bar{\sigma}_{1z}^2 + F_{uu}\bar{\sigma}_{2z}^2 + F_z\bar{\sigma}_{zz} + F_t\bar{\sigma}_{1z} + F_u\bar{\sigma}_{2z} = 1 \qquad (2.5)$$

where the coefficients could be determined by relevant in-plane shear and transverse strength tests. After eliminating terms dependent on the sign of shear stress, the criterion reduces to:

$$F_{zz}\bar{\sigma}_{zz}^2 + F_{tt}\bar{\sigma}_{1z}^2 + F_{uu}\bar{\sigma}_{2z}^2 + F_z\bar{\sigma}_{zz} = 1 \qquad (2.6)$$

They achieved good agreement with their data.

The linear term in interlaminar normal stress is quite significant. It implies that compressive average interlaminar normal stress can inhibit delamination initiation in cases in which interlaminar shear stress dominates. Kim and Soni performed no experiment to directly test this hypothesis.

Brewer and Lagace [34] proposed a similar criterion for delamination initiation. The Quadratic Delamination Criterion states that delamination will initiate when:

$$\left(\frac{\bar{\sigma}_{1z}}{Z^{s1}}\right)^2 + \left(\frac{\bar{\sigma}_{2z}}{Z^{s2}}\right)^2 + \left(\frac{\bar{\sigma}^c_{zz}}{Z^c}\right)^2 + \left(\frac{\bar{\sigma}^t_{zz}}{Z^t}\right)^2 = 1 \qquad (2.7)$$

where: $\bar{\sigma}^t_{zz}$ = tensile values of $\bar{\sigma}_{zz}$
$\bar{\sigma}^c_{zz}$ = compressive values of $\bar{\sigma}_{zz}$
Z^{s1} = interlaminar shear strength for σ_{1z}
Z^{s2} = interlaminar shear strength for σ_{2z}
Z^t = tensile interlaminar normal strength
Z^c = compressive interlaminar normal strength

The averaging dimension is a fit parameter rather than set equal to a value determined by composite material producers. The interlaminar strength parameters can, in theory, be measured by direct experiment. Lagace and Weems [35] have shown that there can be a significant difference between in-plane transverse strength and out-of-plane normal strength. The difference between the effects of tensile and compressive average interlaminar normal strength are accounted for by explicitly separate quadratic terms rather than a linear term. This dismisses the ability of compressive average interlaminar normal stress to suppress initiation controlled by interlaminar shear stress.

Brewer and Lagace [34] tested $[\pm15_n]_s$, $[\pm15_n/0_n]_s$, and $[0_n/\pm15_n]_s$ laminates to find delamination initiation stress. A computer-controlled testing program was used. The program automatically stopped a test when a drop in load, possibly indicative of the increase in compliance accompanying delamination initiation, was detected. Delamination initiation was verified using the edge replication techniques described by Klang and Hyer [36]. They obtained excellent agreement with their data. The averaging dimension was found to be on the order of a ply thickness but not equal to it. This was verified by using prepregs of the same material with two different nominal ply thicknesses.

Brewer and Lagace found that the use of O'Brien's approach [26] resulted in calculated values of G_c that varied by a factor of up to three for laminates of the same lamination sequence with different effective ply thicknesses even though the percentage of mode I contribution was the same. Calculations showed that the delamination initiation of the $[\pm 15_n]_s$, $[\pm 15_n/0_n]_s$, and $[0_n/\pm 15_n]_s$ laminates were dominated by the interlaminar shear stress σ_{1z}.

Delamination initiation appears to be controlled by strength considerations. The strain energy release rate cannot consistently predict behavior in laminates with different ply thicknesses and different fractions of G_I. It may not apply directly to delamination before initiation occurs. The average stress mechanics of materials approaches appear to work well for the laminate types tested to date. Nonetheless, more work needs to be done to verify the applicability of these approaches to laminates which are not dominated by interlaminar shear and in which other effects, such an thermally-induced interlaminar stresses, are important. The Quadratic Delamination Criterion will be used to correlate delamination initiation in this investigation because it relies on an experimentally derived averaging dimension rather than a manufacturing parameter.

2.3 Delamination Growth

The next phase of damage development is delamination growth. If delamination initiation can serve as a sufficiently large interlaminar crack, fracture mechanics methodologies are more likely to be sufficient as well as necessary conditions. The strain energy release rate curves that were generated to describe delamination initiation [5,6,22-29] can also be used to describe delamination growth. Rybicki et al. [5] calculated the critical value for strain energy release rate as a function of delamination size. They found it was nearly constant during growth.

Wang et al. [6,24] believed they could describe growth using the virtual crack closure approach. They argued that the asymptote of the R-curve could be approximated by the constant G_c as shown in Figure 2.3. Recall that the strain energy available for release is proportional to the square of the strain level. The hump in the strain energy release rate curve and the R-curve crossed at stable delamination sizes as long as the R-curve extended above the strain energy release rate curve at larger delamination sizes. For an asymptotic

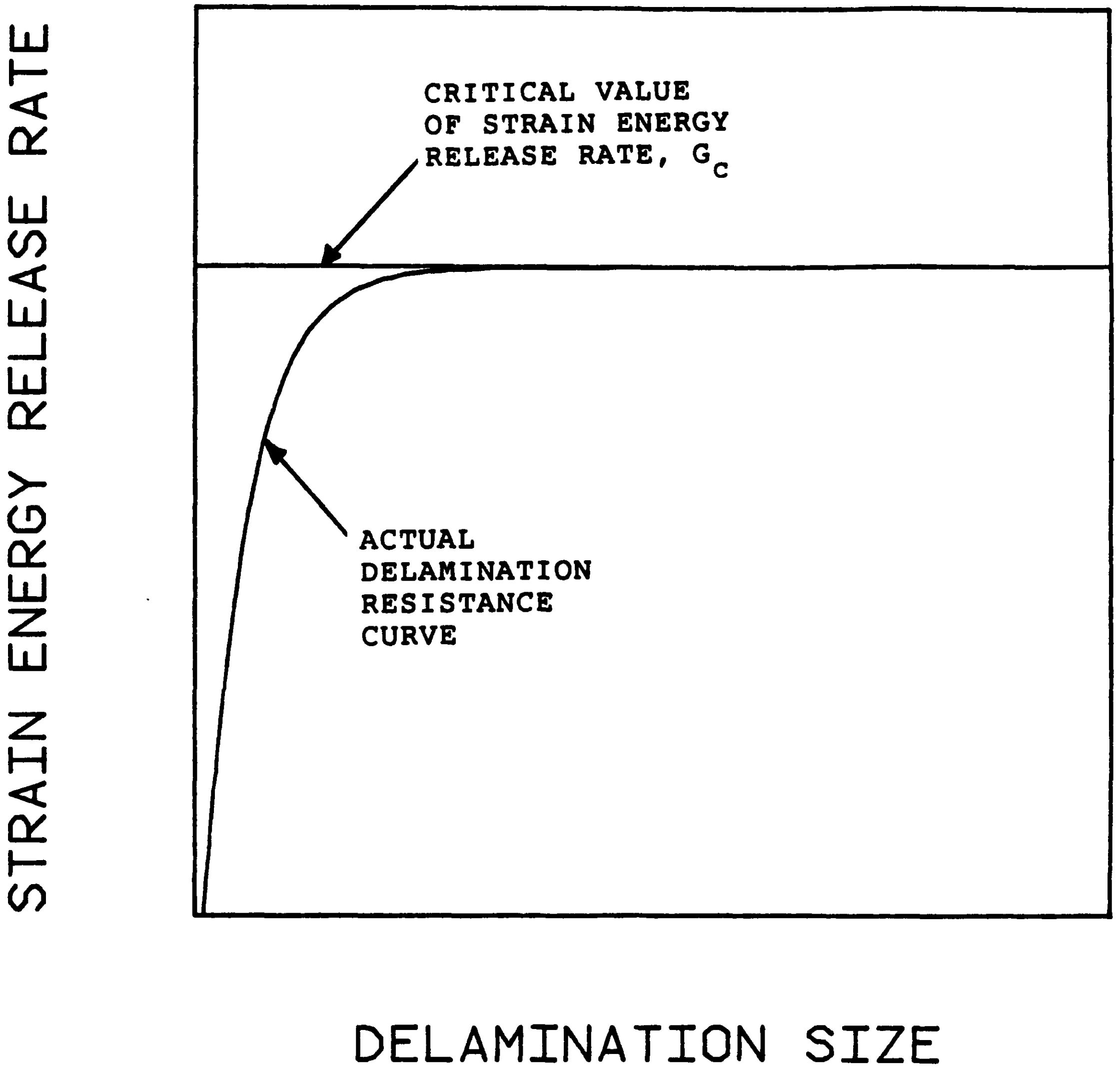

FIGURE 2.3 SCHEMATIC OF THE DELAMINATION RESISTANCE CURVE AS APPROXIMATED BY A CRITICAL VALUE OF STRAIN ENERGY RELEASE RATE

R-curve, this is only possible when the strain energy release rate curve has a negative slope, such as on the back side of the hump as shown in Figure 2.4. As the strain level increased and the strain energy release rate curve shifted upward, stable delamination growth would occur. The local minimum in the strain energy release rate curve represents a maximum stable delamination size. Once the strain energy release rate curve shifted above the R-curve unstable delamination growth could occur. Since the virtual crack closure method is based on a two-dimensional finite element model, the direct applicability of the results to delaminations other than constant width delaminations along the free edge is questionable.

In a subsequent paper by Crossman and Wang [23], the observed behavior did not match the predicted delamination growth pattern for several $[\pm 25/90_n]_s$ laminates. These specimens incurred transverse cracking before delamination initiation. The authors were prompted to conclude that "a more detailed analysis is shown to be necessary for the prediction of ... delamination growth." Kim and Hong [25] stated that the strain energy release rate approach describes the delamination growth region they observed in angle ply laminates.

O'Brien [26] proposed that his approach could be used to describe delamination growth. The assumptions made in his derivation make his approach directly applicable only if the delamination has a constant width along the free edge and no

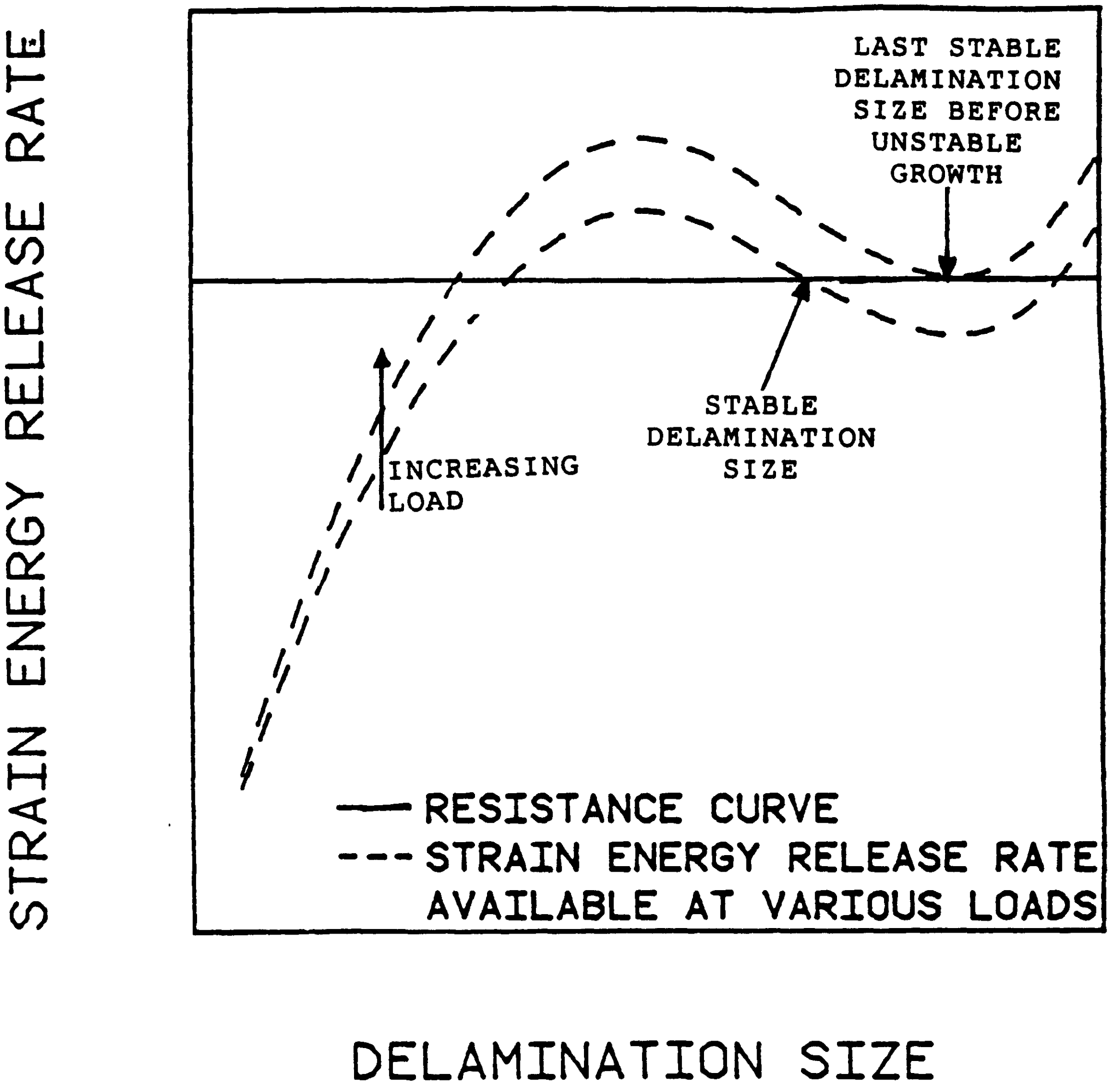

FIGURE 2.4 SCHEMATIC OF THE STRAIN ENERGY RELEASE RATE CURVES AT VARIOUS POINTS DURING STABLE AND UNSTABLE DELAMINATION GROWTH

quantity such as longitudinal strain is a function of longitudinal position. The equation predicts strain energy release rate to be independent of delamination size. He merely assumes that the delamination resistance curve is a more general function of delamination size. He uses his expression and actual data of delamination size and strain level for $[\pm 30/\pm 30/90/\overline{90}]_s$ specimens to generate an R-curve that he believes can be extended to other laminate types.

The strain energy release rate approach may be able to describe delamination growth in the general case. In its present form, it has limited applicability to general delamination shapes with complicated strain fields. An approach should be developed which accounts for the characteristics of more general delamination geometries.

2.4 Delamination Failure

The experimental trend documented in the literature is that laminates prone to delamination will fail at lower stresses as the layer thickness increases. Herakovich [20] found this for his alternating and clustered laminates. Lagace et al. [37] found this for $[\pm 15_n]_s$, $[\pm 15_n/0_n]_s$, $[0_n/\pm 15_n]_s$, and $[\pm 45_n/0_n]_s$ specimens. No difference in strength was found for $[[0/\pm 15]_s]_n$ specimens. Strain energy release rate approaches would suggest that this would be the trend for delamination initiation and growth, but not explicitly for final failure. Wang et al. [24] do however imply in their conclusion that unstable growth is "for all practical purposes ... a good estimate of ultimate strength."

Kim and Hong [25] noted that final failure is not as simple as that. The delamination has caused the resulting sublaminates to release their constraint on one another, not necessarily to fail. They suggested that final failure should be evaluated after delamination in terms of the in-plane strength of the sublaminates, in their case, unconstrained angle plies.

The in-plane strength of laminates and sublaminates is therefore relevant to this investigation. One criterion which shows good agreement with in-plane tensile fracture data of graphite/epoxy is the generalized stress interaction criterion of Tsai and Wu [38]. The criterion is applied on a ply by ply basis to the in-plane stress state calculated by Classical Laminated Plate Theory. The criterion can be written as a general polynomial of order n. The most useful version is the quadratic form. In tensor notation, the criterion is written as:

$$F_{\alpha\beta}\sigma_{\alpha\beta} + F_{\alpha\beta\sigma\gamma}\sigma_{\alpha\beta}\sigma_{\sigma\gamma} = 1 \qquad (2.8)$$

Since the criterion is applied to the in-plane stress state, the indices α, β, σ, and γ can assume the values of 1 and 2. It can be reasoned that terms linear in shear stress should be eliminated because the definition of positive shear stress is dependent on the selection of the coordinate system. Once these terms are removed, six $F_{\alpha\beta}$ and $F_{\alpha\beta\sigma\gamma}$ coefficients remain. Five of these can be determined for a composite material by performing uniaxial compressive and tensile tests along the two major axes and a shear test of the basic material (e.g. a $[0_n]$ laminate for unidirectional tape) [38]. The sixth coefficient is F_{1122}. This quantifies the interaction between the longitudinal and transverse stresses in biaxial loading. If the general criterion is assumed to take the form of a von Mises criterion in the principal loading axes, the value of the interaction term is given by [38]:

$$F_{1122} = -\frac{1}{2} \sqrt{F_{1111} F_{2222}} \qquad (2.9)$$

This is the form of F_{1122} used in the version of the criterion that has been used to achieve good agreement.

Little work has been done explicitly on the correlation of final in-plane failure of specimens which experience significant delamination damage. Although the generalized criterion of Tsai and Wu shows good agreement with in-plane failure when there is no delamination, its applicability to the final in-plane failure of delaminated specimens should be evaluated.

CHAPTER 3

APPROACH TO PRESENT WORK

3.1 Overview

The present work is a synthesis of related experimental and analytical efforts designed with the objective of describing and understanding the sequence of events which lead to failure of graphite/epoxy laminates induced by delamination. Delamination has three major phases [6]: initiation, growth, and final failure. The approach for investigating each phase will be put forth in subsequent sections in this chapter. Details of the experiments, analysis, and results will be discussed in the appropriate chapters.

Although a great deal of work has been done on initiation, two important issues remain to be resolved. They are the applicability of criteria when the interlaminar normal stress is the primary interlaminar stress contributing to delamination and the importance of thermally-induced interlaminar stresses. In the delamination initiation portion of this investigation, these issues will be explored experimentally and explained in terms of existing models.

The objective of the delamination growth and final failure portion of this investigation is to gain insight into the details of the damage sequence in general laminates. The strain energy release rate approach has been touted as being capable of describing all phases of delamination [6]. Although it has been shown to give poor correlation when describing delamination initiation [34], the versions presently available can describe some stable and unstable growth behavior. The models in their present forms have limitations, however. For example, the virtual crack closure and O'Brien methods do not model transverse cracks in 90° sublaminates. Modifications would need to be made to accurately predict the "premature" initiation that often accompanies transverse cracks. The Quadratic Delamination Criterion could be applied with minimal modification if the interlaminar stress state were known in the vicinity of the transverse crack. The issue of whether or not final failure is coincident with unstable delamination growth will be explored. The validity of failure models will also be ascertained.

The results of the experiments will be used to delineate possible modifications to the strain energy release rate models so that these models more closely reflect the observed damage progression. Modifications will be made and evaluated.

3.2 Interlaminar Normal Stress and Delamination Initiation

Excellent correlation of the delamination initiation stress for the various laminates tested in Reference 34 has been achieved with the Quadratic Delamination Criterion. One averaging dimension gave excellent correlation for all laminates and all ply thicknesses, suggesting that the averaging dimension is a material parameter. However, two issues remain with regard to the use of this criterion for general prediction of delamination initiation. The criterion was tested only on laminates in which delamination initiation was controlled primarily by the interlaminar shear stress, σ_{1z}, and the contributions of thermally-induced interlaminar stresses were relatively small. The average value of the other interlaminar shear stress, σ_{2z}, will normally be negligible in these cases since it is required by the boundary conditions to be zero both in the laminate interior and at the free edge. However, there are laminates in which the interlaminar normal stress, σ_{zz}, can be important. The Quadratic Delamination Criterion can be further verified by isolating the effects of the interlaminar normal stress as well as by choosing laminates with large contributions of thermally-induced interlaminar stresses.

Kassapoglou and Lagace [16] have shown that in uniaxially loaded specimens, σ_{1z} is mainly a function of the in-plane shear stress σ_{12}. In cases where σ_{12} is zero throughout the laminate, the σ_{1z} component will be identically zero [17]. Only if all the plies have extensional-shear coupling terms (A_{1112} and A_{2212} in standard tensorial notation for Classical Laminated Plate Theory) equal to zero can σ_{12} be avoided. The only plies of orthotropic fibrous materials with this behavior are those with angular orientations of the fibers of 0° and

90° to the longitudinal axis. A cross-ply laminate could therefore potentially have significant σ_{zz} and no σ_{1z} [17].

Conventional cross-ply laminates have an unacceptable disadvantage in the context of this investigation. As has been noted in the literature [e.g. 23], 90° plies in laminates are often susceptible to transverse cracking. The points where the transverse cracks meet the interlaminar interface are potential sites of "premature" delamination initiation. The effects of these transverse cracks (e.g. on the local interlaminar stress state or the strain energy release rate) would have to be evaluated before the presently available delamination initiation models could be properly applied. Solutions for this effect are not available. It is therefore desirable to avoid 90° plies.

The only other option is to use 0° plies of two or more composite systems with different elastic parameters. Other unidirectional materials such as kevlar/epoxy and glass/epoxy have two distinct disadvantages. First, they usually contain different matrix systems which are not necessarily compatible with the graphite/epoxy cure cycle. The experimentally determined averaging dimension and the interlaminar normal strength parameter would have questionable applicability to either system. Second, there is not a sufficient difference in transverse properties to induce significant transverse stresses, σ_{22}. The interlaminar normal stress is a function of the in-plane transverse stresses. Hence, the interlaminar normal stress would most likely be too small to cause delamination initiation before in-plane failure.

The only composite material which will suit the needs of the experiment is a woven graphite/epoxy fabric material. A fabric made from the same fiber and matrix would be compatible for curing and more likely to give consistent values for interlaminar normal strength and averaging dimension. The desired interlaminar stress state can be obtained by including plies of graphite/epoxy fabric in the laminate. Although there are 90° fiber tows in the fabric, splitting of these tows before delamination initiation is likely to be inhibited by the weave of the fabric.

The materials used in this investigation were Hercules AS4/3501-6 unidirectional preimpregnated graphite/epoxy tape and Hercules AW370-5H/3501-6 five-harness satin weave preimpregnated graphite/epoxy fabric. Both material systems are manufactured with the AS4 fiber and 3501-6 epoxy.

Three laminate types were chosen for this experiment. They are $[0_{5U}/0_F]_s$, $[0_{5U}/0_F/0_U]_s$, and $[0_{10U}/0_F]_s$, where the subscripts "U" and "F" denote unidirectional and fabric plies, respectively. These gave reasonable values of interlaminar normal stress. The mechanically-induced components of the interlaminar normal stress were calculated using the method of Kassapoglou and Lagace [17]. These components, as related to the applied far-field stress, for the three laminate types are depicted in Figure 3.1. The material parameters used in the calculations are given for the unidirectional and fabric systems in Table 3.1. The interlaminar normal stresses were

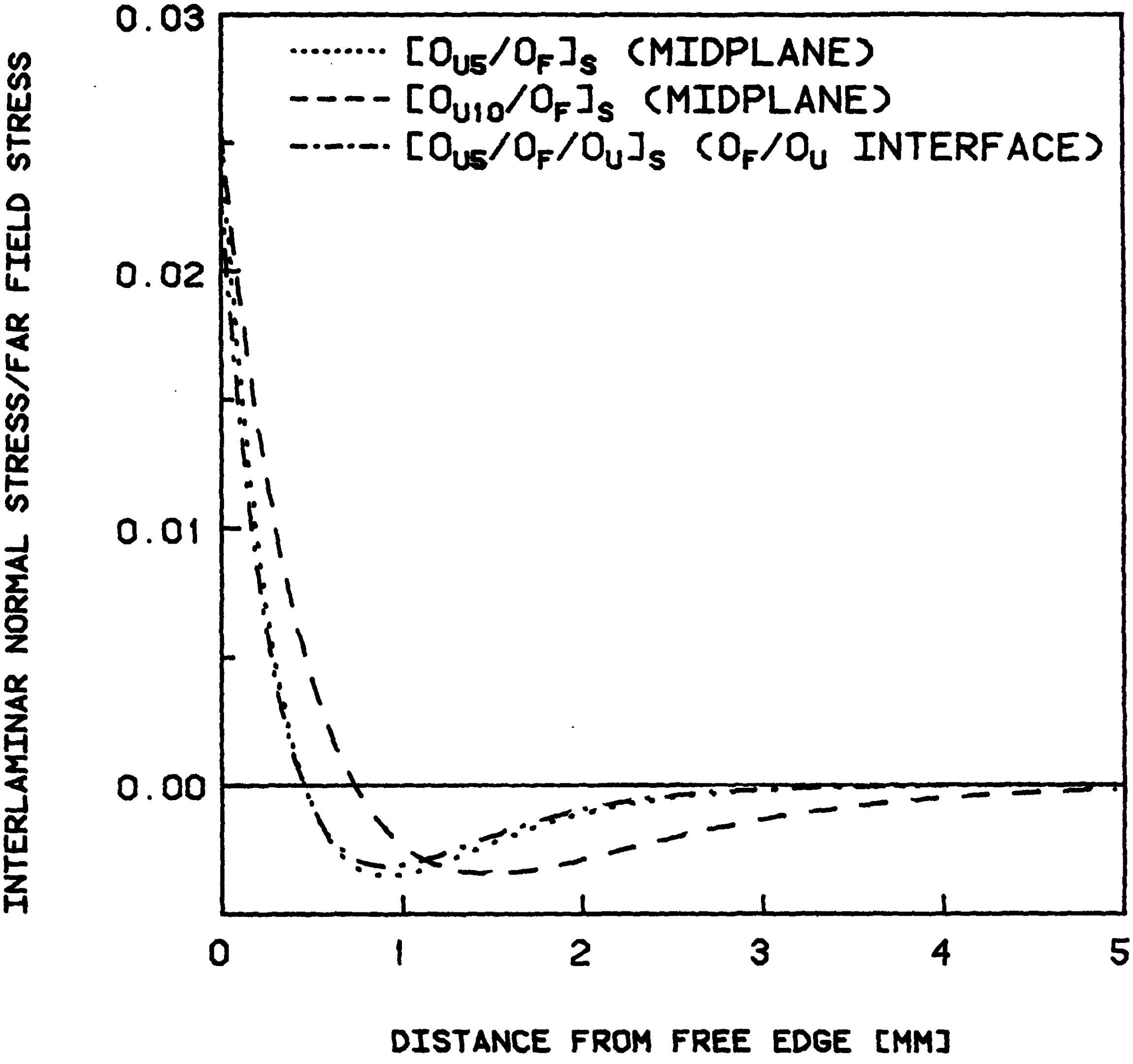

FIGURE 3.1 MECHANICALLY-INDUCED INTERLAMINAR NORMAL STRESS FOR $[0_{U5}/0_F]_s$, $[0_{U10}/0_F]_s$, AND $[0_{U5}/0_F/0_U]_s$ SPECIMENS

TABLE 3.1

MATERIAL PARAMETERS OF
HERCULES AS4/3501-6 UNIDIRECTIONAL GRAPHITE/EPOXY
AND HERCULES AW370-5H/3501-6 FABRIC GRAPHITE/EPOXY

	AS4/3501-6	AW370-5H/3501-6
t_{ply}	0.134 mm	0.35 mm
E_{11}	142 GPa	72.5 GPa
E_{22}	9.81 GPa	72.6 GPa
E_{33}	9.81 GPa	10 GPa
G_{12}	6.0 GPa	4.43 GPa
G_{13}	6.0 GPa	4.43 GPa
G_{23}	4.8 GPa	4.43 GPa
ν_{12}	0.3	0.059
ν_{13}	0.3	0.3
ν_{23}	0.34	0.3
α_{11}	-0.2 μstrain/°F	1.29 μstrain/°F
α_{22}	16.0 μstrain/°F	1.29 μstrain/°F

plotted for the critical interfaces. Since only the interlaminar normal stress was significant for these specimens, the critical interface was the one with the highest value of this component of interlaminar stress. The critical interface was the midplane for the $[0_{5U}/0_F]_s$ and $[0_{10U}/0_F]_s$ specimens and the $0_F/0_U$ interface for the $[0_{5U}/0_F/0_U]_s$ specimens.

The thermally-induced components of the interlaminar normal stress were calculated using the method of Lagace, Kassapoglou, and Brewer [18] and found to be significant. The change in temperature used to calculate the thermally-induced stress state was -156°C. This is the difference between the set temperature of the epoxy matrix during curing (177°C) and room temperature (21°C). The influence of thermally-induced stresses can thus be evaluated. The thermally-induced interlaminar normal stress components are depicted in Figure 3.2. The stress distribution for each specimen type is plotted for the critical interface. The critical interfaces are the same ones observed for the mechanically-induced stresses.

One laminate of each type was constructed. From each laminate, five standard TELAC specimens were manufactured. The standard specimen is 50 mm wide and 350 mm long with a 200 mm long test section as illustrated in Figure 3.3. These specimens were tested to determine their delamination initiation stress. Table 3.2 is the test matrix for this portion of the investigation.

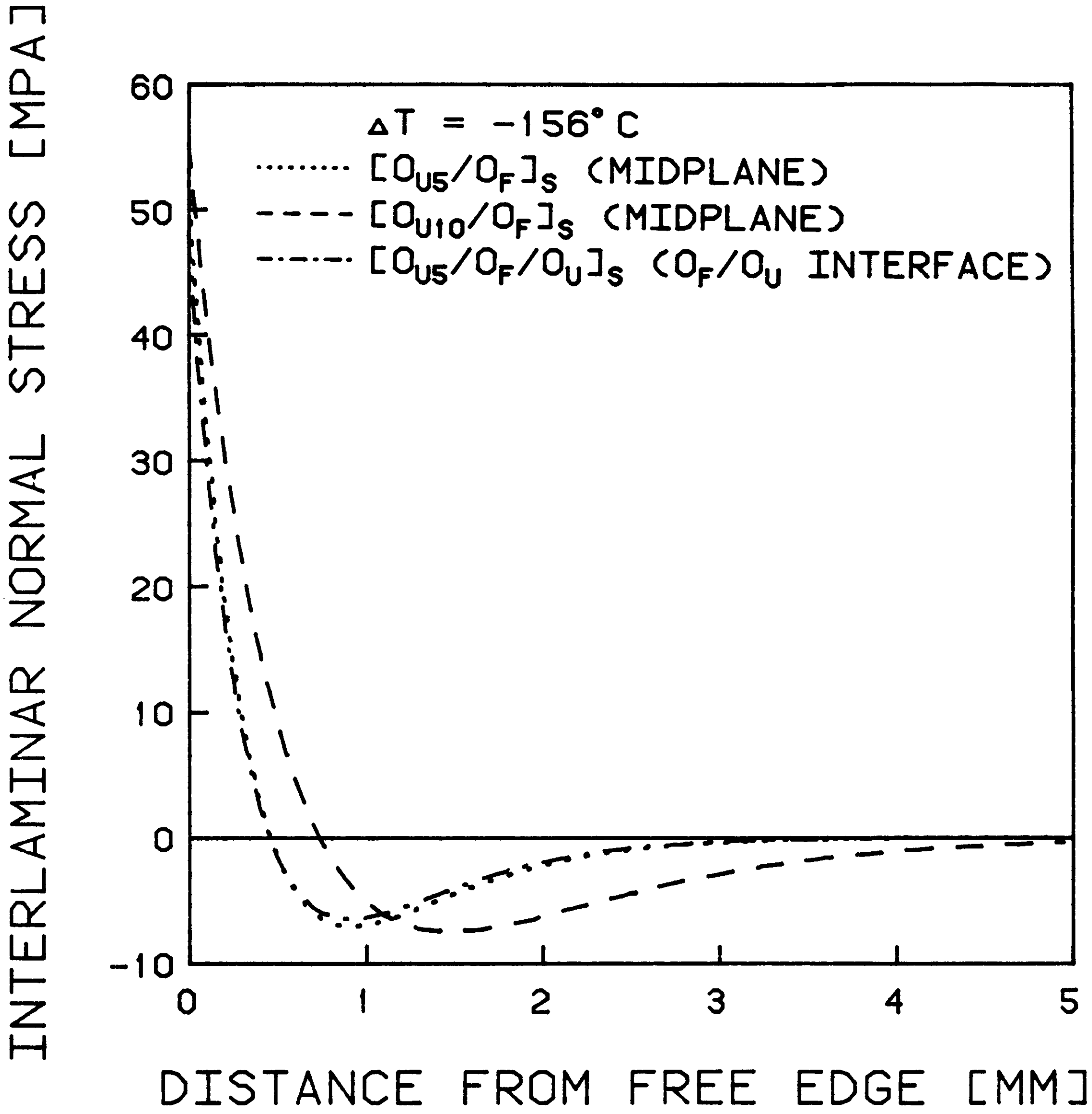

FIGURE 3.2 THERMALLY-INDUCED INTERLAMINAR NORMAL STRESS FOR $[0_{U5}/0_F]_s$, $[0_{U10}/0_F]_s$, AND $[0_{U5}/0_F/0_U]_s$ SPECIMENS

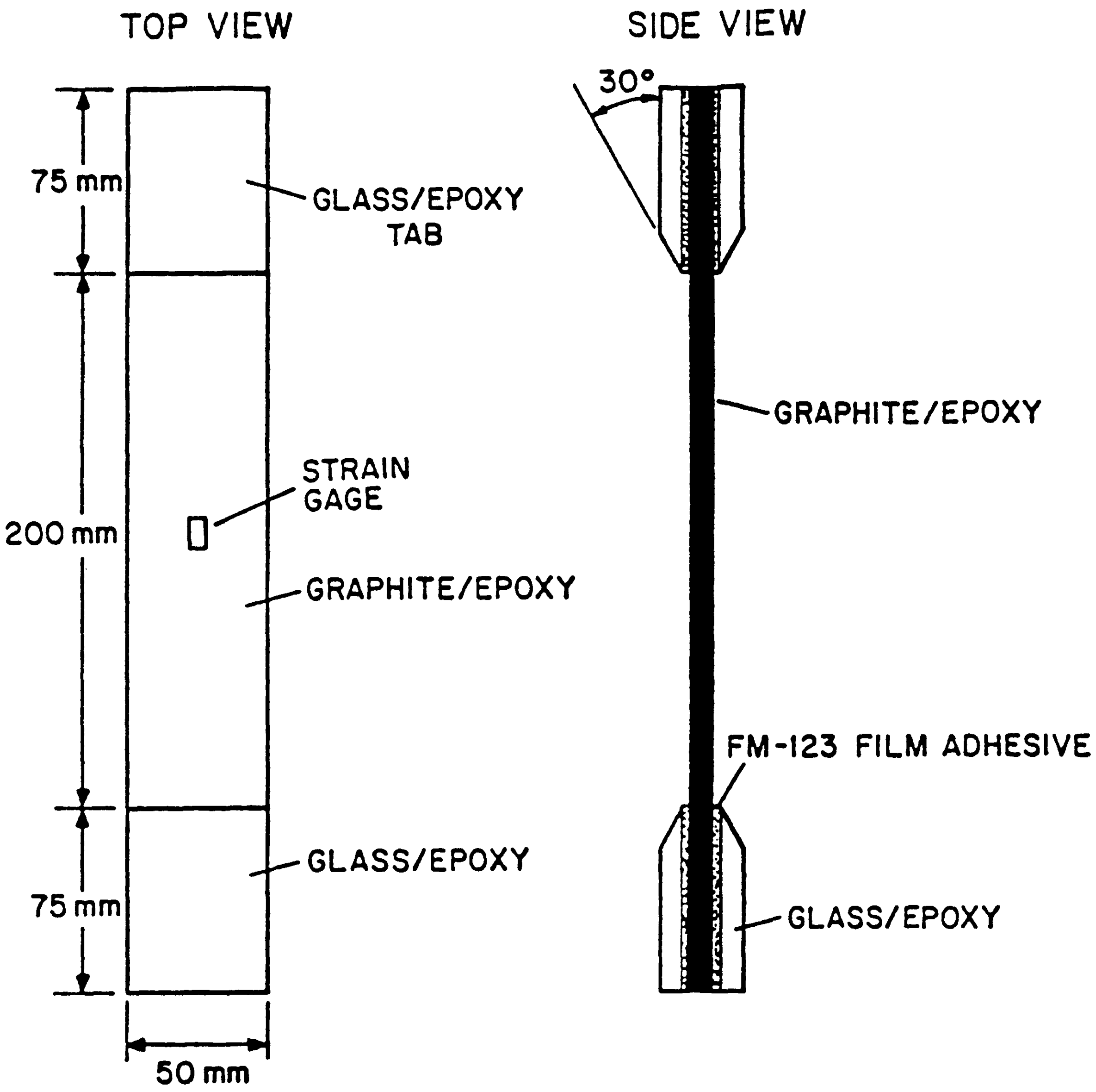

FIGURE 3.3 STANDARD TELAC TEST SPECIMEN

TABLE 3.2

TEST MATRIX FOR DELAMINATION INITIATION SPECIMENS

Laminate Type[a]	Number of Specimens
$[0_{5U}/0_F]_s$	5
$[0_{5U}/0_F/0_U]_s$	5
$[0_{10U}/0_F]_s$	5

[a] Subscript "U" refers to plies of unidirectional graphite/epoxy tape. Subscript "F" refers to plies of woven graphite/epoxy fabric.

3.3 Delamination Growth and Final Failure

Several variables were investigated to determine their effect on delamination growth and final failure. These are specimen width, effective ply thickness, lamination sequence, character of the ply interface, and implantation of simulated delaminations and angle ply splits.

The majority of research involving delamination has been done on specimens containing 90° plies. Transverse cracks often develope in these plies and serve as sites for "premature" delamination initiation. In order to avoid this phenomenon, laminates containing 90° plies were not used in this investigation.

An excellent method for observing internal damage such as delamination is a non-destructive evaluation technique such as dye penetrant-enhanced x-radiography. An x-radiograph can determine delamination shape and size, as well as other characteristics including quantity and position of splits within the plies. Many specimens in this portion of the investigation were tested to predetermined loads, their damage state evaluated using x-radiography, and retested. All specimens were eventually tested to failure.

The first variable investigated was specimen width. This was selected to evaluate the hypothesis that a critical delamination area may exist for unstable delamination growth or in-plane failure. The results from the specimens with nonstandard widths can be used to determine if such a critical size exists and if this size is a function of specimen width. For example, the critical delamination area could be a percentage of test section area or an absolute value independent of specimen width. These experiments may also detect other finite width effects.

The $[\pm15_3]_s$ laminate was chosen for these experiments because it had been shown to delaminate in a previous investigation [34] when manufactured from a similar material (Hercules AS1/3501-6). The specimens used were standard TELAC specimens except in width. The widths used in these tests were 10 mm, 20 mm, 30 mm, 50 mm, and 70 mm. These widths ranged from approximately seven to approximately 50 times the width of the interlaminar stress boundary region. The aspect ratio of the test section varied from slightly less than three to 20.

To determine the appropriate loads to which to test these specimens, it was necessary to know the delamination initiation stress and final failure stress of the $[\pm15_3]_s$ laminate. An additional two 10 mm wide specimens and two 30 mm wide specimens were manufactured and tested to determine these values. Five specimens of each width were then tested using constant stress increments from approximately 90% of the observed delamination initiation stress to final failure. Damage was assessed by dye penetrant-enhanced x-radiography after each stress increment. Table 3.3 is a test matrix for this portion of the investigation.

The next variables investigated were the lamination

TABLE 3.3

TEST MATRIX FOR $[\pm 15_3]_s$ SPECIMENS OF NONSTANDARD WIDTH

Specimen Width [mm]	Number of Specimens Tested for Delamination Initiation and Final Failure	Number of Specimens Tested to Incremental Load Levels and Monitored with Dye Penetrant-Enhanced X-Radiography
10	2	5
20	0	5
30	2	5
50	0	5
70	0	5

sequence and the effective ply thickness. Two similar laminate types were used: $[\pm15_n/0_n]_s$ and $[0_n/\pm15_n]_s$. In the AS1/3501-6 graphite/epoxy version of these laminates tested in Reference 34, delamination initiation was first observed at the +15°/-15° interface as was predicted using the Quadratic Delamination Criterion. The same interface is predicted to be the site of delamination initiation for the specimens made from AS4/3501-6 graphite/epoxy. The two laminate types have nearly identical interlaminar stress states at the +15°/-15° interface except that the interlaminar normal stress at the free edge is tensile for the $[\pm15_n/0_n]_s$ case and compressive for the $[0_n/\pm15_n]_s$ case. Another significant difference between the two laminate types is that the 0° plies can constrain delaminated and damaged angled plies in the $[0_n/\pm15_n]_s$ case. The plies can then be loaded through friction. In contrast, the $[+15_n]$ sublaminate in the $[\pm15_n/0_n]_s$ case is prone to out-of-plane peeling. That is, the delaminated portion of the sublaminate between the angle ply split and the free edge peels away from the specimen. No load can be carried by this portion of the sublaminate.

Varying the effective ply thickness has distinct effects on the interlaminar stress state as noted by Lagace et al. [37]. Increasing the effective ply thickness has the effect of "spreading out" the distributions of the interlaminar stress components while not altering the free edge magnitude. This effect is illustrated in Figure 3.4.

The strain energy release rate curve is scaled upward and

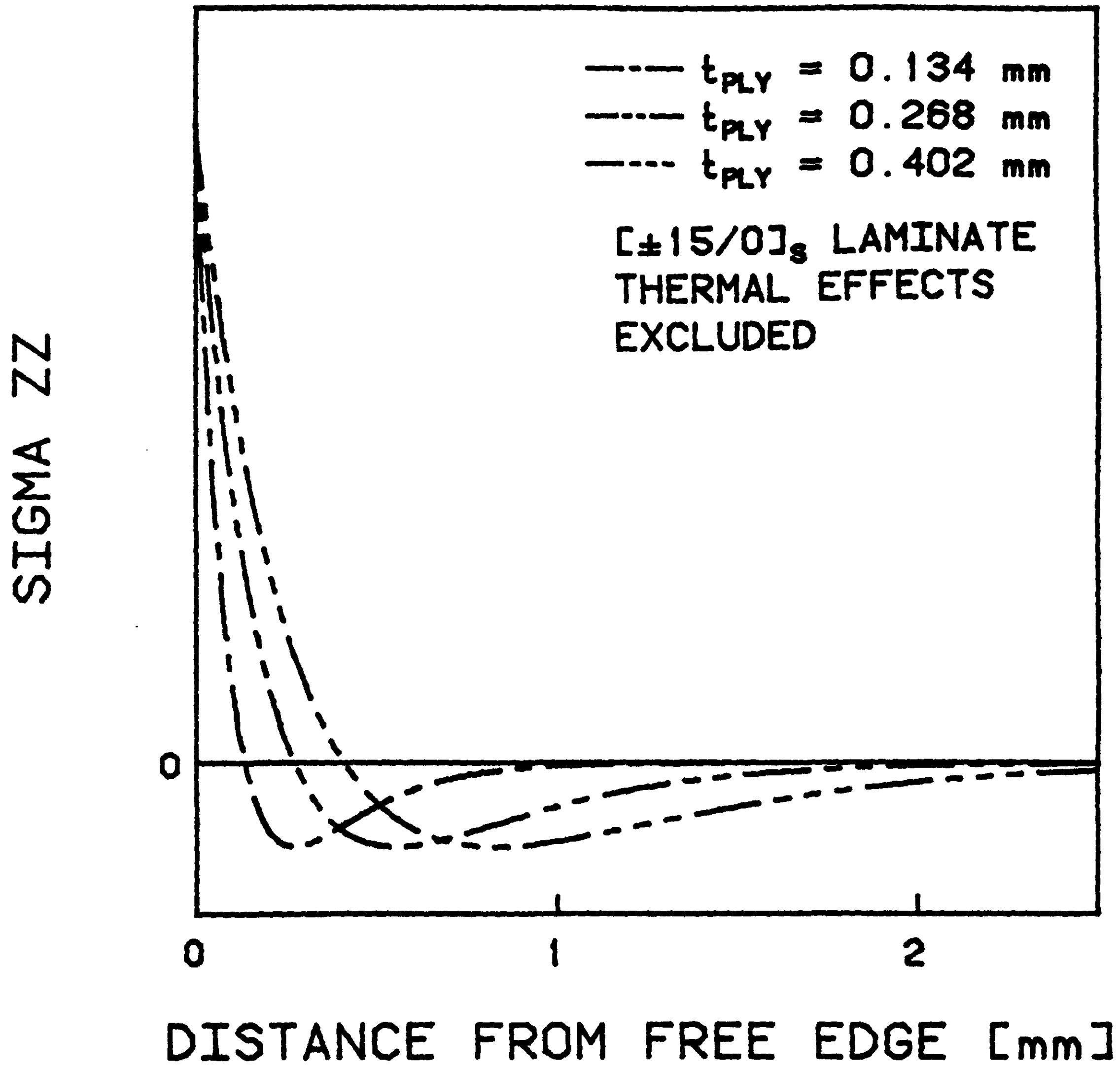

FIGURE 3.4 EFFECT OF PLY THICKNESS ON THE INTERLAMINAR STRESS STATE

spread out by the effective ply thickness factor n. This is the result of two effects. First, the energy available per unit delaminated area is directly proportional to the laminate thickness and, thus, n. Second, the interlaminar stress boundary region which influences the shape of the strain energy release rate curve near the free edge is shifted outward. The effect on the strain energy release rate curve is shown schematically in Figure 3.5. The shifting of the strain energy release rate curve does not apply as the delamination width approaches the width of the specimen. At this point, interaction with the interlaminar stress boundary region of the far side free edge must be considered. This was not an issue for any specimen in this investigation.

When the Quadratic Delamination Criterion is applied to interlaminar stress solutions with a finite free edge value such as that of Kassapoglou and Lagace [16], it gives an asymptotic lower limit for delamination initiation stress. This limit results from the fact that as the effective ply thickness becomes large, the calculated average interlaminar stress components approach the free edge values. The asymptote is the predicted initiation stress computed using the free edge values of the interlaminar stresses.

The effects on the strain energy release rate and delamination initiation stress of effective ply thickness have significant consequences. Thin laminates require a high strain level for delamination growth to be energetically feasible. Since the strain energy release rate is

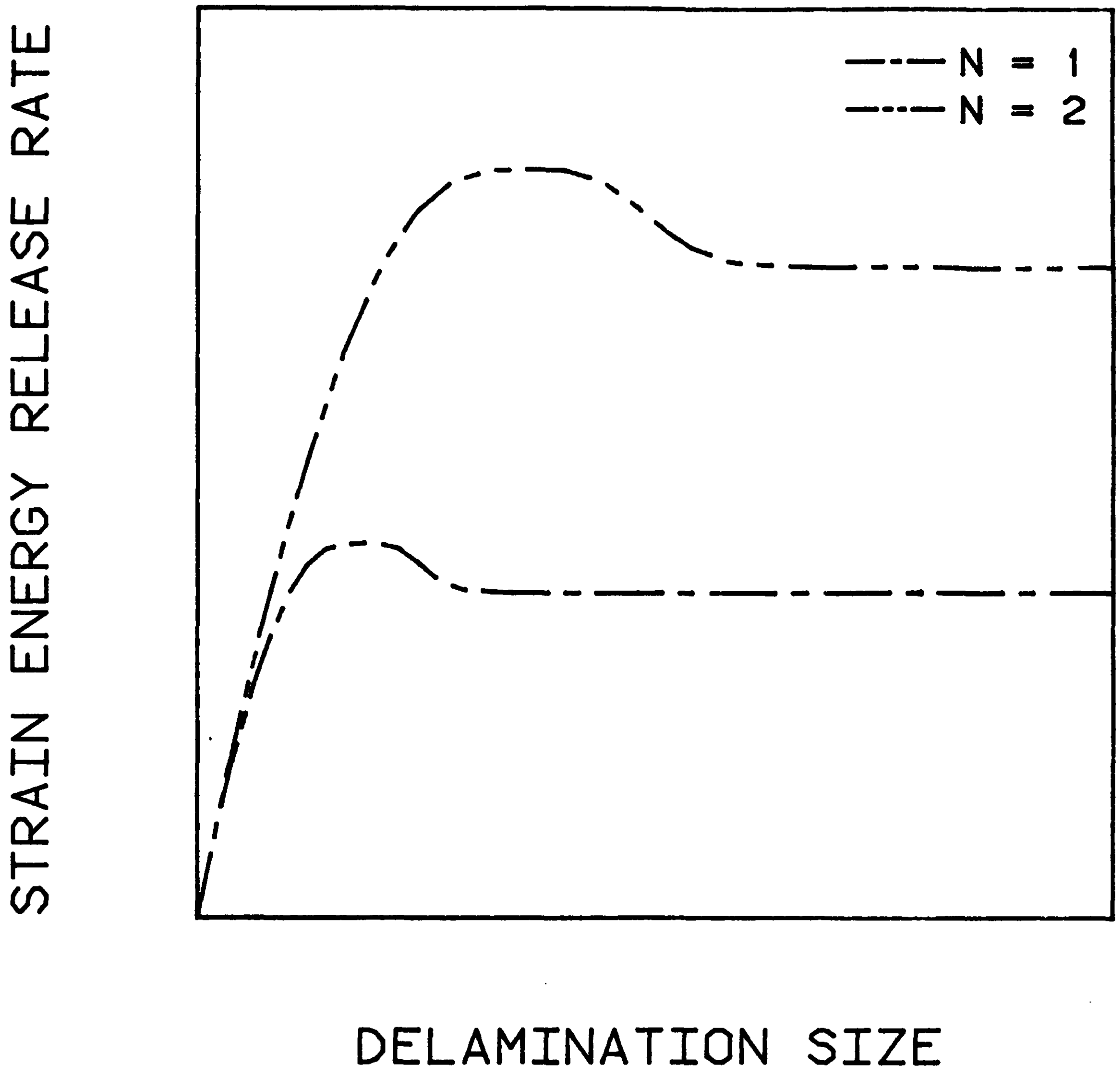

FIGURE 3.5 EFFECT OF PLY THICKNESS ON THE STRAIN ENERGY RELEASE RATE

proportional to effective ply thickness, delamination growth is energetically feasible at much lower strain levels in thick laminates. Since delamination initiation stress may have an asymptotic lower limit, delamination growth in thick laminates may be energetically feasible before delamination initiation. Thick laminates can therefore be used to determine if delamination growth can occur before the Quadratic Delamination Criterion predicts delamination initiation. To allow for a wide range of possible behavior, the values of the effective ply thickness factor, n, used in this set of experiments were 1, 2, 3, 5, and 8.

One laminate of each specimen type and effective ply thickness was manufactured. This yielded five specimens of each type. Of the five specimens, the first three were tested monotonically to failure. The remaining two were then tested incrementally from approximately 75% of the failure stress to final failure in 5% increments. The damage state was evaluated after each loading increment by dye penetrant-enhanced x-radiography. Table 3.4 is a test matrix for this set of experiments.

The third set of experiments investigated the role of angle ply split propagation in delamination growth. Two types of fabric laminates were chosen. They were both nominally $[\pm 20_F]_S$ laminates. That is, the warp fiber tows were angled at ±20° to the longitudinal axis of the specimen. All the components of the interlaminar stress state at the midplane of an angle ply laminate are identically zero. Therefore, any

TABLE 3.4

TEST MATRIX FOR $[\pm15_n/0_n]_s$ AND $[0_n/\pm15_n]_s$ SPECIMENS WITH DIFFERENT EFFECTIVE PLY THICKNESSES

Lamination Sequence	Number of Specimens Tested Monotonically to Failure	Number of Specimens Tested to Incremental Load Levels and Monitored with Dye Penetrant-Enhanced X-Radiography
$[\pm15/0]_s$	3	2
$[\pm15_2/0_2]_s$	3	2
$[\pm15_3/0_3]_s$	3	2
$[\pm15_5/0_5]_s$	3	2
$[\pm15_8/0_8]_s$	3	2
$[0/\pm15]_s$	3	2
$[0_2/\pm15_2]_s$	3	2
$[0_3/\pm15_3]_s$	3	2
$[0_5/\pm15_5]_s$	3	2
$[0_8/\pm15_8]_s$	3	2

delamination would initiate and grow at the the +20°/-20° interface. The 20° fiber angle was chosen because of the high interlaminar shear stress (σ_{1z}) obtained in this configuration and the resulting low predicted delamination initiation stress.

The difference between the experimental laminates was the character of the ply surfaces at the +20°/-20° interface. A five-harness satin weave has an "over four - under one" weave of the fiber tows as shown in Figure 3.6. This means that 80% of the exposed fibers on one face of the ply are warp fibers while 80% of the exposed fibers on the other face are fill fibers. These are referred to as the "warp face" and "fill face" of the ply, respectively. One laminate was made with only warp faces at the +20°/-20° interfaces while the other was made with only fill faces at the +20°/-20° interfaces.

Splits are observed to form within plies in association with delamination initiation. The delamination initiation is believed to be the primary damage mode since delamination initiations have been observed without splits in fabric plies, but not vice versa. It is reasoned that splits in the warp fiber tows emanating from the +20°/-20° interface at the free edge could be inhibited from growing at the point where the tows crossed "under" the fill tows. By contrast, splits in the fill fiber tows could grow farther from the free edge before crossing under a tow. The two types of specimens therefore allow for the direct comparison of specimens with essentially the same in-plane behavior and interlaminar stress

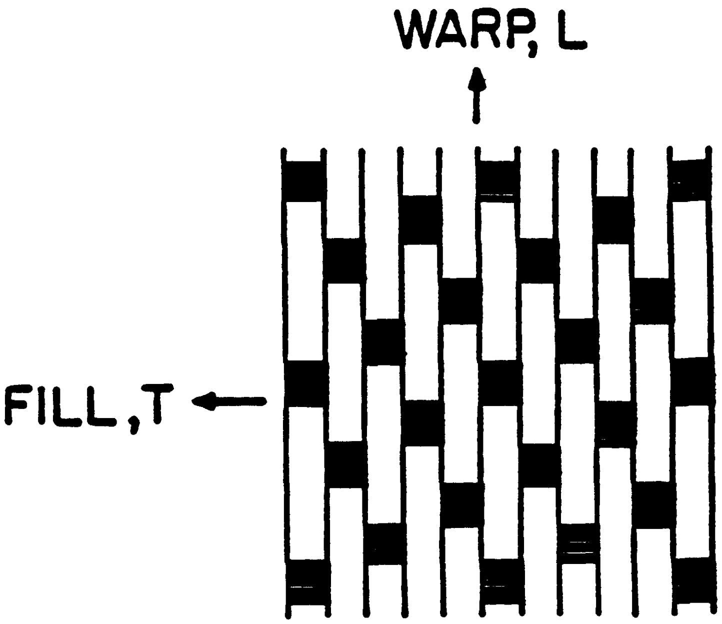

FIGURE 3.6 SCHEMATIC OF 5-HARNESS SATIN WEAVE FABRIC GRAPHITE/EPOXY

state, but a different character of the splitting state of the fiber tows closest to the delaminating interface.

The laminates each yielded five standard specimens. As with the previous set of specimens, the first three of each group were tested to failure and the remaining two were tested incrementally to failure from 75% of the failure stress, measured from the first three specimens, to failure in 5% increments. The damage state was evaluated after each loading increment by dye penetrant-enhanced x-radiography. The test matrix for this portion of this investigation is given in Table 3.5.

The interaction of the delamination front and angle ply splits was investigated in the final set of experiments. The test specimens contained "implanted" delaminations and angle ply splits. These features were achieved by implanting thin teflon film between and within the plies of a specimen before curing. The nonstick property of the teflon caused the plies to decouple at a relatively low load in a prescribed shape simulating the delamination shape observed in other experiments. This approximates a naturally occurring delamination.

The delamination shape to be investigated was triangular, bounded by the free edge, an angle ply split, and a delamination front approximately perpendicular to the split, as illustrated in Figure 3.7. The relative importance of the split and the delamination front were evaluated by manufacturing one set of specimens with no angle ply split and

TABLE 3.5

TEST MATRIX FOR $[\pm 20_F]_S$ FABRIC SPECIMENS

Character of the +20°/-20° Interface	Number of Specimens Tested Monotonically to Failure	Number of Specimens Tested to Incremental Load Levels and Monitored with Dye Penetrant-Enhanced X-Radiography
Warp/Warp	3	2
Fill/Fill	3	2

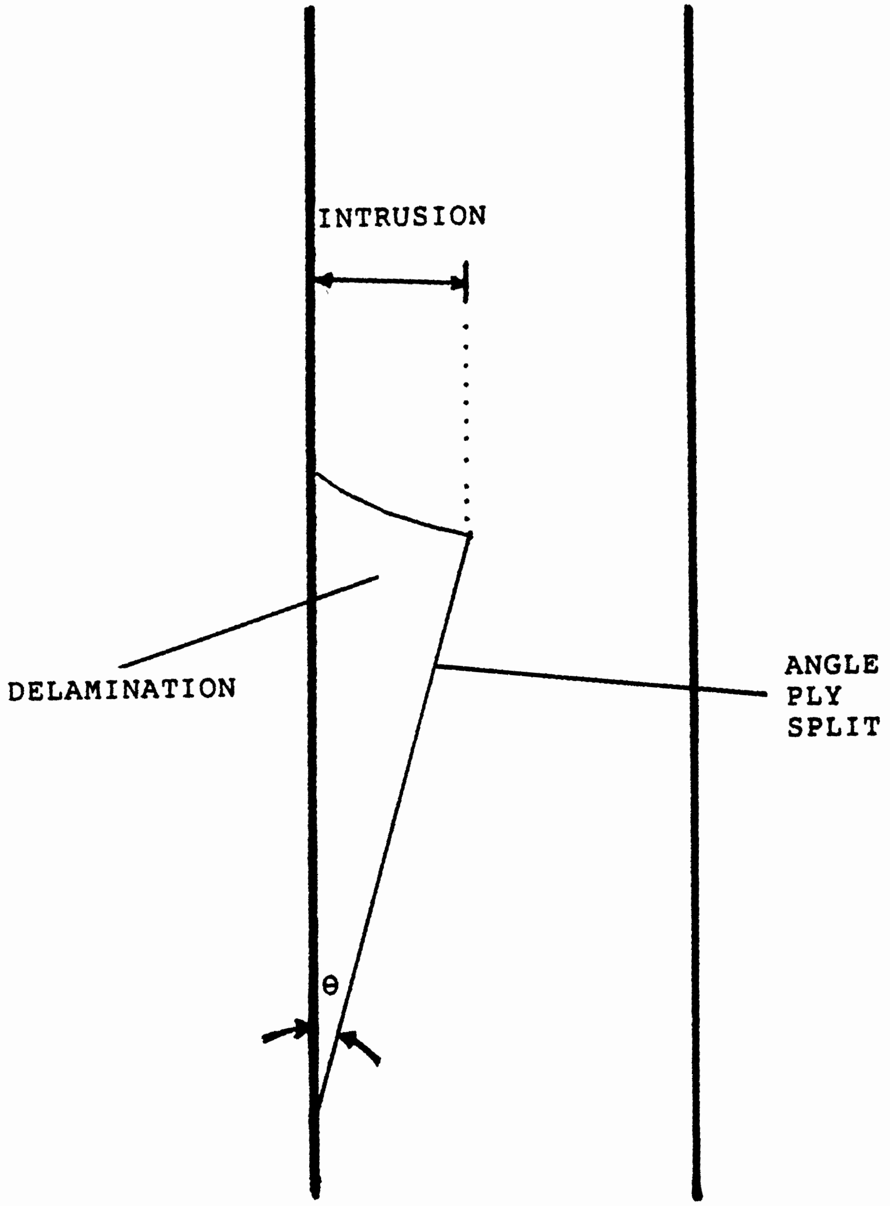

FIGURE 3.7 SCHEMATIC OF OBSERVED DELAMINATION DAMAGE

one set with an angle ply split extending beyond the delamination front, as illustrated in Figure 3.8. No specimens were made with the angle ply split extending exactly to the delamination front because that would be equivalent to the naturally occurring damage.

Six specimens of each type were made. The lamination sequence used was $[0_3/\pm15_3]_s$. This sequence was chosen because it was observed to delaminate at the +15°/-15° interface with an associated angle ply split in the $[-15_6]$ sublaminate. The $[0_3/\pm15_3]_s$ laminate has an advantage over comparable $[\pm15_n/0_n]_s$ laminate types because the angle ply split is confined to one sublaminate (rather than both $[+15_n]$ sublaminates in the $[\pm15_n/0_n]_s$ case). Having one relatively thick sublaminate with an angle ply split instead of two thinner ones simplifies the manufacturing process. An implanted delamination was positioned at each +15°/-15° interface. They were aligned through the thickness so as to be symmetric with respect to the midplane of the specimen.

The size of a delamination can be characterized by the maximum distance from the free edge or "intrusion" as illustrated in Figure 3.7. The intrusion of the delamination in both cases was nominally 10 mm. The intrusion of the angle ply split was 20 mm. A test matrix for this portion of the investigation is given in Table 3.6.

The experiments described in this section were designed to give information about the progression of damage in delamination growth. They were tested to the same load levels

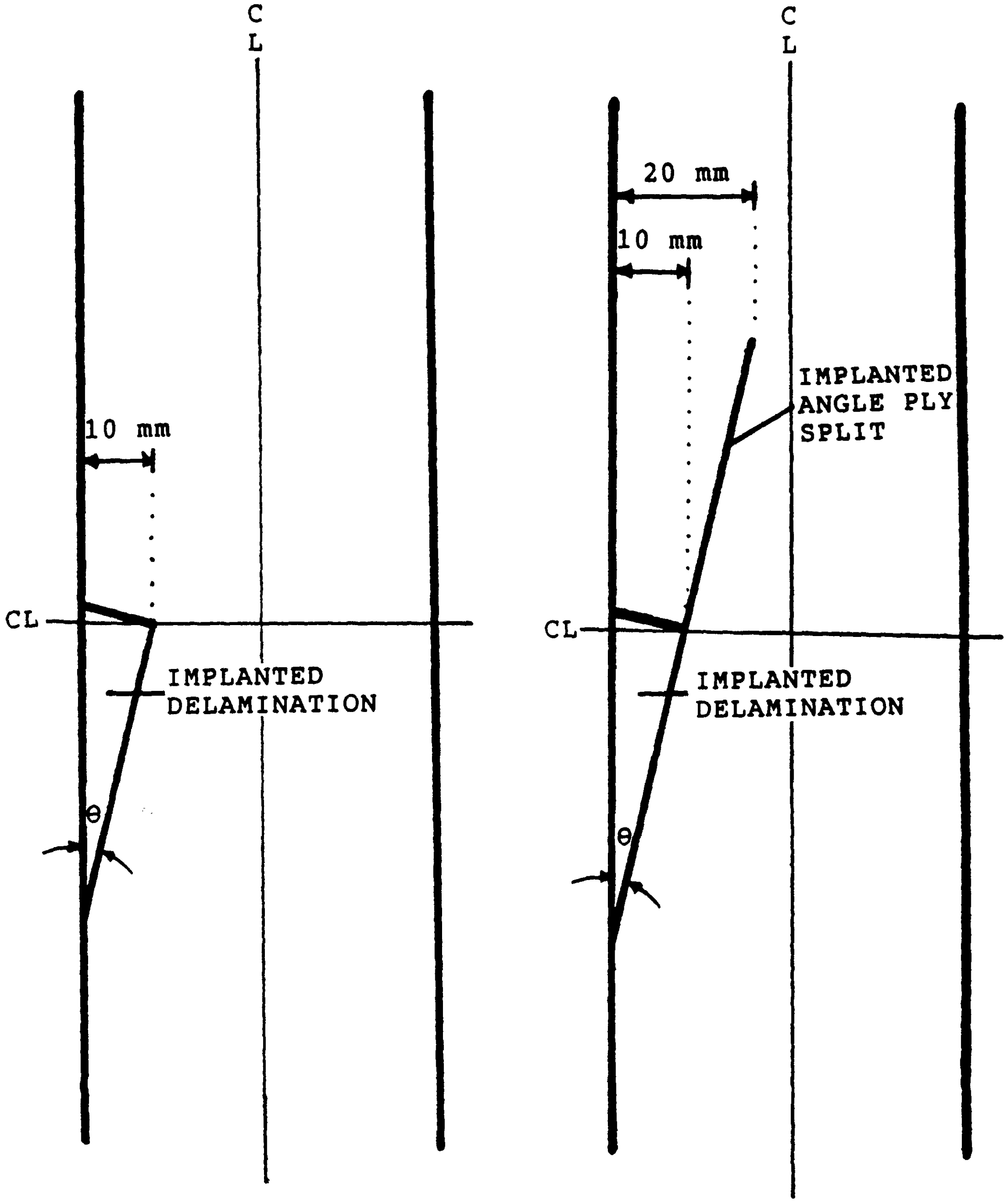

FIGURE 3.8 SCHEMATIC OF SPECIMENS WITH IMPLANTED DELAMINATIONS

TABLE 3.6

TEST MATRIX FOR $[\pm15_3/0_3]_s$ SPECIMENS WITH IMPLANTED DELAMINATIONS AND ANGLE PLY SPLITS

Nominal Intrusion of the Implanted Delamination [mm]	Nominal Intrusion of the Implanted Angle Ply Split [mm]	Number of Specimens Tested to Incremental Load Levels and Monitored with Dye Penetrant-Enhanced X-Radiography
10	0	6
10	20	6

as the $[0_3/\pm15_3]_s$ specimens with no implanted damage. The damage state was monitored after each test with dye penetrant-enhanced x-radiography. The specimens were eventually tested to final failure.

The data generated by the four sets of experiments should aid in the evaluation of the available models in their ability to describe stable and unstable delamination growth and final failure induced by delamination.

3.4 Analysis of Delamination Growth

The delamination shapes observed in this investigation were significantly different from those reported and modeled in the literature. Although the strain energy release rate models work well for some cases in the literature, they do not work well for the damage observed in this investigation. In the literature, the delaminations were generally modeled as strips along the free edge. All quantities, including delamination width, were taken to be constant with respect to longitudinal position, thus effectively transforming this into a two-dimensional problem. The laminates investigated in the literature usually contained 90° plies with transverse cracks. Some of the delaminations shapes observed by Crossman and Wang [23] were somewhat rounded but could be approximated as having constant width. Most of the delaminations observed in the current investigation, however, were similar to that illustrated in Figure 3.7. The differences are important.

The delamination shape is triangular. Thus, the width is in no sense constant. Most of the delamination is bounded by an angle ply split, meaning that a portion of the ply near the split may be partially or totally unloaded. The delamination is not as long as the entire free edge. Since the delaminated region has a higher compliance than the rest of the specimen, the strain level is a strong function of longitudinal position. The models of constant width delaminations cannot account for the effects of these differences.

The analysis found in the literature is therefore inadequate to describe the delaminations observed in this investigation. The objective of the analysis developed herein is to model the observed delamination more accurately and to account for some of these effects in an attempt to extend the strain energy release rate approach to delamination growth in general laminates. Modifications need to be made to the existing methods to make them more applicable to the observed damage modes. A finite element method equivalent to the virtual crack closure method will provide baseline information about the strain energy available for release near the free edge. This information is incorporated into a more general model.

CHAPTER 4

GENERAL MANUFACTURING PROCEDURES

This chapter contains descriptions of the general manufacturing procedures used throughout this investigation. Certain specimens require the use of specialized manufacturing procedures which are detailed in the appropriate chapters.

4.1 Preparation and Layup

The specimens manufactured in this investigation were constructed using the basic procedures developed at TELAC [39]. The unidirectional and fabric graphite/epoxy both arrive from the manufacturer in rolls of semicured preimpregnated tape or "prepreg". The unidirectional graphite/epoxy rolls are 305 mm wide (12 inch nominal). The fabric graphite/epoxy rolls are 990 mm wide (39 inch nominal). The epoxy matrix is B-staged and is thus stored at or below -18°C. Before prepreg is prepared for curing, it is allowed to warm to room temperature for 30 minutes in a sealed bag. This minimizes condensation on its surface.

The prepreg is cut into individual plies and laid up into laminates in a "clean room". The temperature in this room is kept below 25°C and the relative humidity is kept low. Rubber gloves are worn during the cutting and laying up procedures to avoid contamination of the ply surface with skin oil.

Razor blades and precisely milled aluminum templates covered with teflon-coated glass fabric (TCGF) are used to cut the prepreg into individual plies. Angle plies of unidirectional prepreg are first cut into precise trapezoidal shapes. These are cut in half in such a way that the two halves can be put together to form a 305 mm by 350 mm rectangular ply with a precise angular orientation of the fibers. The advantage of this method is that no fibers are cut in any ply. The region where the two halves meet is a "matrix joint" which becomes indistinguishable from the remainder of the ply during the curing process. Plies which have the fibers aligned with the longitudinal axis (0° plies) and fabric prepreg plies can be cut using a rectangular template. This makes a matrix joint unnecessary.

The plies are stacked in a jig which allows for their precise alignment. The jig consists of an aluminum plate with two aluminum beams attached. The two beams form a 90° angle. Plies are carefully positioned into the corner of the jig. This "good corner" becomes a reference corner in later manufacturing steps and facilitates proper identification of the longitudinal axis of the laminate. The plies are tacky enough at room temperature to stick together and maintain proper fiber orientation.

Both sides of the laminate are covered with a sheet of "peel-ply" material. The peel-ply is a porous nylon material which protects the laminate surface before milling. The peel-ply extends approximately 50 mm past the end of the laminate opposite the good corner. It is trimmed to fit the remaining three sides of the laminate exactly.

4.2 The Cure

The laminate is cured on an aluminum caul plate. The plate is coated with a mold release agent and covered with a sheet of nonporous TCGF. Aluminum dams with a "T" shape are positioned on the TCGF and held in position with pressure sensitive tape. These dams are also coated with a mold release agent. With the aid of aluminum top plates, corprene rubber ("cork") dams are placed next to the aluminum dams to form 305 mm by 350 mm curing areas for the laminates. The configuration of a cure plate prepared to cure six laminates simultaneously is shown in Figure 4.1. The corner formed by the aluminum dams is the location of the good corner of the laminate.

The laminate is surrounded by several "curing materials" during the preparation for curing. First, a slightly oversized sheet of nonporous TCGF is placed in the curing area. Then the laminate covered with peel-ply is positioned with the reference corner in the corner formed by the aluminum dams. An oversized sheet of porous TCGF is placed on top of the laminate. Precisely cut layers of a paper bleeder material are then positioned in the curing area. One layer of bleeder material is used for every two unidirectional plies in the laminate. Three plies of bleeder material are used for every two fabric plies in the laminate. An oversized sheet of

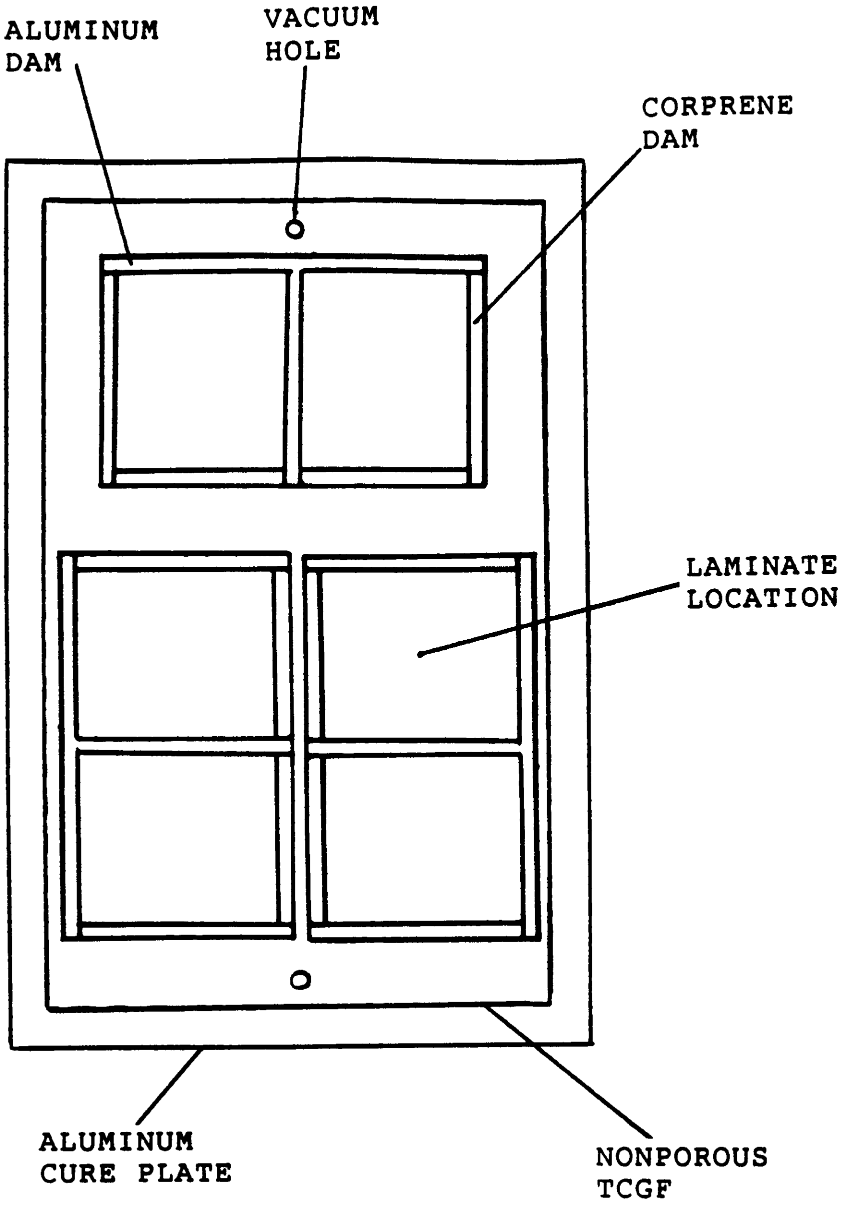

FIGURE 4.1 CONFIGURATION OF THE CURE PLATE FOR CURING OF GRAPHITE/EPOXY LAMINATES

nonporous TCGF is placed on top of the bleeder. An aluminum top plate is coated with a mold release agent and placed on top of the TCGF.

After all laminates to be cured are prepared in a similar manner, the cure assembly is covered with a large sheet of porous TCGF and a sheet of fiberglass fabric. The fiberglass serves as an "air breather", providing a path for air and volatiles to be drawn to the vacuum hole and out of the system during the cure. The assembly is then surrounded with a vacuum tape sealant and covered with a high temperature vacuum bag. A schematic of a cross-section of the cure assembly is shown in Figure 4.2.

The curing of the 3501-6 matrix in Hercules AS4/3501-6 and Hercules AW370-5H/3501-6 graphite/epoxies takes place in an autoclave at an applied pressure of 0.59 MPa (85 psig). A vacuum is drawn on the plate through the vacuum holes. The nominal value of the vacuum is 760 mm (30 in) of mercury pressure differential below atmospheric pressure.

The cure is a two stage process. The first stage is a one hour "flow stage" at 117°C. The 3501-6 epoxy is at its minimum viscosity at this temperature. This facilitates the flow or "bleeding" of excess epoxy into the bleeder plies which in turn assures proper bonding of the plies and aids in the removal of voids by vacuum and pressure. The second stage is a two hour "set stage" at 177°C. The polymer chains in the epoxy complete most of their crosslinking during this stage. Heat-up and cool-down rates are in the range of 1 to 3°C/min

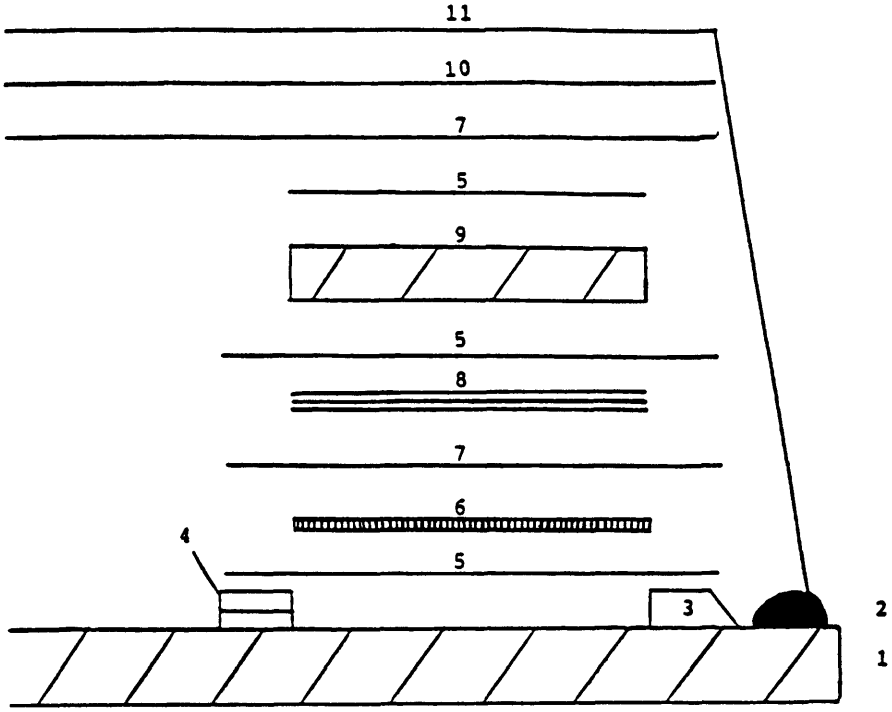

Key:
1. Cure Plate
2. Vacuum Tape
3. Aluminum Dam
4. Corprene Rubber Dam
5. Nonporous Teflon Coated Glass Fabric
6. Laminate Covered with Peel-Ply
7. Porous Teflon Coated Glass Fabric
8. Paper Bleeder Plies
9. Aluminum Top Plate
10. Fiberglass Fabric Air Breather
11. Vacuum Bag

FIGURE 4.2 SCHEMATIC OF THE CROSS-SECTION OF THE CURE ASSEMBLY to avoid thermal shocking of the composites. An eight hour postcure at 177°C in an unpressurized oven is used to drive the crosslinking process to completion. The cure cycle is shown schematically in Figure 4.3.

4.3 Machining and Measuring

The peel-ply is removed from the postcured laminates before machining. A water-cooled diamond grit cutting wheel mounted on a specially outfitted milling machine is used to mill the graphite/epoxy laminates. This setup allows for precise high quality cuts. Each 305 mm by 350 mm plate is cut into five 50 mm by 350 mm specimens. Approximately 25 mm is cut from the reference edge of the laminate and discarded prior to the cutting of the specimens.

The width of each specimen is measured using calipers at three points along the specimen length. The thickness of the specimen is measured using a micrometer at nine points in the specimen test section. (Fewer points are used for the specimens with nonstandard width that are less than 50 mm wide.) The locations of the measurement points for a standard width specimen are shown in Figure 4.4. The average value for measured width and thickness are reported for each specimen in the data tables.

The measured thickness values are used as a quality control check. It can be seen under a microscope that "dimpling" occurs in a surface layer of pure epoxy. This is a

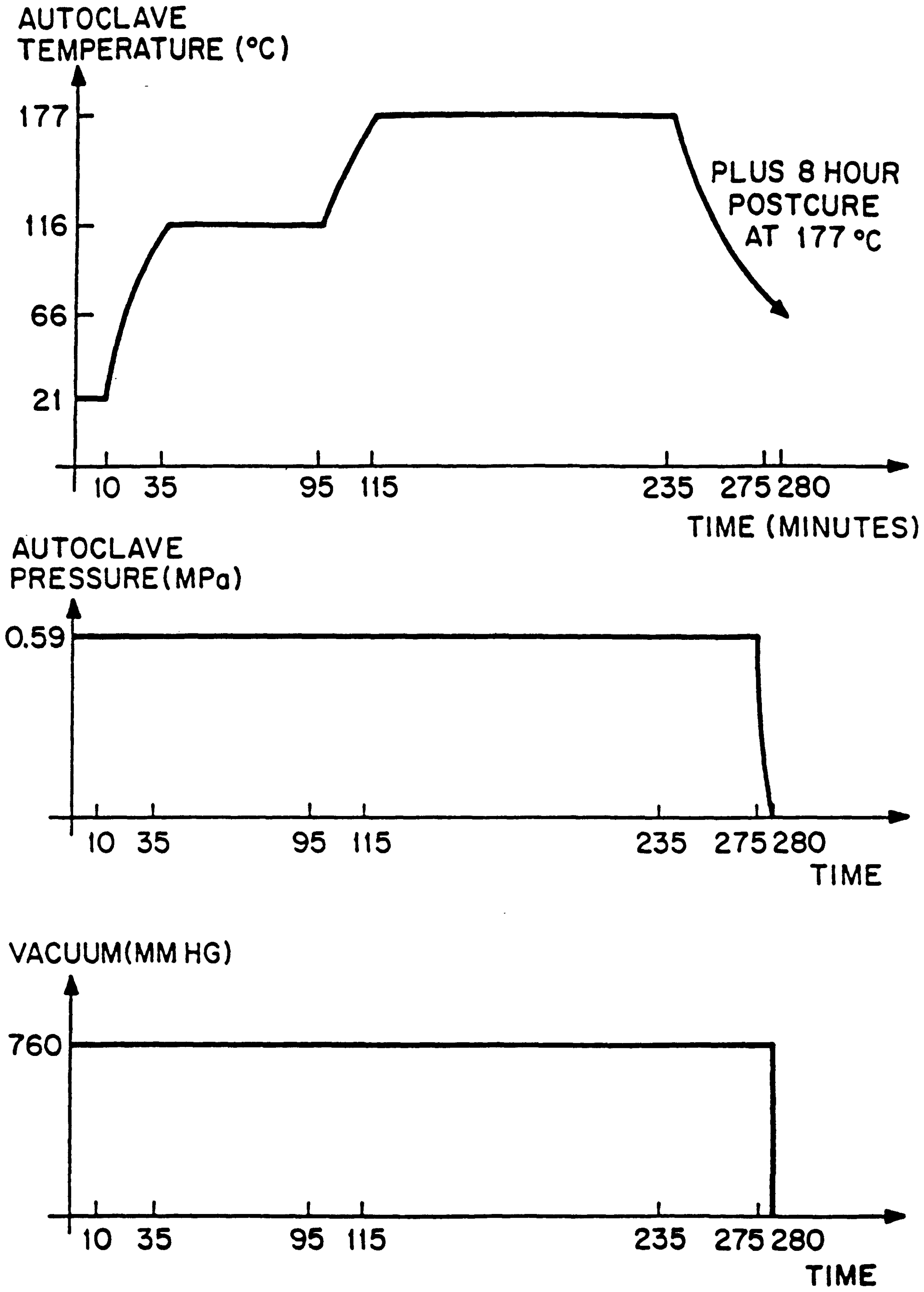

FIGURE 4.3 CURE CYCLE FOR AS4/3501-6 UNIDIRECTIONAL GRAPHITE/EPOXY AND AW370-5H/3501-6 WOVEN GRAPHITE/EPOXY FABRIC

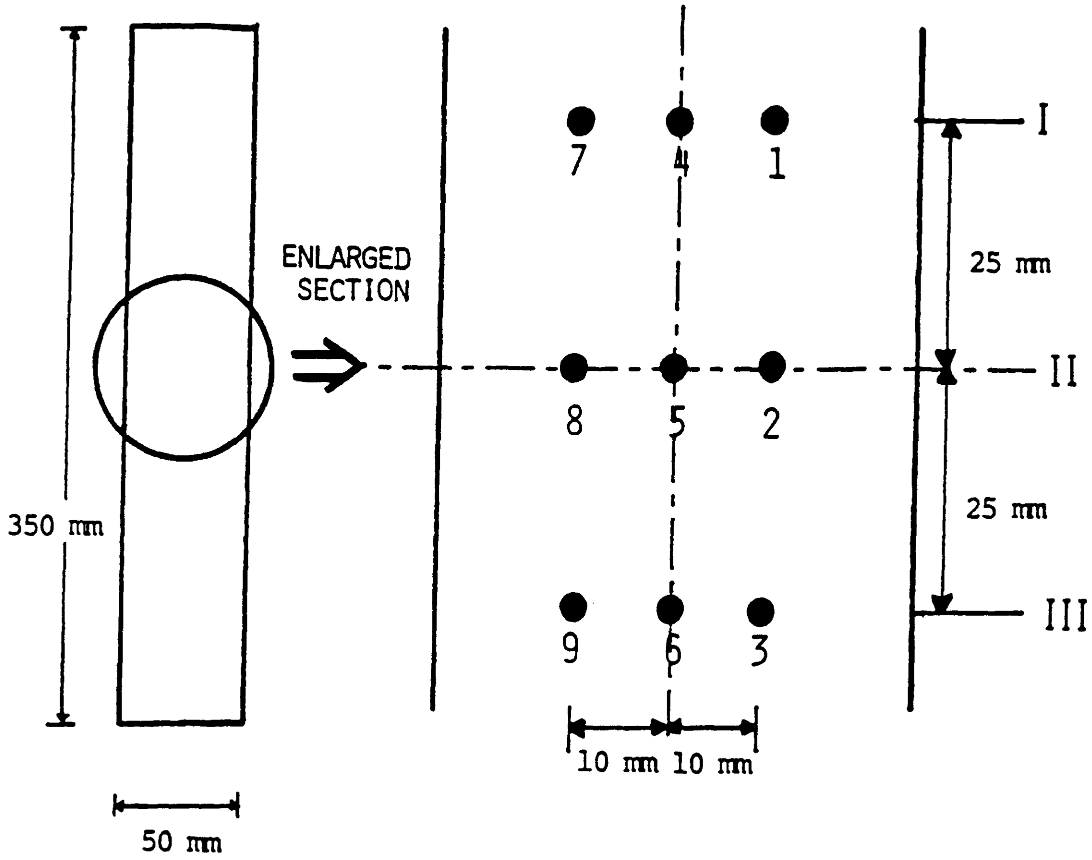

FIGURE 4.4 LOCATION OF MEASUREMENT POINTS ON A STANDARD TELAC SPECIMEN

result of microscopic surface features left by the peel-ply. These features are helpful for the bonding of loading tabs and strain gages, but they can distort the measured thickness. This distortion is most evident in thin laminates. In order to properly evaluate the effects of laminate thickness, nominal thickness is used in all stress and modulus calculations. The nominal thickness of a ply of AS4/3501-6 unidirectional graphite/epoxy is 0.134 mm. The nominal thickness of a ply of AW370-5H/3501-6 fabric graphite/epoxy is 0.35 mm. The measured laminate thicknesses are compared to the nominal values in Table 4.1. Almost all average thicknesses were within five percent of their nominal values.

4.4 Loading Tabs

Glass/epoxy loading tabs are manufactured for each specimen from 305 mm by 710 mm laminates of 3M Scotchply type SP-1002 precured glass/epoxy. The American Society for Testing and Materials [40] recommends that the loading tab thickness be between 1.5 and four times the laminate thickness. The nominal thickness of the laminates and the loading tabs are compared in Table 4.2. The layup for the tabs is $[(0/90)_n/0/\overline{90}]_s$, with n varying with the thickness requirements of the tab. Each glass/epoxy ply has a nominal thickness of 0.254 mm (0.01 in).

The $[\pm15_5/0_5]_s$, $[\pm15_8/0_8]_s$, $[0_5/\pm15_5]_s$, and $[0_8/\pm15_8]_s$ specimens require thicker glass/epoxy loading tabs than are

TABLE 4.1

NOMINAL AND MEASURED LAMINATE THICKNESSES

Laminate	Nominal Thickness [mm]	Measured Thickness [mm]
$[0_{5U}/0_F]_s$	2.040	1.97 (1.2%)[a]
$[0_{5U}/0_F/0_U]_s$	2.308	2.20 (1.0%)
$[0_{10U}/0_F]_s$	3.380	3.28 (0.5%)
$[\pm15_3]_s$	1.608	1.56 (3.0%)
$[\pm15/0]_s$	0.804	0.86 (2.4%)
$[\pm15_2/0_2]_s$	1.608	1.59 (5.1%)
$[\pm15_3/0_3]_s$	2.412	2.34 (3.7%)
$[\pm15_5/0_5]_s$	4.020	3.96 (4.6%)
$[\pm15_8/0_8]_s$	6.432	6.55 (1.4%)
$[0/\pm15]_s$	0.804	0.85 (2.4%)
$[0_2/\pm15_2]_s$	1.608	1.57 (4.1%)
$[0_3/\pm15_3]_s$	2.412	2.36 (4.6%)
$[0_5/\pm15_5]_s$	4.020	3.85 (7.8%)
$[0_8/\pm15_8]_s$	6.432	6.24 (8.4%)
$[\pm20_F]_s$	1.400	1.41 (0.8%)
$[0_3/\pm15_3]_s$[b]	2.412	2.21 (1.4%)

[a] Numbers in parentheses are coefficients of variation.

[b] Specimens containing implanted delaminations.

TABLE 4.2

NOMINAL LAMINATE AND LOADING TAB THICKNESSES

Laminate Type	Nominal Laminate Thickness [mm]	Nominal Tab Thickness [mm]	Tab to Laminate Thickness Ratio
$[0_{5U}/0_F]_s$	2.040	4.32	2.12
$[0_{5U}/0_F/0_U]_s$	2.308	4.83	2.09
$[0_{10U}/0_F]_s$	3.380	7.11	2.10
$[\pm15_3]_s$	1.608	3.30	2.05
$[\pm15/0]_s$	0.804	2.29	2.85
$[\pm15_2/0_2]_s$	1.608	3.30	2.05
$[\pm15_3/0_3]_s$	2.412	6.35	2.63
$[\pm15_5/0_5]_s$	4.020	8.13	2.02
$[\pm15_8/0_8]_s$	6.432	12.19	1.90
$[0/\pm15]_s$	0.804	2.29	2.85
$[0_2/\pm15_2]_s$	1.608	3.30	2.05
$[0_3/\pm15_3]_s$	2.412	6.35	2.63
$[0_5/\pm15_5]_s$	4.020	8.13	2.02
$[0_8/\pm15_8]_s$	6.432	12.19	1.90
$[\pm20_F]_s$	1.400	3.30	2.05

readily available from the manufacturer. Two 305 mm by 710 mm $[(0/90)_{16}]_s$ laminates and two 305 mm by 710 mm $[(0/90)_{24}]_s$ laminates of Scotchply type SP-1003 (an uncured version of type SP-1002) were manufactured using standard TELAC procedures [39] to be used as loading tabs for these specimens. The nominal cured ply thickness for SP-1003 is also 0.254 mm (0.01 in).

The glass/epoxy laminates are milled into 50 mm wide by 75 mm long loading tabs on the same milling machine used for cutting graphite/epoxy. One of the 50 mm edges of each tab is beveled to a 30° angle to the plane of the tab using a belt sander.

The tabs are bonded onto the specimens with American Cyanamid FM-123-2 film adhesive. The film adhesive is stored at or below -18°C. It becomes tacky enough at room temperature to hold the tab in place while preparing the bonding cure. The specimens are placed on an aluminum caul plate which has been covered with nonporous TCGF. The specimens are spaced far enough apart that any "bubbling" of the excess film adhesive will not cause specimens to bond to each other. The specimens are covered with TCGF and 6.35 mm (0.25 in) thick steel top plates. The top plates are taped together with mylar tape and immobilized with stacks of corprene dam material. This prevents shifting of the top plates and the associated slipping of the loading tabs during the bonding cure. This assembly is covered with TCGF and a fiberglass air breather. The assembly is surrounded with vacuum tape and covered with a vacuum bag.

The film adhesive is cured in an autoclave with a full vacuum (nominally 760 mm of mercury pressure differential below atmospheric) under 0.068 MPa (10 psig) of applied pressure. This yielded an effective pressure of 0.34 MPa (50 psia) of pressure of the top plates on the bonding surface of the tabs. The film adhesive is cured for two hours at 107°C.

4.5 Instrumentation

A strain gage is mounted on each specimen to monitor longitudinal strain level during testing. In most specimens, the gage is placed in the center of the test section as shown in Figure 3.3. The gages are aligned with the longitudinal axis of the specimen using lines that are lightly scribed onto the thin surface layer of pure epoxy. M-Bond 200 adhesive is used to bond the gages to the specimen.

The gages used are Micro Measurements EA-06-125AD-120 strain gages. These gages contain a 3.175 mm square constantan wire element on a 0.025 mm thick polyimide backing. The resistance of these gages is 120 ohms ± 0.15%. The gage factor is given as either 2.04 ± 0.5% or 2.055 ± 0.5%. Once the gage is bonded to the test section, the test specimen is complete as shown in Figure 3.3 and is ready for testing.

CHAPTER 5

DELAMINATION INITIATION EXPERIMENTS

Three sets of specimens were tested and evaluated for delamination initiation stress. Testing and evaluation methods are described in this chapter and the results are discussed in the context of the objectives of this investigation.

5.1 Edge Replication

The study of delamination initiation requires that the damage state of the free edge be nondestructively monitored. The method used for detection of delamination initiation in this investigation was edge replication. An edge replication is a strip of cellulose acetate film with an impression of the specimen edge. This method has been shown to be effective in detecting the first signs of initiation [34].

The specimen edges must be polished before testing to give a clear replication. The specimens in this portion of the investigation were polished with a 25 mm diameter felt bob. The felt bobs are continually dipped in a colloidal solution of a fine abrasive, Kaopolite SF, which has an average particle size of 0.7 microns. The solution is mixed by hand and contains approximately two parts water to one part abrasive. A smooth back and forth motion of the specimen edge against the felt bob is used for polishing. The specimen edges are rinsed after polishing to prevent the solution from solidifying on the free edge. Polishing gives the specimen a smooth glossy finish.

Specimens are replicated before testing and after each test. The original replications are made to show detail of the specimen edge before any load is applied. These replications are made outside of the testing machine. All subsequent replications are made in the testing machine at half the maximum applied stroke level of a test. Except for deviations caused by large gripping loads, the load level is approximately half the maximum applied value.

In preparation for each replication, a 25 mm wide strip of replicating tape is cut to the approximate length of the free edge. A small length of the edge is inaccessible because of the hydraulic grips of the testing machine. The replicating tape is therefore slightly shorter than the test section. The specimen edge is wiped clean with a piece of cheesecloth soaked in acetone. The acetone is allowed to evaporate and the replicating tape is placed against the specimen edge as shown in Figure 5.1. A squirt bottle of acetone is placed next to the tape. The acetone is sprayed on the side of the specimen closest to the specimen. The acetone softens the tape for the replication. The tape is then smoothed against the edge with a finger or other smooth object. While the replication is drying, a mark is placed on the tape with a marker. The mark corresponds to a line on the test section of the specimen and is used as a longitudinal

FIGURE 5.1 POSITION OF REPLICATING TAPE DURING APPLICATION OF ACETONE

reference. This mark is usually 30 to 40 mm from a loading tab.

Once a replication has dried for approximately one minute, it is removed. It is immediately examined for image clarity. If smudges or bubbles are visible with the naked eye, the replication is discarded and another one is made. This is repeated until two clear replications of each side exist. The replications are placed between two clean flat surfaces to finish drying. This keeps the replications from curling which would make them difficult to examine.

Replications can show free edge surface features as small as an individual fiber. The surface texture of different plies and the interply matrix layer can be identified. Softened acetate can seep into tight delamination initiations and angle ply splits, especially when they may be "opened" as a result of applied load. The difference in surface texture of these features are highlighted on replications when inspected under a microscope. The replications are illuminated from a light source behind and to the side. Delamination initiations and angle ply splits appear as bright thin lines. When these features are viewed directly under a microscope, they appear as dark features against a dark background and can be indistinguishable.

5.2 General Testing Procedures

All specimens in this investigation were tested in an

MTS 810 Material Test System equipped with hydraulic grips. The machine was programmed to control the total stroke of the grips. The constant stroke rate was 1.07 mm/min. The resulting strain rate in the 200 mm test section of the specimen is approximately 5400 microstrain/minute.

Specimens are aligned in the upper grip using a plastic right triangle. The upper grip is closed around the upper loading tabs. The lower grip is then positioned around the lower tabs. This is taken to be the "no load" position at which the strain gages can be calibrated.

The strain gages are attached to Vishay strain gage conditioners which are in turn connected to the computer-controlled data acquisition system. The computer obtains data about the load, strain, and stroke through analog-to-digital devices which divide the full range of the channel into ±2048 computer units. For example, the stroke range setting used in this investigation was ±12.7 mm. Thus, one computer unit represents 0.0062 mm of stroke. This is the resolution of the stroke data.

The gage is first "balanced" so that it registers no strain in the no load position. Then, the value of a computer unit of strain is adjusted using the gain control on the strain gage conditioner. A calibration value of a shunt resistance is connected in parallel with the strain gage such that the apparent resistance of the gage corresponds with a prescribed strain level. The gain is then adjusted so that the data acquisition system registers the equivalent number of computer units. In this investigation, the conditioner was calibrated so that each computer unit represented six microstrain.

After the gages are calibrated, the specimen is ready for testing. The lower grips are closed and the gripping load recorded in the notebook. The specimens in this portion of the investigation are tested using a computer-controlled testing program that allowed for simultaneous commencement of the loading ramp and the data acquisition. Load, strain, and stroke data are recorded at prescribed time intervals. When the loading and data acquisition are stopped by computer control, the residual load, maximum load, and final stroke level are recorded in the notebook.

5.3 Load Drop Testing

Delamination initiation is associated with a drop in load resulting from the increase in compliance. Halting tests upon the detection of a load drop and checking for evidence of a new delamination initiation has been demonstrated to be a useful tool for detecting the delamination initiation stress [34].

The computer program used to control the tests of the specimens in this portion of the investigation continually evaluates the value of the load at the current data point and the one immediately previous. The data acquisition time increment for these specimens was 0.3 seconds. When the load at a given data point is less than the value at the previous data point, the loading and data acquisition are immediately stopped. This load drop is taken to be an indication of a possible delamination initiation. The stroke level is then reduced by a factor of two. Two clear replications are made of each free edge. The specimen is then completely unloaded and removed from the testing machine.

The replications are inspected under a microscope. The magnification ranges from 7X to 50X. They are compared directly with the replications from the previous loading and examined for new features indicative of delamination initiation. If an initiation is discovered, the data point associated with the maximum load (i.e. the data point just before the load drop) is taken to be the point of delamination initiation. If no new features are found, the apparent load drop is assumed to be a result of noise in the data acquisition system. The specimen is then retested. In all subsequent tests of that specimen, load drops observed to take place at lower values of load than those seen in earlier tests are also assumed to be the result of system noise.

5.4 Results

Delamination initiation was detected before final failure in all of the specimens in this portion of the investigation. The stress-strain behavior was linear until delamination for all specimens. The initiation stress, initiation strain, and modulus data for each specimen are given in Data Table 1.

The $[0_{10U}/0_F]_s$ specimens were all seen to have delamination initiation after one test. Careful inspection of the edge replications taken before the test revealed that the delaminations had in fact initiated before any mechanical loading had been applied. This implies that thermally-induced interlaminar stresses can be important in initiating delamination. The initiations occurred along the fill fiber tows and were generally closer to the midplane than the unidirectional plies. A micrograph of an edge replication showing a delamination initiation in a $[0_{10U}/0_F]_s$ specimen is shown in Figure 5.2.

Three of the five $[0_{5U}/0_F]_s$ specimens showed initiation after a load drop was detected by the load drop testing program. The tests of the remaining two specimens were not stopped by the testing program. Instead, the tests were stopped manually when visible damage was observed at the free edge. Edge replications confirmed damage at the free edge including extensive delamination initiation. Apparently, the magnitude of the load drops associated with the initiations in these specimens was below the resolution of the testing equipment and computer program. The delamination initiation stress for these two specimens can therefore only be narrowed down to a range of stresses. The initiation stress for the three specimens exhibiting detectable load drops was 528 MPa with a coefficient of variation of 2.6%. The average of the lower bound for the other two specimens was 520 MPa. It is

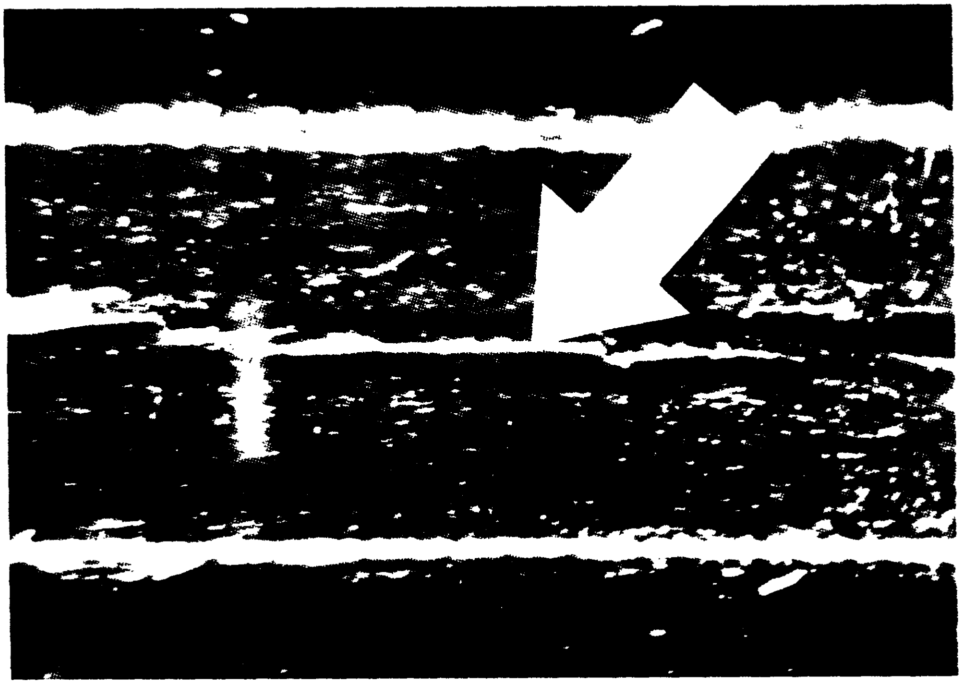

FIGURE 5.2 MICROGRAPH OF EDGE REPLICATING SHOWING DELAMINATION INITIATION IN A $[0_{10U}/0_F]_s$ SPECIMEN (7X)

therefore likely that the load drop associated with delamination initiation occurred at approximately this level and that 528 MPa is a reasonable value to use for delamination initiation stress for these laminates. All delamination initiations for these specimens were seen along the fill fiber tow close to the midplane.

The same difficulty in finding a delamination initiation point occurred with all five $[0_{5U}/0_F/0_U]_s$ specimens. The initiation stress could only be narrowed to a range of values for each specimen. The average lower bound of the range was 451 MPa with a coefficient of variation of 6.5%. The average upper bound of the range was 744 MPa with a coefficient of variation of 3.9%. The delamination initiations were detected along fill fiber tows near the $0_F/0_U$ interface closer to the midplane.

The delamination initiation data was correlated using the Quadratic Delamination Criterion. The interlaminar stresses were determined using the method of Kassapoglou and Lagace [17]. Thermally-induced stresses were also calculated [18]. The elastic parameters used in the analysis for the AS4/3501-6 unidirectional graphite/epoxy and the AW370-5H/3501-6 fabric graphite/epoxy were given in Table 3.1. The averaging dimension used was 0.178 mm which was the value determined for AS1/3501-6 unidirectional graphite/epoxy [34].

The interlaminar normal stress was the only nonzero interlaminar stress in these three lamination sequences. The interlaminar normal strength parameter used was 43 MPa. This is the value determined experimentally for AS4/3501-6 unidirectional graphite/epoxy by direct through-the-thickness tests [35].

The thermally-induced interlaminar stresses were dominant in all three lamination sequences. The contributions of mechanically-induced stresses were relatively small at delamination initiation. For example, thermally-induced interlaminar normal stresses accounted for 79% of the average interlaminar normal stress at delamination initiation in $[0_{5U}/0_F]_s$ specimens. The thermally-induced and mechanically-induced components of the interlaminar normal stress at the delamination initiation stress are depicted for this laminate type in Figure 5.3. The relatively small contribution allows for a precise experimental determination of the average interlaminar normal stress at initiation. This can be regarded as a calculated value for the interlaminar strength parameter which can be compared with the interlaminar normal strength measured from direct testing. The predicted delamination initiation stress, the measured delamination initiation stress, and the calculated interlaminar normal strength are given in Table 5.1.

5.5 Discussion

The Quadratic Delamination Criterion correlated the delamination initiation stress for all three lamination

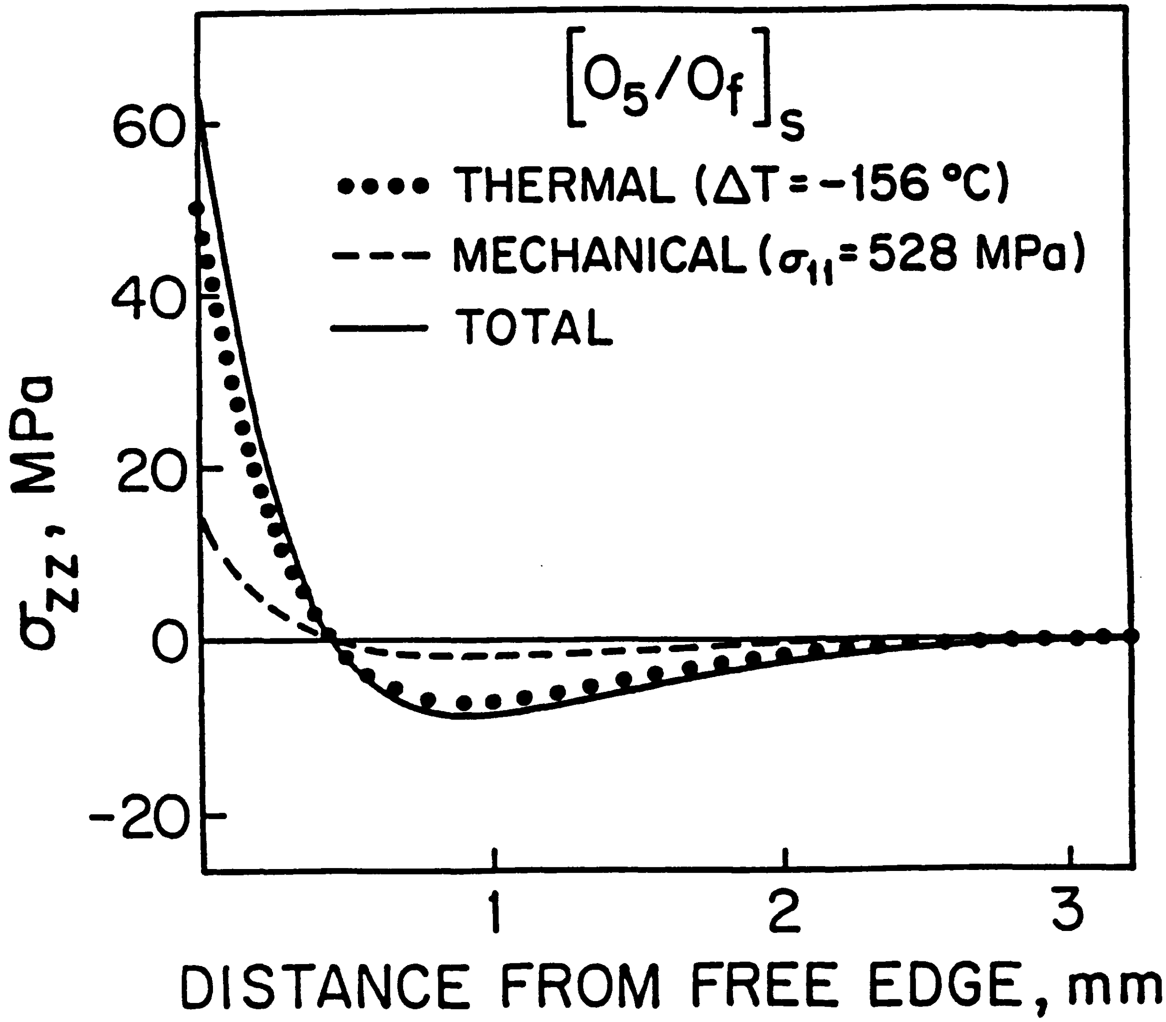

FIGURE 5.3 THERMAL AND MECHANICAL COMPONENTS OF INTERLAMINAR NORMAL STRESS AT DELAMINATION INITIATION AT THE MIDPLANE OF A $[0_{5U}/0_F]_s$ SPECIMEN

TABLE 5.1

PREDICTED VERSUS ACTUAL INITIATION STRESS AND CALCULATED INTERLAMINAR NORMAL STRENGTH

Lamination Sequence	Predicted Initiation Stress [MPa]	Actual Initiation Stress [MPa]	Calculated Interlaminar Normal Strength[a] [MPa]
$[0_{5U}/0_F]_s$	436	528	44.6
$[0_{5U}/0_F/0_U]_s$	681	451-744	39.4-44.0
$[0_{10U}/0_F]_s$	0	0	≤43.4

[a] Calculated at experimental initiation stress.

sequences. This was done with an interlaminar normal strength parameter that was measured directly. Comparison of calculated values from the data in this investigation with the actual value shows excellent agreement. The importance of thermally-induced stresses and interlaminar normal stresses were also demonstrated. For example, thermally-induced interlaminar normal stress alone was responsible for the delamination initiation of the $[0_{10U}/0_F]_s$ specimens. The averaging dimension used to obtain this agreement was one determined for a similar material. It can be reasoned that the averaging dimension should be independent of the fiber strength. Since the AS1 and AS4 fibers are similar in other respects, it is reasonable to assume the averaging dimension determined for a composite system containing the AS1 fiber is a good estimate of the value for a composite system using the AS4 fiber. The good correlation is further evidence that the averaging dimension is a material parameter. The fact that the delaminations initiated at the boundary of fabric plies is an indication that the averaging dimension may be independent of the form of the material system (i.e. unidirectional versus fabric).

The initiations occurred at the interfaces predicted by the Quadratic Delamination Criterion. They did, however, tend to form along fill fiber tows on the boundary of the fabric plies. This could not be predicted by the Quadratic Delamination Criterion since the criterion and the supporting interlaminar stress analysis assume smeared homogeneous plies. Micromechanical effects play a role in the exact position of the delamination initiation, but important parameters such as delamination initiation stress and critical interface can be predicted without relaxing the smeared homogenous ply assumptions made in Classical Laminated Plate Theory and related analyses.

The strain energy release rate approach as proposed by O'Brien [26] cannot predict delamination initiation at the midplane such as was observed for the $[0_{5U}/0_F]_s$ and $[0_{10U}/0_F]_s$ specimens. The simple rule of mixtures approach used for determining the modulus of the delaminated region predicts no loss of modulus for a delamination at the midplane of a symmetric laminate. This implies no energy would be available for formation of a fracture surface. The energy for delaminations results from the fact that the bending-stretching parameters, which are characterized by the B matrix in standard Classical Laminated Plate Theory notation, become nonzero when the delamination divides the specimen into two unsymmetric halves. Thus, this approach would fail to predict delamination initiation in these laminates.

CHAPTER 6

DELAMINATION GROWTH AND FINAL FAILURE EXPERIMENTS

The delamination growth and final failure behavior of graphite/epoxy are explored in this portion of the investigation. Four sets of experiments were conducted. Some experiments required specialized manufacturing and testing procedures which are described in this chapter. The results of the experiments are reported and discussed in the context of the objectives of the investigation.

6.1 Specialized Specimen Manufacturing Procedures

The specimens for this portion of the investigation were manufactured using the basic procedures described in Chapter 4. Variations or additions to these procedures were used to manufacture specialized specimens. These variations are described here.

6.1.1 Specimens of Nonstandard Width

The $[\pm15_3]_S$ specimens of nonstandard width are constructed with only one variation on the standard procedures. When a 50 mm wide specimen is milled, a metal spacer is placed against a reference edge on the cutting surface. The laminate is placed against the spacer and clamped in place. The cutting surface is then moved in the direction of the cut. The cutting wheel extends down into a groove in the cutting surface. As the laminate passes the wheel, a 50 mm wide strip is cut. When nonstandard width specimens and loading tabs are cut, nonstandard spacers are used. The widths used in this investigation were 10 mm, 20 mm, 30 mm, 50 mm, and 70 mm.

Not all specimens of the same width are milled from the same laminate for two reasons. First, it would not be possible to mill all five 70 mm wide specimens from the same laminate. Second, milling specimens of a given width from the different laminates reduces the possibility that slight manufacturing differences between laminates will affect trends in the data.

6.1.2 Fabric Specimens

Since there are two primary fiber directions in the fabric weave, a pure matrix joint is not possible. Any joint would necessarily contain cut fibers. Fortunately, the prepreg is available in 990 mm (39 in) wide prepreg. This makes it possible to cut angle plies in one rectangular sheet with no joints. Angle ply templates are used to align the rectangular template to assure the proper angle of the warp fibers with respect to the longitudinal axis of the laminate. Care must be taken to properly position the warp and fill faces of each ply.

6.1.3 Specimens with Implanted Delaminations and Angle Ply Splits

The unique configuration of the implanted delaminations and angle ply splits makes it necessary to manufacture these specimens individually rather than to cut several specimens out of a single cured laminate. The laminate type used is $[0_3/\pm15_3]_s$. In the process of laying up individual specimens, it is convenient to lay up 305 mm by 350 mm major prepreg sublaminates using standard techniques and then cut them into four 76 mm by 350 mm sublaminates. Each specimen consists of three major sublaminates: $[0_3/+15_3]_T$, $[-15_6]$, and $[+15_3/0_3]_T$. The teflon film is implanted between and within these sublaminates before curing.

A slight variation from standard procedure is used to layup $[-15_6]$ sublaminates. Normally the trapezoid of prepreg that is cut to form the angle ply is cut exactly in half. If this were done for the $[-15_6]$ sublaminate, the matrix joints of all six plies would be aligned through the thickness and the uncured sublaminate would have no in-plane strength at this joint. This could result in undetected separation of the two halves during critical steps in the manufacturing process. To avoid this problem, the plies were cut such that the position of the matrix joint varied from ply to ply. In two of the six plies, the joint was approximately 20 mm in one direction from the normal position. In two of the remaining plies, the joint was approximately 20 mm in the other direction. In the remaining two plies, the joint was in the normal position.

Delaminations were formed by implanting a thin teflon film between two uncured sublaminates. Angle ply splits were formed by implanting the film within the $[-15_6]$ sublaminate along the fiber direction. The teflon film is manufactured by DuPont and is designated PFA 100 LP fluorocarbon film. It has a nominal thickness of 0.0254 mm (0.001 in).

In the specimens with no implanted angle ply split, a 25 mm by 50 mm rectangle of the teflon film is placed on the surface of a 76 mm by 350 mm $[-15_6]$ sublaminate. The implant is positioned such that the long edge is along the fiber angle and the point of farthest intrusion from the edge of the sublaminate is 20 mm. The point of maximum intrusion is positioned so that it is at the longitudinal center of the specimen. This position is illustrated in Figure 6.1. A $[0_3/+15_3]_T$ sublaminate is then placed on the $[-15_6]$ sublaminate. The two sublaminates stick together and hold the film in place. The process is repeated on the other side of the $[-15_6]$ sublaminate. Care is taken so that the two implanted delaminations line up through the thickness. The excess teflon film protruding from the free edge is not trimmed.

The manufacturing of specimens with implanted angle ply splits requires that a slit be made along the fiber direction in the uncured $[-15_6]$ sublaminate. The slit is cut using a razor blade and a straight edge. The straight edge is placed

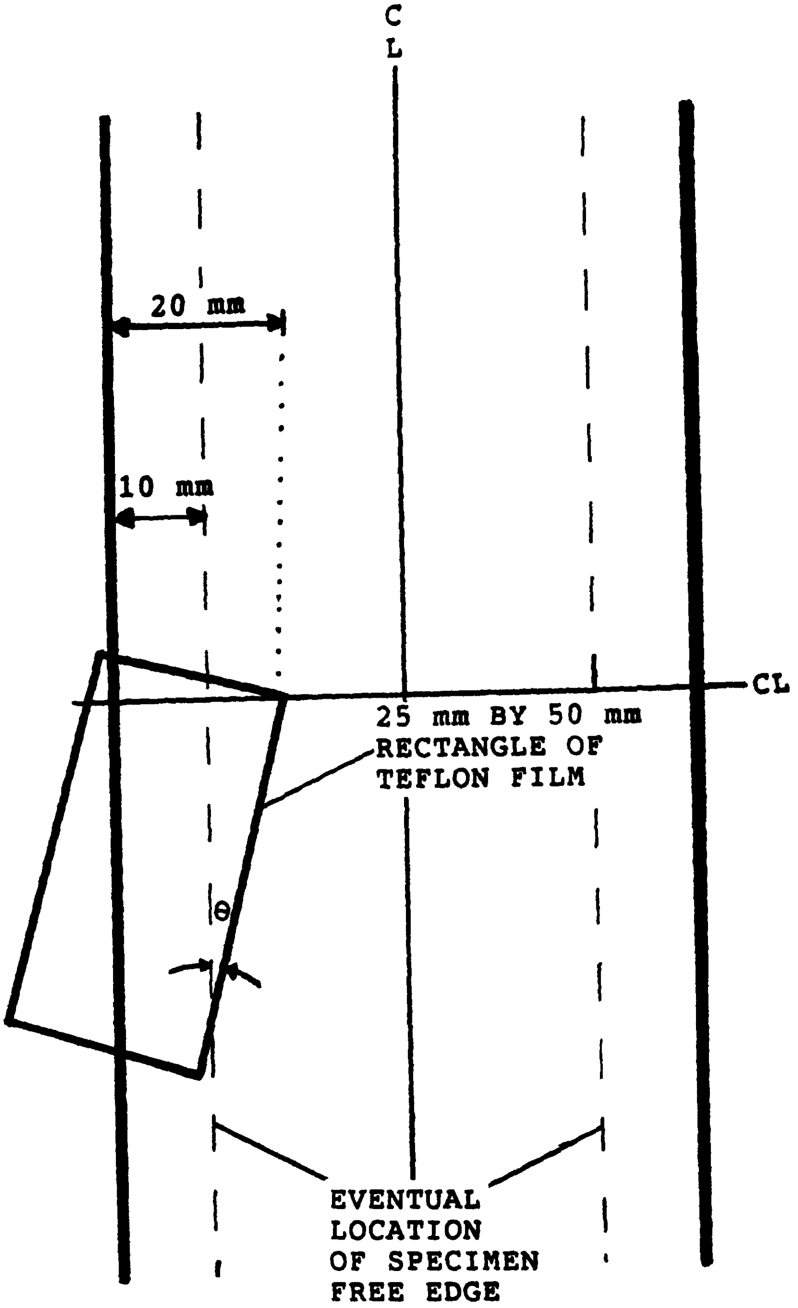

FIGURE 6.1 NOMINAL POSITION OF THE TEFLON FILM AT THE +15°/-15° INTERFACES WHEN CONSTRUCTING A $[0_3/\pm15_3]_s$ SPECIMEN WITH AN IMPLANTED DELAMINATION

on clean backing paper from the prepreg to avoid contamination of the sublaminate surface by the straight edge. The slit has a maximum intrusion of 30 mm from the edge of the sublaminate. The position of the point where the intrusion from the free edge is 20 mm coincides with the longitudinal center of the sublaminate as illustrated in Figure 6.2. A 10 mm by 50 mm strip of teflon film is carefully placed inside the slit. When the end of the strip is flush with the tip of the slit, the excess film can be trimmed from one side. Unfortunately, the inability of the film to stick to the prepreg (which is desirable in context) makes it impossible to trim both sides without dislodging the film. Therefore, it is preferable to have most of the excess on one side and to trim that side. The excess film on the other side must be folded into the interface region.

A 50 mm by 50 mm square of teflon film is then positioned in the slit such that its maximum intrusion from the free edge is 20 mm at the midpoint of the free edge. The square can then be folded over on both sides of the sublaminate to form two implanted delaminations similar to those in the specimens without implanted angle ply splits. The positions of the slit and teflon films are shown in Figure 6.2. The laminate is completed by placing a $[0_3/+15_3]_T$ sublaminates on each side of the $[-15_6]$ sublaminate.

Sheets of peel-ply are cut so that they are the nominal size of the faces of the laminates with an extra 50 mm extending from one end. The peel-ply is applied to the faces

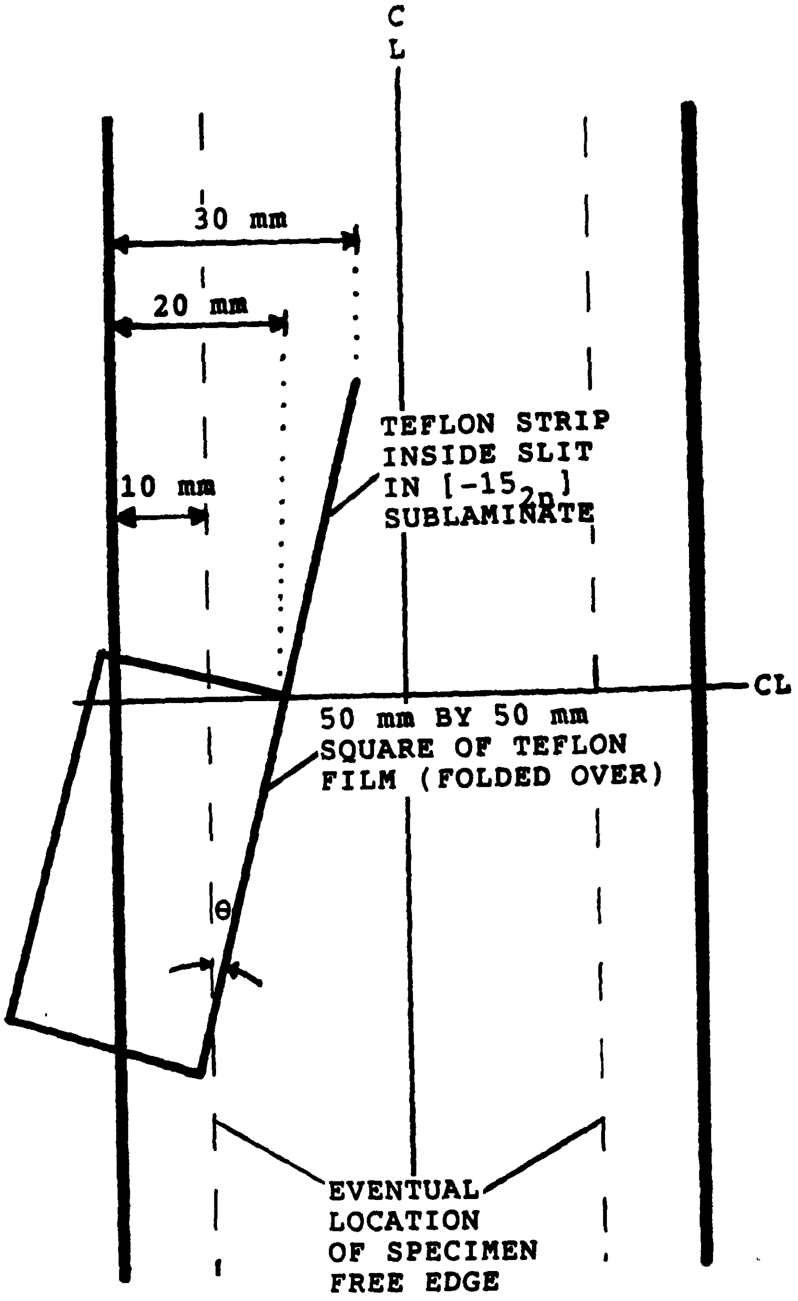

FIGURE 6.2 NOMINAL POSITION OF THE TEFLON FILM AT THE +15°/-15° INTERFACES AND WITHIN THE $[-15_6]$ SUBLAMINATE WHEN CONSTRUCTING A $[0_3/\pm15_3]_s$ SPECIMEN WITH AN IMPLANTED DELAMINATION AND ANGLE PLY SPLIT

of the laminates. Neither the peel-ply nor the extra teflon film protruding from the free edge is trimmed. The cure setup is essentially the same as for standard specimens with two exceptions. First, only corprene dam material is used. Second, no top plates are used. The absence of top plates makes it critical that all wrinkles in the cure materials, air breather, and vacuum bag be eliminated before curing.

Approximately 10 mm is milled from the free edge of the postcured specimens. The resulting nominal intrusions of the delamination and angle ply split (in those specimens containing them) are 10 mm and 20 mm, respectively. Since excess epoxy collects at the free edge during curing, the exact position of the boundaries of the teflon film cannot be precisely ascertained. Thus, the actual intrusion may vary from the nominal value.

A strain gage was mounted on each specimen in the same manner described in Chapter 4. However, the gage was located halfway between the center and corner of the test section. This allowed the gage to measure far field strain with minimum effects from the implanted delamination and loading tabs. The location of the gage is depicted in Figure 6.3.

6.2 Dye Penetrant-Enhanced X-radiography

The study of delamination growth and final failure requires that the damage state be nondestructively monitored over a series of tests. The method used for monitoring

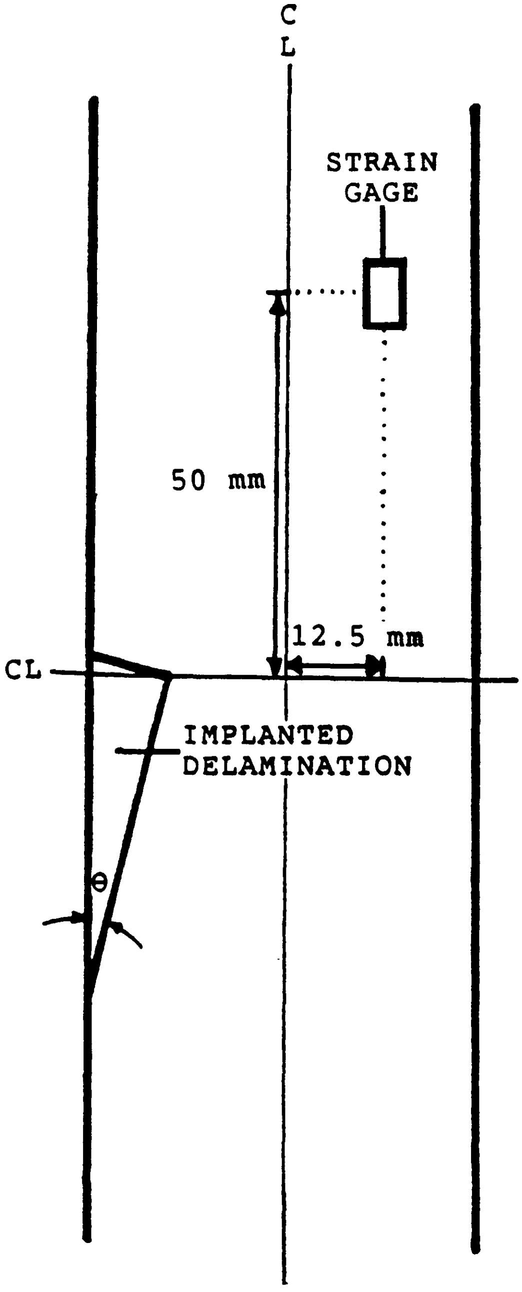

FIGURE 6.3 LOCATION OF THE STRAIN GAGE ON A SPECIMEN WITH AN IMPLANTED DELAMINATION

delamination growth is dye penetrant-enhanced x-radiography. The dye penetrant used is di-iodobutane (DIB) which is a liquid. DIB is applied to the free edge of a specimen with a cotton swab. It is applied after a test while the specimen is at half the maximum stroke level. The DIB has a low viscosity and can seep into delaminated regions via capillary action.

After DIB has been applied, the specimen is removed from the testing machine. The location of the DIB can be detected with x-radiography. The x-ray machine used in this investigation is a Scanray Torrex 150D X-ray Inspection Device. The machine is used in "timed radiation" (TIMERAD) mode. An unexposed sheet of black and white instant film is placed on a sensor in the x-ray chamber. The film used is 100 mm by 125 mm (4 in by 5 in nominal) Polaroid PolaPan instant sheet film type 52. The portion of the specimen to be x-rayed is placed on top of the film. The door to the x-ray chamber is closed and the x-ray generator is activated. When the sensor detects a certain quantity of radiation, the x-ray generator is shut off. The quantity of radiation detected by the sensor is set to 240 mR (milliRoentgens). This gives an optimal level of contrast.

The film can be developed using a standard Polaroid camera back. The resulting x-radiograph essentially shows three shades of gray. The region of the film which is not shielded by any portion of the specimen is for all practical purposes white. This is a result of the interaction of the x-rays and the light sensitive chemicals in the film. The region under the undelaminated section of the laminate is a medium gray. This results from the fact that the specimen absorbs a significant portion of the x-rays passing through it. The delaminated region shows up as a dark gray. This is a result of the fact that the thin layers of DIB in the delaminations absorb a large fraction of the x-rays passing through them.

Two x-radiographs are necessary for each specimen after each test. Each details the damage on one half of the 200 mm long test section. There is a small amount of overlap between the two x-radiographs. The longitudinal position of damage can usually be determined by referencing the position to either a loading tab or a strain gage. Both features are visible in most x-radiographs.

6.3 Incremental Load Testing

The same general testing procedures are used in this portion of the investigation. The specimens are either tested using manually controlled loading and data acquisition or with a computer-controlled testing program that allows for simultaneous commencement of the loading ramp and the data acquisition. Load, strain, and stroke data are recorded at prescribed time intervals.

Four specimens of nonstandard width (two 10 mm wide specimens and two 30 mm wide specimens) were tested using the load drop technique described in Chapter 5 to determine delamination initiation stress. Most of the remaining specimens were tested using an incremental loading technique. In these tests, a predetermined load level is entered into the computer program before each test is started. When the program determines that that load level has been reached, the test is stopped. The stroke is reduced by a factor of two and DIB is applied to both free edges of the specimen. The specimen is unloaded and removed from the testing machine. X-radiographs are then taken. The load increment between subsequent tests of the same specimens is dependent on the type of specimen.

Only one of the four specimens of nonstandard width exhibited a load drop at delamination initiation large enough to be detected by the load drop testing program. The delamination initiation stress was 513 MPa. The four specimens were all tested to failure. The average failure stress was 534 MPa with a coefficient of variation of 1.0%. An initial loading to 450 MPa and subsequent loading increments equivalent to stress increments of 10 MPa were chosen to be sufficient to document all delamination growth of the specimens of nonstandard width. The data acquisition time increment for these specimens was 0.3 second.

The $[\pm 20_F]_s$ fabric specimens and the $[\pm 15_n/0_n]_s$ and $[0_n/\pm 15_n]_s$ specimens were tested in groups of five specimens of the same laminate type and effective ply thickness. The first three specimens in each group were tested monotonically to failure under manual control. The remaining specimens are then tested incrementally starting at 75% of the average observed failure stress of the first three specimens. The maximum load level in subsequent tests was increased in increments equivalent to 5% of the average observed failure stress. The data acquisition time increment for these specimens was 0.5 second.

The specimens with implanted delaminations were first tested at 40% of the average observed failure load of the five $[0_3/\pm15_3]_s$ without implanted damage. The stress increment in subsequent tests was 10% of the failure stress until the 100% level was reached. The increment after that level was reduced to 5% of the failure stress. The data acquisition time increment for these specimens was 0.5 second.

6.4 Results

The experimental results are reported by specimen type.

6.4.1 Specimens of Nonstandard Width

In previous work with AS1/3501-6 $[\pm15_3]_s$ specimens, the delamination always initiated before any splits in the angle plies [34]. This was also observed for the AS4/3501-6 $[\pm15_3]_s$ specimen in which delamination initiation was verified by edge replication before failure.

Each specimen was tested to failure. For one 20 mm wide specimen, two 30 mm wide specimens and all wider specimens, "failure" did not include the breaking of the specimen into two separate pieces. Failure in these cases was defined to have occurred when a large fraction of the load was lost. The load decrease was in the range of 60% to 98%. Failure was accompanied by massive splitting and delamination of the outer plies across the entire width of the specimen. Fibers of the inner plies ran from undelaminated regions of the specimen across the failed region to the loading tab. The specimen was therefore not in two pieces and could carry some in-plane load.

The stress-strain behavior was essentially linear to the point of visible delamination in the $[\pm 15_3]_s$ laminates. A typical stress-strain graph is shown in Figure 6.4. The modulus, failure stress, and failure strain are reported for each specimen in Data Table 2. The average values are given in Table 6.1. Data from the four specimens used to determine delamination initiation stress were included in the appropriate calculations of average modulus, failure stress, and failure strain. The average moduli are within experimental scatter of the Classical Laminated Plate Theory prediction of 116 GPa. The failure stress and failure strain appear to be independent of the specimen width to within the resolution of the experiment.

The delaminated area and intrusion of the specimens of nonstandard width were determined after each incremental loading. The data were obtained from x-radiographs. The shape of the delamination during growth was usually

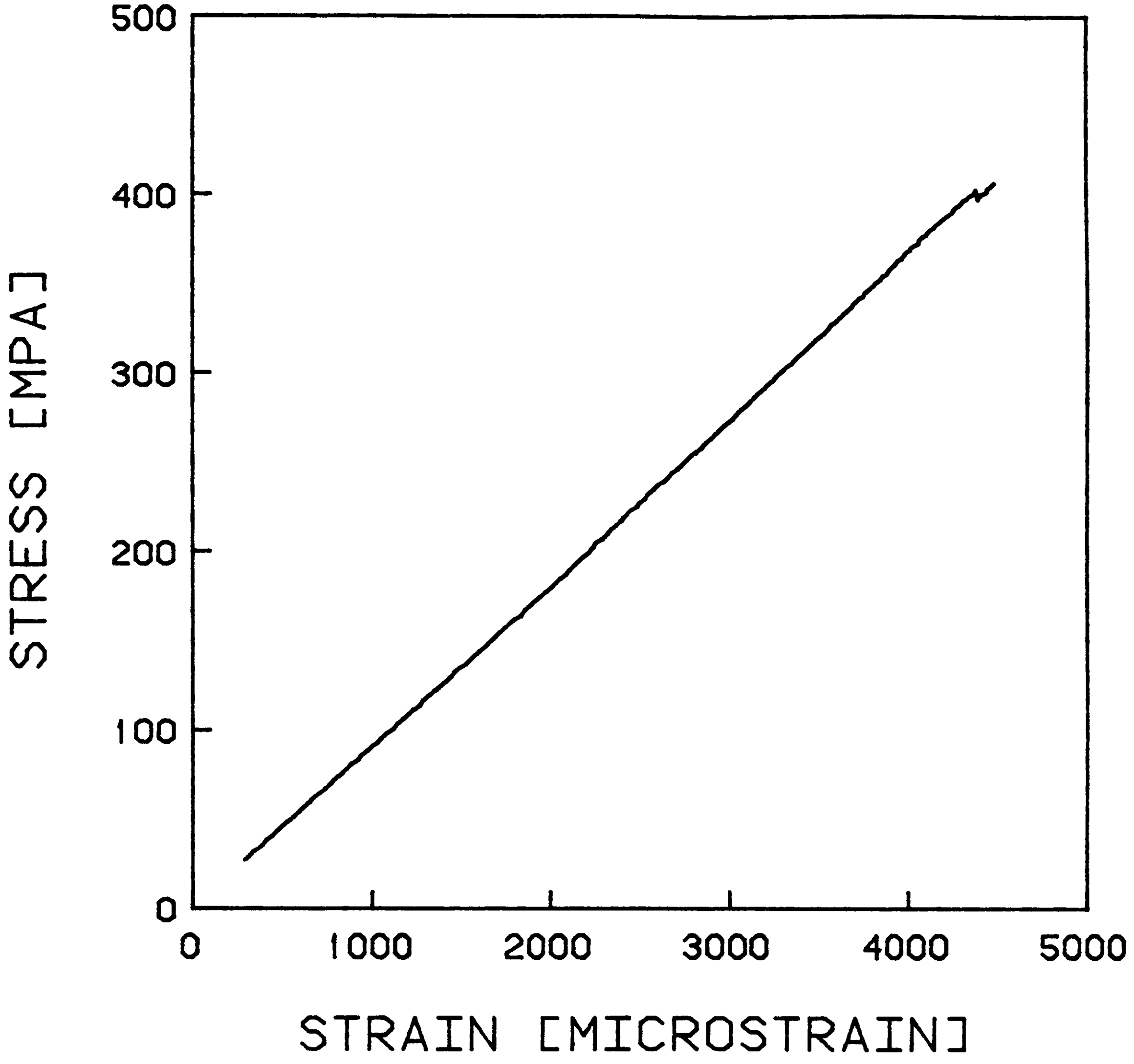

FIGURE 6.4 TYPICAL STRESS-STRAIN GRAPH FOR A $[\pm15_3]_s$ SPECIMEN

TABLE 6.1

AVERAGE MODULUS, FAILURE STRESS, AND FAILURE STRAIN FOR $[\pm15_3]_s$ SPECIMENS OF NONSTANDARD WIDTH

Width [mm]	Modulus [GPa]	Failure Stress [MPa]	Failure Strain [μstrain]
10	115 (8.8%)[a]	508 (4.1%)	4336 (5.8%)
20	116 (2.5%)	502 (3.3%)	4318 (2.7%)
30	116 (4.0%)	515 (3.6%)	4348 (3.5%)
50	110 (1.2%)	505 (2.8%)	4600 (3.2%)
70	110 (5.3%)	488 (7.3%)	4687 (13.5%)

[a] Numbers in parentheses are coefficients of variation.

triangular. The triangle was always bounded on one side by the free edge and on another by a split in the +15° ply. The third side of the triangle was the delamination front. The delamination front usually extended from the angle ply split toward the free edge at approximately a right angle. This delamination shape is depicted schematically in Figure 3.7. There were occasionally splits along the fiber direction in the $[-15_6]$ sublaminate which extended from the split in the $[+15_3]$ sublaminate to the free edge. In some instances, the delaminated region enlarged slightly such that the delamination front coincided with one of these splits. Typical x-radiographs of both types of delamination fronts are shown in Figure 6.5. Larger delaminations were usually accompanied by visible out-of-plane peeling of the $[+15_3]$ sublaminate in the region between the split and the free edge. This peeling is depicted in the photograph in Figure 6.6.

The specimens which exhibited detectable delamination growth before failure are listed in Appendix A with the maximum stress, the strain associated with the maximum stress, the number of observed delaminations, the maximum intrusion, and the total delaminated area associated with each test. The range of stresses during which the first delamination growth occurs is bounded for each specimen by the maximum stress of the last test in which no delamination was detected and the maximum stress of the first test in which a delamination was observed. An average first growth stress range can be

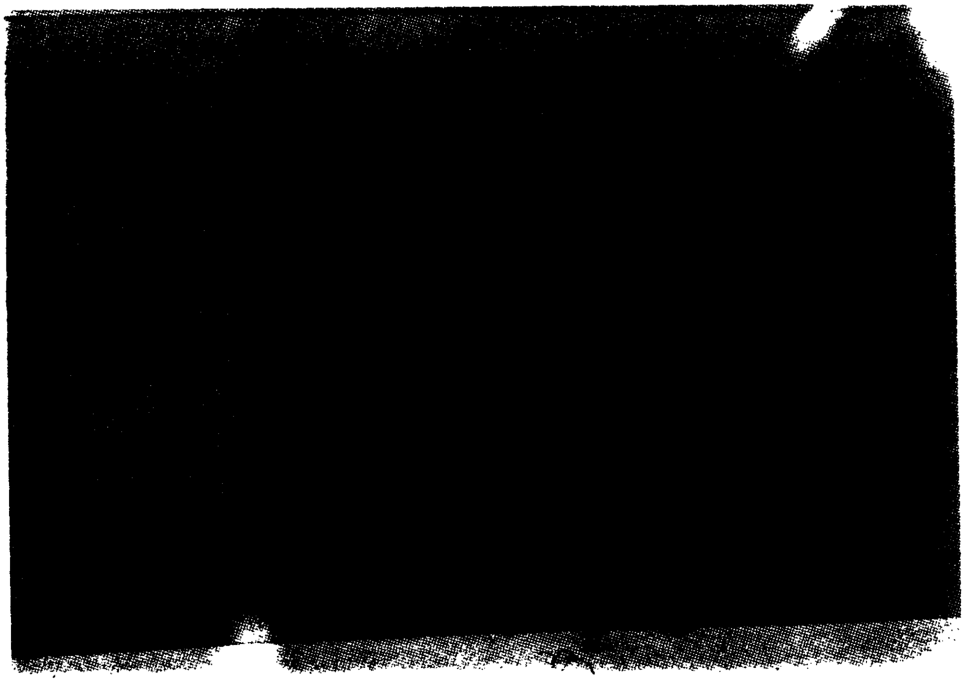

(a) DELAMINATION FRONT APPROXIMATELY PERPENDICULAR TO ANGLE PLY SPLIT

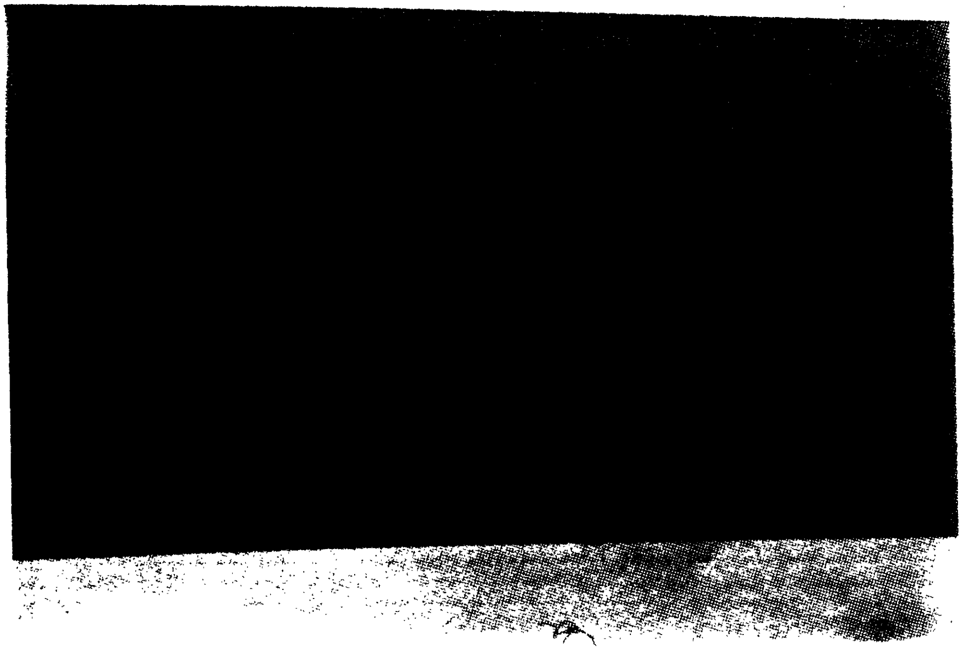

(b) DELAMINATION BORDERED BY TWO ANGLE PLY SPLITS

FIGURE 6.5 X-RADIOGRAPHS OF TYPICAL DELAMINATIONS IN $[\pm 15_3]_s$ SPECIMENS

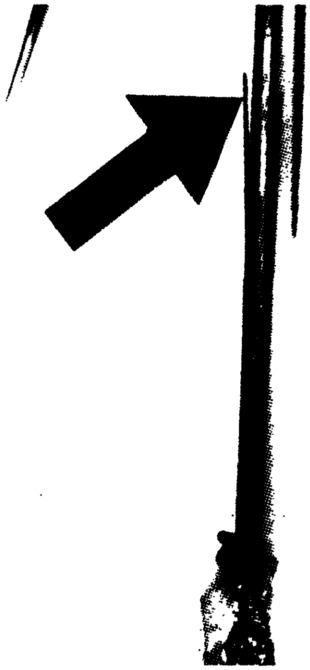

FIGURE 6.6 PEELING AND UNLOADING OF A [$+15_3$] SUBLAMINATE IN A [$\pm15_3$]$_s$ SPECIMEN

determined for a group of specimens by averaging the lower bounds and then the upper bounds. The average first growth stress range, average maximum intrusion before failure, and maximum delaminated area before failure are reported for the specimens of nonstandard width in Table 6.2.

6.4.2 $[\pm15_n/0_n]_s$ and $[0_n/\pm15_n]_s$ Specimens

The $[\pm15_n/0_n]_s$ and $[0_n/\pm15_n]_s$ specimens exhibited linear stress-strain behavior until visible damage occurred. Typical stress-strain graphs for the two lamination sequences are shown in Figures 6.7 and 6.8, respectively. All specimens were tested to failure. For specimens with values of n greater than one, failure did not always include the breaking of the specimen into two separate pieces. Failure was again defined to have occurred when a large fraction of the load was lost. In most of these cases, the load decreased by between 40% and 80% at failure. Failure was usually accompanied by the delamination and in-plane failure of the angled plies and splitting of the 0° plies. Nonetheless, the 0° plies could still carry substantial longitudinal load. The modulus, failure stress, and failure strain for each specimen is given in Data Tables 3 ($[\pm15_n/0_n]_s$ specimens) and 4 ($[0_n/\pm15_n]_s$ specimens). The average values for each specimen type are given in Table 6.3. The moduli are all within experimental scatter of the value of 126 GPa predicted by Classical Laminated Plate Theory for these laminate types.

TABLE 6.2

AVERAGE FIRST GROWTH STRESS RANGE, MAXIMUM INTRUSION, AND DELAMINATION AREA BEFORE FAILURE FOR $[\pm15_3]_s$ SPECIMENS OF NONSTANDARD WIDTH

Width [mm]	Average First Growth Stress Range [MPa]	Average Maximum Intrusion Before Failure [mm]	Average Delaminated Area Before Failure [cm²]
10	492-497	0	0
20	487-502	0	0
30	496-505	3	2
50	474-482	8	2
70	478-483	31	22

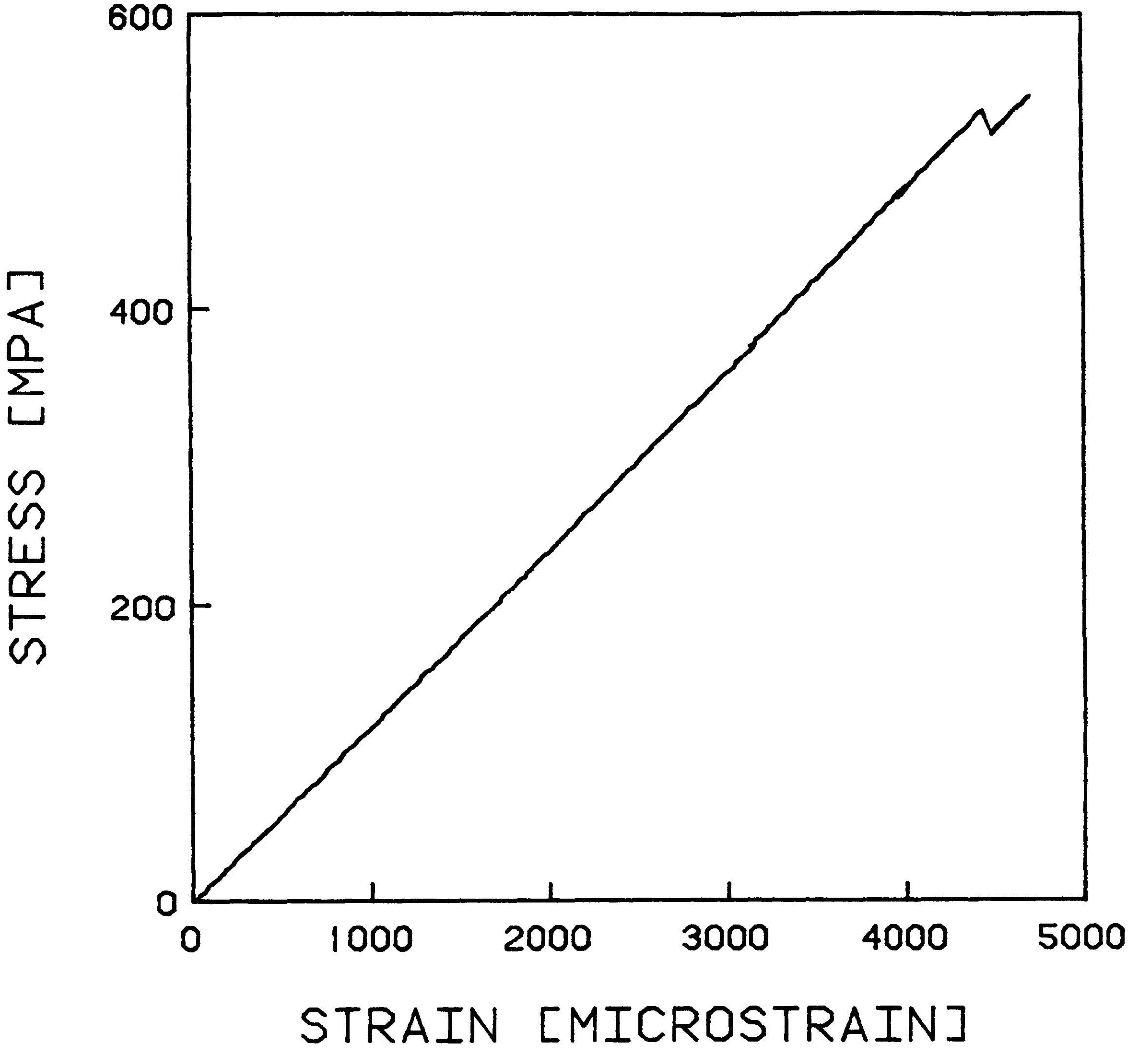

FIGURE 6.7 TYPICAL STRESS-STRAIN GRAPH FOR A $[\pm15_n/0_n]_s$ SPECIMEN

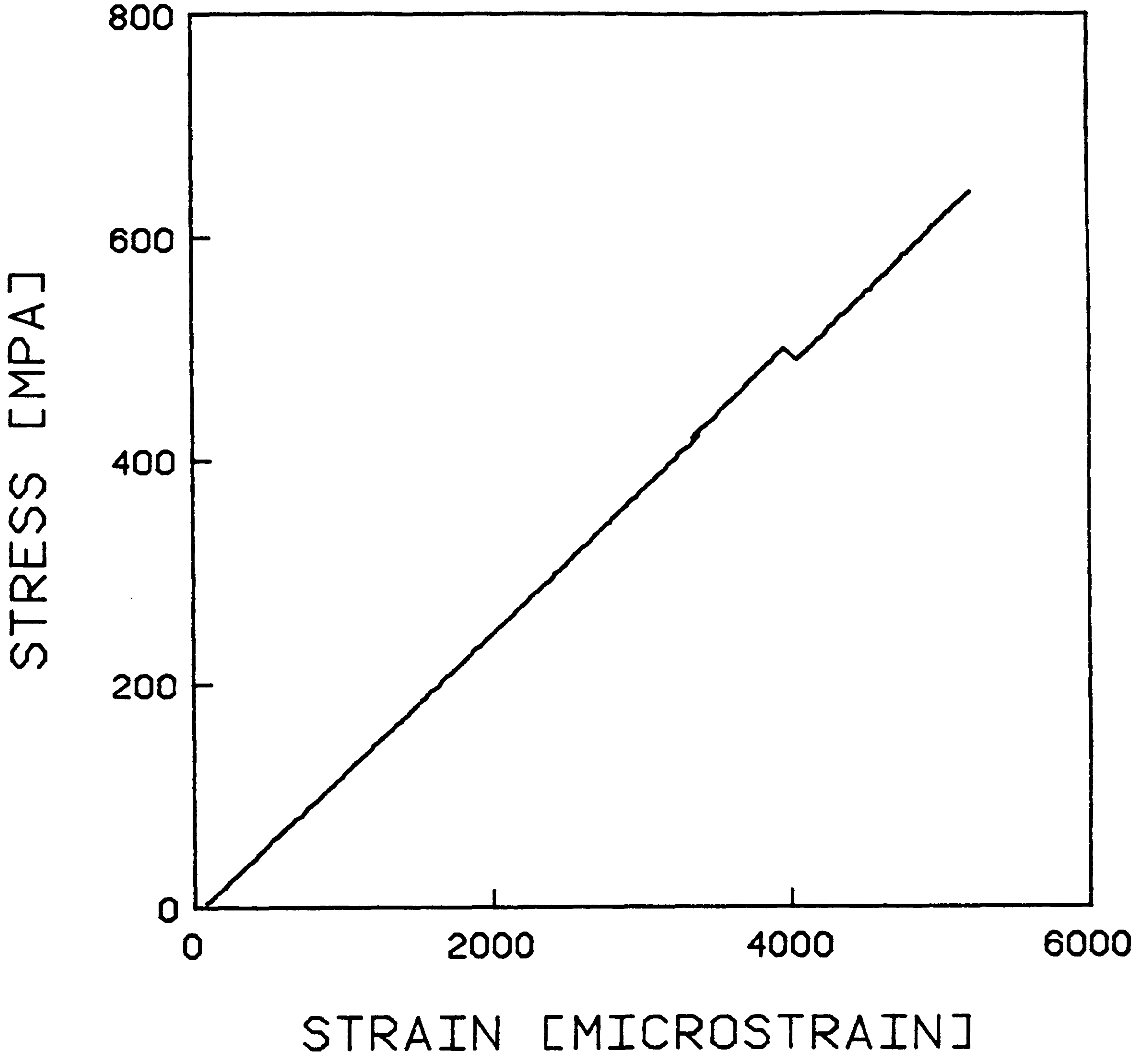

FIGURE 6.8 TYPICAL STRESS-STRAIN GRAPH FOR A $[0_n/\pm15_n]_s$ SPECIMEN

TABLE 6.3

AVERAGE MODULUS, FAILURE STRESS, AND FAILURE STRAIN FOR $[\pm15_n/0_n]_s$ AND $[0_n/\pm15_n]_s$ SPECIMENS

Laminate Type	Modulus [GPa]	Failure Stress [MPa]	Failure Strain [μstrain]
$[\pm15/0]_s$	125 (3.2%)[a]	1003 (4.1%)	7935 (6.5%)
$[\pm15_2/0_2]_s$	122 (5.7%)	747 (8.1%)	6312 (10.7%)
$[\pm15_3/0_3]_s$	123 (5.0%)	642 (6.6%)	5997 (19.5%)
$[\pm15_5/0_5]_s$	117 (8.0%)	618 (10.5%)	5626 (17.0%)
$[\pm15_8/0_8]_s$	115 (6.1%)	541 (2.5%)	5137 (11.5%)
$[0/\pm15]_s$	124 (3.1%)	1160 (3.3%)	9028 (5.5%)
$[0_2/\pm15_2]_s$	123 (6.4%)	863 (4.7%)	7463 (9.4%)
$[0_3/\pm15_3]_s$	123 (8.1%)	760 (8.8%)	6570 (19.1%)
$[0_5/\pm15_5]_s$	119 (10.5%)	669 (7.1%)	6289 (15.1%)
$[0_8/\pm15_8]_s$	114 (14.1%)	618 (5.9%)	5371 (6.3%)

[a] Numbers in parentheses are coefficients of variation.

Two trends are evident in the failure data. First, failure stress and strain decrease as effective ply thickness increases. Second, the values for $[0_n/\pm15_n]_s$ specimens are consistently higher than those of the $[\pm15_n/0_n]_s$ specimens. These trends were observed by Lagace et al. for AS1/3501-6 specimens [37].

The specimens which exhibited detectable delamination growth are listed in Appendix B ($[\pm15_n/0_n]_s$ specimens) and Appendix C ($[0_n/\pm15_n]_s$ specimens) with the maximum stress, the strain associated with the maximum stress, the number of observed delaminations, the maximum intrusion, and the total delaminated area of each test. The average first growth stress range, average maximum intrusion before failure, and maximum delaminated area before failure are reported in Table 6.4. Each of these averages is calculated using data from only two specimens since three of the five specimens of each type were used to determine only the failure stress.

The damage changed as effective ply thickness increased for both laminate types. The thinnest specimens (n = 1) broke into two pieces upon failure. The fracture surface had rough segments approximately perpendicular to the free edge. These segments contained portions of several delaminated plies. The fracture surface also had segments which were relatively smooth and extended along the +15° and -15° directions. There were relatively small delaminations along the edge of these segments. An x-radiograph showing damage of a failed $[\pm15/0]_s$ specimen is shown in Figure 6.9. For the other $[\pm15_n/0_n]_s$

TABLE 6.4

AVERAGE FIRST GROWTH STRESS RANGE, MAXIMUM INTRUSION, AND DELAMINATION AREA BEFORE FAILURE FOR $[\pm15_n/0_n]_s$ AND $[0_n/+15_n]_s$ SPECIMENS

Laminate Type	Average First Growth Stress Range [MPa]	Average Maximum Intrusion Before Failure [mm]	Average Delaminated Area Before Failure [cm²]
$[\pm15/0]_s$	785-837	6	2
$[\pm15_2/0_2]_s$	629-666	15	13
$[\pm15_3/0_3]_s$	512-541	34	31
$[\pm15_5/0_5]_s$	<495[a]	15	13
$[\pm15_8/0_8]_s$	<414[a]	32	31
$[0/\pm15]_s$	1001-1059	2	0
$[0_2/\pm15_2]_s$	733-772	20	22
$[0_3/\pm15_3]_s$	<540[a]	25	23
$[0_5/\pm15_5]_s$	<502[a]	13	8
$[0_8/\pm15_8]_s$	<484[a]	9	2

[a] Delamination occurred in the first test of both specimens.

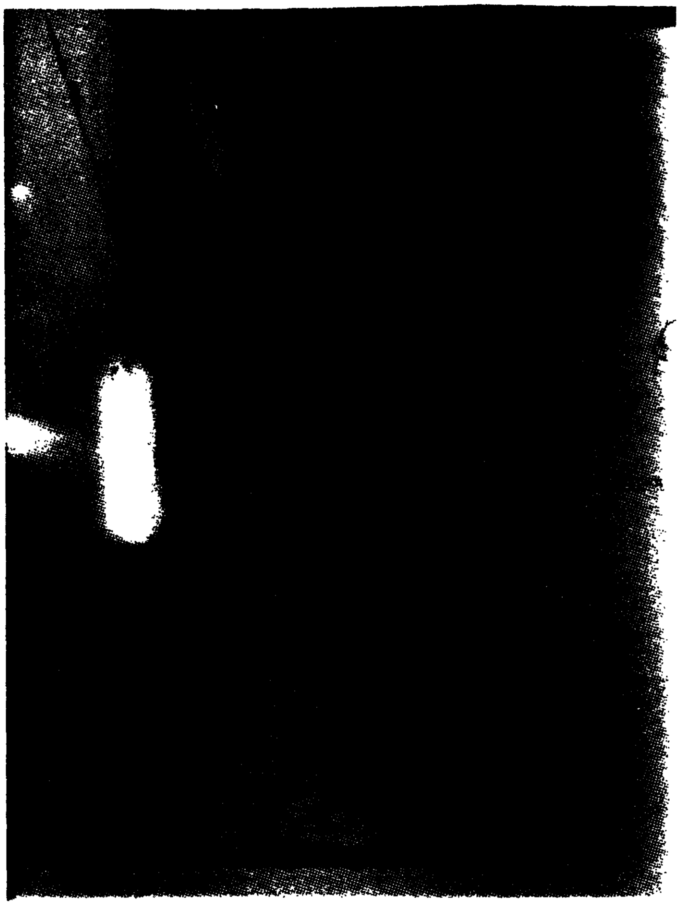

FIGURE 6.9 X-RADIOGRAPH OF A $[\pm 15/0]_s$ SPECIMEN AFTER FAILURE

specimens, the thinner specimens tended to have more delaminations before failure, but they were considerably smaller. Few of these specimens broke into two pieces. Thicker specimens exhibited more pronounced peeling of the delaminated $[+15_n]$ sublaminates before and after failure. The thicker specimens also showed greater spacing between the splits in the plies upon failure. A photograph of failed $[\pm 15_n/0_n]_s$ specimens is shown in Figure 6.10.

The $[0/\pm 15]_s$ specimens exhibited fewer delaminations before failure than the $[\pm 15/0]_s$ specimens. Upon failure, the fracture surfaces were cleaner and were predominantly along the +15° and -15° directions. An x-radiograph which illustrates the damage state of a failed $[0/\pm 15]_s$ specimen is shown in Figure 6.11.

Many of the thicker $[0_n/\pm 15_n]_s$ specimens experienced more delaminations than their $[\pm 15_n/0_n]_s$ counterparts before failure. None of these specimens broke into two pieces upon failure. There was no peeling of the $[0_n]$ sublaminate on the surface. In many cases, the portion of the $[-15_{2n}]$ sublaminate which had delaminated from the neighboring sublaminates and split away from the rest of the $[-15_{2n}]$ sublaminate rotated slightly such that part of the sublaminate extended out from the free edge. This "shear out" behavior is illustrated in Figure 6.12. The thicker specimens also showed greater spacing between the splits in the plies upon failure. A photograph of failed $[0_n/\pm 15_n]_s$ specimens is shown in Figure 6.13.

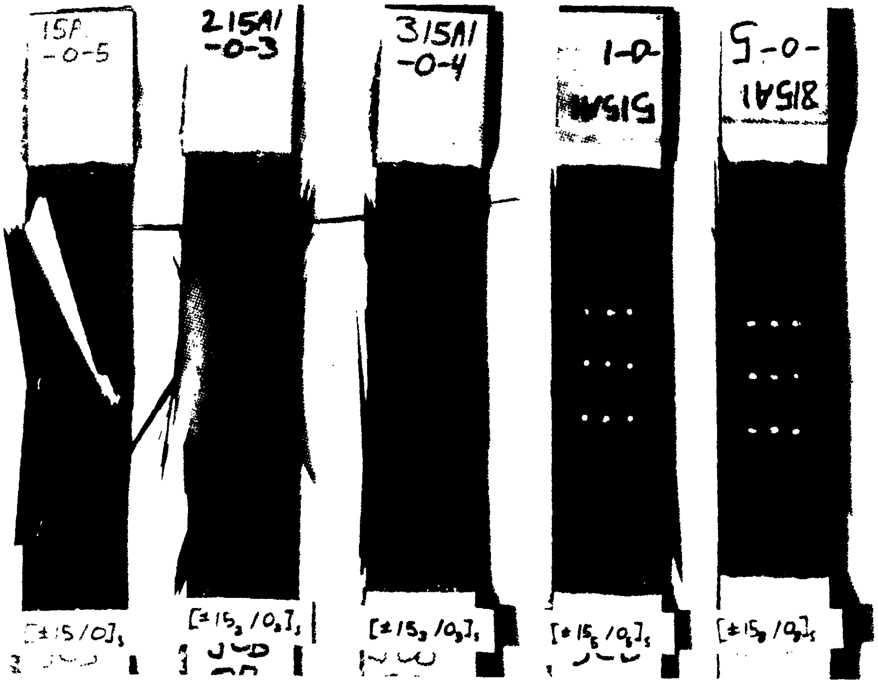

FIGURE 6.10 PHOTOGRAPH OF FAILURE MODES OF $[\pm 15_n/0_n]_s$ SPECIMENS

FIGURE 6.11 X-RADIOGRAPH OF A $[0/\pm 15]_s$ SPECIMEN AFTER FAILURE

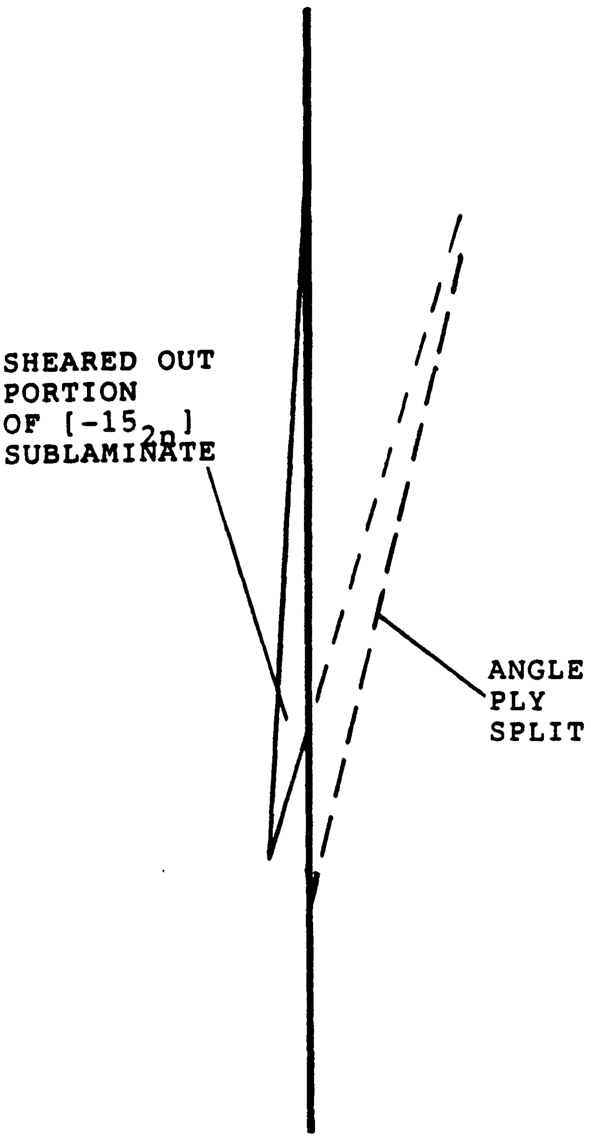

FIGURE 6.12 SCHEMATIC OF THE "SHEAR OUT" OF THE [-15_{2n}] SUBLAMINATE IN A [$0_n/\pm15_n]_s$ SPECIMEN

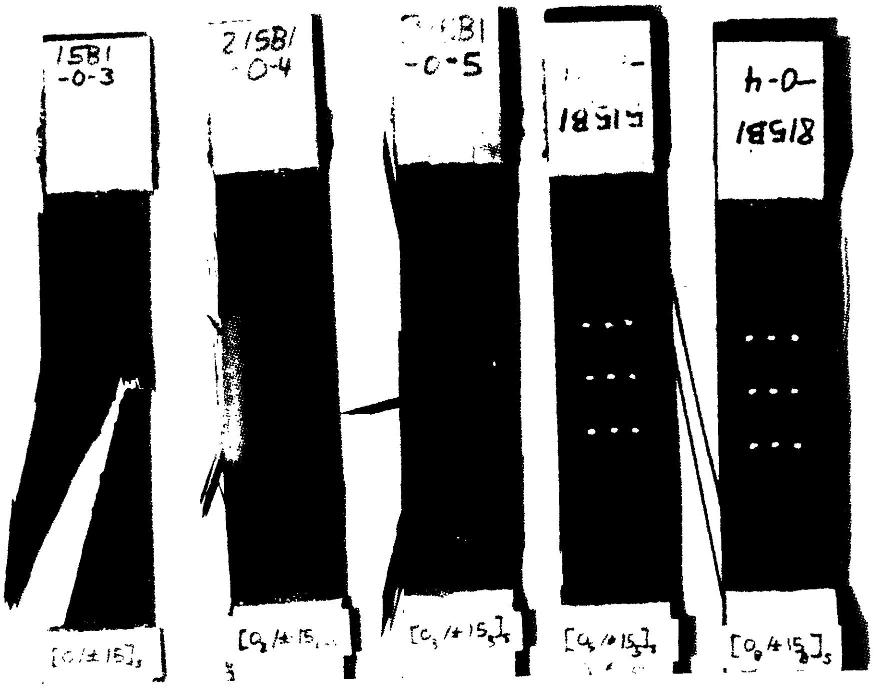

FIGURE 6.13 PHOTOGRAPH OF FAILURE MODES OF $[0_n/\pm15_n]_s$ SPECIMENS

It is not clear how unstable delamination growth might manifest itself in these experiments. Final failure, as defined above, was always accompanied by complete or nearly complete delamination of the +15°/-15° and 0°/15° interfaces for all specimens with values of n greater than one. However, in many of these specimens, delaminations grew to a loading tab and stopped prior to final failure. In other specimens, growth of the delamination to a loading tab was coincident with final failure. It is likely that delaminations that grew to the loading tab and stopped would have continued to grow in an actual part. Thus, such delaminations may be indicative of unstable growth. This is evidence that unstable delamination growth is not necessarily equivalent to final failure.

A substantial amount of delamination growth may be necessary before failure can be induced by delamination. If the delaminated region were to remain small and stable, the strength of the specimen would not vary significantly from the predicted in-plane strength. As the delaminated region grows, however, the strength of the specimen is degraded. Final failure in the specimens in this portion of the investigation usually occurred at or soon after delamination growth to the loading tab.

Delaminations did not grow to the loading tabs in the thin (n = 1) specimens. Nonetheless, there may have been some "unstable" growth associated with final failure. It can be seen in Figures 6.9 and 6.11 that considerable delamination is associated with the fracture surface.

When growth to a loading tab was not accompanied by complete delamination and final failure, it could usually be detected with the naked eye and was accompanied by an audible click. In the $[\pm15_n/0_n]_s$ specimens, there was usually peeling of the surface plies. In the $[0_n/\pm15_n]_s$ specimens, there was usually some shear out of the inner plies. The load data also usually showed a significant drop in load when growth to the tab occurred.

The data acquisition program had the ability to mark data points if such events occurred. Thus, the growth-to-tab stress could usually be determined quite accurately for all specimens regardless of whether or not they were monitored with x-radiography. The growth-to-tab stresses and associated strains are listed in Appendix D with the average values for each specimen type are given in Table 6.5. The growth-to-tab stresses were quite close to the final failure stresses. As with failure stress and strain, the trends are for the stress and strain level to decrease with increasing effective ply thickness and for the values for $[\pm15_n/0_n]_s$ specimens to be lower than the values for $[0_n/\pm15_n]_s$ specimens.

6.4.3 Fabric Specimens

The $[\pm20_F]_s$ fabric specimens exhibited linear stress-strain behavior until delaminations detectable on the x-radiographs were formed. A typical stress-strain graph is shown in Figure 6.14. The specimens were all tested to

TABLE 6.5

AVERAGE GROWTH-TO-TAB STRESSES FOR $[\pm15_n/0_n]_s$ AND $[0_n/\pm15_n]_s$ SPECIMENS

Laminate Type	Average Growth-to-Tab Stress [MPa]	Average Growth-to-Tab Strain [μstrain]	Laminate Type	Average Growth-to-Tab Stress [MPa]	Average Growth-to-Tab Strain [μstrain]
$[\pm15_2/0_2]_s$	713 (8.8%)[a]	6355 (8.9%)	$[0_2/\pm15_2]_s$	830 (7.2%)	6905 (7.6%)
$[\pm15_3/0_3]_s$	603 (6.5%)	5004 (10.1%)	$[0_3/\pm15_3]_s$	710 (2.9%)	5838 (10.8%)
$[\pm15_5/0_5]_s$	567 (7.5%)	4824 (6.9%)	$[0_5/\pm15_5]_s$	656 (6.1%)	5726 (16.9%)
$[\pm15_8/0_8]_s$	525 (6.3%)	4651 (8.4%)	$[0_8/\pm15_8]_s$	602 (7.6%)	5584 (11.5%)

[a] Numbers in parentheses are coefficients of variation.

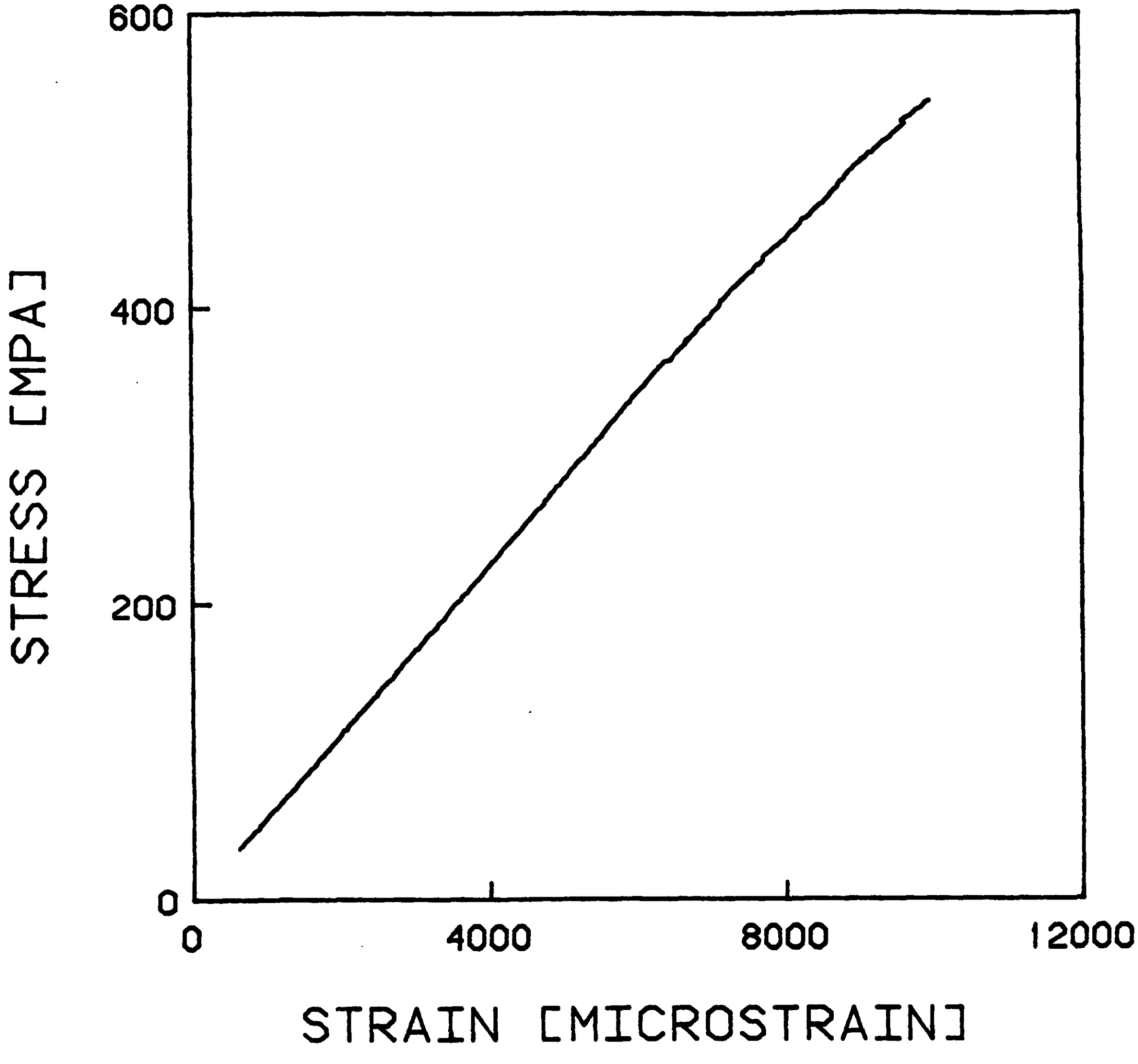

FIGURE 6.14 TYPICAL STRESS-STRAIN GRAPH FOR A $[\pm 20_F]_S$ SPECIMEN

failure. The modulus, failure stress, and failure strain for each specimen is given in Data Table 5. The average values for both specimen types are given in Table 6.6. The moduli are well within experimental scatter of the Classical Laminated Plate Theory value of 56 GPa. The average failure stresses are significantly less than the value of 647 MPa predicted for in-plane failure by the generalized criterion of Tsai and Wu [38]. This value was obtained using the strength properties for Hercules AW370-5H/3501-6 listed in Table 6.7.

The specimens with only warp faces at the +20°/-20° interface had a failure stress of 530 MPa with a coefficient of variation of 4.0%. Those with only fill faces at that interface had a failure stress of 530 MPa with a coefficient of variation of 2.7%. Given these relatively small coefficients of variation, a difference in failure stress of 12.8% is significant.

The delamination growth behavior varied for the two specimen types. Details regarding the number of delaminations, maximum intrusion, and total delaminated area after each test are given for the specimens monitored by dye penetrant-enhanced x-radiography in Appendix E.

The specimens with only fill faces at the +20°/-20° interface exhibited delaminations detectable from the x-radiographs at lower stresses. These delaminations are most likely not formed concurrently with delamination initiation, which should be the same for both specimen types. The delaminations tended to be triangularly shaped. They were

TABLE 6.6

AVERAGE MODULUS, FAILURE STRESS, AND FAILURE STRAIN FOR $[\pm 20_F]_s$ FABRIC SPECIMENS

Interface Type	Modulus [GPa]	Failure Stress [MPa]	Failure Strain [μstrain]
Fill/Fill	56 (3.8%)[a]	470 (2.7%)	9291 (8.9%)
Warp/Warp	55 (5.3%)	530 (4.0%)	9895 (5.2%)

[a] Numbers in parentheses are coefficients of variation.

TABLE 6.7

STRENGTH PARAMETERS FOR HERCULES AW370-5H/3501-6 FABRIC GRAPHITE/EPOXY

Test Type	Strength [MPa]
Longitudinal Tension	817
Longitudinal Compression	779
Transverse Tension	728
Transverse Compression	712
Shear	105

bounded on one side by the free edge and on the other two sides by lines at ±20° to the longitudinal axis. The lines were apparently splits in warp fiber tows. The boundaries of the delaminated region did not coincide exactly with these splits. There were also some delaminations which were rounded with no clear boundaries. Both types of delaminations are visible in the x-radiograph in Figure 6.15.

The specimens with only warp faces at the +20°/-20° interface exhibited smaller, more clearly defined delaminations. These delaminations were bounded on one side by a line at 20° to the longitudinal axis and on the other side by a line roughly perpendicular to that. The contrast of the x-radiographs of these features is quite low. An example of one of these delaminations in an x-radiograph is therefore indicated with an arrow in Figure 6.16.

Light lines at ±70° to the longitudinal direction were visible in most x-radiographs in which delaminations were visible. These lines indicate splits in the fill fiber tows of all the plies. They apparently formed after the delaminations.

6.4.4 Specimens with Implanted Delaminations and Angle Ply Splits

The specimens with implanted delaminations and angle ply splits were all tested to failure. As was observed for the $[0_3/\pm15_3]_s$ specimens with no implanted damage, the specimens

FIGURE 6.15 X-RADIOGRAPH OF TYPICAL DELAMINATIONS IN $[\pm 20_F]_S$ SPECIMENS WITH FILL FACES AT THE +20°/-20° INTERFACE

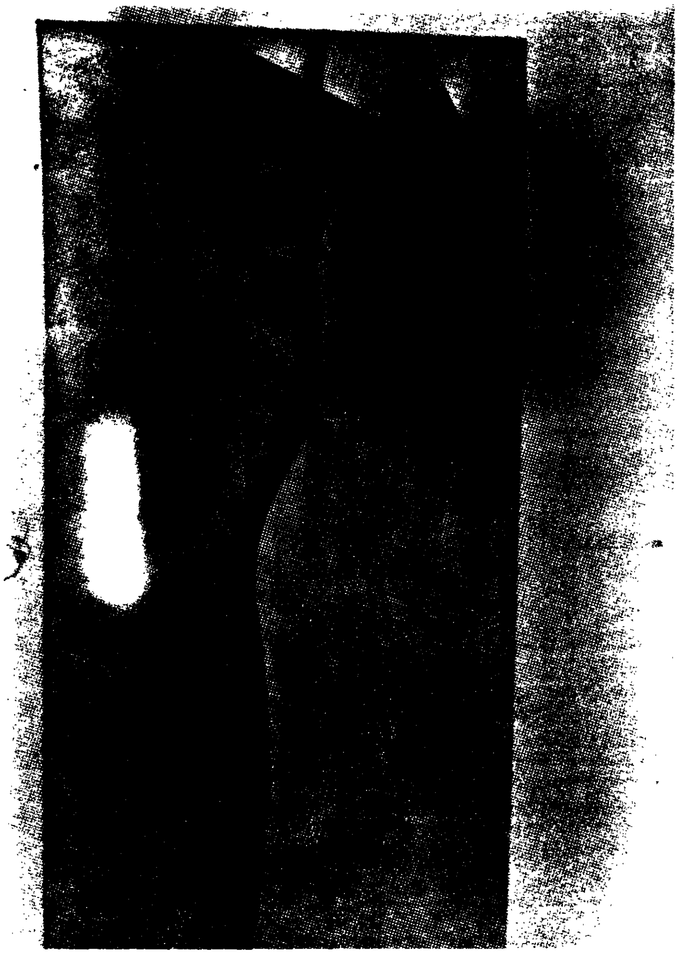

FIGURE 6.16 X-RADIOGRAPH OF TYPICAL DELAMINATIONS IN $[\pm 20_F]_S$ SPECIMENS WITH WARP FACES AT THE +20°/-20° INTERFACE

did not break into two pieces at failure. The failure stress and failure strain are given for each specimen in Data Table 6 with the average values given in Table 6.8. The average moduli are within experimental scatter of 116 GPa which is the value predicted by Classical Laminated Plate Theory. The average failure stress of specimens with implanted angle ply splits was 11.1% lower than that for specimens with implanted delaminations alone. The specimens with implanted delaminations and no angle ply splits failed at a 2.0% higher stress than those with no implanted damage. This difference is within experimental scatter.

During the curing process, the teflon film is weakly bonded to the neighboring sublaminates. When this bond was broken, the specimens emitted an audible "click" and experienced a detectable increase in the strain data. This is the "formation point" of the implanted delamination in that the sublaminates were still bonded and strain continuity applied through the thickness before this event. The stress-strain behavior was linear until this event. A typical stress-strain graph exhibiting this formation point is shown in Figure 6.17 The modulus of each specimen is given in Data Table 6. The average values are given in Table 6.8.

In specimens with an implanted angle ply split, the implanted split "formed" at the same time as the delamination. In the specimens without an implanted angle ply split, a split formed spontaneously in the $[-15_6]$ sublaminate at the edge of the delaminated region. This usually occurred

TABLE 6.8

MODULUS AND FAILURE DATA FOR $[0_3/\pm15_3]_s$ SPECIMENS WITH IMPLANTED DELAMINATIONS

Nominal Intrusion of the Implanted Delamination [mm]	Nominal Intrusion of the Implanted Angle Ply Split [mm]	Modulus [GPa]	Failure Stress [MPa]	Failure Strain [μstrain]
10	0	114 (3.1%)[a]	775 (1.8%)	6708 (2.5%)
10	20	112 (5.2%)	697 (2.4%)	6253 (5.9%)

[a] Numbers in parentheses are coefficients of variation.

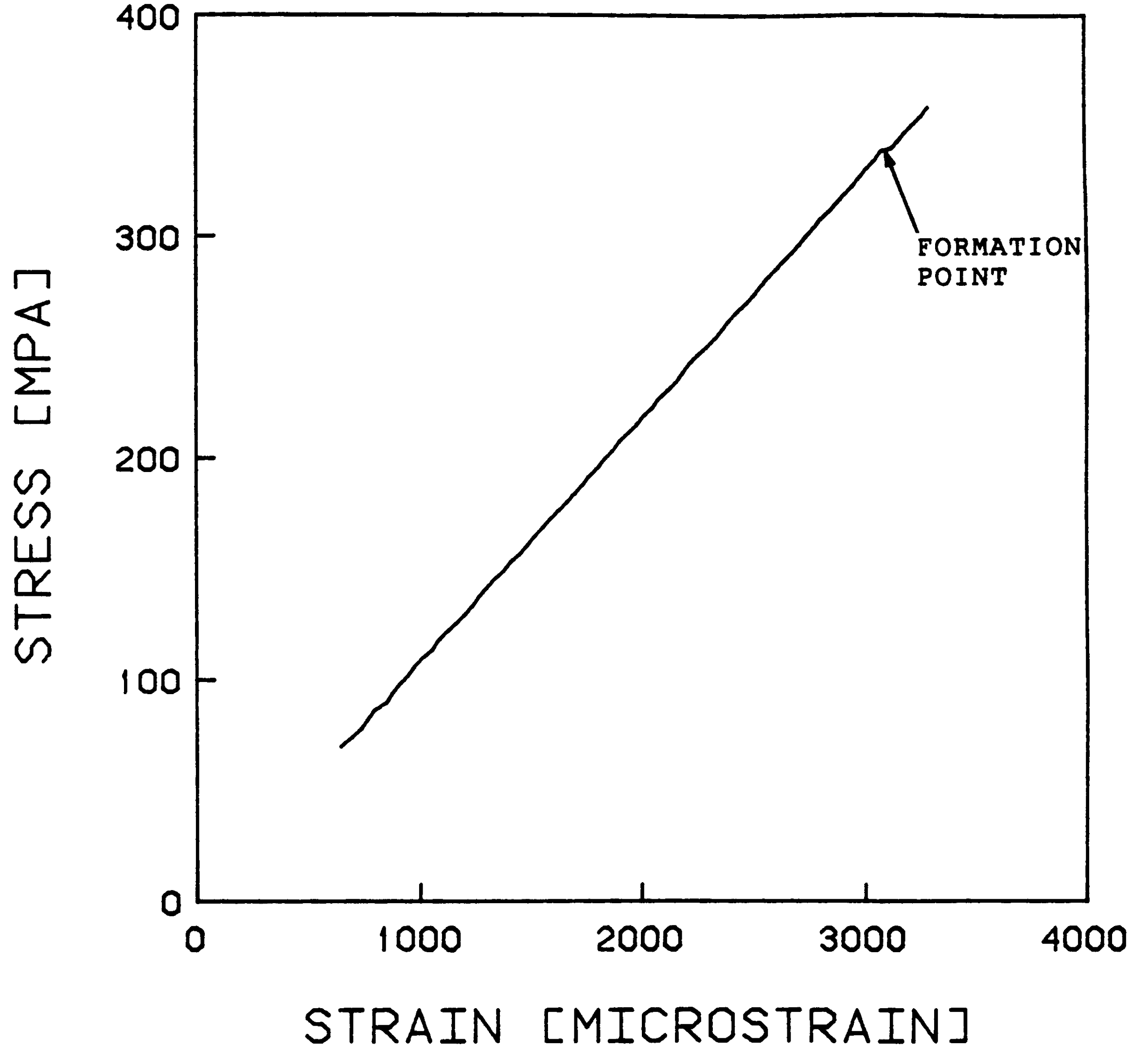

FIGURE 6.17 TYPICAL STRESS-STRAIN GRAPH FOR A $[0_3/\pm15_3]_s$ SPECIMEN WITH AN IMPLANTED DELAMINATION SHOWING THE "FORMATION POINT" OF THE DELAMINATION

at a higher stress than the delamination formation. The formation of these angle ply splits was confirmed from the x-radiographs. An x-radiograph showing an implanted delamination and the associated angle ply split is shown in Figure 6.18. The stresses and strains at the formation of the delamination and angle ply split are given for each specimen in Appendix F. The average values are given in Table 6.9. The delamination formation stresses were approximately the same for both types of specimens. The angle ply split formation stress was approximately twice as high for the cases in which it was not implanted, although the coefficient of variation was quite high (34.5%). In all cases, however, both the delamination and the angle ply split had formed well before failure. This indicates that the global stress fields surrounding the delaminated region correctly approximated those of a naturally occurring delamination through nearly all of the testing.

The nominal intrusions of the delaminations were 10 mm. The nominal intrusions of the angle ply splits were 20 mm. After the delamination formation point, the actual intrusion could be determined from the x-radiographs. The intrusions of the implanted delaminations and angle ply splits are given for each specimen in Data Table 6. The actual average values were 15 mm with a coefficient of variation of 8.4% for the specimens without an implanted angle ply split and 13 mm with a coefficient of variation of 13.9% for the specimens with an implanted angle ply split. The nominal intrusion of the angle

FIGURE 6.18 X-RADIOGRAPH OF A $[0_3/\pm15_3]_s$ SPECIMEN WITH AN IMPLANTED DELAMINATION AND THE ASSOCIATED SPONTANEOUSLY FORMED ANGLE PLY SPLIT

TABLE 6.9

DELAMINATION AND ANGLE PLY SPLIT FORMATION DATA FOR $[0_3/\pm 15_3]_s$ SPECIMENS WITH IMPLANTED DELAMINATIONS

Nominal Intrusion of the Implanted Delamination [mm]	Nominal Intrusion of the Implanted Angle Ply Split [mm]	Delamination Formation[a]		Angle Ply Split Formation[b]	
		Stress [MPa]	Strain [μstrain]	Stress [MPa]	Strain [μstrain]
10	0	140 (8.3%)[a]	1186 (8.4%)	301 (34.5%)	2593 (34.5%)
10	20	152 (14.6%)	1372 (13.0%)	152 (14.6%)	1372 (13.0%)

[a] The point at which the implanted teflon debonded from neighboring plies.

[b] The point at which an angle ply split was first visible on an x-radiograph.

[c] Numbers in parentheses are coefficients of variation.

ply split was 20 mm. The actual average value was 26 mm with a coefficient of variation of 8.4%.

There was usually little delamination growth seen in either specimen type before failure. Angle ply splits did form in the $[+15_3]$ and $[-15_6]$ sublaminates in the delaminated region. In some instances, the splits in the $[+15_3]$ sublaminates extended between the region of the implanted delamination and the free edge. In these cases, the delamination front advanced slightly to include this region. This behavior is illustrated in the x-radiograph in Figure 6.19.

In three of the six specimens with angle ply splits, delamination grew to the end of the implanted angle ply split before final failure. This behavior is exhibited in the x-radiograph in Figure 6.20. The stress and strain were determined for each of the six specimens. In three specimens, the delamination did not stop at the end of the implanted angle ply split. The delamination was total and failure ensued. For these specimens, therefore, the stress and strain at which growth to the end of the implanted angle ply split occurred were set equal to the final failure values. These stresses and strains are reported in Appendix G. The average stress for the six specimens was 690 MPa with a coefficient of variation of 3.1%.

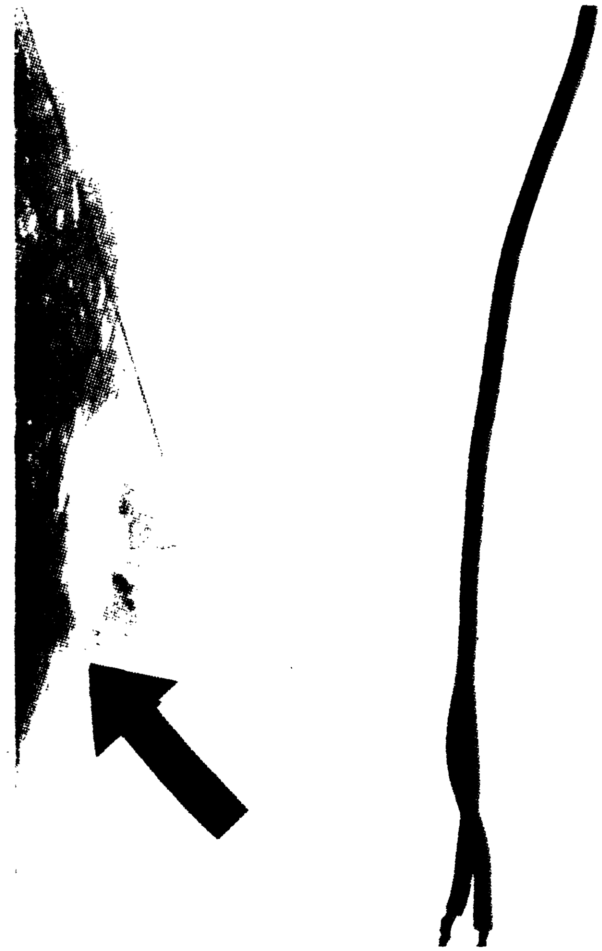

FIGURE 6.19 X-RADIOGRAPH OF A $[0_3/\pm15_3]_s$ SPECIMEN WITH AN IMPLANTED DELAMINATION SHOWING LIMITED EXTENSION OF THE DELAMINATION FRONT

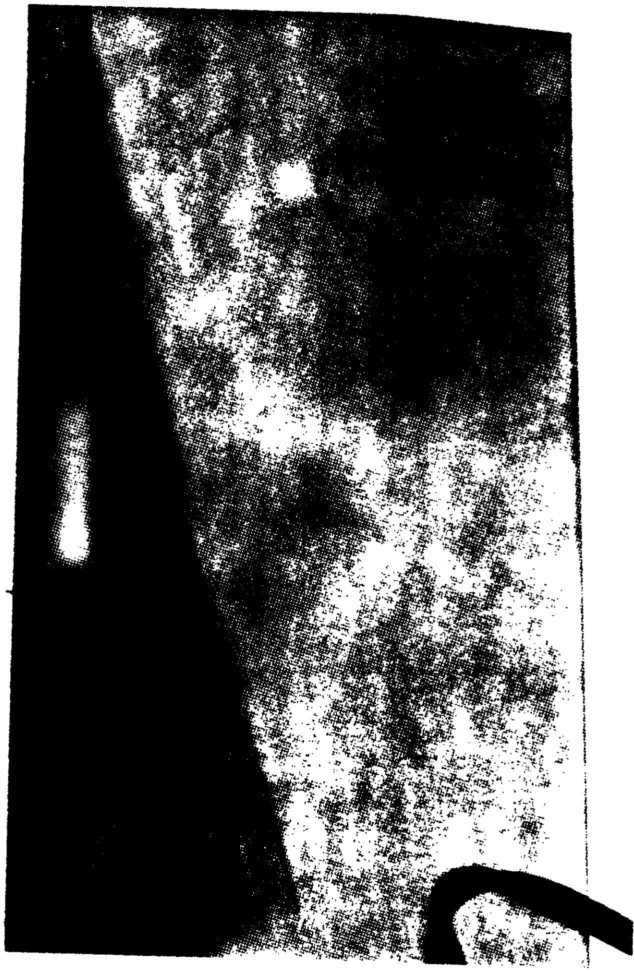

FIGURE 6.20 X-RADIOGRAPH OF A $[0_3/\pm15_3]_s$ SPECIMEN WITH AN IMPLANTED DELAMINATION AND ANGLE PLY SPLIT SHOWING DELAMINATION GROWTH TO THE END OF THE IMPLANTED ANGLE PLY SPLIT

6.5 Discussion

The experimental results are discussed in the context of the objectives of this investigation. The discussions are divided into sections by specimen type.

6.5.1 Specimens of Nonstandard Width

The average failure stress for the five sets of specimens were within experimental scatter of one another. Thus, failure stress is independent of specimen width for these specimens. This indicates that the mechanism controlling failure is also independent of specimen width.

Once a delamination starts to grow, the plies decouple and the local strength drops rapidly. The in-plane strength predicted by the criterion of Tsai and Wu [38] using the strength parameters given in Table 6.10 are 1516 MPa for the laminate and 349 MPa for the delaminated sublaminates. The predicted failure strain drops from 13057 μstrain to 5842 μstrain. The failure strain obtained from the strain gage data does not quite reach this value at failure. However, it should be noted that the reported failure strain is the far-field strain at the strain gage position and is not an accurate estimate of the local strain in the delaminated region.

Since the failure stress is approximately the same for all specimen widths, the failure of these specimens appears to

TABLE 6.10

STRENGTH PARAMETERS FOR HERCULES AS4/3501-6 UNIDIRECTIONAL GRAPHITE/EPOXY

Test Type	Strength [MPa]
Longitudinal Tension	2356
Longitudinal Compression	1466
Transverse Tension	49.4
Transverse Compression	186
Shear	105

be controlled by the strength of the sublaminates. Apparently, local in-plane failure of the delaminated sublaminate causes stress gradients which can trigger further delamination and the corresponding sublaminate failure.

The average first growth stress ranges were close together. There is a possible trend of the first delamination growth occurring slightly earlier in the wider specimens. In addition, the wider specimens have larger reported delaminations before failure. The delaminations are apparently better able to start and stop in the wider specimens. There are a number of possible explanations for this. There may be finite width effects on the strain energy release rate curves that may affect growth. There may be other mechanisms at work that are related to the probability of arresting a delamination as a function of amount of growth. Nonetheless, when the sublaminates started to fail, total delamination and final failure followed.

Nearly all the specimens exhibited delamination and failure before the experimentally determined delamination initiation stress of the one specimen which exhibited a detectable delamination initiation on an edge replication. This indicates that the specimen was a statistical anomaly. Fortunately, the stress increments for this portion of the investigation were chosen conservatively to insure that all delamination behavior was observed. Initiation is a local effect which should be unaffected by specimen width so long as the specimen is substantially wider than the interlaminar stress boundary layer.

Within the resolution of these experiments, there does not appear to be a definitive critical delamination size for unstable delamination growth or final failure. This set of experiments shows that unstable growth and final failure can coincide. However, these experiments do not prove that the two necessarily do coincide. For example, it is possible that the final failure of similar specimens would not coincide with unstable delamination growth if the in-plane strength of the delaminated sublaminates were higher.

There were two observed positions of the delamination front for stable delaminations. In most cases, the delamination front was roughly perpendicular to the angle ply split in the angle ply sublaminate isolated by the delamination. In some cases, the delamination front coincided with an angle ply split in the angle plies in the sublaminate containing the 0° plies. The fact that there are two positions raises the question of the mechanism for arresting delamination growth in each case.

6.5.2 $[\pm 15_n/0_n]_s$ and $[0_n/\pm 15_n]_s$ Specimens

The trend in both sets of data is that average failure stress, average first growth stress range, and average growth-to-tab stress decrease with increasing effective ply thickness. The explanation for this is based on the effect of effective ply thickness on the interlaminar stress state. At any stress level, laminates with thicker plies have larger regions of high interlaminar stress (although not higher free edge magnitudes of interlaminar stress) near the free edge. This affects phenomena controlled by energy considerations as well as those controlled by average stress considerations. Since delamination initiation and growth appear to be influenced by such considerations, the thicker specimens tend to accumulate damage at lower stresses. This in turn subjects them to failure at lower stresses.

The difference between the behavior of the $[\pm 15_n/0_n]_s$ and $[0_n/\pm 15_n]_s$ specimens is most likely not related to delamination initiation considerations. The interlaminar stress state that controls initiation is similar for the two types of specimens. This was the case for the specimens constructed of AS1/3501-6 in Reference 34. Brewer and Lagace found that the difference in interlaminar normal stresses was not large enough to make the predicted delamination initiation stresses significantly different for the two specimen types. They also observed this experimentally. The same is predicted for the AS4/3501-6 specimens in this investigation. Although these specimens were not explicitly monitored for delamination initiation, it can be assumed that the initiation stresses are not substantially different for the AS4/3501-6 $[\pm 15_n/0_n]_s$ and $[0_n/\pm 15_n]_s$ specimens.

The difference in behavior after initiation can be attributed to the physical characteristics of the lamination sequence. The angle plies in the $[0_n/\pm 15_n]_s$ specimens are constrained from out-of-plane deformation after damage by the 0° plies. The difference in energy directly attributable to bending was evaluated in a simple experiment. Several small masses were placed on a peeled sublaminate. The deflection of the ply gave an indication of the energy needed to restore it to its original position. This was found to be negligible when compared to other quantities of energy, such as the strain energy calculated by the O'Brien method.

Even if a region of a ply is completely debonded from the neighboring plies, frictional loads can still be applied. In contrast, the surface plies of the $[\pm 15_n/0_n]_s$ specimens are free to peel away and unload. The net effect is that more strain energy is available for delamination growth in the $[\pm 15_n/0_n]_s$ specimens at any stress level. Hence, the $[\pm 15_n/0_n]_s$ specimens experience delamination growth earlier which in turn subjects them to redistribution of in-plane stresses and the associated in-plane failure at lower stresses.

The thinnest specimens (n = 1) exhibited failure modes which could be associated with in-plane failure. The delamination initiation stress for these specimens is quite high. When a significant area of the specimen delaminated, there was a sudden increase in local compliance. The local stresses and strains apparently exceeded the level necessary for local in-plane failure of the remaining sublaminates. When this occurred, the compliance in the local region increased. The local stresses and strains at the edge of the failing region apparently exceeded the level necessary for in-plane failure of the laminate and failure propagated across the specimen width.

Failure of a laminate appears to be governed by in-plane strength. When delamination is involved, the relevant in-plane strength is the local in-plane strength of the delaminated sublaminates.

If growth is governed by an energy consideration, then there should be a general trend toward earlier growth for thicker specimens. This is because the available energy is directly proportional to laminate thickness. Details may vary as a result of effects of the interlaminar stress boundary region and finite dimensions. Since strain energy is proportional to the square of the strain (or stress) level, milestones of delamination growth (e.g. delamination growth to the loading tab) should occur at stresses that are roughly inversely proportional to effective ply thickness.

The fact that delamination growth is energetically feasible is not a sufficient condition for growth to occur. Delamination initiation appears to be a necessary prerequisite. Hence, no growth should occur before delamination initiation.

The data from this portion of the investigation can be used to verify some of these premises. The average first growth stress range, growth-to-tab stress, and final failure stress are plotted as a function of effective ply thickness for the $[\pm 15_n/0_n]_s$ specimens in Figure 6.21 and for the

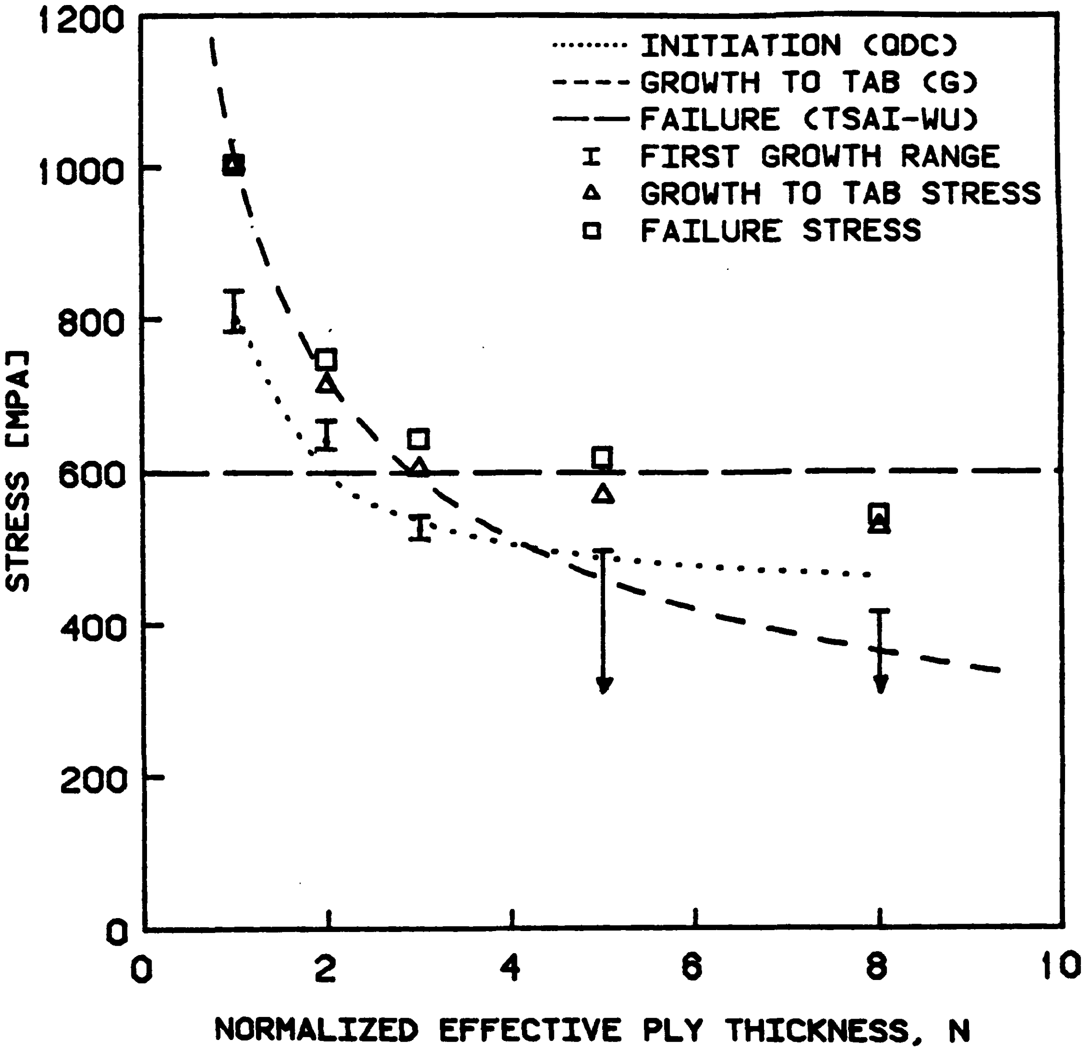

FIGURE 6.21 EXPERIMENTAL VALUES AND ANALYTICAL CURVES FOR DELAMINATION INITIATION, GROWTH, AND FINAL FAILURE OF $[\pm 15_n/0_n]_s$ SPECIMENS

$[0_n/\pm 15_n]_s$ specimens in Figure 6.22.

Also plotted are three theoretical curves. The first is the delamination initiation stress predicted by the Quadratic Delamination Criterion. The value of the interlaminar shear strength Z^{s1} used in the Quadratic Delamination Criterion was 105 MPa. This was the value determined for AS1/3501-6 graphite/epoxy specimens in Reference 34. Since this quantity should not be a strong function of fiber strength, the value obtained for AS1/3501-6 should be a good estimate of the value for AS4/3501-6.

The second curve is the failure stress predicted for damaged $[0_n/\pm 15_n]_s$ or $[\pm 15_n/0_n]_s$ specimens using the Tsai-Wu in-plane failure criterion [38]. The damage to the specimens was assumed to be complete delamination at the +15°/-15° interface and in-plane failure (in the form of splitting) of the isolated angle ply sublaminate. This is a reasonable characterization of the damage state of the specimens after delamination growth to the tab. The failed sublaminate was assumed to carry no load and therefore contribute no strength or stiffness to the specimen.

The third curve is generated by a constant strain energy release rate as predicted by the O'Brien method. The value of strain energy release rate available at the time of the delamination growth to the loading tab (or final failure, for the specimens with n equal to one) was computed using O'Brien's equation. These values are given in Table 6.11. In both the $[\pm 15_n/0_n]_s$ and $[0_n/\pm 15_n]_s$ cases, the values for the

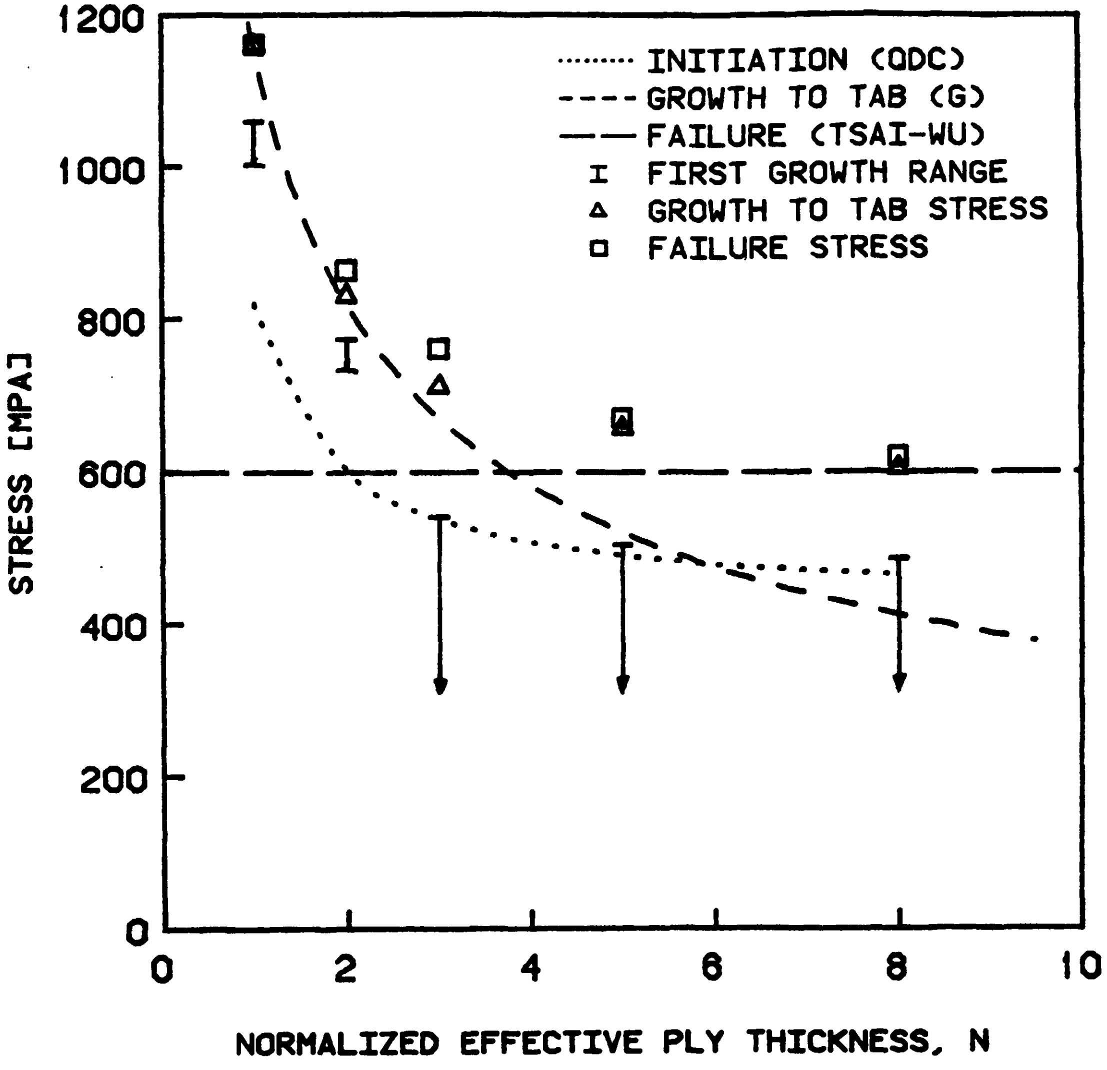

FIGURE 6.22 EXPERIMENTAL VALUES AND ANALYTICAL CURVES FOR DELAMINATION INITIATION, GROWTH, AND FINAL FAILURE OF $[0_n/\pm 15_n]_s$ SPECIMENS

TABLE 6.11

STRAIN ENERGY RELEASE RATE AT AVERAGE GROWTH-TO-TAB STRESSES FOR $[\pm15_n/0_n]_s$ AND $[0_n/\pm15_n]_s$ SPECIMENS

Laminate Type	Average Growth-to-Tab Stress [MPa]	Strain Energy Release Rate[a] [J/m²]	Laminate Type	Average Growth-to-Tab Stress [MPa]	Strain Energy Release Rate[a] [J/m²]
$[\pm15/0]_s$	1003	830	$[0/\pm15]_s$	1160	1110
$[\pm15_2/0_2]_s$	713	839	$[0_2/\pm15_2]_s$	830	1137
$[\pm15_3/0_3]_s$	603	900	$[0_3/\pm15_3]_s$	710	1248
$[\pm15_5/0_5]_s$	567	1326	$[0_5/\pm15_5]_s$	656	1775
$[\pm15_8/0_8]_s$	525	1819	$[0_8/\pm15_8]_s$	602	2392

[a] Calculated using O'Brien's method.

three thinnest specimen types were within experimental scatter while the values for the thicker specimen types were substantially higher. This is what would be expected if the growth of delamination to the loading tab were delayed until delamination initiation occurred. Thus, the average values of strain energy release rate for the three thinnest specimen types were used to generate theoretical curves which can be used to estimate the stress at which similar damage becomes energetically feasible. The average values of strain energy release rate were 856 J/m² with a coefficient of variation of 4.5% for the $[\pm15_n/0_n]_s$ specimens and 1165 J/m² with a coefficient of variation of 6.3% for the $[0_n/\pm15_n]_s$ specimens.

There are several possible sources for the discrepancy in these values of strain energy release rate. In both the $[\pm15_n/0_n]_s$ and $[0_n/\pm15_n]_s$ specimens, the isolated angle ply sublaminate is assumed to carry load. In the $[\pm15_n/0_n]_s$ specimens, however, the peeled portion of the sublaminate carries no load and therefore has no internal strain energy. If the modulus of this region of the sublaminate were set to zero for the purpose of calculating strain energy release rate with O'Brien's method, the value of strain energy release rate would rise from 856 J/m² to 1381 J/m². In the $[0_n/\pm15_n]_s$ specimens, the delaminated and split portion of the isolated angle ply sublaminate may carry some load applied via friction, but it has most likely yielded more internal strain energy than has been accounted for by O'Brien's method. It is therefore conceivable that the values for the two types of specimens are actually quite close. An alternative explanation may involve the details of the situation at the delamination front (e.g. frictional loading versus peeling of the isolated angle ply sublaminate, tensile versus compressive values of the local interlaminar normal stress). The differences between the two lamination sequences may mean different conditions of applied stress may need to be met in order to initiate dynamic unstable delamination growth.

The plots have several important features. First, there was no delamination growth until approximately the predicted delamination initiation stress, even when significant delamination growth was theoretically possible as determined by the strain energy release rate curve. This shows conclusively that initiation must occur before any growth can occur and that the strain energy release rate criterion is a necessary but not a sufficient condition for delamination growth. It can also be surmised that the strain energy release rate criterion is a necessary but not a sufficient condition for delamination initiation. If the criterion were necessary and sufficient in both cases and each event were governed by its own critical value of strain energy release rate, delamination growth could never be delayed by the lack of delamination initiation.

Once delamination had initiated, it did not grow to the loading tab until it was energetically feasible as determined by the curve. This emphasizes that strain energy release rate criterion is a necessary condition for certain types of damage. Failure occurred soon thereafter as long as the stress was near or above the post first ply failure stress predicted by the Tsai-Wu criterion [38].

The average maximum intrusion and delaminated area before failure were based on only two specimens per data point. Nonetheless, there was no trend suggesting that a critical value of delamination size for unstable growth or final failure can be determined for these specimens using this type of experiment.

6.5.3 Fabric Specimens

The $[\pm 20_F]_S$ fabric specimens all broke into two separate pieces at stress levels well below their predicted in-plane failure stress. Delaminations were observed to occur in all of these specimens before final failure. It is clear that the delaminations contributed to the final failure and that there is a significant effect of the character of the ply interface on the failure stress.

The differences in character of the interface were manifested in the character of the delaminations. In the specimens with warp faces at the +20°/-20° interfaces, the boundaries of the delamination were delineated by splits in the warp fiber tows on one side and the fill fiber tows on the other side. The splits had the effect of "blunting" the delamination front. This affects the energy required for extension of the delamination front. It appears that when growth beyond the splits becomes energetically feasible, the delaminated region grows across the specimen width. Once this occurs, the in-plane strength of the specimen decreases and the specimen fails.

In specimens with fill faces at the +20°/-20° interfaces, the delamination growth seems to have been unrestricted by any splits in the fill fiber tows. Only when splits in the warp fibers caused a disturbance in the stress field did these delaminations appear to be arrested. This apparently either increased the energy needed to extend the delaminated region (perhaps by inducing small cracks at the +20°/-20° interface which blunted the delamination front) or decreased the energy available on a local level. The difference between the two specimen types seems to have affected the stress at which delamination grows across the width and therefore the final failure stress.

6.5.4 Specimens with Implanted Delaminations and Angle Ply Splits

The results of the experiments with implanted delaminations and angle ply splits underscore the interaction of angle ply splits and delaminations. The initiation or growth of either apparently induce conditions favorable for the initiation or growth of the other in these specimens.

Neither specimen type experienced substantial growth of the delamination beyond its implanted boundaries before failure with the exception of the three specimens which experienced growth to the end of the implanted angle ply splits. The growth to the end of the implanted angle ply splits, coupled with the fact that the specimens with implanted angle ply splits failed at a lower average stress, indicates that a preexisting angle ply split can aid in the extension of the delamination front.

Since angle ply splits formed spontaneously at the edge of the delaminated region in specimens with implanted delaminations alone, the state of stress in the vicinity of that edge of the delamination must be conducive to their formation. The fact that they did not extend beyond the edge of the implanted delamination indicates that they cannot extend arbitrarily beyond the delamination and that their growth is not independent of the growth of the delamination.

The implanted delaminations and angle ply splits seldom grew beyond their boundaries until final failure. This may be the result of a small pocket of resin at the edge of the teflon film. Although the global stress state is appropriate, the local crack tip stress field may be affected. Russell and Street [41] verified the existence of these resin rich regions and determined that they can increase at least the mode II component of delamination resistance.

The interaction of the delaminations and the angle ply splits appears quite strong in these specimens. Understanding the details of what occurs at their intersection may be instrumental to understanding how growing delaminations can be arrested and how arrested delaminations can reinitiate. A study of this interaction is warranted.

CHAPTER 7

ANALYSIS OF GROWTH PHENOMENON

Modifications made to strain energy release rate models of delamination growth are described in this chapter. These modifications are compared to existing models and their ability to accurately correlate data is evaluated.

7.1 Existing Models of Growth Phenomenon

There are two popular models of delamination growth based on strain energy releases rate methodologies. They are the simple model by O'Brien and the virtual crack closure method which is based on finite element calculations.

7.1.1 O'Brien's Method

As noted in Chapter 2, O'Brien [26] developed a simple method for the calculation of strain energy release rate. His model was based on the calculated internal energy of laminated and delaminated regions of a composite specimen. The model assumes that there is no variation with longitudinal position. The calculation is independent of delamination size. O'Brien proposed that this model could be used to predict initiation by using a critical value of strain energy release rate and that growth can be described in terms of an experimentally determined resistance curve. Experimental evidence showed that the critical value of strain energy release rate [28] was not a material parameter. It therefore cannot be assumed that the delamination resistance curve is a material parameter either. O'Brien proposed that the critical value of strain energy release rate might be a function of the relative contribution of mode I. This contribution would have to be determined by an alternative method such as the finite element method. Brewer and Lagace [34] found that the critical value of strain energy release rate for delamination initiation was a function of effective ply thickness for AS1/3501-6 specimens. Since the modal contribution is independent of ply thickness, this indicates that the critical value of strain energy release rate must also be affected by this factor.

The derivation of O'Brien's method does not account for any out-of-plane effects such as interlaminar stress or energy involved in out-of-plane deformation (bending) of sublaminates. Increased accuracy in the evaluation of the strain energy release rate can be achieved with a more general approach.

7.1.2 Virtual Crack Closure

The virtual crack closure method has been shown to give good correlation in some instances [e.g. 6] for delamination growth data. As presently applied in the literature, the three-dimensional problem has been modeled by assuming that there is no variation with respect to the longitudinal position. The problem is thus reduced from a three-dimensional analysis to a two-dimensional analysis.

The virtual crack closure method requires that the nodal forces and displacements be accurately determined at the crack tip. They can be used to determine the change in energy and the relative modal contributions. The software available during this investigation offered a nearly equivalent and less computationally intensive finite element method. Since it does not specifically use the product of nodal forces and nodal displacements, it cannot technically be considered the virtual crack closure method. This alternative finite element method is described in the next section.

7.2 Finite Element Method

The alternative finite element method used as a basis for the present analysis was also a two-dimensional model. The internal energy per unit length of the specimen was computed directly from nodal displacements and the stiffness matrix. Normally, this would require a great deal of computational effort. In the model used, however, there were few enough elements that this calculation was convenient. The difference in internal energy for an incremental unit of delamination growth could be found by comparing two cases in which the crack was slightly extended. This is equivalent to releasing a crack tip node in the virtual crack closure method.

The finite element code used was the Finite Element Analysis Basic Library (FEABL) which was developed in the Department of Aeronautics and Astronautics at the Massachusetts Institute of Technology [42]. The two-dimensional rectangular element used had eight nodes (one at each corner and one at the midpoint of each side). Each node had three displacement degrees of freedom (linear displacement in each direction).

As a result of symmetry considerations, only one quarter of the specimen needed to be modeled as long as the specimen width was substantially wider than the interlaminar stress boundary layer and the delamination itself. Each ply contained four layers of elements of equal thickness. Each layer was modeled along its length by twelve elements. Each layer was divided into three regions. Four elements were used to represent the layer from the free edge to the tip of the delamination. Three elements were used to represent a 0.1 mm long region in front of the delamination tip. The remainder of the layer between the crack tip region and the centerline of the specimen was represented by five elements. The elements in each region were skewed toward the crack tip. The sizing of elements and the size of the mesh used for various ranges of delamination size are discussed in Appendix H.

Each ply was represented by a mesh of four by twelve elements. Since only one quarter of a specimen was modeled, a six ply specimen could be modeled by a twelve by twelve element mesh with 144 elements and 489 nodes. This mesh is shown in Figure 7.1.

The elastic parameters used for AS4/3501-6 were the same ones use in the interlaminar stress software analysis and listed in Table 3.1. The only exception was that the software calculated the value of an out-of-plane shear modulus, G_{2Z}, to be 3.62 GPa from elasticity considerations. The value listed in Table 3.1 is 4.8 GPa. This difference is not believed to have a significant effect on the results.

The strain energy release rate in this context is defined as the negative of the derivative of internal energy of a partially delaminated specimen with respect to the area of the delamination:

$$G \equiv -\frac{\partial U_{del}}{\partial A_{del}} \tag{7.1}$$

If the two-dimensional finite element model is used, a quantity $\bar{U}_{del}$ can be defined as the internal energy per unit length of the specimen. $\bar{U}_{del}$ is a function of delamination length, a. Since $\bar{U}_{del}$ is internal energy per unit length, the strain energy release rate can be written as:

$$G \equiv -\frac{\partial \bar{U}_{del}}{\partial a} \tag{7.2}$$

Strain energy release rate curves were calculated for the $[\pm 15_3]_s$, $[\pm 15/0]_s$, and $[0/\pm 15]_s$ specimens. The derivative was

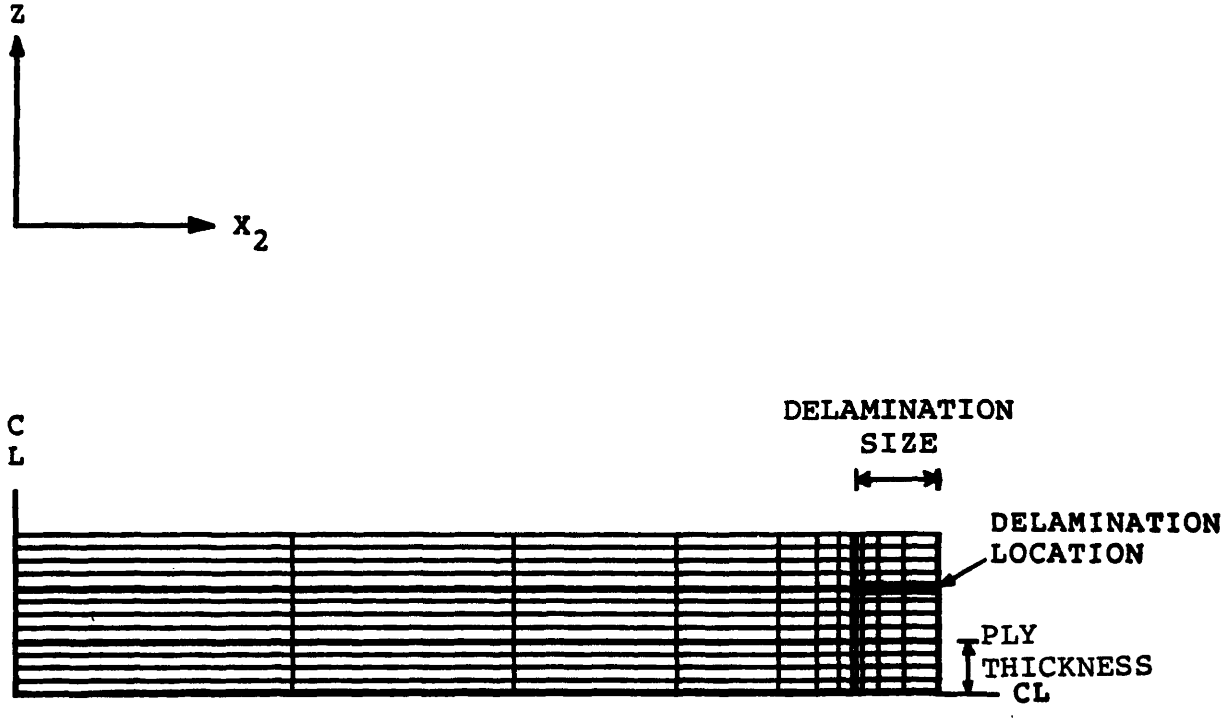

FIGURE 7.1 FINITE ELEMENT MESH USED FOR A SIX PLY LAMINATE

approximated as the change in the internal energy per unit length divided by the change in delamination width. The curves are shown in Figures 7.2 through 7.4, respectively. The applied strain level in these and all subsequent plots of strain energy release rate as a function of delamination size is 10000 μstrain (1.0%). The value of strain energy release rate can be calculated for other strain levels by considering that it is proportional to the square of the strain level. The strain energy release rate curves can be computed for $[\pm 15_n/0_n]_s$ and $[0_n/\pm 15_n]_s$ specimens by scaling the values of strain energy release rate and the delamination size by the factor n as discussed in Chapter 3.

The strain energy release rate curves calculated for the $[\pm 15_3]_s$ specimens seem to monotonically approach an asymptote. In fact, there is a slight hump before the asymptote. The hump is much more visible for the $[\pm 15/0]_s$ and $[0/\pm 15]_s$ specimens. This hump was observed for other laminate types by Wang and Crossman [6] in their virtual crack closure analyses.

The analysis of the $[0_n/\pm 15_n]_s$ specimens contained a complication which could not be rectified with the available software. The computed displacements of the upper and lower surfaces of the delamination were in opposite directions longitudinally and toward each other in the through-the-thickness direction as shown in Figure 7.5. Although this is possible for an infinitely thin element, it would require portions of two different sublaminates to occupy

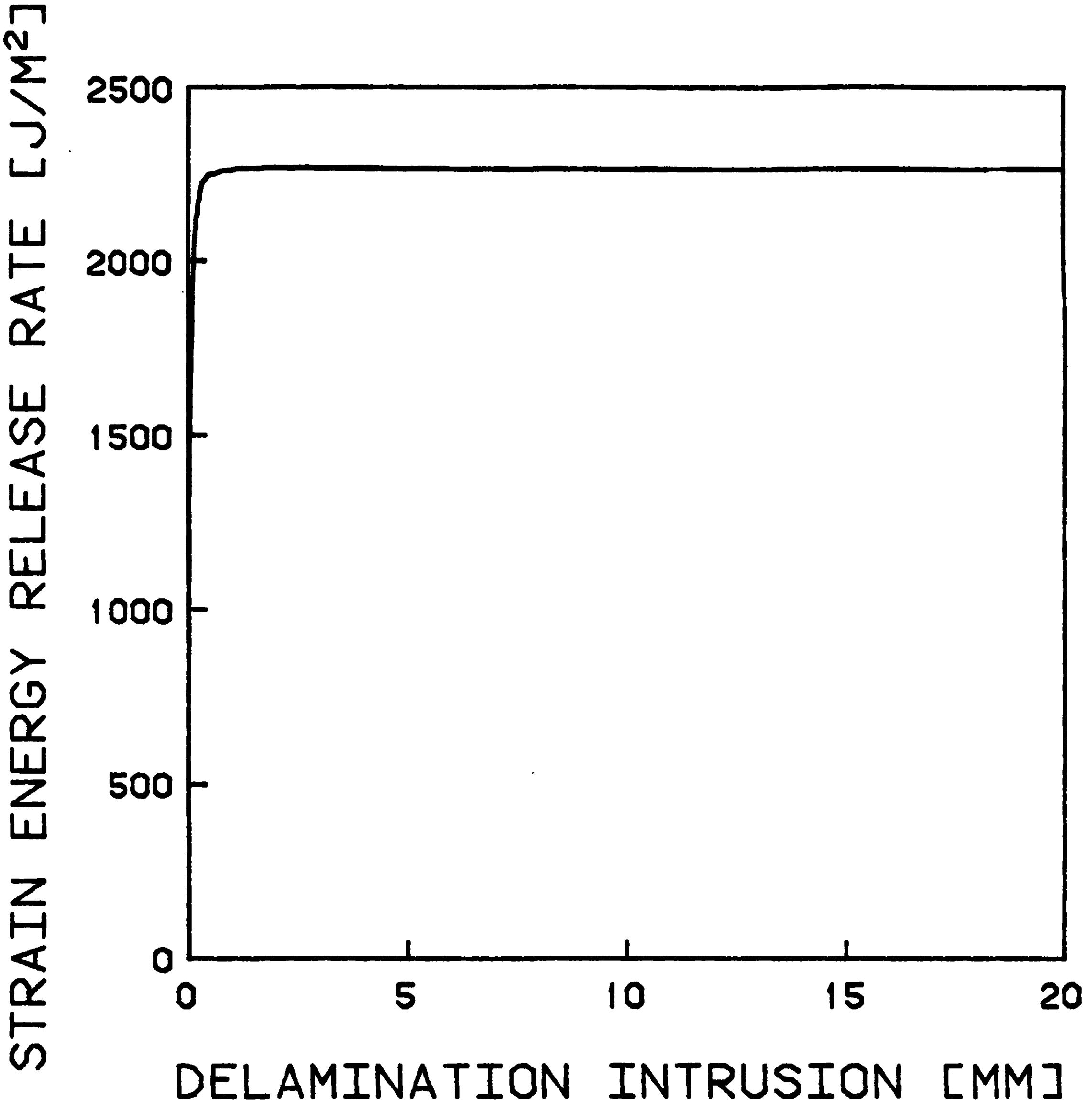

FIGURE 7.2 STRAIN ENERGY RELEASE RATE AS A FUNCTION OF DELAMINATION INTRUSION FOR A $[\pm 15_3]_s$ SPECIMEN USING A TWO-DIMENSIONAL FINITE ELEMENT MODEL

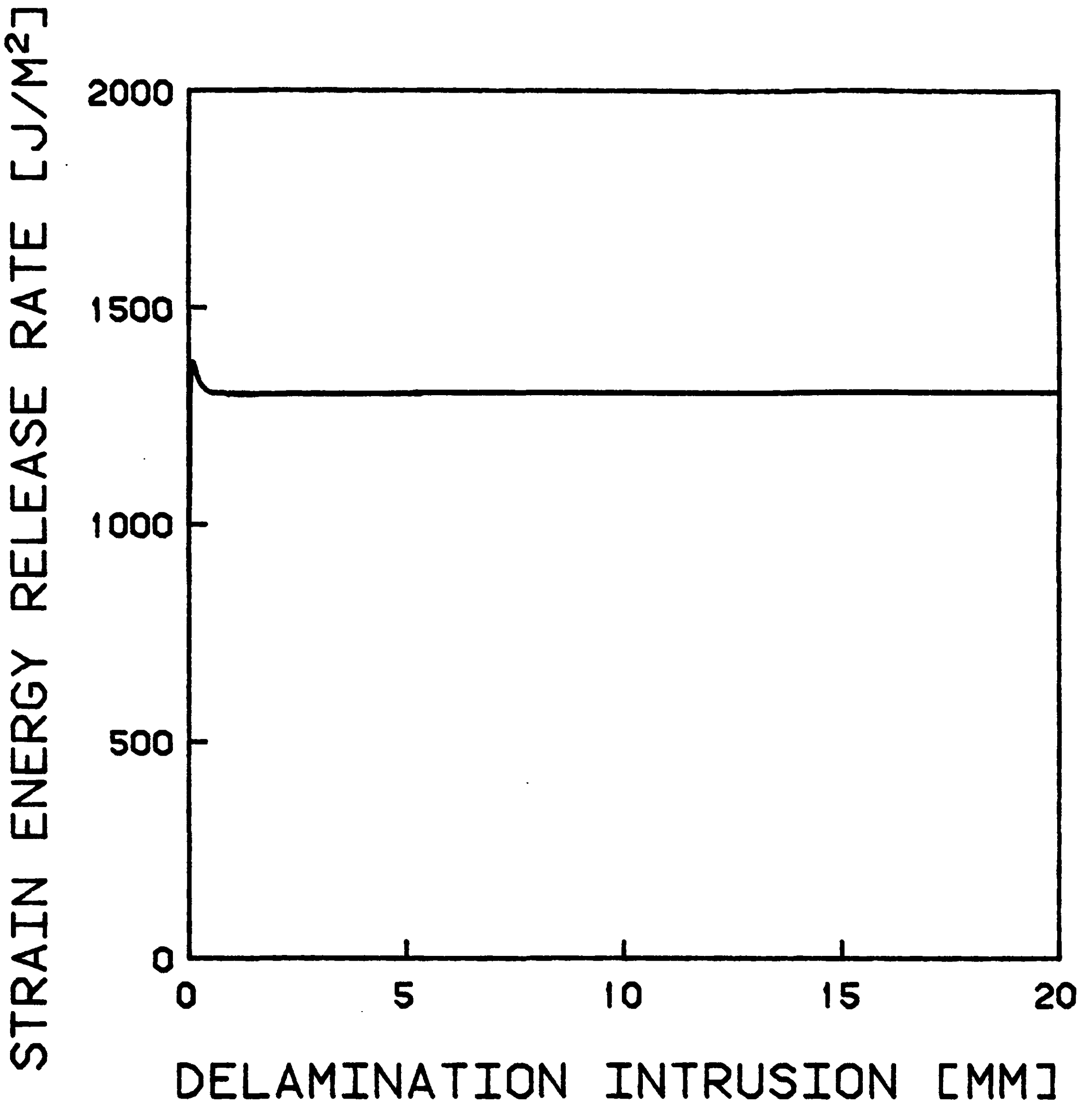

FIGURE 7.3 STRAIN ENERGY RELEASE RATE AS A FUNCTION OF DELAMINATION INTRUSION FOR A $[\pm15/0]_s$ SPECIMEN USING A TWO-DIMENSIONAL FINITE ELEMENT MODEL

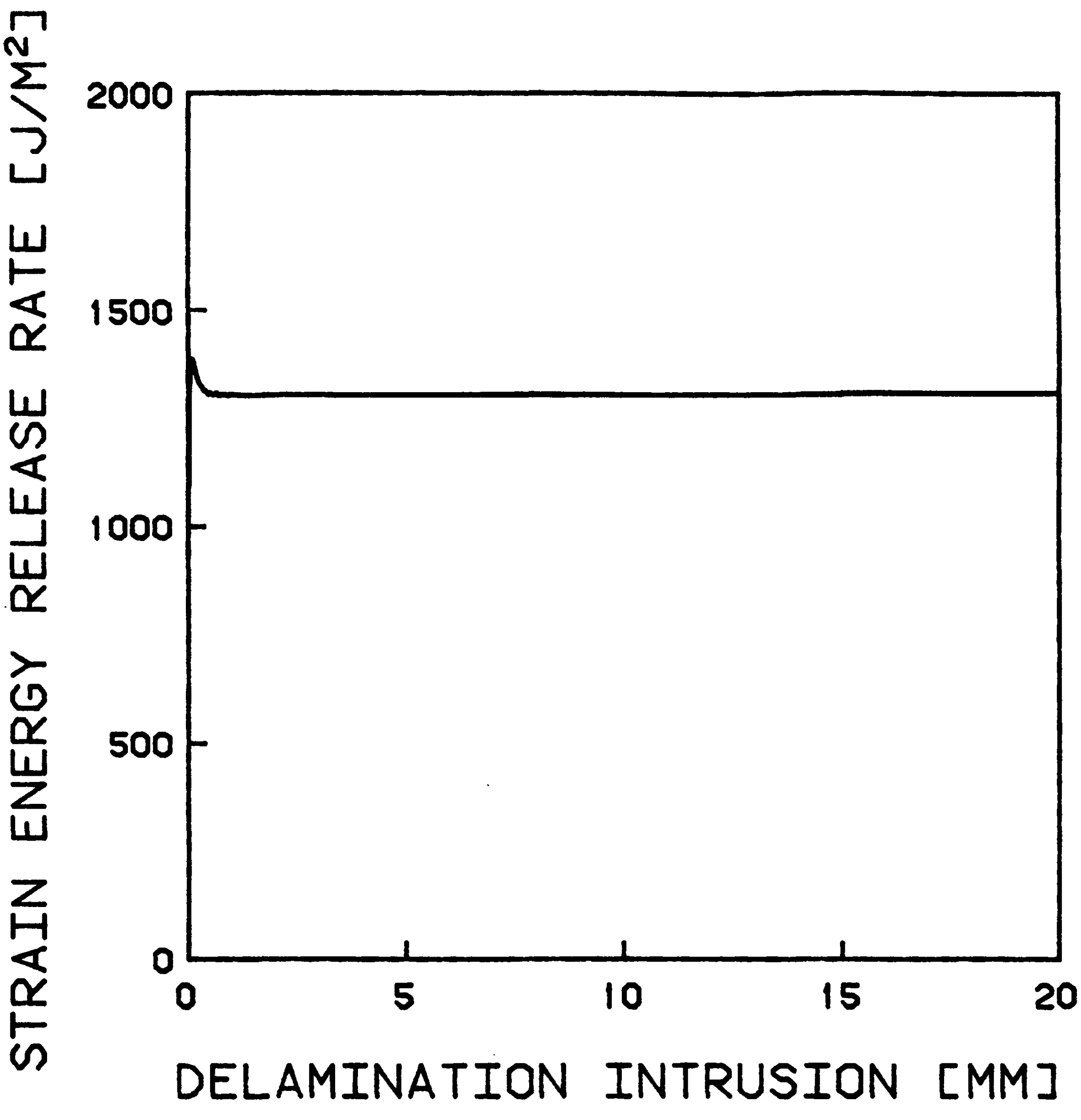

FIGURE 7.4 STRAIN ENERGY RELEASE RATE AS A FUNCTION OF DELAMINATION INTRUSION FOR A $[0/\pm15]_s$ SPECIMEN USING A TWO-DIMENSIONAL FINITE ELEMENT MODEL

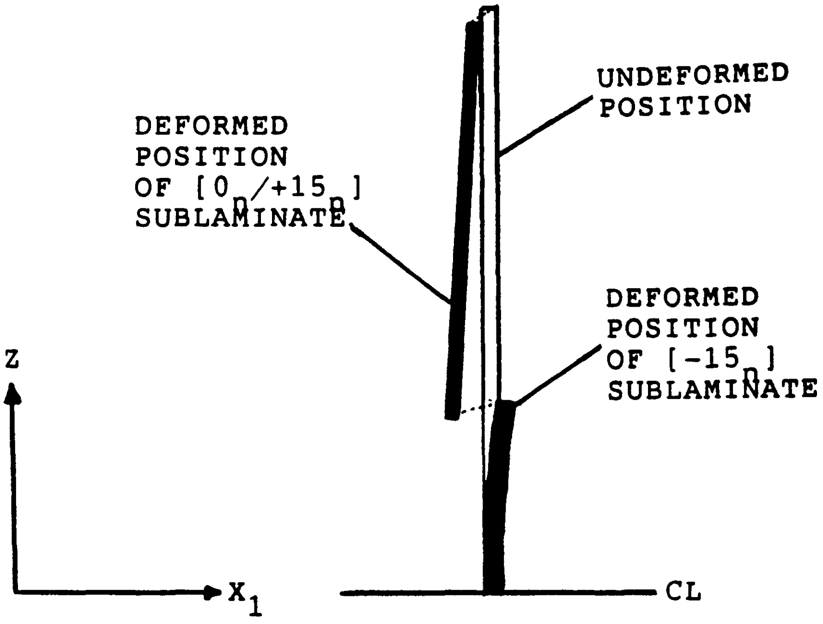

FIGURE 7.5 DISPLACEMENTS OF THE DELAMINATION SURFACE FOR $[0_n/\pm15_n]_s$ SPECIMENS AS DETERMINED BY THE FINITE ELEMENT METHOD

the same space at the same time, which is, of course, physically impossible. Thus, the actual energy state is higher than that calculated by the finite element method. That is, not as much energy has been released as was computed to have been. The frictional forces that would result cannot be easily determined. In the limit, they could approach those which occur during perfect bonding. If this were the case, there would be in effect no delamination and no energy released. Therefore, the analysis can only provide an upper bound for strain energy release rate values for the $[0_n/\pm15_n]_s$ specimens.

7.3 Geometrically Integrated Finite Element Method

A problem with the O'Brien method and the various finite element models is that they are based on two-dimensional analyses which ignore variations in width in actual delaminations. In many specimen types, the effects of such variations could be significant.

In the specimens in this investigation, the majority of the observed delaminations were roughly triangular. The stress fields associated with these specimens are thus not constant with respect to longitudinal position. The existing models must be modified to include details of varying delamination width.

The finite element model can serve as a good point from which to start. It contains the basic elements of strain energy release rate analyses, including the effect of the interlaminar stress boundary region. The finite element method can be modified to a more general delamination shape if the delamination width, a, is allowed to be a function of longitudinal position.

The premise of the proposed analysis is that the delaminated specimen can be broken down conceptually into differentially thin dx_1 strips. The contribution of each strip can be calculated in terms of a two-dimensional finite element model. The strips are then assembled into a three-dimensional model. The differential change in energy with respect to a differential change in delamination area can then be determined.

Since the contribution of each strip is calculated in terms of a model of constant width delaminations, the accuracy of the analysis should be satisfactory if the delamination width does not change rapidly with respect to longitudinal position. This is the case in the portion of the delamination between the free edge and the angle ply split. The accuracy should also be acceptable along the delamination front because any effects of the different delamination widths on one side of any dx_1 slice in question should be approximately counteracted by the effects of the delamination widths on the other side. The most likely source of inaccuracy should be the contribution of the region near the intersection of the delamination front and the angle ply split. At this point, the stress fields surrounding the delamination front and angle ply split interact. In addition, there are stress perturbations associated with the tip of the angle ply split. Fortunately, this area is relatively small, so any error introduced should also be small.

This method does not explicitly account for the stress fields at the delamination front. Since this is the actual location of growth, no claim can be made as to any knowledge of the conditions at the crack tip (e.g. the relative modal contributions of strain energy release rate). This method should, however, give a good estimate of the total strain energy release rate.

The proposed analysis thus evaluates the change in energy in each differential dx_1 strip of the specimen for differential changes in the delaminated area. This is integrated over the entire specimen and divided by the differential change in area to obtain a global value for the strain energy release rate. By integrating the definition of strain energy release rate as applied to the two-dimensional model (equation 7.2), the change in energy per unit specimen length can then be found for any change in delamination size by integrating the strain energy release rate with respect to delamination width. A reference energy can be defined. A convenient choice is the energy in a laminated specimen. The delamination size of zero can be chosen as a limit of integration. The value of $\overline{U}_{del}$ for a delamination size of zero is the energy per unit length of a laminated specimen:

$$\bar{U}_{lam} - \bar{U}_{del} = \int_0^a \hat{G}(x)dx \tag{7.3}$$

where: $\bar{U}_{lam}$ = internal energy per unit length of a laminated specimen

$\hat{G}$ = the strain energy release rate determined from the two-dimensional finite element model (as opposed to the overall value for the specimen)

x = distance from the free edge.

If equation 7.3 is integrated along the entire length of the specimen, it gives the change in internal energy as a function of delamination width:

$$U_{lam} - U_{del} = \int_{-l}^{l}\int_0^a \hat{G}(x)\ dx\ dx_1 \tag{7.4}$$

where: U_{lam} = internal energy of the laminated specimen

U_{del} = internal energy of the partially delaminated specimen

$2l$ = length of the specimen.

In practice, the integration of strain energy release rate with respect to distance from the free edge was not necessary for this approach. Since an output of the finite element analysis was a value for energy per unit width, this integral was equal to the difference between this quantity at the limits of integration. That quantity was easily determined for a wide range of delamination sizes.

Since the internal energy of a specimen with no delamination is a constant, the strain energy release rate can be recovered identically by differentiating the integral in equation 7.4 with respect to the delaminated area:

$$\frac{\partial\left(U_{lam} - U_{del}\right)}{\partial A_{del}} = \frac{-\partial U_{del}}{\partial A_{del}} \equiv G \qquad (7.5)$$

The integral which describes the difference in energy between the laminated and delaminated states can be written:

$$U_{lam} - U_{del} = \int_{-1}^{1}\int_{0}^{a(x_1)} \hat{G}(x)\ dx\ dx_1 \qquad (7.6)$$

An observed triangular delamination shape was used to analyze all the delaminations in this investigation. The analysis can be directly applied to triangles with other dimensions or even more general shapes. The triangle modeled was bordered on one side by the free edge, on the second side by a split in an angle ply, and on the third side by a delamination front which is modeled as perpendicular to the angle ply split. The model of the delamination is shown schematically in Figure 7.6.

In the specimens in this investigation, one sublaminate was always observed to be totally delaminated (i.e. the $[+15_n]$ sublaminates in the $[\pm15_3]_s$ and $[\pm15_n/0_n]_s$ specimens and the $[-15_{2n}]$ sublaminate in the $[0_n/\pm15_n]_s$ specimens). These sublaminates also contained an angle ply split bordering the delaminated region. No load can be transferred into this

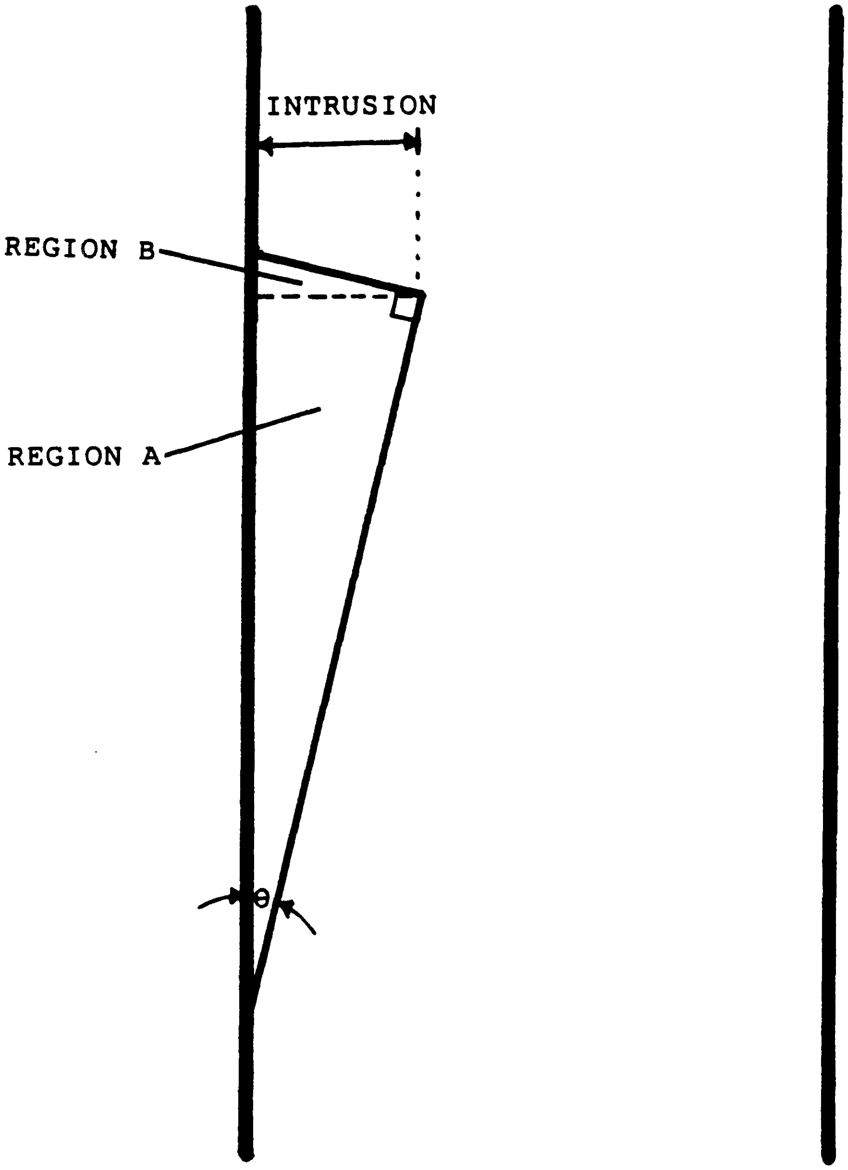

FIGURE 7.6 SCHEMATIC MODEL OF THE DELAMINATION IN THE ANALYSIS

portion of the sublaminate with the possible exception of frictional loading of the $[-15_{2n}]$ sublaminate in the $[0_n/\pm15_n]_s$ specimens. This implies that this portion of the ply is unloaded and contains no internal energy. This region is indicated as region A in Figure 7.6. The region between the free edge and the delamination front could conceivably be loaded by in-plane shear mechanisms. As a rough approximation, the strain level in region B as shown in Figure 7.6 is set equal to the strain level for the rest of the specimen at that longitudinal position. Thus, this area can be modeled with the two-dimensional finite element model.

The unloaded portion of a sublaminate was modeled in the finite element analysis by totally removing the elements in that region. This accounts for the lack of internal energy in that portion of the sublaminate. The finite element mesh changes accordingly. An example of the modified mesh for a six ply specimen is shown in Figure 7.7. The modified mesh accounts for the fact that this portion of the sublaminate carried no load and contained no internal energy. As was noted for the original finite element analysis, there is a complication with the model for the $[0_n/\pm15_n]_s$ specimens. The results show that the angle plies intrude into the space actually containing the $[-15_{2n}]$ sublaminate. Again, this shows that the change in internal energy for this condition may be overestimated and therefore that the calculated strain energy release rate is an upper bound. The strain energy release rate curves calculated for the $[\pm15_3]_s$, $[\pm15_n/0_n]_s$,

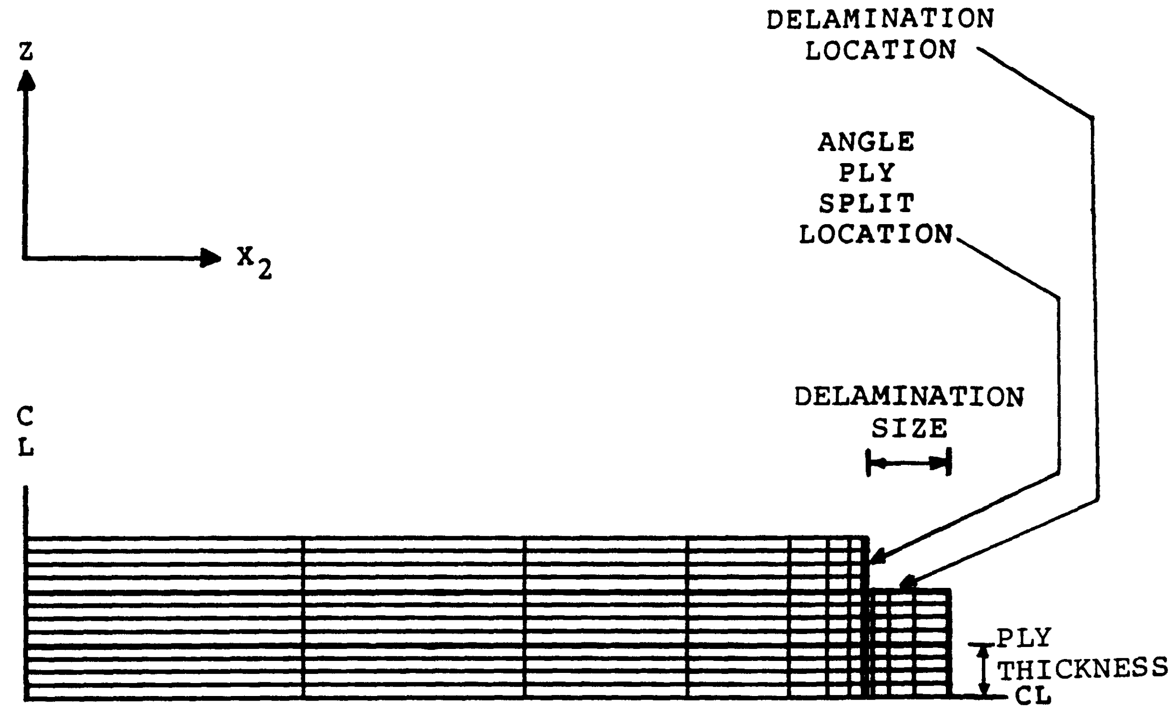

FIGURE 7.7 MODIFIED FINITE ELEMENT MESH USED FOR A SIX PLY LAMINATE WHICH ACCOUNTS FOR A PORTION OF A PLY TO BE UNLOADED

and $[0_n/\pm15_n]_s$ specimens from the two-dimensional model with an unloaded portion are shown in Figures 7.8, 7.9, and 7.10, respectively.

The strain energy release rate curves calculated for the $[\pm15_3]_s$, $[\pm15_n/0_n]_s$, and $[0_n/\pm15_n]_s$ specimens using the geometrically integrated finite element model and the assumed delamination configuration shown in Figure 7.6 are shown in Figures 7.11, 7.12, and 7.13, respectively. The asymptotes of the curves generated by the geometrically integrated finite element method are approximately equal to the weighted averages (i.e. by the areas of regions A and B in Figure 7.6) of the asymptotes of the curves generated by the two-dimensional finite element method.

7.4 Effects of Finite Specimen Size

The modifications to the analysis up to this point are accurate for an infinitely wide and infinitely long specimen. Delaminations in actual specimens, however, have dimensions which are not negligible when compared to the dimensions of the test section. The primary assumption that breaks down is that the strain level is a constant for all longitudinal positions. This is implicitly assumed in the derivation of O'Brien's equation and in the selection of a two-dimensional finite element in the virtual crack closure and finite element methods. In actuality, the local compliance in the delaminated region is substantially higher than elsewhere.

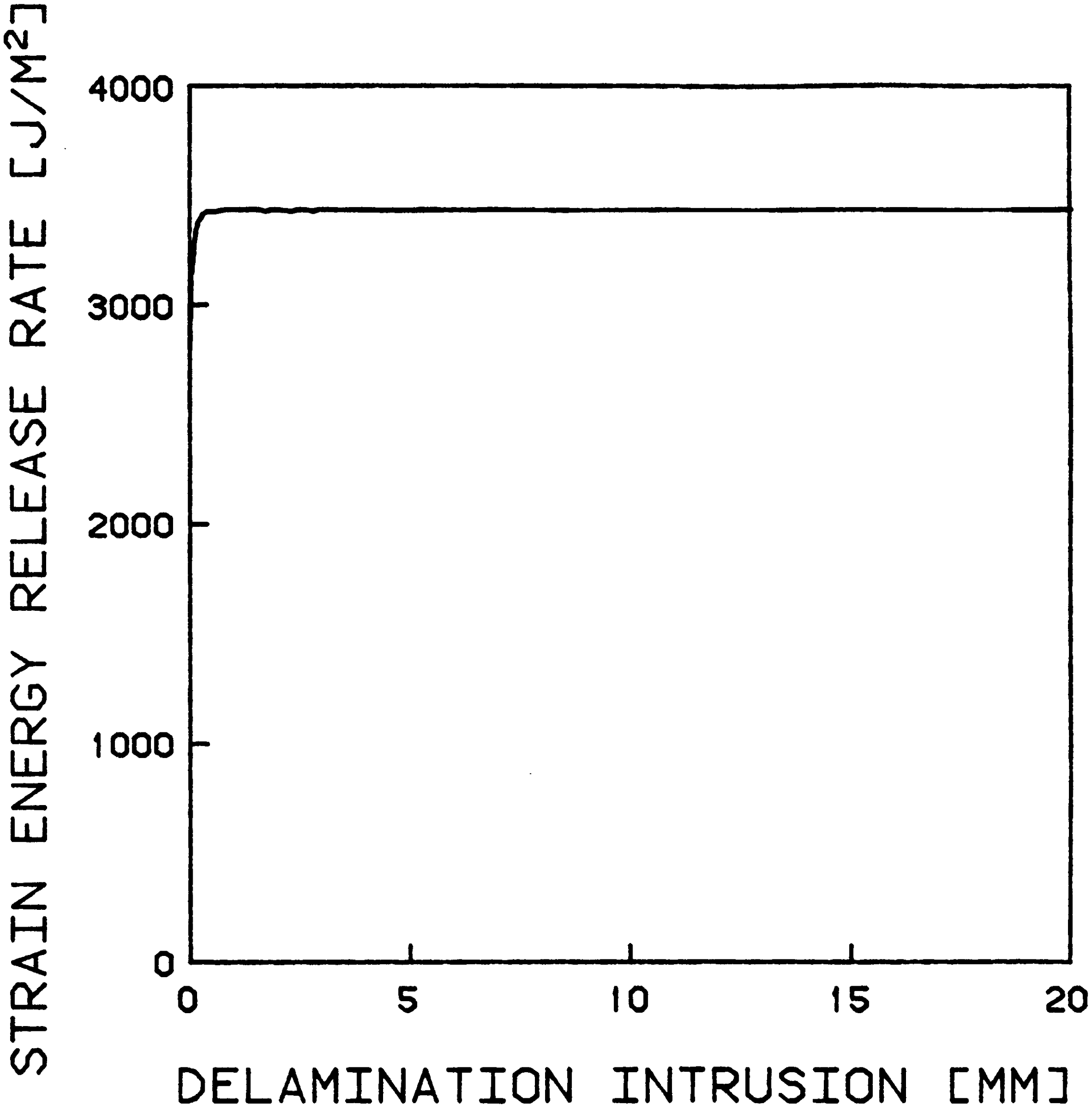

FIGURE 7.8 STRAIN ENERGY RELEASE RATE AS A FUNCTION OF DELAMINATION INTRUSION FOR A $[\pm15_3]_s$ SPECIMEN WITH A PARTIALLY UNLOADED $[+15_3]$ SUBLAMINATE USING A TWO-DIMENSIONAL FINITE ELEMENT MODEL

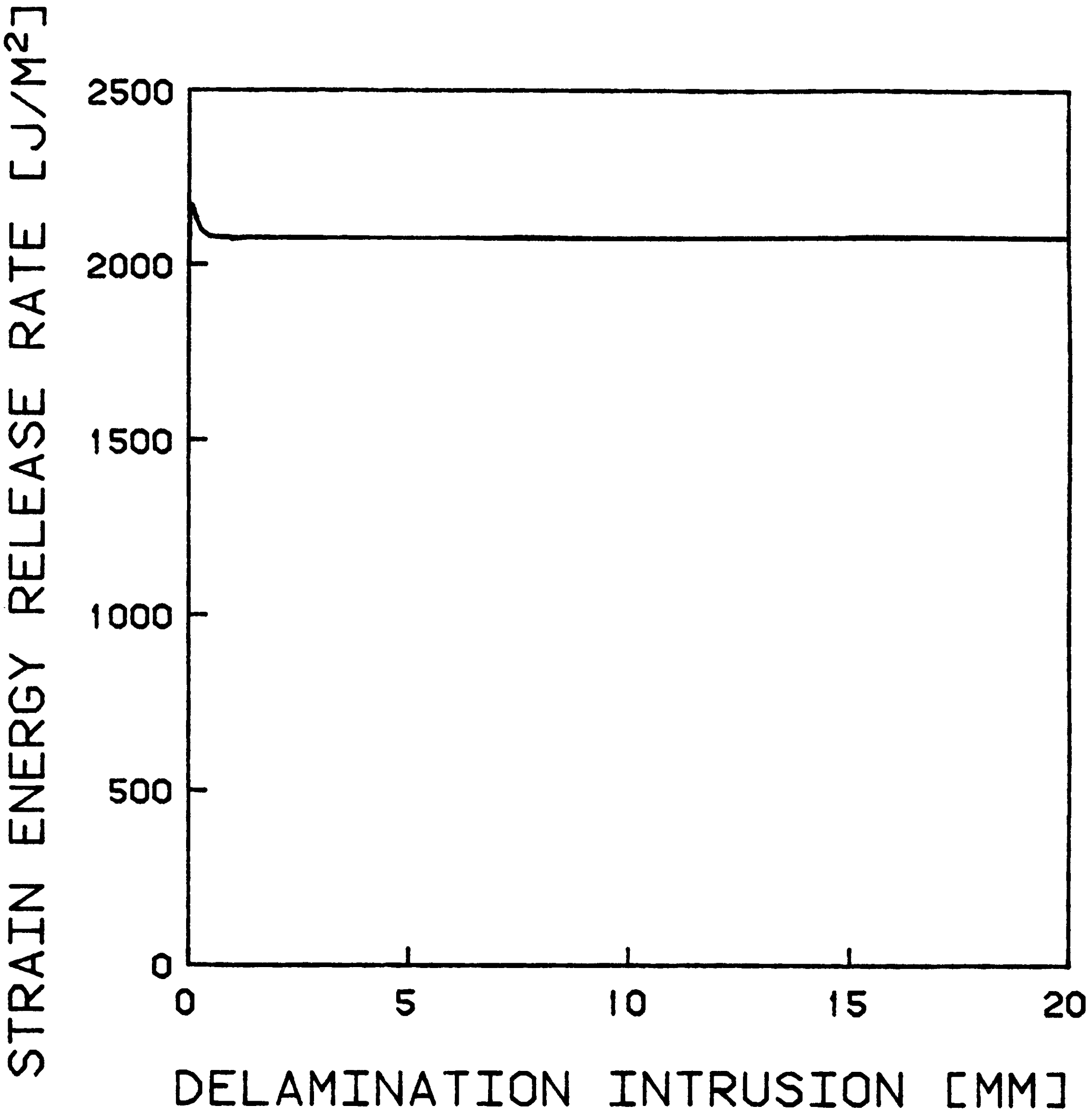

FIGURE 7.9 STRAIN ENERGY RELEASE RATE AS A FUNCTION OF DELAMINATION INTRUSION FOR A $[\pm 15/0]_s$ SPECIMEN WITH A PARTIALLY UNLOADED [+15] SUBLAMINATE USING A TWO-DIMENSIONAL FINITE ELEMENT MODEL

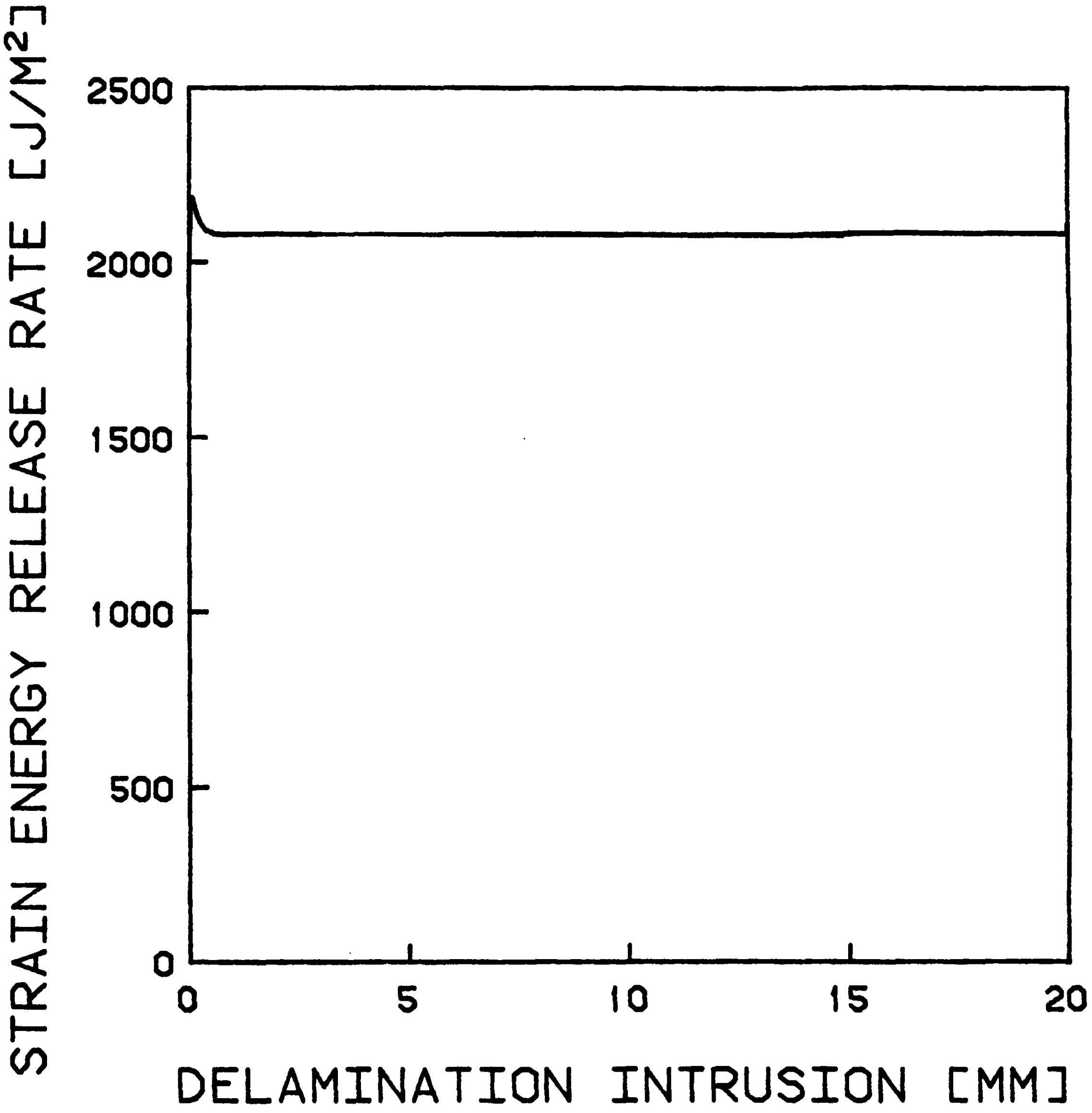

FIGURE 7.10 STRAIN ENERGY RELEASE RATE AS A FUNCTION OF DELAMINATION INTRUSION FOR A $[0/\pm15]_s$ SPECIMEN WITH A PARTIALLY UNLOADED [-15] SUBLAMINATE USING A TWO-DIMENSIONAL FINITE ELEMENT MODEL

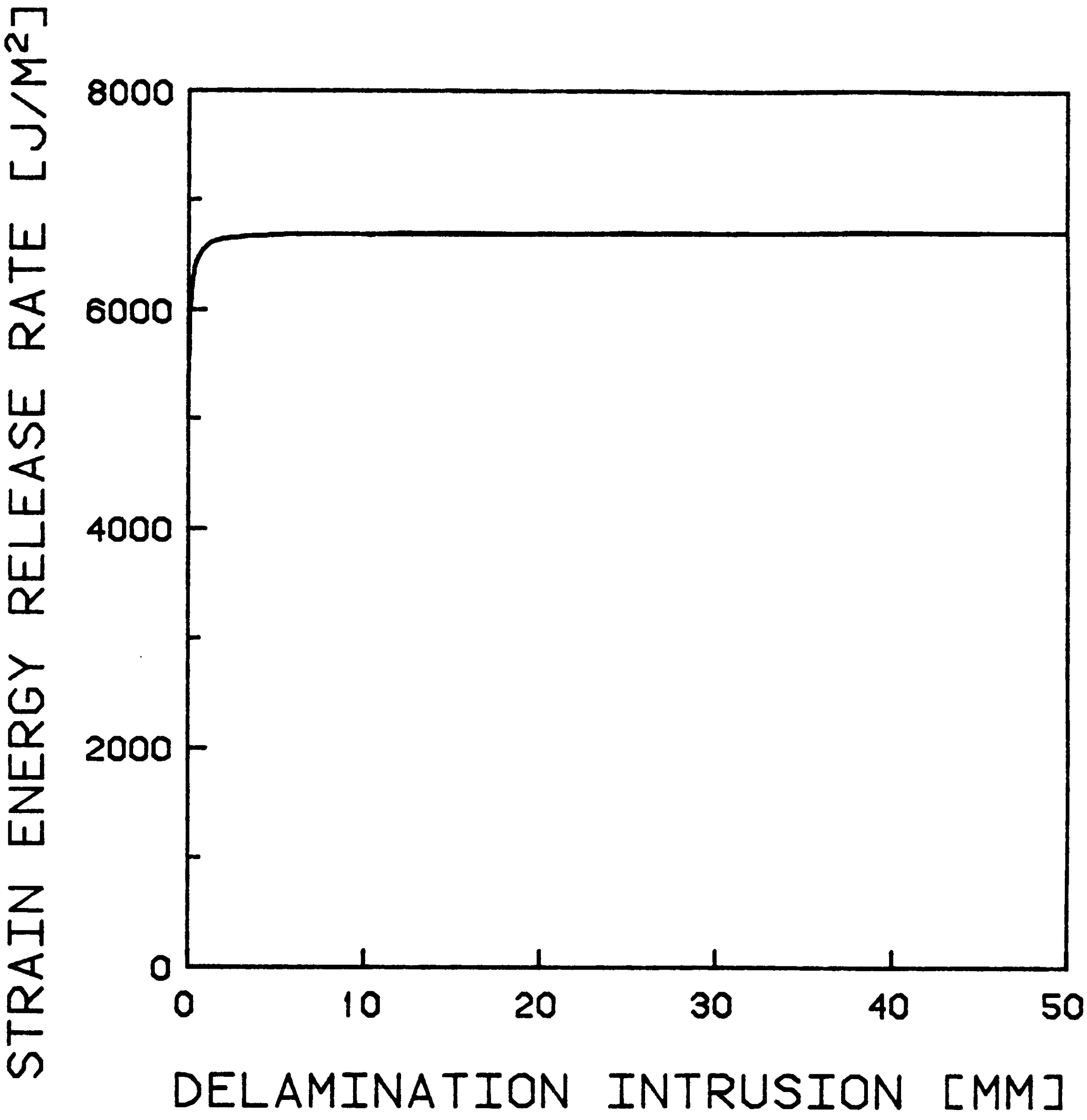

FIGURE 7.11 STRAIN ENERGY RELEASE RATE AS A FUNCTION OF DELAMINATION INTRUSION FOR A $[\pm 15_3]_s$ SPECIMEN USING A GEOMETRICALLY INTEGRATED FINITE ELEMENT MODEL

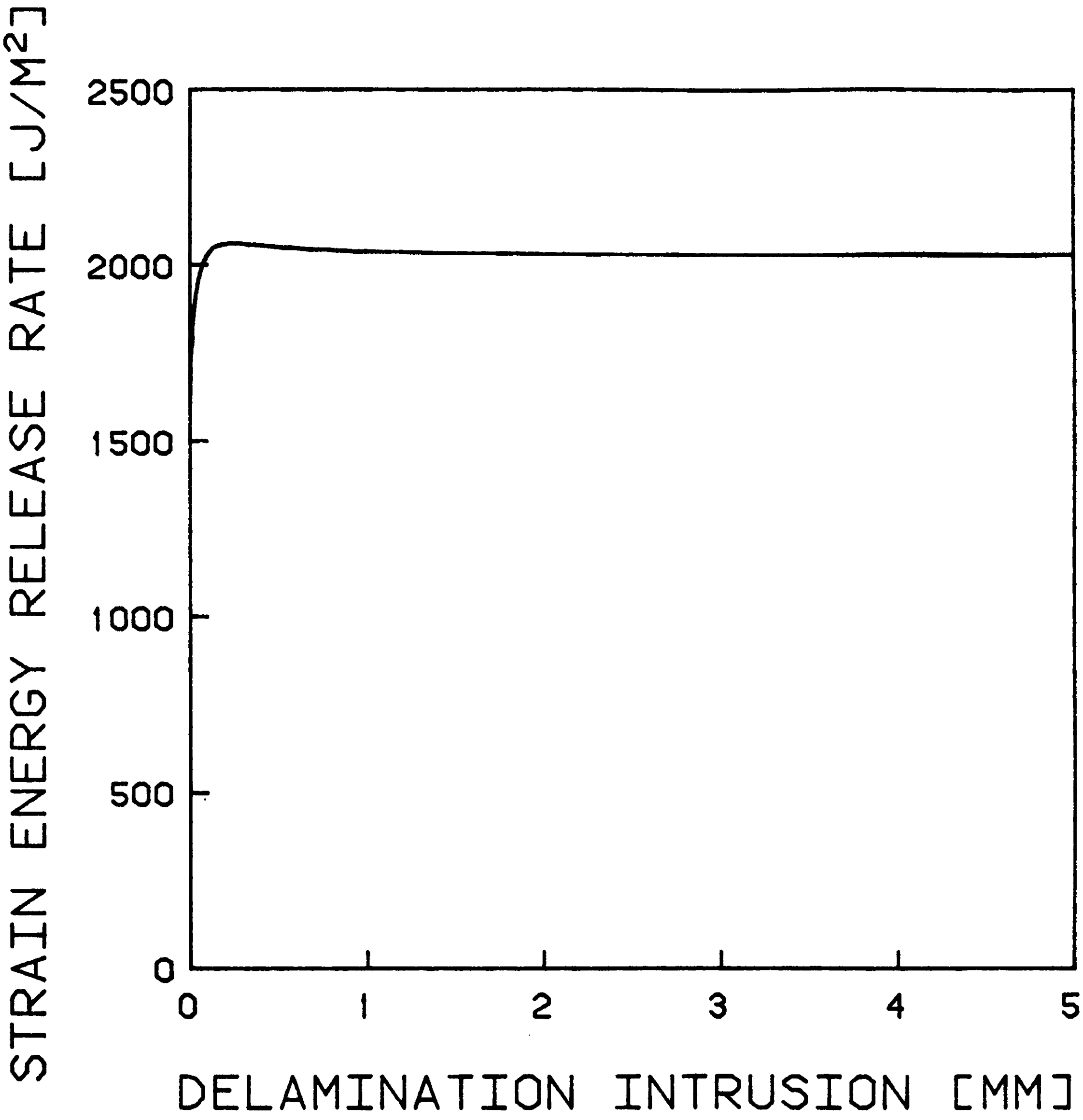

FIGURE 7.12 STRAIN ENERGY RELEASE RATE AS A FUNCTION OF DELAMINATION INTRUSION FOR A $[\pm 15/0]_s$ SPECIMEN USING A GEOMETRICALLY INTEGRATED FINITE ELEMENT MODEL

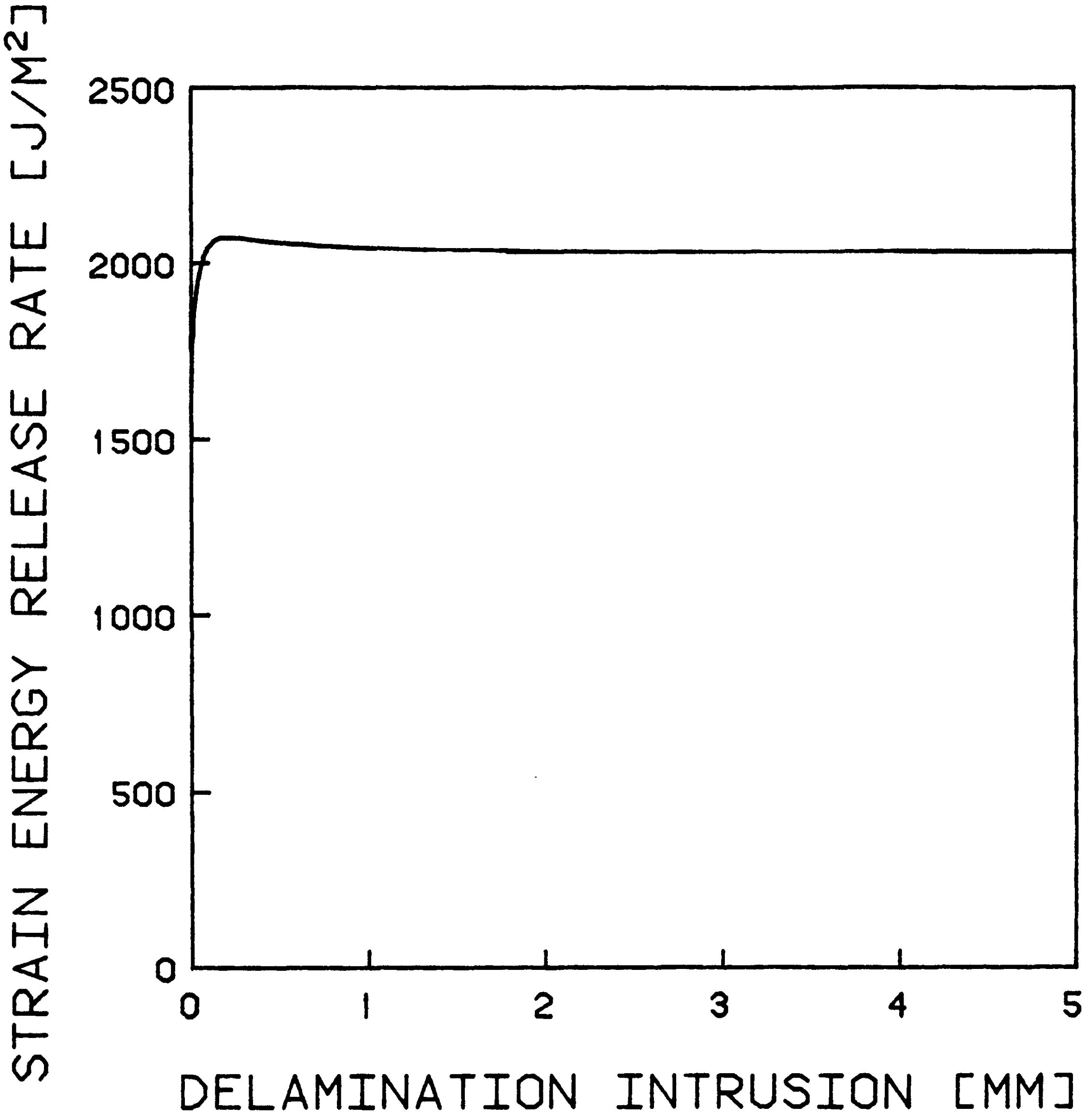

FIGURE 7.13 STRAIN ENERGY RELEASE RATE AS A FUNCTION OF DELAMINATION INTRUSION FOR A $[0/\pm15]_s$ SPECIMEN USING A GEOMETRICALLY INTEGRATED FINITE ELEMENT MODEL

Since the loading is quasistatic displacement controlled loading, any delamination growth is accompanied by an increase in the local strain level in the delaminated region and and a decrease in the local strain level in the laminated region. This behavior was observed experimentally in cases where the delamination occurred far from the gage.

The differential change in internal energy must be evaluated explicitly. The internal energy can be expressed as:

$$U_{del} = \iiint \frac{1}{2} \; \varepsilon_{11}^{2} \; E_{loc} \; dV \qquad (7.7)$$

where: E_{loc} = local longitudinal modulus

ε_{11} = local longitudinal strain.

After a differential change, the internal energy becomes:

$$U_{del} + dU_{del} = \iiint \frac{1}{2} \left(\varepsilon_{11} + d\varepsilon_{11} \right)^{2} \left(E_{loc} + dE_{loc} \right) dV \qquad (7.8)$$

After simplification and removal of higher order terms, this becomes:

$$dU_{del} = \iiint \frac{1}{2} \left(2\varepsilon_{11} \; E_{loc} \; d\varepsilon_{11} + \varepsilon_{11}^{2} \; dE_{loc} \right) dV \qquad (7.9)$$

An approximate model for describing the longitudinal strain level was used. The strain level and modulus were assumed to be functions solely of longitudinal position. The local modulus at each longitudinal position was set equal to the weighted average (by width) of the values for the laminated and delaminated regions. As with O'Brien's model, the modulus of the delaminated region was set equal to the weighted average (by thickness) of the sublaminates. The modulus of an unloaded sublaminate was set to zero in these calculations.

It becomes convenient to carry out all calculations in terms of an average strain level, ε^*. The average strain level is defined as the total applied displacement divided by the specimen length:

$$\varepsilon^* = \frac{\delta}{2l} \tag{7.10}$$

where: δ = total applied displacement.

An effective specimen modulus can be defined in terms of the resultant stress level at the given applied displacement:

$$E_{eff} = \frac{\sigma_o}{\varepsilon^*} \tag{7.11}$$

where: E_{eff} = effective longitudinal modulus for the specimen

σ_o = resultant stress level.

It can be shown that the effective modulus is given by:

$$E_{eff} = \frac{2l}{\int_{-l}^{l} \frac{1}{E_{loc}(x_1)}\, dx_1} \qquad (7.12)$$

When both sides of equation 7.9 are divided through by a differential change in delamination area, it can be shown using this model that the first term in the integrand integrates to zero. Physically, this means that when a differential amount of delamination growth occurs in a specimen under quasistatic displacement loading, the energy released in the laminated region by the decrease in strain level is exactly equivalent to the energy obtained in the delaminated region by the corresponding increase in strain level. Thus, the derivative of internal energy with respect to delaminated area is equivalent to:

$$\frac{dU_{del}}{dA_{del}} = \iiint \frac{1}{2}\, \varepsilon_{11}^2\, \frac{dE_{loc}}{dA_{del}}\, dV \qquad (7.13)$$

This is equivalent to differentiating the quantity in equation 7.6. In order to perform the integration in terms of the overall strain level, ε^*, the ratio β is introduced to express the difference between the square of the local strain level and the square of the overall strain level:

$$\beta(x_1) = \left(\frac{\varepsilon_{11}(x_1)}{\varepsilon^*}\right)^2 \qquad (7.14)$$

After the proper substitutions, the expression for strain energy release rate becomes:

$$G = \frac{d}{dA_{del}}\left(\int_{-1}^{1}\int_{0}^{a(x_1)} \beta(x_1)\ \hat{G}(x,\varepsilon^{*})\ dx\ dx_1\right) \qquad (7.15)$$

The strain energy release rate curves generated for the five $[\pm 15_3]_s$ specimen types (i.e. widths of 10 mm, 20 mm, 30 mm, 50 mm, and 70 mm) are shown in Figure 7.14. The curves for the five $[\pm 15_n/0_n]_s$ specimens types (i.e. n = 1, 2, 3, 5, and 8) are shown in Figures 7.15. The curves for the five $[0_n/\pm 15_n]_s$ specimens types (i.e. n = 1, 2, 3, 5, and 8) are shown in Figures 7.16.

The shape of the curves for the $[\pm 15_n/0_n]_s$ and $[0_n/\pm 15_n]_s$ specimens does not vary a great deal with increasing effective ply thickness. The curves are for all practical purposes scaled with respect to effective ply thickness. The only major difference in shape is related to the relative width of the interlaminar stress boundary region.

The shapes of the five curves for the $[\pm 15_3]_s$ specimens of nonstandard width are quite different. The effective ply thickness is the same for all the curves. The difference in the curves is a function of the aspect ratio of the specimen. For thin specimens, a delamination which stretches completely across the specimen is still not very long compared to specimen length. The compliance is relatively high in the delaminated region. Thus, the ratio of local strain in the

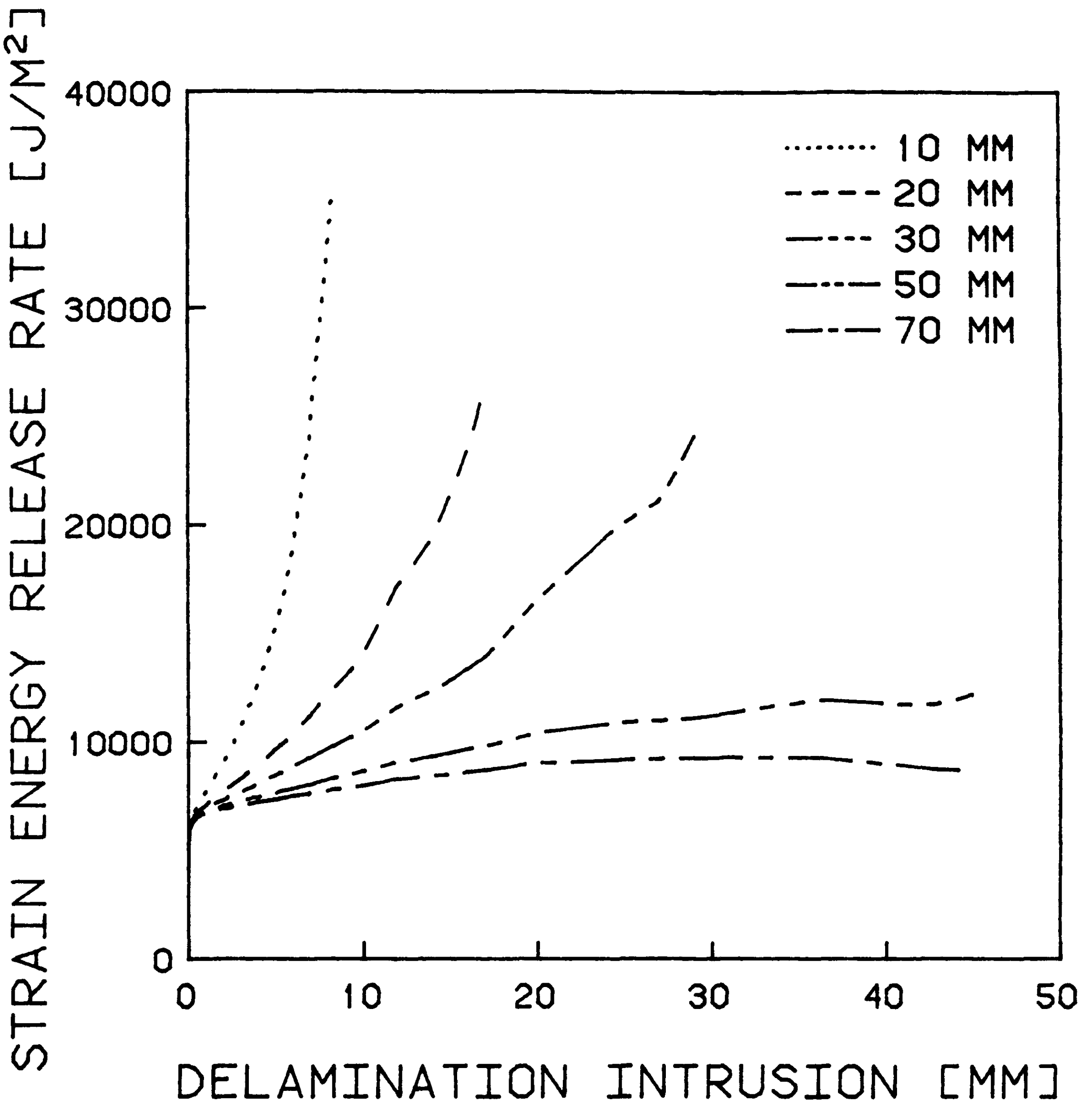

FIGURE 7.14 STRAIN ENERGY RELEASE RATE AS A FUNCTION OF DELAMINATION INTRUSION FOR $[\pm15_3]_s$ SPECIMENS OF NONSTANDARD WIDTH USING A GEOMETRICALLY INTEGRATED FINITE ELEMENT MODEL INCLUDING THE EFFECTS OF FINITE SPECIMEN DIMENSIONS

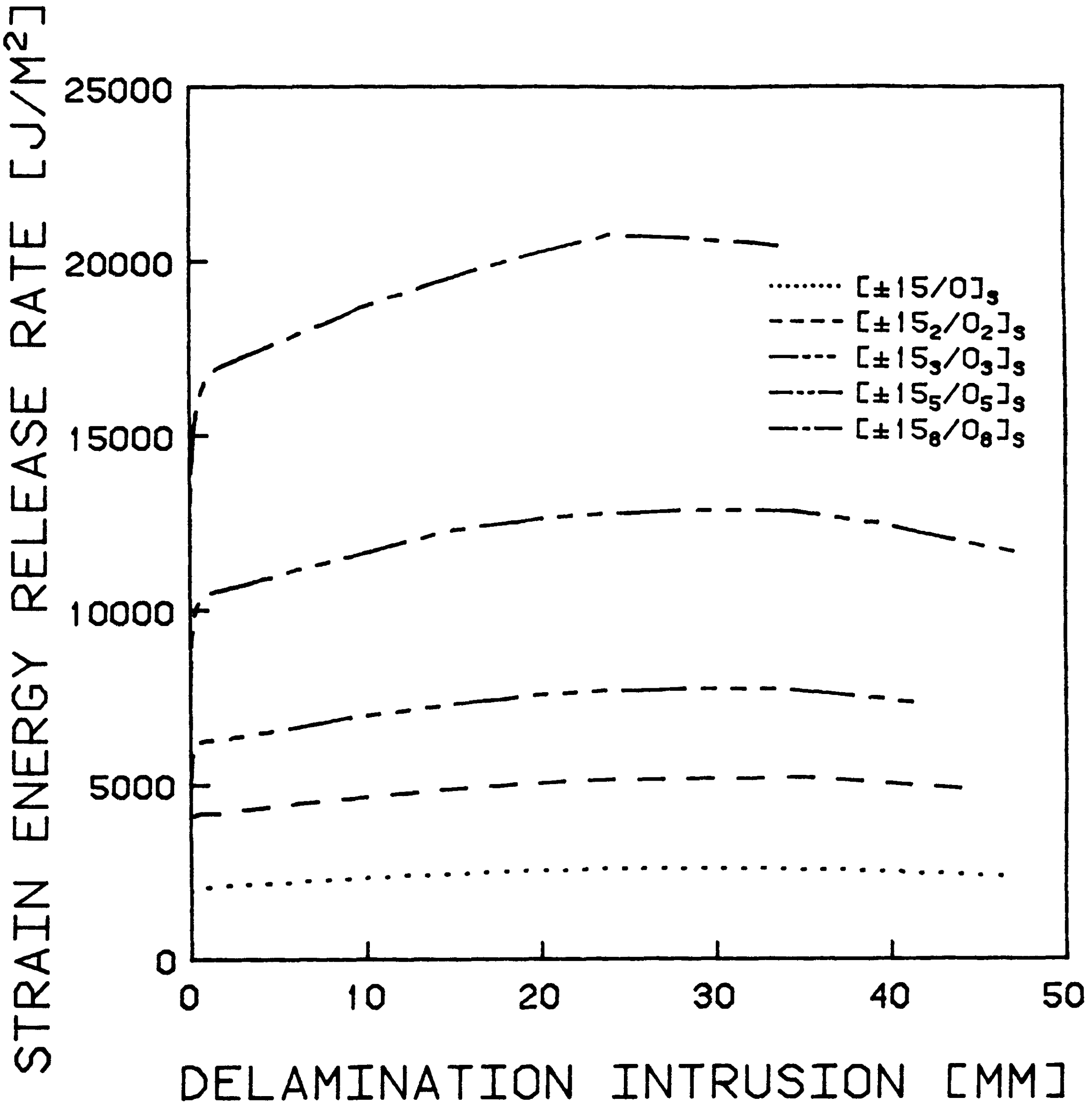

FIGURE 7.15 STRAIN ENERGY RELEASE RATE AS A FUNCTION OF DELAMINATION INTRUSION FOR $[\pm15_n/0_n]_s$ SPECIMENS USING A GEOMETRICALLY INTEGRATED FINITE ELEMENT MODEL INCLUDING THE EFFECTS OF FINITE SPECIMEN DIMENSIONS

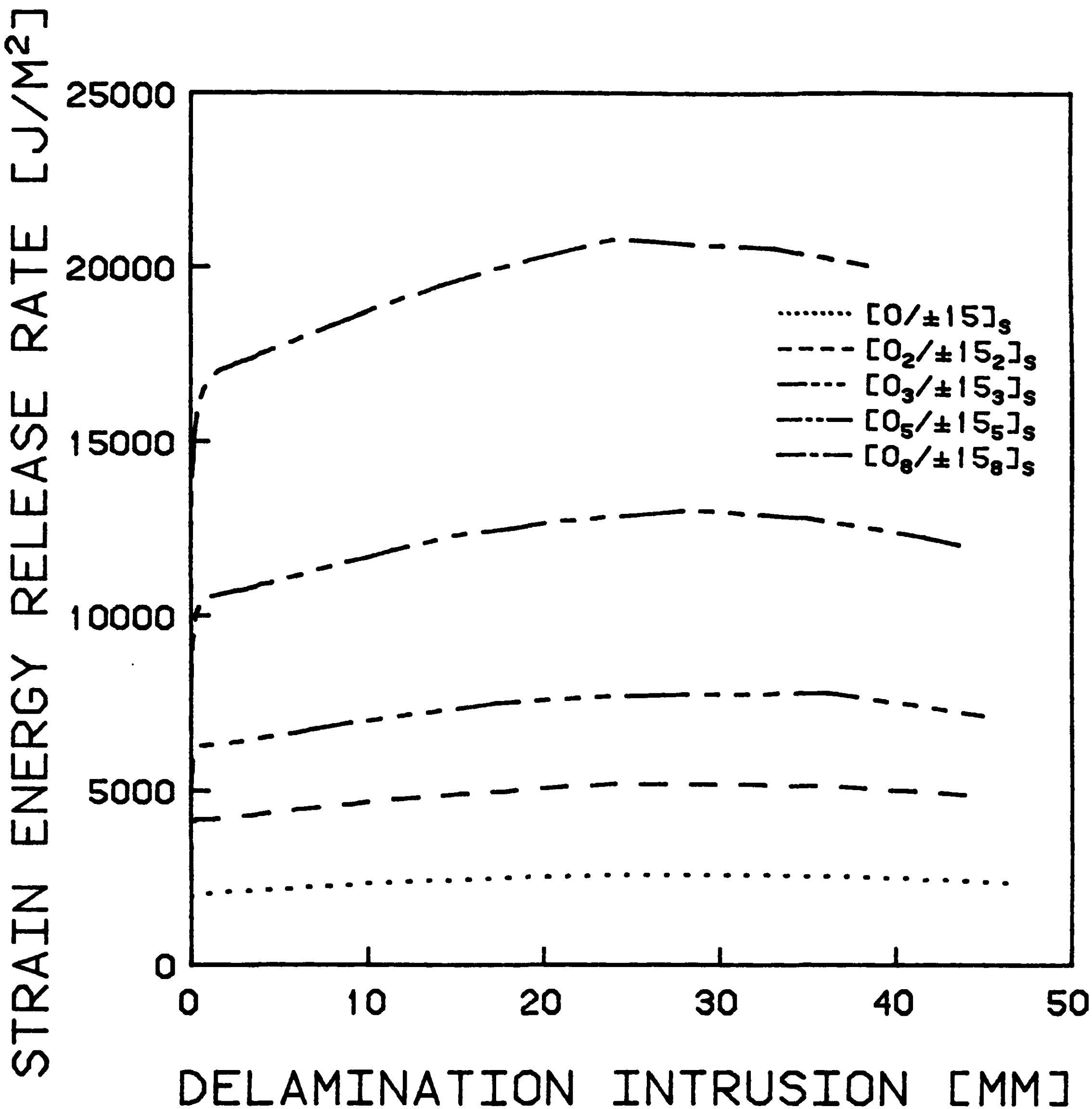

FIGURE 7.16 STRAIN ENERGY RELEASE RATE AS A FUNCTION OF DELAMINATION INTRUSION FOR $[0_n/\pm15_n]_s$ SPECIMENS USING A GEOMETRICALLY INTEGRATED FINITE ELEMENT MODEL INCLUDING THE EFFECTS OF FINITE SPECIMEN DIMENSIONS

delaminated region to the average strain level and therefore the ratio β in Equation 7.15 is quite high. The high local strains imply high local energy density which in turn implies a large amount of energy available for release per unit of delaminated area. Hence, the strain energy release rate curve rises rapidly with increasing delamination size.

In wider specimens, a delamination along most of the specimen length does not necessarily imply a large ratio of local strain to average strain level. In fact, most of the specimen has a relatively high compliance, implying that the ratio β will not be large at most longitudinal positions. Thus, the curve will not rise rapidly. In the limit, an infinitely wide specimen has no significant changes in local modulus and has a strain energy release rate curve such as the one shown in Figure 7.11.

Care must be taken when determining the overall strain level from data. The strain level obtained from the gage is a local strain level and is affected by its location with respect to the delamination. The overall strain level cannot be inferred from the stroke data because of uncertainty about strain applied during gripping and significant shear deformation of the relatively thick loading tabs. The stress level is an excellent parameter with which to characterize a loading situation, but care must be taken to divide it by the effective modulus rather than the nominal modulus to determine the overall strain level.

The maximum stress recorded in each test in which growth occurred cannot be arbitrarily associated with the maximum intrusion of that test. In fact, there is undoubtedly a significant load drop associated with delamination growth in displacement controlled loading. Although the intrusion of the delamination at the point of maximum stress cannot be definitively determined, it can be approximated in most cases as the maximum intrusion observed in the previous test of that specimen.

7.5 Results

The strain energy release rate was calculated for each test in which the maximum intrusion increased in value from the previous test. The intrusion used was the value from the previous test. The case in which the delamination grew to a detectable size was not considered because the size of the delamination initiation could not be determined. Four calculation methods were used: O'Brien's equation, the two-dimensional finite element method with no assumed unloading, the geometrically integrated finite element method with no finite dimension effects, and the geometrically integrated finite element method with finite dimension effects. The calculated values of strain energy release rate are given for the various methods of calculation in Appendices I ($[\pm 15_3]_s$ specimens), J ($[\pm 15_n/0_n]_s$ specimens), and K ($[0_n/\pm 15_n]_s$ specimens).

This strain energy release rate data can be used to plot points on a delamination resistance curve. Plots for $[\pm 15_3]_s$ specimens using each calculation method (O'Brien's equation, two-dimensional finite element method with no assumed unloading, geometrically integrated finite element method with no effects of finite specimen dimensions, and geometrically integrated finite element method including the effects of finite specimen dimensions) are shown in Figures 7.17 through 7.20, respectively. Plots for $[\pm 15_n/0_n]_s$ specimens using each calculation method are shown in Figures 7.21 through 7.24, respectively. Plots for $[0_n/\pm 15_n]_s$ specimens using each calculation method are shown in Figures 7.25 through 7.28, respectively.

7.6 Discussion

The critical value of strain energy release rate is a measure of the change in global internal energy necessary to cause the delamination of a unit area. This should be independent of specimen width, delamination intrusion, and effective ply thickness. Thus, the delamination resistance curve should be relatively flat for each specimen type. However, all four methods of calculation and all three specimen types show a marked deviation from a constant value in the experimental delamination resistance curve. There is often a factor of two or more between values for similar delamination sizes.

There are several possible sources for these

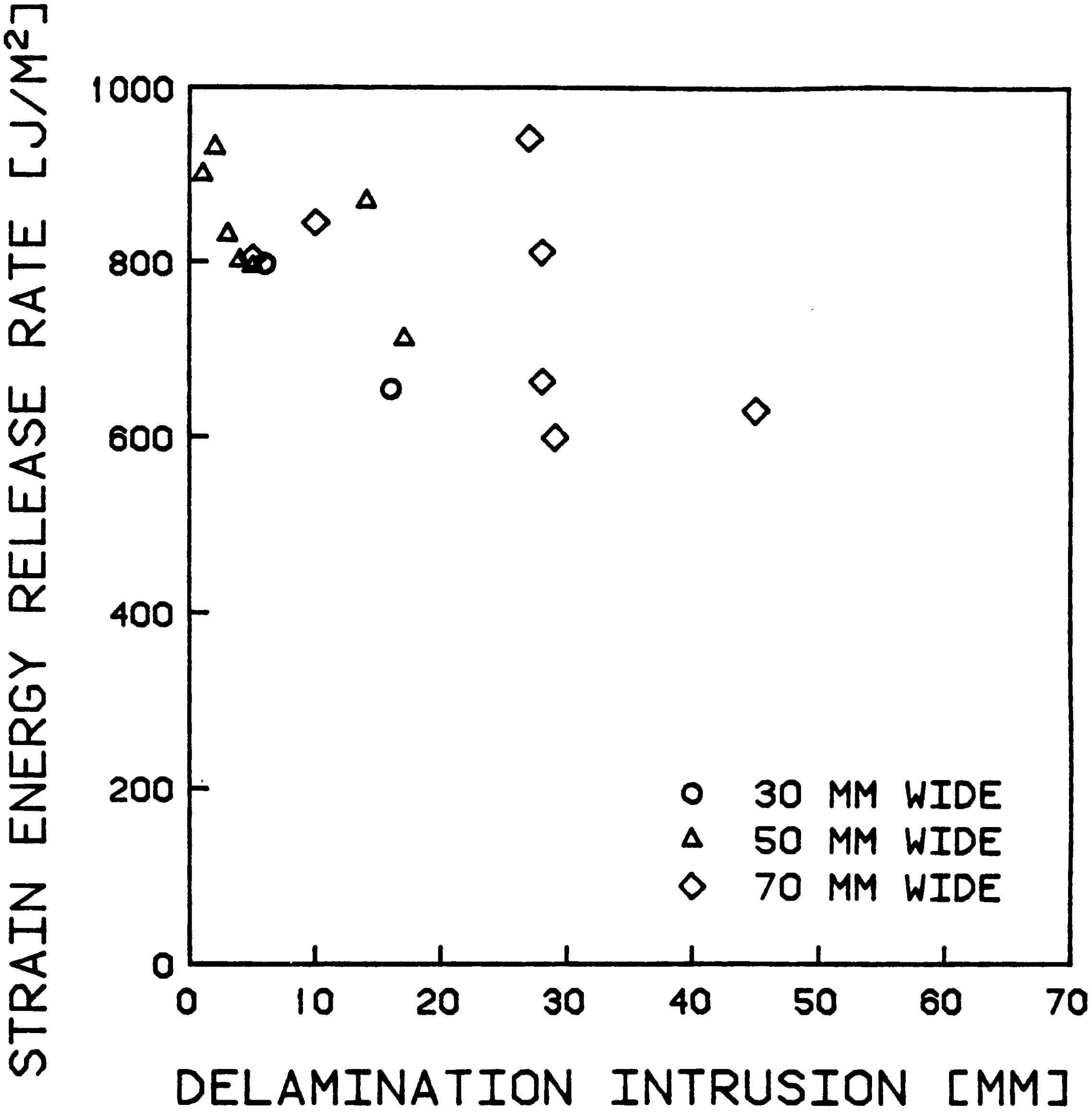

FIGURE 7.17 EXPERIMENTAL VALUES OF STRAIN ENERGY RELEASE RATE AS A FUNCTION OF DELAMINATION INTRUSION FOR $[\pm15_3]_s$ SPECIMENS USING O'BRIEN'S METHOD

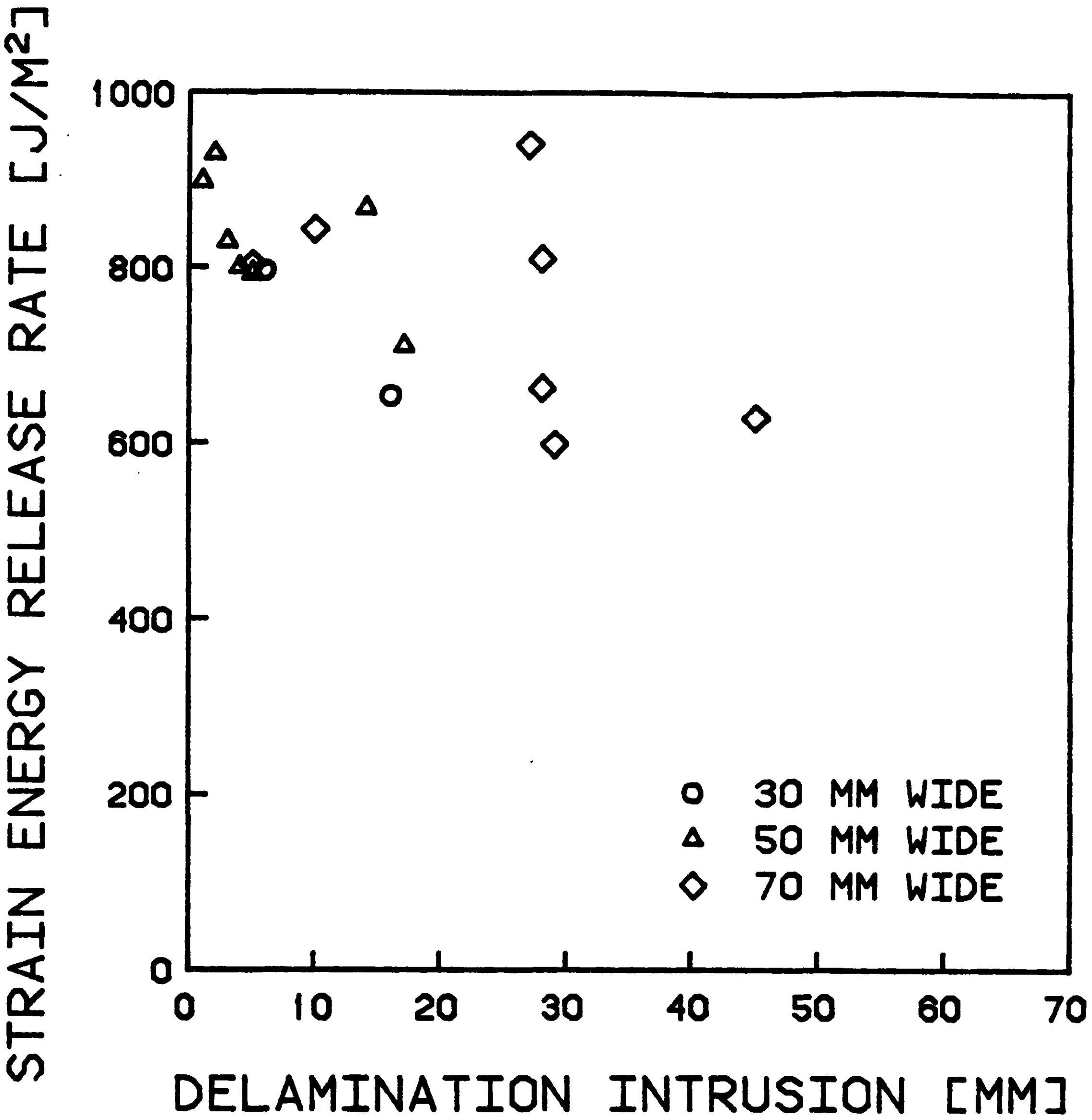

FIGURE 7.18 EXPERIMENTAL VALUES OF STRAIN ENERGY RELEASE RATE AS A FUNCTION OF DELAMINATION INTRUSION FOR $[\pm15_3]_s$ SPECIMENS USING A TWO-DIMENSIONAL FINITE ELEMENT MODEL

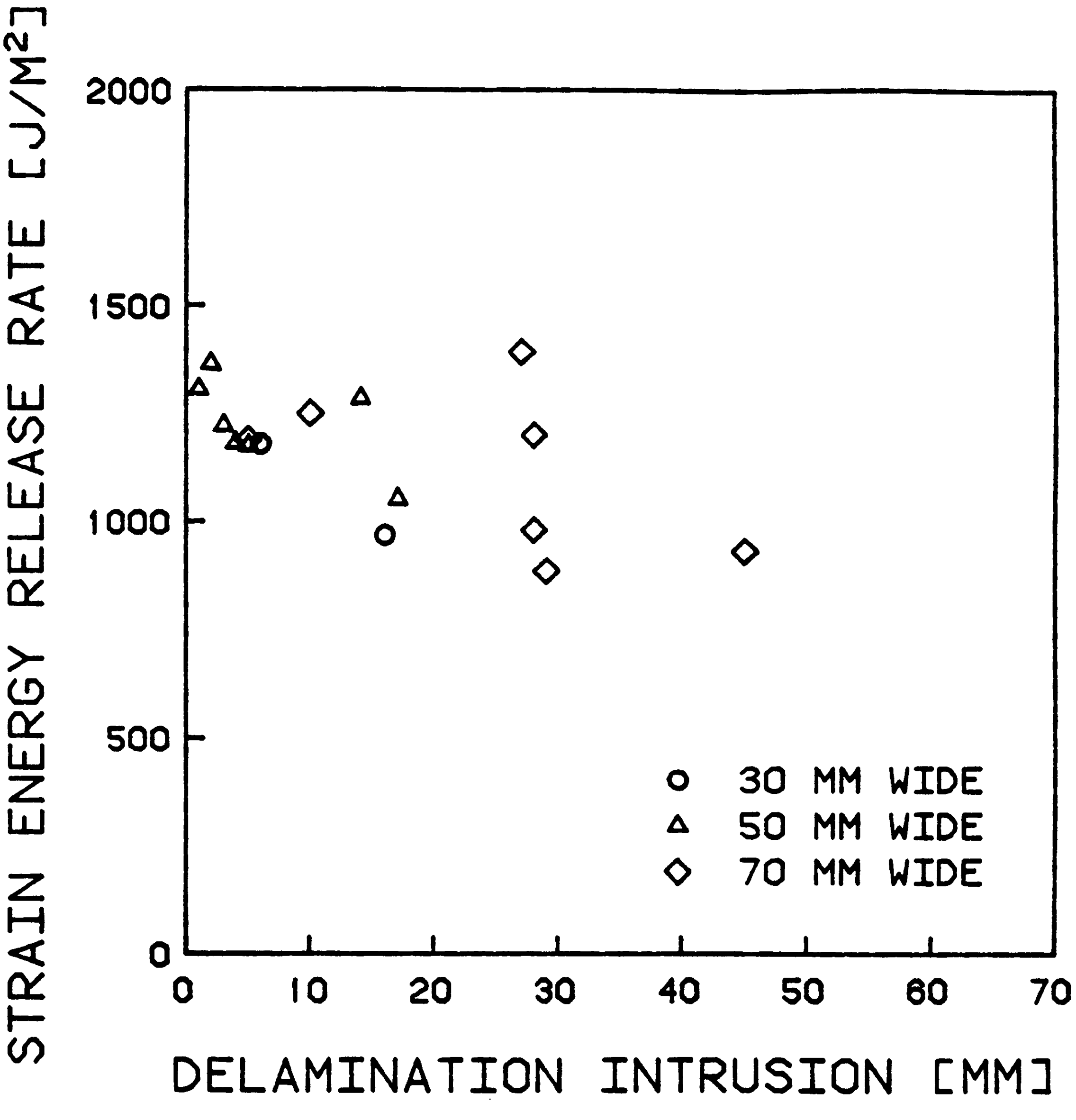

FIGURE 7.19 EXPERIMENTAL VALUES OF STRAIN ENERGY RELEASE RATE AS A FUNCTION OF DELAMINATION INTRUSION FOR $[\pm15_3]_s$ SPECIMENS USING A GEOMETRICALLY INTEGRATED FINITE ELEMENT MODEL

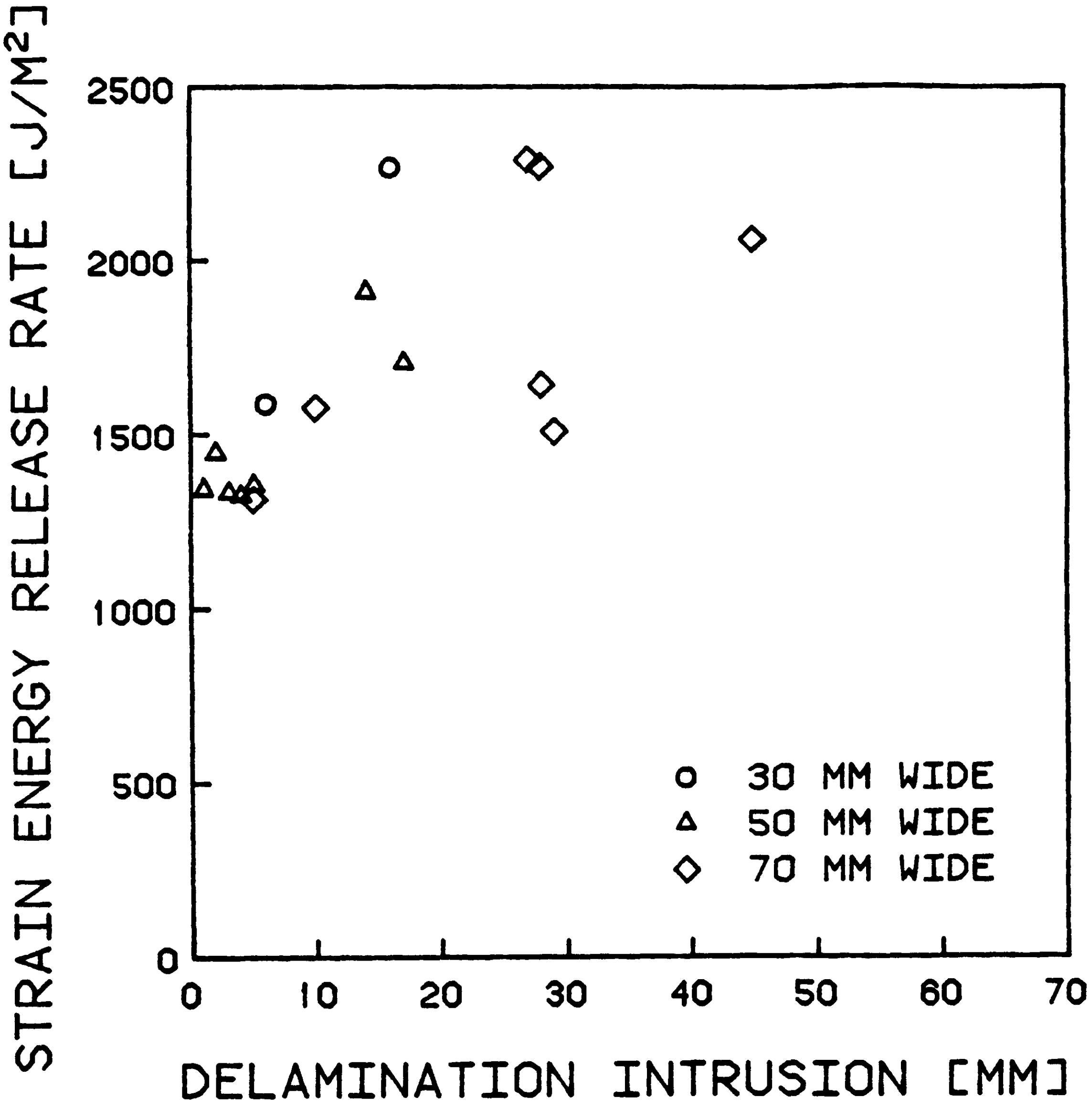

FIGURE 7.20 EXPERIMENTAL VALUES OF STRAIN ENERGY RELEASE RATE AS A FUNCTION OF DELAMINATION INTRUSION FOR $[\pm15_3]_s$ SPECIMENS USING A GEOMETRICALLY INTEGRATED FINITE ELEMENT MODEL INCLUDING THE EFFECTS OF FINITE SPECIMEN DIMENSIONS

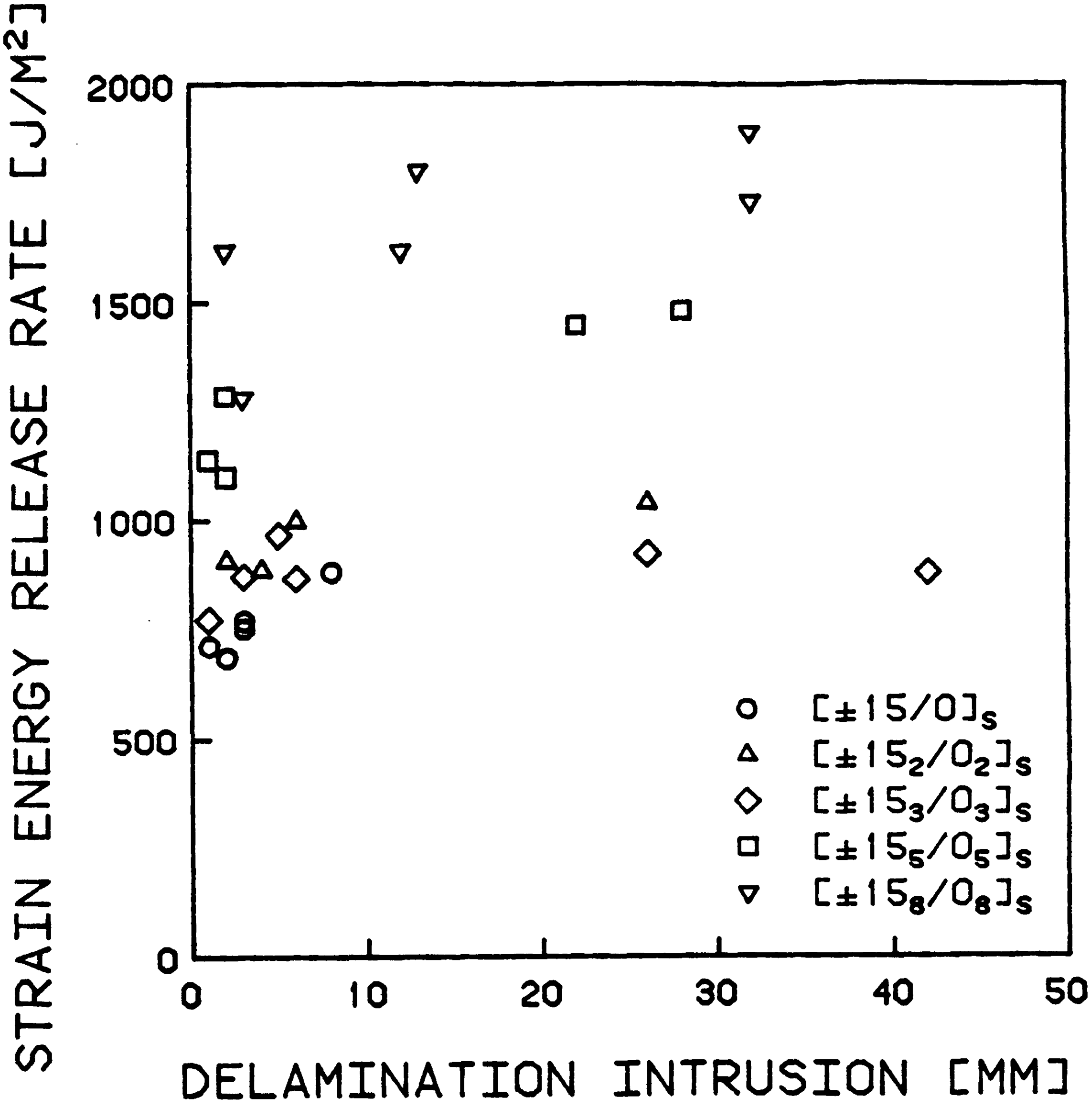

FIGURE 7.21 EXPERIMENTAL VALUES OF STRAIN ENERGY RELEASE RATE AS A FUNCTION OF DELAMINATION INTRUSION FOR $[\pm 15_n/0_n]_s$ SPECIMENS USING O'BRIEN'S METHOD

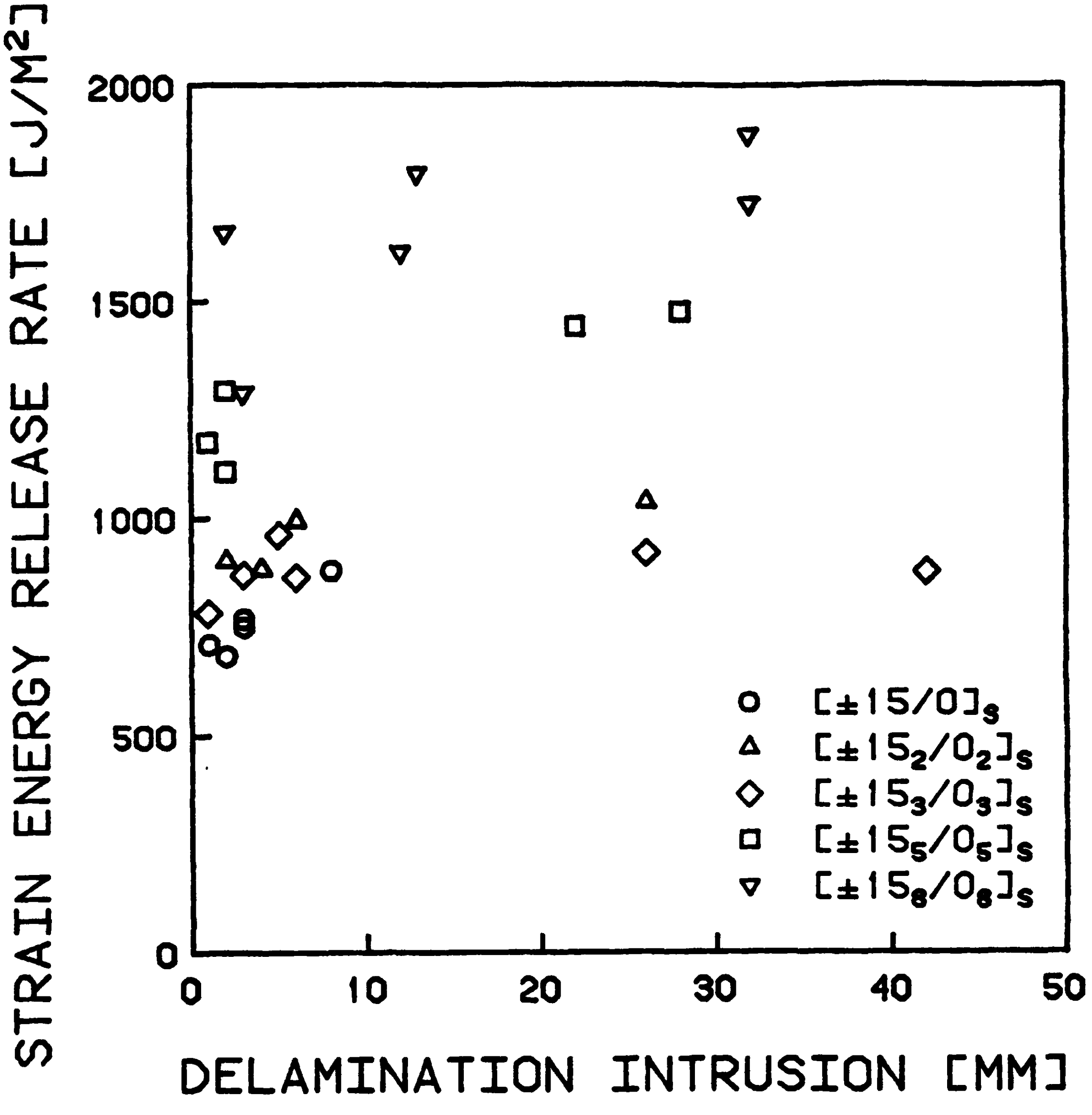

FIGURE 7.22 EXPERIMENTAL VALUES OF STRAIN ENERGY RELEASE RATE AS A FUNCTION OF DELAMINATION INTRUSION FOR $[\pm 15_n/0_n]_s$ SPECIMENS USING A TWO-DIMENSIONAL FINITE ELEMENT MODEL

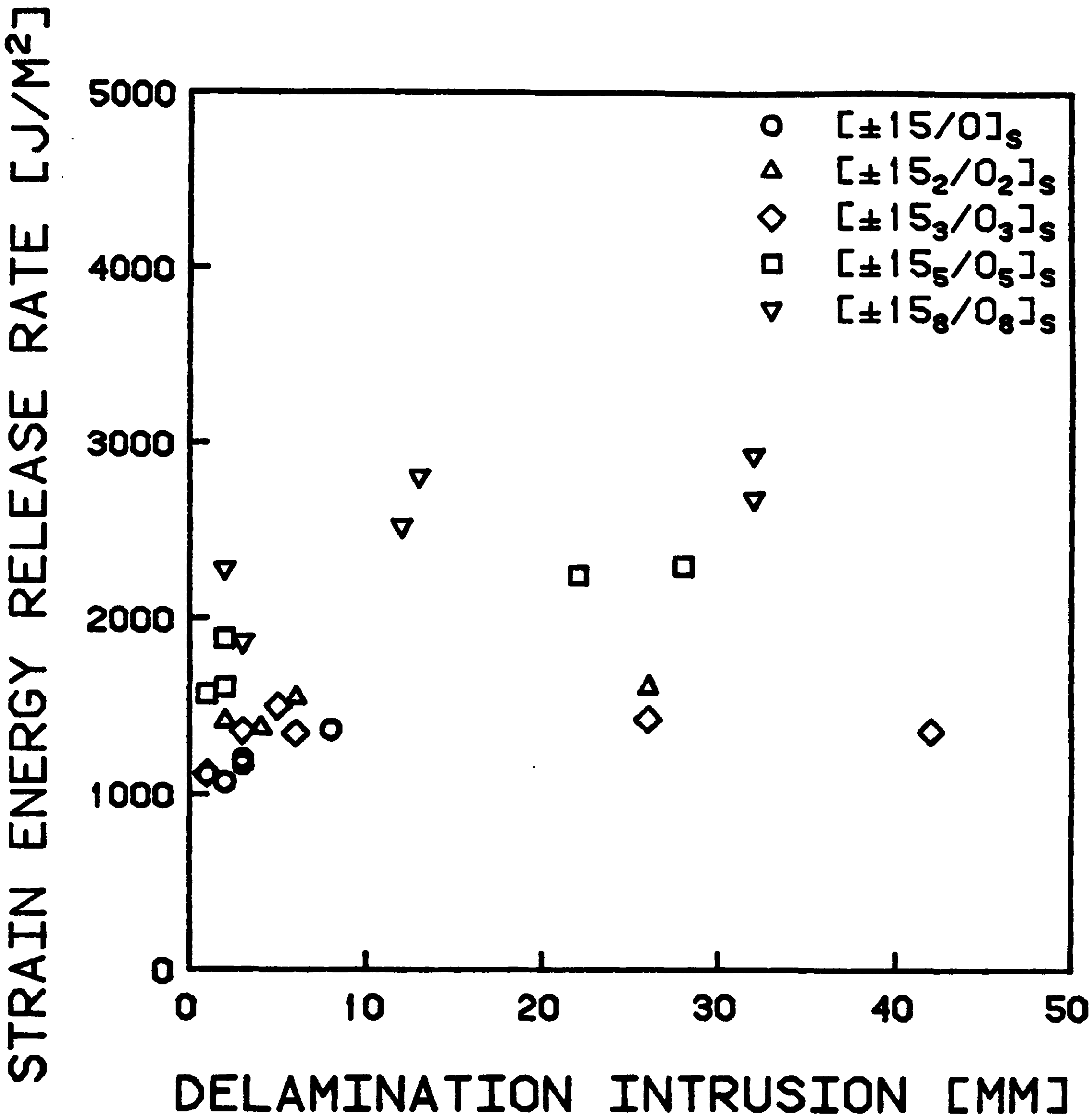

FIGURE 7.23 EXPERIMENTAL VALUES OF STRAIN ENERGY RELEASE RATE AS A FUNCTION OF DELAMINATION INTRUSION FOR $[\pm 15_n/0_n]_s$ SPECIMENS USING A GEOMETRICALLY INTEGRATED FINITE ELEMENT MODEL

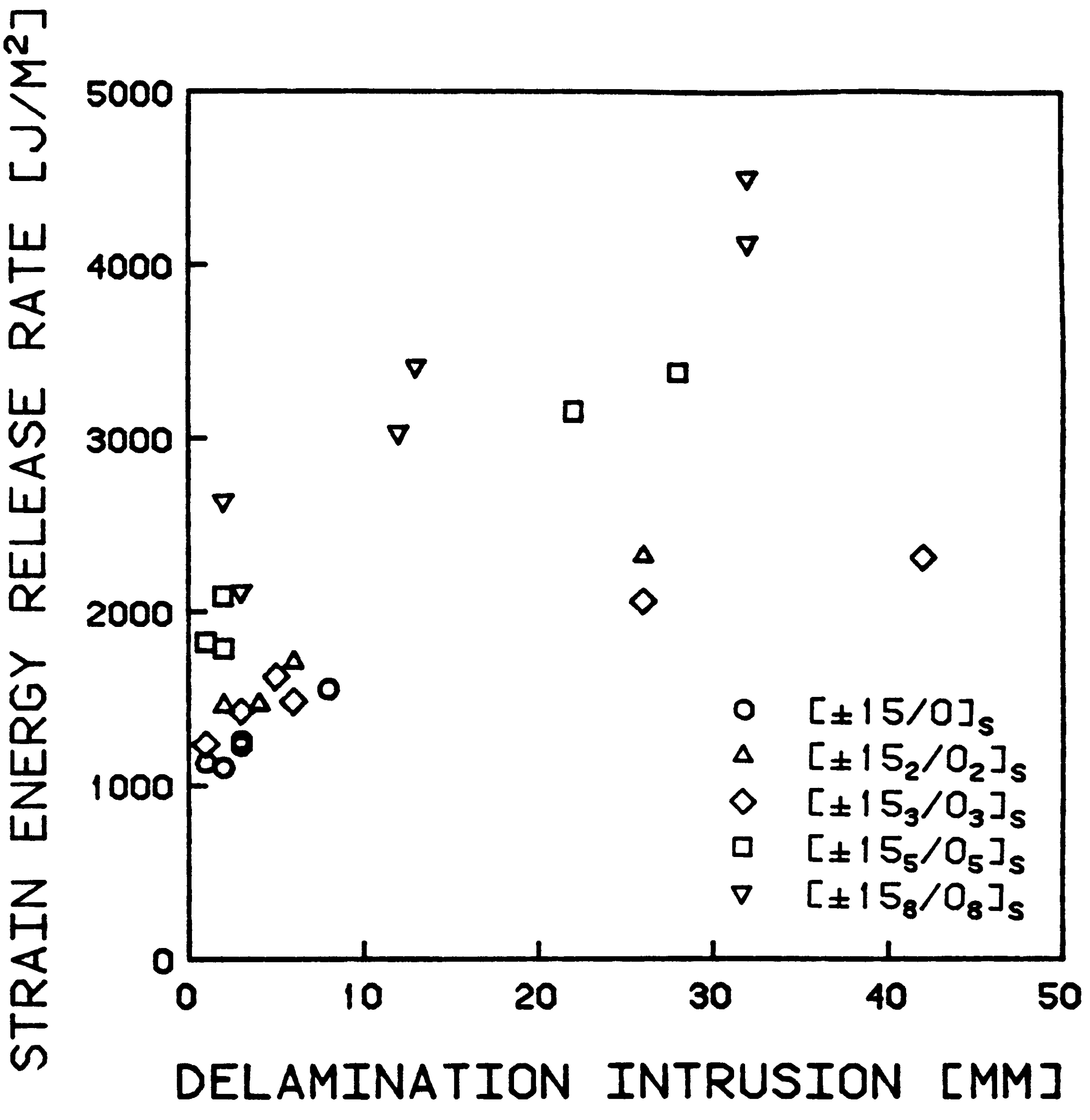

FIGURE 7.24 EXPERIMENTAL VALUES OF STRAIN ENERGY RELEASE RATE AS A FUNCTION OF DELAMINATION INTRUSION FOR $[\pm15_n/0_n]_s$ SPECIMENS USING A GEOMETRICALLY INTEGRATED FINITE ELEMENT MODEL INCLUDING THE EFFECTS OF FINITE SPECIMEN DIMENSIONS

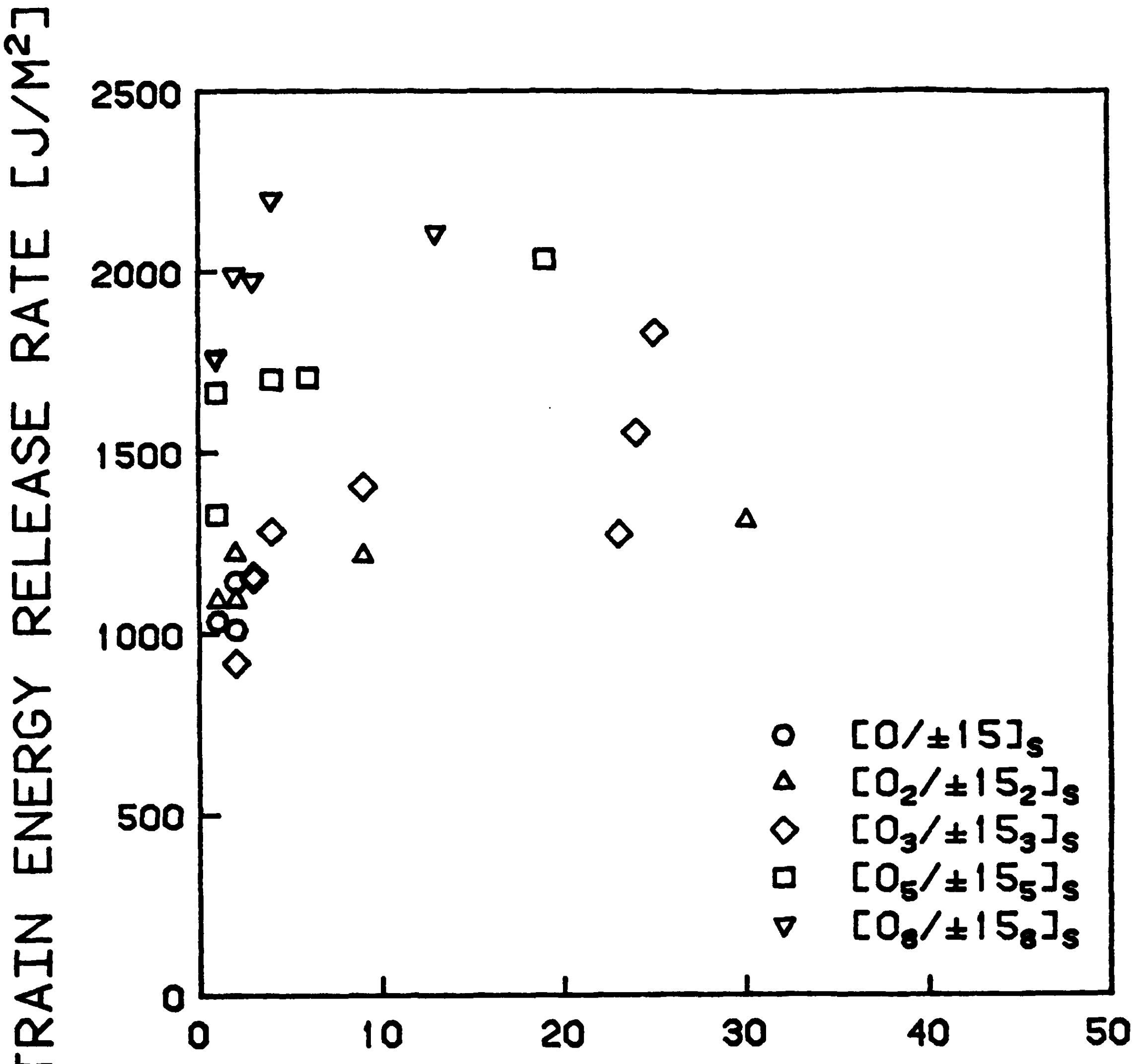

FIGURE 7.25 EXPERIMENTAL VALUES OF STRAIN ENERGY RELEASE RATE AS A FUNCTION OF DELAMINATION INTRUSION FOR $[0_n/\pm15_n]_s$ SPECIMENS USING O'BRIEN'S METHOD

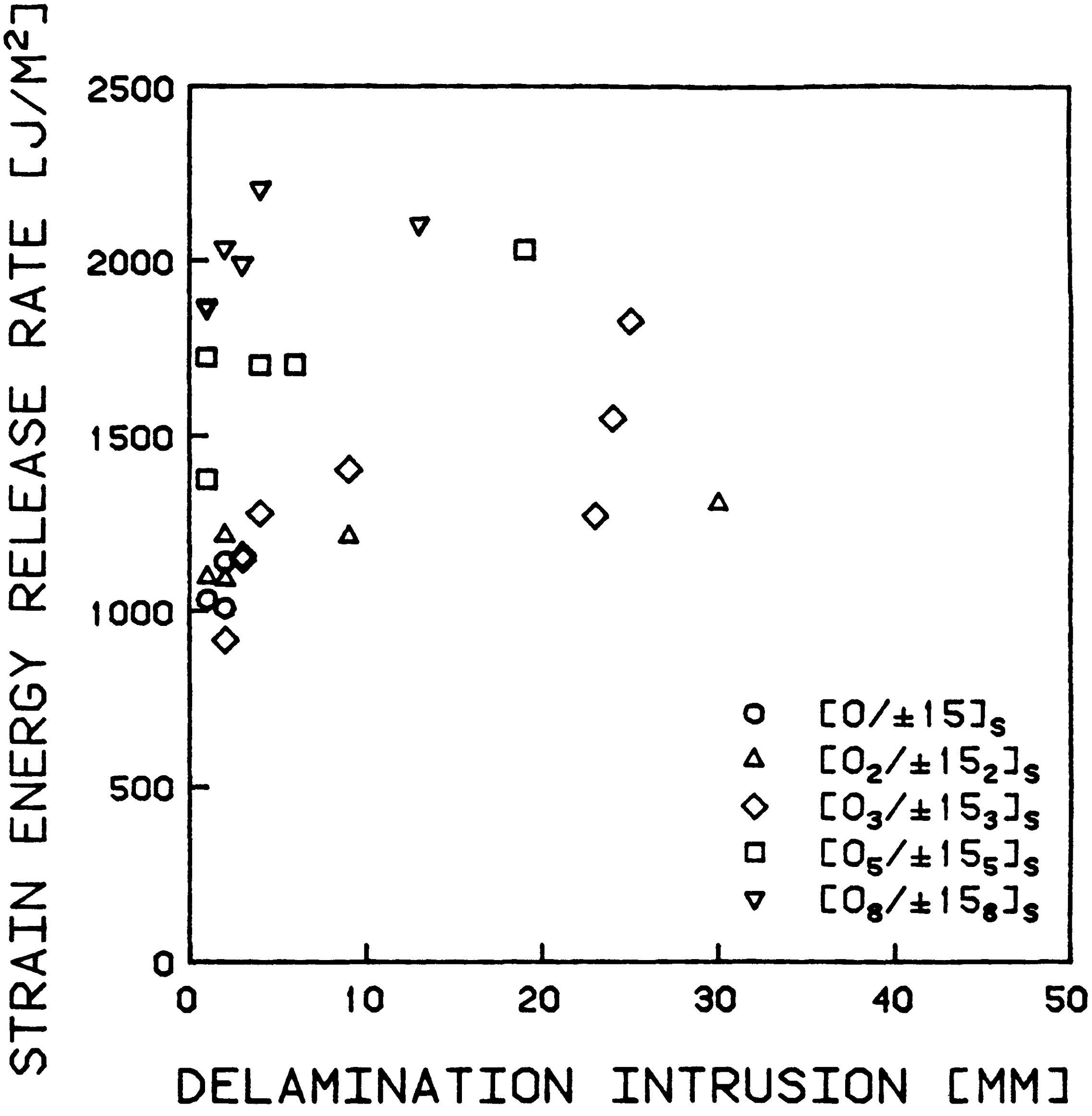

FIGURE 7.26 EXPERIMENTAL VALUES OF STRAIN ENERGY RELEASE RATE AS A FUNCTION OF DELAMINATION INTRUSION FOR $[0_n/\pm 15_n]_s$ SPECIMENS USING A TWO-DIMENSIONAL FINITE ELEMENT MODEL

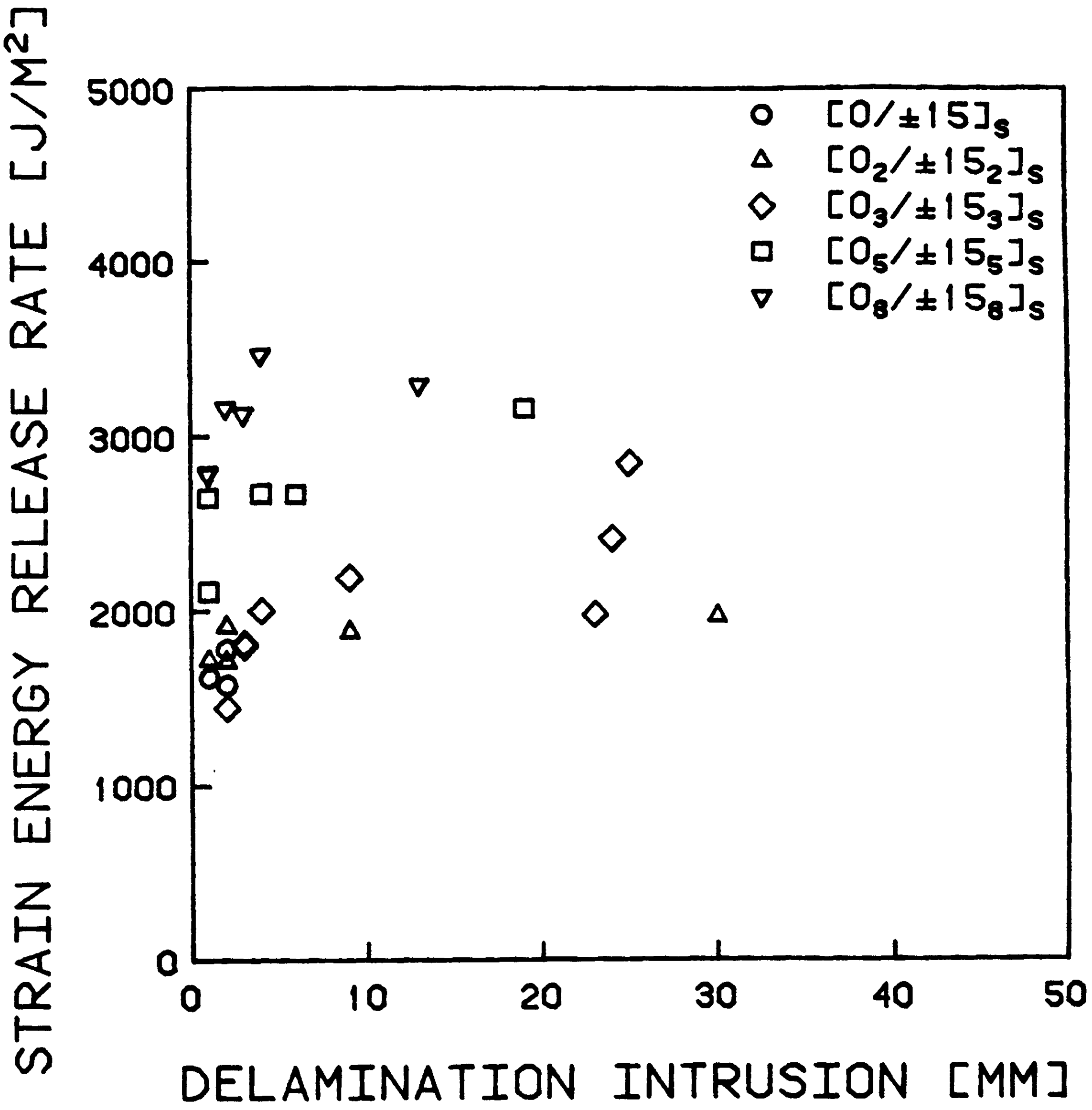

FIGURE 7.27 EXPERIMENTAL VALUES OF STRAIN ENERGY RELEASE RATE AS A FUNCTION OF DELAMINATION INTRUSION FOR $[0_n/\pm 15_n]_s$ SPECIMENS USING A GEOMETRICALLY INTEGRATED FINITE ELEMENT MODEL

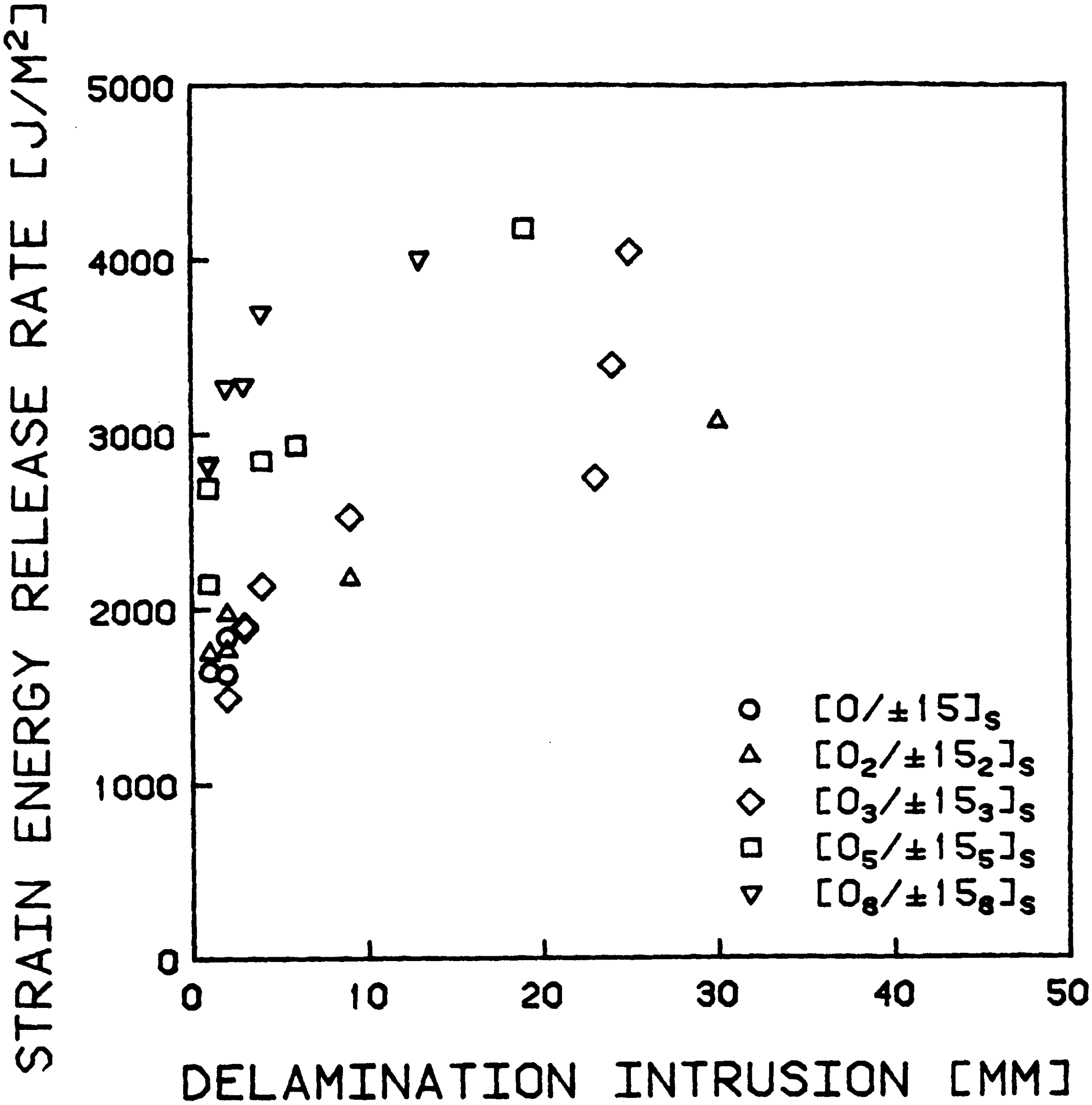

FIGURE 7.28 EXPERIMENTAL VALUES OF STRAIN ENERGY RELEASE RATE AS A FUNCTION OF DELAMINATION INTRUSION FOR $[0_n/\pm15_n]_s$ SPECIMENS USING A GEOMETRICALLY INTEGRATED FINITE ELEMENT MODEL INCLUDING THE EFFECTS OF FINITE SPECIMEN DIMENSIONS

discrepancies. It can be argued that many of the larger delamination sizes correspond to growth after growth to the loading tab and it therefore may be inappropriate to characterize them with the models presented. Nonetheless, the large degree of scatter is also observed for small delamination sizes, especially for the $[\pm 15_n/0_n]_s$ and $[0_n/\pm 15_n]_s$ specimens.

Some of the observed scatter may result from variations in the material and from experimental procedures. The order of magnitude of this variation should be approximately equal to the scatter observed for nominally identical specimens with the same or similar delamination sizes. The amount of such variation occasionally can be seen to be as much as 20% in the data in Appendices I, J, and K. It is thus unlikely that material and experimental variation is a primary source for the observed deviations. Two 70 mm wide $[\pm 15_3]_s$ specimens with similar sized delaminations showed a large discrepancy in the calculated critical value of strain energy release rate (34%), but in both cases the "delamination growth" was final failure after growth to the loading tab. In such cases, the applicability of the present models is questionable.

It is expected that the critical value of strain energy release rate would be independent of effective ply thickness. There should be no change in the local constraint or the relative modal contributions to strain energy release rate when the effective ply thickness is changed for a given lamination sequence. Nonetheless, it can be seen in

Figures 7.21 through 7.28 that the experimental delamination resistance curves calculated using these models are strong functions of effective ply thickness. The dependence on effective ply thickness would limit the utility of the general approach unless it can be shown that the resistance curve determined for a thin laminate of a given specimen type will in general give a lower bound for the values of thicker specimens. This appears to be the case for the laminate types in this investigation.

The experimental delamination resistance curve calculated using these methods is also a strong function of lamination sequence. Since the constraint of intact sublaminates on damaged sublaminates and the relative modal contributions to strain energy release rate were not incorporated into the model, the calculated critical value of the strain energy release rate could be different for different lamination sequences. However, it would not be expected to vary with delamination size for a given specimen type. It can be seen from the data in Appendices I, J, and K, however, that it can vary substantially for a single specimen. For example, the experimental delamination resistance curve obtained using the present model for a $[0_3/\pm15_3]_s$ specimen is shown in Figure 7.29. A clear upward trend is observed.

Given the significant deviations from a constant strain energy relase rate calculated from the data, it is impossible to state definitively which strain energy release rate model is most accurate. The geometrically integrated finite element

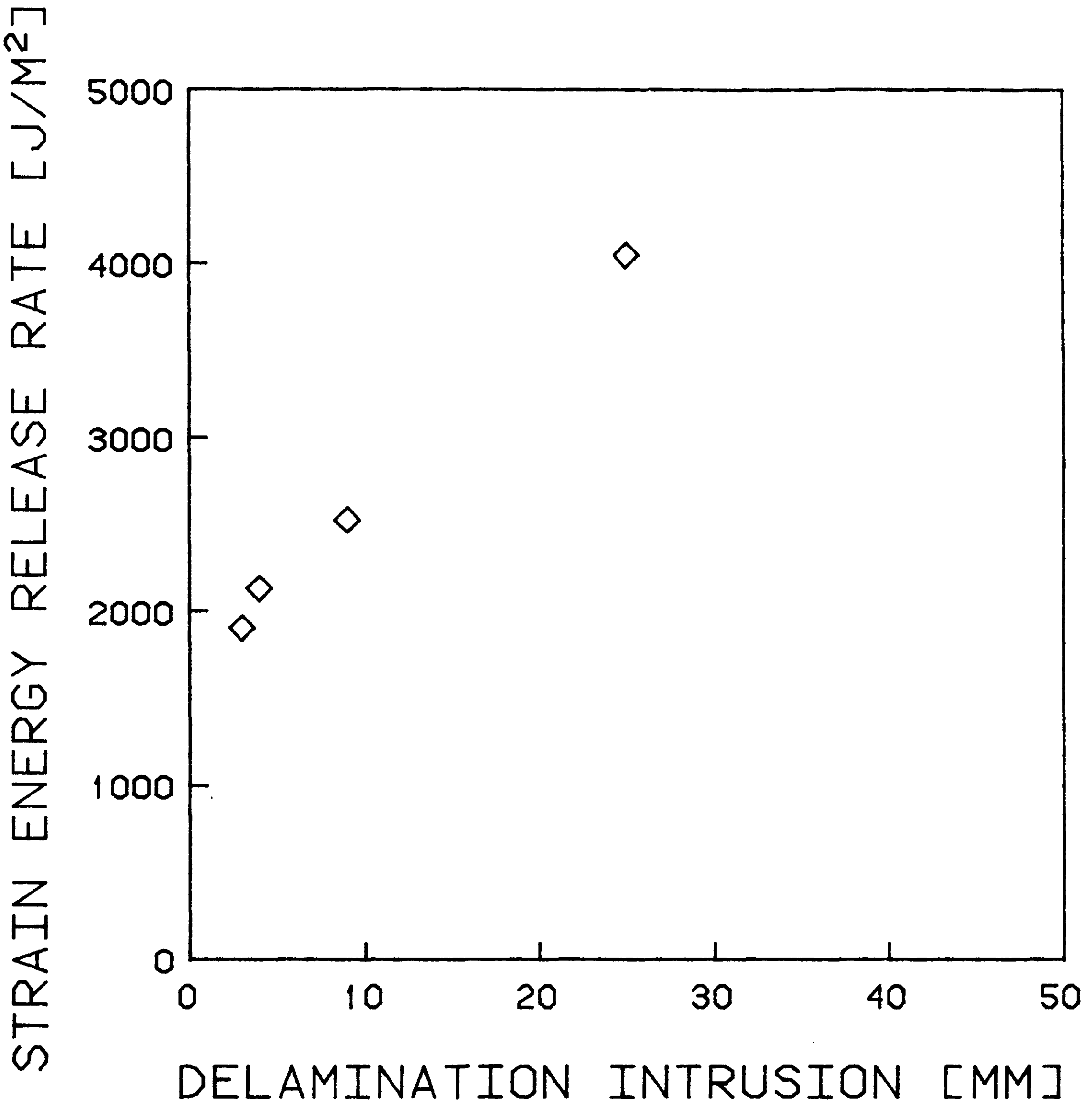

FIGURE 7.29 EXPERIMENTAL VALUES OF STRAIN ENERGY RELEASE RATE AS A FUNCTION OF DELAMINATION INTRUSION USING A GEOMETRICALLY INTEGRATED FINITE ELEMENT MODEL INCLUDING THE EFFECTS OF FINITE SPECIMEN DIMENSIONS

method with corrections for the effects of finite specimen dimensions should give more reliable results than the methods which do not account for delamination shape or the effects of finite specimen dimensions. However, with the data obtained herein, this cannot be directly ascertained.

A possible extension of the strain energy release rate approach might involve the close examination of the stress field and strain energy release conditions near the angle ply splits. These splits were not explicitly modeled in the present analysis. The key to understanding the process of initiating and arresting dynamic delamination growth may lie in determining the interaction of the angle ply splits and the delamination. The stress fields surrounding the tip of the angle ply split bordering the delamination, the delamination front, and any angle ply split in a ply adjacent to the delaminated interface which is lying across the path of the delamination front should be ascertained.

Other mechanisms may also be at work. These mechanisms could account for the observed difference between the calculated critical value of strain energy release rate for specimens of different effective ply thickness, different intrusion size, and different stacking sequence. If some of the mechanisms were shown to be totally local rather than global, they might explain the different values obtained for nominally identical specimens with similar intrusions. The growth of the delamination is observed to be a dynamic event. The energy criterion is a necessary but not sufficient condition for growth. The conditions necessary to start and arrest a dynamic delamination growth event are not ascertainable from the data in this investigation. One hypothesis is that the delamination front can be blunted and arrested when it runs across splits in the adjoining angle plies. Their presence would then increase the energy needed to reinitiate dynamic growth above the value needed for simple growth. Such splits were not visible in the x-radiographs. However, this could be the result if the crack opening of these splits were too small to allow a detectable amount of DIB to seep in. The timing of the formation of these hypothesized splits is also unknown. If they form away from the delamination, they could be difficult to detect. Alternatively, they could result dynamically from a stress wave preceding the delamination front. More work should be done to evaluate these possibilities.

CHAPTER 8

SUMMARY OF PRESENT WORK

Jamison's statement regarding the failure of advanced composites [43] is an eloquent summary of the problem: "Failure can be preceded by a complex and interacting global ensemble of discrete damage modes." Delamination of graphite/epoxy composites is a complicated process which has defied numerous attempts at simple explanation. Research has shown that it has several stages, each of which appears to reveal additional intricacies with every investigation. The present work has attempted, with some success, to resolve issues of delamination initiation, growth, and final failure.

8.1 Delamination Initiation

Delamination initiation is a critical stage in the failure of graphite/epoxy induced by delamination. Delamination initiation, like any event, is controlled to some extent by energy considerations. Nonetheless, energy criteria are in general necessary rather than sufficient conditions. Fracture mechanics methodologies, such as the strain energy release rate, are derived in terms of crack tip stress fields. The delamination initiation occurs, by definition, without a preexisting interlaminar crack. Local stress levels may be insufficient over large enough areas to form the initiation even though initiation and growth may be energetically feasible.

The existence of high stress gradients and possible weak singularities near free edges makes point stress criteria inappropriate. Inhomogeneity and initial flaw distribution become potentially important micromechanical issues. The use of an average stress approach mitigates these effects by considering a large enough region that these issues effectively become unimportant. Thus, an average stress approach can be used to characterize this complex behavior.

The Quadratic Delamination Criterion has been shown to be an acceptable criterion for delamination initiation for several reasons. First, it gives excellent agreement of the data in this and previous [34] investigations. Second, the experimentally determined averaging dimension appears to be a material parameter. Third, the interlaminar normal strength parameter determined by direct experiment worked well. Fourth, the potential importance of thermally-induced interlaminar stresses and interlaminar normal stresses were demonstrated. It appears that the Quadratic Delamination Criterion is sufficient to describe the initiation of delamination in graphite/epoxy composites.

The Quadratic Delamination Criterion can thus be used to accurately predict delamination initiation. Care must be taken, however, to include the effects of thermally-induced stresses and interlaminar normal stress (σ_{zz}) as well as the interlaminar shear stress (σ_{1z}).

8.2 Delamination Growth and Final Failure

Energy criteria are necessary but insufficient conditions for delamination growth as well as delamination initiation. The data in this investigation show that there must be delamination initiation before there can be delamination growth. Thus, the difference between initiation and growth is that an interlaminar crack is already present. This makes fracture mechanics methodologies such as the strain energy release rate more likely to apply once the delamination initiation has formed.

Laminates with greater effective ply thicknesses were shown to be susceptible to delamination initiation at lower stresses. These laminates have larger regions of high interlaminar stress near the free edge. Thus, they are susceptible to delamination initiation, growth, and final failure at lower stresses, as was shown experimentally.

The analysis described in Chapter 7 contains more details of the observed damage state than previous models in evaluating the strain energy available for release at various delamination sizes. Unfortunately, any increased accuracy cannot be adequately evaluated with the available data. The theoretical curves of strain energy release rate as a function of delamination intrusion depicted in Chapter 7 show that delamination shape and finite specimen dimensions may affect delamination growth. The previous models did not account for this possibility. The experimentally determined delamination resistance curves indicated that the critical value of strain energy release rate was not constant with effective ply thickness, stacking sequence, or delamination intrusion. It can be reasoned that these factors (with the possible exception of stacking sequence) should not affect this value. Thus, the modifications in analytical methods were not sufficient to explain the observed behavior.

There are phenomena at work which are not modeled in the strain energy release rate approaches used in this investigation. The delamination grows in a thin resin layer between two inhomogenous layers. These layers can affect the global and local stress fields and present obstacles to crack extension. It is important that these phenomenon be investigated.

These neighboring plies are subject to their own damage modes. The most prevalent one in this investigation was splitting. In most cases, the delaminations induced splitting at their boundaries and within the delaminated region. Depending on the orientation with respect to the delamination front, splits that form ahead of the delamination front can blunt it and hinder its advance. Designers must be wary as parts which are not susceptible to these phenomena may suffer growth at significantly lower stresses.

The evidence shows that the delamination and the angle ply split interact strongly. For example, the ability of a split to arrest delamination growth across it is demonstrated by the fact that one side of the delaminations of the $[\pm15_3]_s$,

$[\pm15_n/0_n]_s$, and $[0_n/\pm15_n]_s$ specimens was bounded by an angle ply split. The details of this interaction should be investigated both analytically and experimentally. The analytical investigation might include a full three-dimensional finite element analysis which models the delamination and the angle ply splits.

No critical delamination size was found for the unstable growth of any specimen type. The strain energy release rate curves calculated using the modified analysis did not exhibit the local minimum needed for a stable critical delamination size as illustrated in Figure 2.4. It is unlikely that any model based solely on global stress fields will exhibit this feature. The specimens of nonstandard width experienced no effect of specimen width on final failure stress. It is conceivable, however, that, since specimen width affects the strain energy release rate, it could delay growth and therefore final failure in some specimen types. If the controlling parameters for initiating and arresting growth are determined on a local level, there may be no definitive global value for critical delamination size.

Final delamination failure is relatively straightforward to describe but rather complicated to actually predict. Final failure can only occur if the in-plane strength of the delaminated sublaminates is exceeded in a local region. The complications lie in determining how and when growth occurs and what the resulting local stress fields are. Only by determining the in-plane stresses as a function of delamination size and shape can an engineer accurately forecast what delamination damage will trigger final failure.

The constraint by intact sublaminates on damaged sublaminates can affect the local stress state and is therefore important. For example, in the $[0_n/\pm15_n]_s$ specimens, the $[0_n/+15_n]$ sublaminates had a significant constraining effect on the damaged $[-15_{2n}]$ sublaminates. The constraint enabled the damaged sublaminate to contribute to the laminate strength and stiffness. In contrast, the damaged sublaminates in the $[+15_n/0_n]_s$ specimens peeled away, leading to lower laminate stiffness and strength.

The only differences for the fabric specimens were the different characteristics of the ply interfaces, yet there was a significant change in failure stress. The strain energy release rate model used in this investigation would not predict any difference in growth behavior between the two specimen types. Nonetheless, unstable delamination growth was delayed in the specimens with warp faces at the critical interface. This in turn lead to delayed final failure. This emphasizes the necessity of modelling the three-dimensional state of stress and interaction of the delaminations and splits.

Since delamination growth cannot occur without delamination initiation, it may be advisable in most applications to keep design stresses below the delamination initiation stress. An appropriate post first ply failure criterion may be to assume that a part has only the strength and stiffness characteristics of the strongest intact sublaminate. However, this could potentially be nonconservative if partially failed neighboring sublaminates can induce stress concentrations in the critical sublaminate.

CHAPTER 9

CONCLUSIONS AND RECOMMENDATIONS

The progression of damage in graphite/epoxy specimens leading to failure induced by delamination has been studied and analyzed. The data presented herein have resulted in the following conclusions:

1. Delamination is the result of a progression of damage stages: delamination initiation, delamination growth, and final in-plane failure of the delaminated sublaminates.

2. Delamination initiation can be accurately predicted with the Quadratic Delamination Criterion.

3. The averaging dimension in the Quadratic Delamination Criterion appears to be a material parameter. The interlaminar strength parameters appear to be equivalent to the values measured directly in interlaminar strength experiments.

4. Thermally-induced interlaminar stresses must be included in delamination initiation calculations. Thermally-induced interlaminar stresses alone can cause delamination initiation.

5. The Quadratic Delamination Criterion is valid even when

the strain energy available for release is greater than that needed to make initiation energetically feasible. The energy criterion is thus a necessary but insufficient condition for delamination initiation.

6. Delamination initiation is a necessary prerequisite to delamination growth.

7. No critical delamination size for unstable delamination growth or final failure was observed.

8. There was no observed effect of specimen width on failure stress.

9. Thicker laminates have larger regions of high interlaminar stresses and therefore tend to suffer delamination initiation, accumulate damage, and fail at lower stresses.

10. The final failure of graphite/epoxy specimens in tension is an in-plane strength phenomenon. The amount of delamination growth and the constraint by intact sublaminates on damaged sublaminates must be known in order to determine the local stress state in the delaminated sublaminates. The local stress state must be known to accurately predict final failure. Delaying delamination growth can therefore delay final failure.

11. The current strain energy release rate model is insufficient to properly model delamination growth.

12. There is a strong interaction between the delamination and the angle ply split. Delaminations can induce angle ply splits. Depending on the relative orientation of the delamination front, angle ply splits can either facilitate delamination growth or hinder its advance. Interface characteristics can therefore affect delamination growth and final failure. This interaction must be fully modeled to achieve more acceptable results.

Although several important aspects of failure induced by delamination have been identified, more knowledge is needed before final failure can be accurately predicted. The extension of this knowledge to realms of loading other than quasistatic uniaxial tensile loading should also be considered. The following recommendations are therefore made:

1. The mechanisms for arresting delamination growth should be investigated and analyzed. Useful experimental information might be gained from specimens with implanted angle ply splits placed strategically in specimens in an attempt to duplicate the arrest of a delamination front.

2. The three-dimensional state of stress and the related

strain energy release rate conditions, including relative modal contributions, should be analyzed for the region near the delamination front and the angle ply split. The special case of a "blunted" delamination front might be investigated, with special attention paid to the tip of the angle ply split as the extension of this split may be the key to reinitiating delamination growth.

3. The applicability of these conclusions to cyclic loading situations should be evaluated. Specifically, the existence of "fatigue limits" for each delamination stage should be determined to ascertain the damage tolerance of composite parts to early stages of delamination damage.

Some questions have been answered regarding failure of graphite/epoxy induced by delamination. More work must be done to give engineers the tools they need to avoid delamination in efficiently designed aerospace structures.

REFERENCES

1. Rodini, B. T., and Eisenmann, J. R., "An Analytical and Experimental Investigation of Edge Delamination in Composite Laminates," Proceedings of the Fourth Conference on Fibrous Composites in Structural Design, 1978, San Diego, California, pp. 441-456.

2. Johannesson, T., Sjöblom, P., and Seldén, R., "The Detailed Structure of Delamination Fracture Surfaces in Graphite/Epoxy Laminates," Journal of Materials Science, Vol. 19, 1984, pp. 1171-1177.

3. Pipes, R. B., Kaminski, B. E., and Pagano, N. J., "Influence of the Free Edge upon the Strength of Angle-Ply Laminates," Analysis of Test Methods for High Modulus Fibers and Composites, ASTM STP 521, American Society for Testing and Materials, 1973, pp. 218-228.

4. Kim, R. Y., and Soni, K. Y., "Experimental and Analytical Studies On the Onset of Delamination in Laminated Composites," Journal of Composite Materials, Vol. 18, 1984, pp. 70-80.

5. Rybicki, E. F., Schmeuser, D. W., and Fox, J., "An Energy Release Rate Approach for Stable Crack Growth in the Free-Edge Delamination Problem," Journal of Composite Materials, Vol. 11, 1977, pp. 470-487.

6. Wang, A. S. D., and Crossman, F. W., "Initiation and Growth of Transverse Cracks and Edge Delamination in Composite Laminates. Part 1. An Energy Method," Journal of Composite Materials, Vol. 14 Supplement, 1980, pp. 71-87.

7. Tsai, S. W., and Hahn, H. T., Introduction to Composite Materials, Technomic Publishing Co., Inc., 1980.

8. Rybicki, E. F., "Approximate Three-Dimensional Solutions for Symmetric Laminates Under In-Plane Loading," Journal of Composite Materials, Vol. 5, 1971, pp. 354-360.

9. Wang, A. S. D., and Crossman, F. W., "Some New Results in Edge Effects in Symmetric Composite Laminates," Journal of Composite Materials, Vol. 11, 1977, pp. 92-106.

10. Pipes, R. B., and Pagano, N. J., "Interlaminar Stresses in Composite Laminates Under Uniform Axial Extension," Journal of Composite Materials, Vol. 4, 1970, pp. 538-548.

11. Pagano, N. J., and Pipes, R. B., "The Influence of Stacking Sequence on Laminate Strength," Journal of Composite Materials, Vol. 5, 1971, pp. 50-57.

12. Puppo, A. H., and Evensen, H. A., "Interlaminar Shear in Laminated Composites Under Generalized Plane Stress," Journal of Composite Materials, Vol. 4, 1970, pp. 204-220.

13. Pipes, R. B., and Pagano, N. J., "Interlaminar Stresses in Composites - An Approximate Elasticity Solution," Journal of Applied Mechanics, Vol. 41, September 1974, pp. 668-672.

14. Hsu, P. W., and Herakovich, C. T., "A Perturbation Solution for Interlaminar Stresses in Bidirectional Laminates," Composite Materials: Testing and Design (Fourth Conference), ASTM STP 617, American Society for Testing and Materials, 1977, pp. 296-316.

15. Pagano, N. J., and Soni, S. R., "Global-Local Variational Model," International Journal of Solids and Structures, Vol. 19, No. 3, 1983, pp. 207-228.

16. Kassapoglou, C., and Lagace, P. A., "An Efficient Method for the Calculation of Interlaminar Stresses in Composite Materials," Journal of Applied Mechanics, Vol. 53, December 1986, pp. 744-750.

17. Kassapoglou, C., and Lagace, P. A., "Closed Form Solutions for the Interlaminar Stress Field in Angle-Ply and Cross-Ply Laminates," Journal of Composite Materials, Vol. 21, 1987,pp. 292-308.

18. Lagace, P. A., Kassapoglou, C., and Brewer, J. C., "An Efficient Method for the Calculation of Interlaminar Stresses in Composite Materials Due to Thermal and Mechanical Effects," International Symposium on Composite Materials and Structures, Beijing, China, June 1986.

19. Wang, S. S., and Choi, I., "Boundary-Layer Effects in Composite Laminates: Part 1 - Free Edge Stress Singularities," Journal of Applied Mechanics, Vol. 49, September 1982, pp. 541-548.

20. Herakovich, C. T., "Influence of Layer Thickness on Strength of Angle-Ply Laminates," Journal of Composite Materials, Vol. 16, 1982, pp. 216-226.

21. Lagace, P. A., "Delamination Fracture under Tensile Loading," Proceedings of the Sixth Conference on Fibrous Composites in Structural Design, AMMRC MC 83-2, Army Materials and Mechanics Research Center, November 1983.

22. Crossman, F. W., Warren, W. J., Wang, A. S. D., and Law, G. E., "Initiation and Growth of Transverse Cracks and Edge Delamination in Composite Laminates. Part 2. Experimental Correlation," Journal of Composite Materials, Vol. 14 Supplement, 1980, pp. 88-108.

23. Crossman, F. W., and Wang, A. S. D., "The Dependence of Transverse Cracking and Delamination on Ply Thickness in Graphite/Epoxy Laminates," Damage in Composite Materials, ASTM STP 775, American Society for Testing and Materials, 1982, pp. 118-139.

24. Wang, A. S. D., Crossman, F. W., and Law, G. E., "Interlaminar Failure in Epoxy Based Composite Laminates," Advanced Composites: Design and Applications, National Bureau of Standards Special Publication 563, 1979, pp. 255-264.

25. Kim, K. S., and Hong, C. S., "Delamination Growth in Angle-Ply Laminated Composites," Journal of Composite Materials, Vol. 20, 1986, pp. 423-438.

26. O'Brien, T. K., "Characterization of Delamination Onset and Growth in a Composite Laminate," Damage in Composite Materials, ASTM STP 775, American Society for Testing and Materials, 1982, pp. 140-167.

27. O'Brien, T. K., Johnston, N. J., Morris, D. H., and Simonds, R. A., "A Simple Test for Interlaminar Fracture Toughness of Composites," SAMPE Journal, July/August 1982, pp. 8-15.

28. O'Brien, T. K., "Mixed-Mode Strain-Energy-Release Rate Effects on Edge Delamination of Composites," NASA Technical Memorandum 84592, January 1983.

29. O'Brien, T. K., Johnston, N. J., Morris, D. H., and Simonds, R. A., "Determination of Interlaminar Fracture Toughness and Fracture Mode Dependence of Composites using the Edge Delamination Test," Proceedings of the International Conference of Testing, Evaluation, and Quality Control of Composites, University of Surrey, Guilford, England, September 1983, pp. 223-232.

30. Broek, D., Elementary Engineering Fracture Mechanics, Third Edition, Martinus Nijhoff Publishers, The Hague, 1982, p. 17.

31. Whitney, J. M., and Nuismer, R. J., "Stress Fracture Criteria for Laminated Composites Containing Stress Concentrations," Journal of Composite Materials, Vol. 8, 1974, pp. 253-265.

32. Kim, R. Y., and Soni, K. Y., "Delamination of Composite Laminates Stimulated by Interlaminar Shear," Composite Materials: Testing and Design (Seventh Conference), ASTM STP 893, 1984, pp. 286-307.

33. Soni, K. Y., and Kim, R. Y., "Failure of Composite Laminates due to Combined Interlaminar Normal and Shear Stresses," Composites '86: Recent Advances in Japan and the United States, 1986, pp. 341-350.

34. Brewer, J. C., and Lagace, P. A., "Quadratic Stress Criterion for Initiation of Delamination," submitted to Journal of Composite Materials

35. Lagace, P. A., and Weems, D. B., "A Through-the-Thickness Strength Specimen for Composites," Proceedings of the ASTM Second Symposium on Test Methods and Design Allowables, Phoenix, Arizona, November 1986.

36. Klang, E. C., and Hyer, M. W., "Damage Initiation at Curved Free Edges: Applications to Uniaxially Loaded Plates Containing Holes and Notches," Proceedings of the ASTM Second United States-Japan Symposium on Composite Materials, Hampton, Virginia, June 1983.

37. Lagace, P., Brewer, J., and Kassapoglou, C., "The Effect of Thickness on Interlaminar Stresses an Delamination in Straight-Edged Laminates," Journal of Composites Technology and Research, Vol. 9, No. 3, Fall 1987, pp. 81-87.

38. Tsai, S. W., and Wu, E. M., "A Generalized Theory for Strength of Anisotropic Materials," Journal of Composite Materials, Vol. 5, 1971, pp. 58-80.

39. Lagace, P. A., Brewer, J. C., and Varnerin, C. F., "TELAC Manufacturing Course Notes," Edition O-3, Technology Laboratory for Advanced Composites, Report 88-4, Massachusetts Institute of Technology, September 1987.

40. "Standard Test Method for Tensile Properties of Fiber-Resin Composites," ASTM Designation D 3039-76, American Society for Testing and Materials, 1976.

41. Russell, A. J., and Street, K. N., "Factors Affecting the Interlaminar Fracture Energy of Graphite/Epoxy Laminates," Progress in Science and Engineering of Composites, Proceedings of the Fourth International Conference on Composite Materials, Tokyo, 1982, pp. 279-286.

42. Orringer, O., and French, S. E., Finite Element Analysis Basic Library User's Guide, Aeroelastic and Structures Research Laboratory, Department of Aeronautics and

Astronautics, Massachusetts Institute of Technology, Cambridge, MA, 1972.

43. Jamison, R. D., "The Role of Microdamage in Tensile Failure of Graphite/Epoxy Laminates," Composites Science and Technology, Vol. 24, 1985, pp. 83-99.

DATA TABLE 1
FABRIC/UNIDIRECTIONAL SPECIMENS

Specimen	Thickness [mm]	Width [mm]	Modulus [GPa]	Delamination Initiation Stress [MPa]	Delamination Initiation Strain [μstrain]
0U5F1-0-1	1.99	49.90	115	518	4320
0U5F1-0-2	1.98	49.86	114	523	4518
0U5F1-0-3	2.00	49.84	121	493-841[a]	4020-6714[a]
0U5F1-0-4	1.94	49.90	112	547-1048[a]	4764-9240[a]
0U5F1-0-5	1.96	49.88	121	544	4398
	1.97	49.88	117	528[b]	4412[b]
	(1.2%)[c]	(0.05%)	(3.6%)	(2.6%)	(2.3%)
0U5F1U1-0-1	2.23	49.88	119	503-755[a]	4152-6204[a]
0U5F1U1-0-2	2.20	49.79	117	431-747[a]	3570-6036[a]
0U5F1U1-0-3	2.20	49.91	118	448-717[a]	3840-6156[a]
0U5F1U1-0-4	2.17	49.87	117	441-717[a]	3756-5982[a]
0U5F1U1-0-5	2.18	49.73	121	435-786[a]	5604-10131[a,d]
	2.20	49.83	118	451-744[a]	4182-6902[a]
	(1.0%)	(0.15%)	(1.4%)		
0U10F1-0-1	3.28	49.87	126	e	e
0U10F1-0-2	3.27	49.83	117	e	e
0U10F1-0-3	3.29	49.98	123	e	e
0U10F1-0-4	3.26	49.87	123	e	e
0U10F1-0-5	3.30	50.03	120	e	e
	3.28	49.92	122		
	(0.5%)	(0.17%)	(2.8%)		

[a] Bounded values - an exact delamination initiation point was not found.
[b] Data from bounded values not included.
[c] Numbers in parentheses are coefficients of variation.
[d] Final strain value was estimated - strain gage was broken.
[e] Delamination existed before mechanical loading.

DATA TABLE 2
NONSTANDARD WIDTH $[\pm 15_3]_s$ SPECIMENS

Specimen	Thickness [mm]	Width [mm]	Modulus [GPa]	Failure Stress [MPa]	Failure Strain [μstrain]
315A0-W10-1	1.58	10.20	105	490	4458
315A0-W10-2	1.55	10.14	113	486	4290
315A0-W10-3	1.54	10.16	101	501	4632
315A0-W10-4	1.58	10.14	113	505	4146
315A0-W10-5	1.62	10.15	127	501	4026
315A0-W10-6	1.64	10.15	128	537	4140
315A0-W10-7	1.51	10.12	115	538	4662
	1.57	10.15	115	508	4336
	(2.9%)[a]	(0.24%)	(8.8%)	(4.1%)	(5.8%)
315A0-W20-1	1.53	20.11	115	509	4374
315A0-W20-2	1.52	20.15	118	527	4404
315A0-W20-3	1.48	20.21	113	494	4416
315A0-W20-4	1.51	20.24	114	484	4236
315A0-W20-5	1.59	20.18	120	496	4158
	1.53	20.18	116	502	4318
	(2.6%)	(0.25%)	(2.5%)	(3.3%)	(2.7%)
315A0-W30-1	1.66	30.08	120	537	4308
315A0-W30-2	1.59	30.17	116	508	4410
315A0-W30-3	1.56	30.13	112	487	4356
315A0-W30-4	1.56	30.04	113	501	4404
315A0-W30-5	1.64	29.94	124	510	4092
315A0-W30-6	1.55	30.00	112	526	4590
315A0-W30-7	1.58	29.94	113	534	4278
	1.59	30.04	116	515	4348
	(2.7%)	(0.30%)	(4.0%)	(3.6%)	(3.5%)
315A0-W50-1	1.52	50.14	110	497	4536
315A0-W50-2	1.53	50.18	109	508	4626
315A0-W50-3	1.54	50.18	111	488	4392
315A0-W50-4	1.58	50.23	112	526	4656
315A0-W50-5	1.53	50.12	109	507	4788
	1.54	50.17	110	505	4600
	(1.5%)	(0.08%)	(1.2%)	(2.8%)	(3.2%)
315A0-W70-1	1.56	69.60	113	452	4020
315A0-W70-2	1.54	70.03	109	509	4572
315A0-W70-3	1.50	69.96	105	501	5004
315A0-W70-4	1.49	70.05	104	450	4236
315A0-W70-5	1.62	69.97	118	529	5604
	1.54	69.98	110	488	4687
	(3.4%)	(0.08%)	(5.3%)	(7.3%)	(13.5%)

[a] Numbers in parentheses are coefficients of variation.

DATA TABLE 3
$[\pm 15_n/0_n]_s$ SPECIMENS

Specimen	Thickness [mm]	Width [mm]	Modulus [GPa]	Failure Stress [MPa]	Failure Strain [μstrain]
15A1-0-1	0.87	50.11	127	1072	8386
15A1-0-2	0.84	49.90	122	1016	8298
15A1-0-3	0.88	49.25	130	941	7086
15A1-0-4	0.88	50.10	124	1033	8058
15A1-0-5	0.84	49.17	120	954	7848
	0.86	49.71	125	1003	7935
	(2.4%)[a]	(0.93%)	(3.2%)	(4.1%)	(6.5%)
215A1-0-1	1.54	50.14	115	680	5862
215A1-0-2	1.48	50.18	117	706	5880
215A1-0-3	1.61	50.10	125	825	7410
215A1-0-4	1.69	50.25	132	793	6516
215A1-0-5	1.62	50.24	119	732	5892
	1.59	50.18	122	747	6312
	(5.1%)	(0.13%)	(5.7%)	(8.1%)	(10.7%)
315A1-0-1	2.27	50.06	121	592	b
315A1-0-2	2.29	50.03	118	672	7608
315A1-0-3	2.46	50.21	132	698	6114
315A1-0-4	2.40	49.75	127	622	5112
315A1-0-5	2.27	49.54	118	624	5154
	2.34	49.92	123	642	5997
	(3.7%)	(0.54%)	(5.0%)	(6.6%)	(19.5%)
515A1-0-1	4.11	50.08	123	616	4962
515A1-0-2	4.03	50.13	118	707	7134
515A1-0-3	4.11	50.09	128	642	5520
515A1-0-4	3.87	50.21	115	599	5832
515A1-0-5	3.69	49.73	103	528	4680
	3.96	50.05	117	618	5626
	(4.6%)	(0.37%)	(8.0%)	(10.5%)	(17.0%)
815A1-0-1	6.59	50.20	120	544	4710
815A1-0-2	6.60	50.19	116	545	5256
815A1-0-3	6.64	49.98	123	558	4620
815A1-0-4	6.53	50.29	112	535	6090
815A1-0-5	6.40	50.02	105	522	5010
	6.55	50.12	115	541	5137
	(1.4%)	(0.25%)	(6.1%)	(2.5%)	(11.5%)

[a] Numbers in parentheses are coefficients of variation.

[b] Broken gage.

DATA TABLE 4
$[0_n/\pm15_n]_s$ SPECIMENS

Specimen	Thickness [mm]	Width [mm]	Modulus [GPa]	Failure Stress [MPa]	Failure Strain [μstrain]
15B1-0-1	0.84	49.78	123	1177	9396
15B1-0-2	0.84	50.03	122	1203	9594
15B1-0-3	0.88	49.69	131	1140	8490
15B1-0-4	0.86	50.20	123	1106	8550
15B1-0-5	0.83	50.13	122	1176	9108
	0.85	49.97	124	1160	9028
	(2.4%)[a]	(0.44%)	(3.1%)	(3.3%)	(5.5%)
215B1-0-1	1.53	50.16	118	908	7560
215B1-0-2	1.50	50.00	115	802	6768
215B1-0-3	1.64	50.26	132	856	7674
215B1-0-4	1.64	50.31	130	891	8484
215B1-0-5	1.56	49.89	118	859	6828
	1.57	50.12	123	863	7463
	(4.1%)	(0.35%)	(6.4%)	(4.7%)	(9.4%)
315B1-0-1	2.29	50.16	120	725	6228
315B1-0-2	2.38	50.24	119	727	6144
315B1-0-3	2.53	50.22	140	694	4932
315B1-0-4	2.35	50.08	122	792	7302
315B1-0-5	2.25	50.25	114	860	8244
	2.36	50.19	123	760	6570
	(4.6%)	(0.14%)	(8.1%)	(8.8%)	(19.1%)
515B1-0-1	4.09	50.23	126	718	6810
515B1-0-2	4.02	50.13	126	681	6564
515B1-0-3	4.06	50.14	131	600	4668
515B1-0-4	3.67	49.88	108	702	7098
515B1-0-5	3.41	50.10	103	643	6306
	3.85	50.10	119	669	6289
	(7.8%)	(0.26%)	(10.5%)	(7.1%)	(15.1%)
815B1-0-1	6.80	50.12	130	659	4998
815B1-0-2	6.57	50.14	120	631	5202
815B1-0-3	6.40	50.14	126	640	5220
815B1-0-4	5.91	50.20	103	581	5592
815B1-0-5	5.50	50.13	92	577	5844
	6.24	50.15	114	618	5371
	(8.4%)	(0.06%)	(14.1%)	(5.9%)	(6.3%)

[a] Numbers in parentheses are coefficients of variation.

DATA TABLE 5
$[\pm 20_f]_s$ FABRIC SPECIMENS

Specimen	Thickness [mm]	Width [mm]	Modulus [GPa]	Failure Stress [MPa]	Failure Strain [μstrain]
F20F-0-1	1.39	50.24	58	467	9258
F20F-0-2	1.41	50.24	53	488	10638
F20F-0-3	1.41	50.23	58	471	8832
F20F-0-4	1.41	50.20	56	452	8436
F20F-0-5	1.39	50.24	55	473	9294
	$\overline{1.40}$[a]	$\overline{50.23}$	$\overline{56}$	$\overline{470}$	$\overline{9291}$
	(0.8%)	(0.03%)	(3.8%)	(2.7%)	(8.9%)
F20W-0-1	1.39	50.16	60	545	9516
F20W-0-2	1.41	50.20	55	551	10674
F20W-0-3	1.42	50.24	54	540	9984
F20W-0-4	1.42	50.24	52	513	9954
F20W-0-5	1.40	50.27	55	502	9348
	$\overline{1.41}$	$\overline{50.22}$	$\overline{55}$	$\overline{530}$	$\overline{9895}$
	(0.9%)	(0.08%)	(5.3%)	(4.0%)	(5.2%)

[a] Numbers in parentheses are coefficients of variation.

DATA TABLE 6
$[0_3/\pm15_3]_s$ SPECIMENS WITH IMPLANTED DELAMINATIONS

Specimen	Thickness [mm]	Width [mm]	Intrusion of the Implanted Delamination [mm]	Intrusion of the Implanted Angle Ply Split [mm]	Modulus [GPa]	Failure Stress [MPa]	Failure Strain [μstrn]
315B1-D10-A0-1	2.22	49.84	14	-	116	787	6756
315B1-D10-A0-2	2.22	50.02	16	-	111	789	6906
315B1-D10-A0-3	2.16	49.91	16	-	111	762	6708
315B1-D10-A0-4	2.20	49.92	15	-	115	775	6636
315B1-D10-A0-5	2.18	49.87	13	-	110	781	6822
315B1-D10-A0-6	2.26	49.98	16	-	119	754	6420
	2.21	49.92	15		114	775	6708
	(1.6%)[a]	(0.13%)	(8.4%)		(3.1%)	(1.8%)	(2.5%)
315B1-D10-A20-1	2.21	50.03	14	26	114	698	5970
315B1-D10-A20-2	2.24	50.13	12	25	117	674	5766
315B1-D10-A20-3	2.20	46.05[b]	10	26	106	719	6372
315B1-D10-A20-4	2.16	50.03	14	26	115	687	6132
315B1-D10-A20-5	2.24	50.19	14	27	104	712	6984
315B1-D10-A20-6	2.23	50.19	15	25	118	694	6498
	2.21	49.44	13	26	112	697	6253
	(1.4%)	(3.36%)	(13.9%)	(2.9%)	(5.2%)	(2.4%)	(5.9%)

[a] Numbers in parentheses are coefficients of variation.
[b] Milling error resulted in the loss of 4 mm from one edge.

APPENDIX TO DATA TABLES

SPECIMEN NOMENCLATURE

Specimens are identified using variations of a standard TELAC three bit code. The first bit indicates the laminate type of the specimen. The second bit or set of bits identifies any unusual characteristic of the specimen, such as a nonstandard width or the size of an implanted delamination. The final bit is the specimen number.

The laminate notation is usually of the form nθQm. The θ represents the angular orientation of the angled plies with respect to the longitudinal axis in degrees. Since the laminates in this investigation were balanced, the angle plies can be represented by numbers between 0 and 90. There is therefore no ambiguity when the prefix n is added as long as angles under 10° are preceded by a zero. The value of n denotes the number of plies of the same orientation stacked together to form an effective ply of greater nominal thickness. The Q represents a letter code indicating the relative position of any 0° plies. An "A" indicates that the 0° plies are located at the midplane while a "B" indicates that they are on the laminate surface. The "m" denotes the number of 0° ply groups in each half of the symmetric laminate. Hence, 15B1 represents a $[0/\pm15]_s$ laminate and 315A1 represents a $[\pm15_3/0_3]_s$ laminate.

A different version of this basic code is used to denote laminates containing fabric plies. The laminates which contained only fabric plies had angles of ±20° to the longitudinal axis. The lamination sequence $[\pm 20]_s$ would normally be designated 20A0. A prefix "F" is used to indicate that fabric plies are used. A suffix "W" or "F" is used to denote whether the ply faces at the +20°/-20° interface are warp or fill faces.

The laminates which contained both unidirectional and fabric plies contained only 0° plies. The lamination sequences were therefore designated by a zero followed by letter/number sequences. A "U" and a number indicated that number of unidirectional plies. An "F" and a number inducated that number of fabric plies. Thus, 0U5F1 indicates a $[0_{5U}/0_F]_s$ laminate, 0U5F1U1 indicates a $[0_{5U}/0_F/0_U]_s$ laminate, and 0U10F1 indicates a $[0_{10U}/0_F]_s$ laminate.

The second bit or set of bits often indicates the type and size of machined notches. Unnotched specimens are usually given a middle bit of "0". No notched specimens were tested in this investigation. Nonetheless, some specimens have features which are denoted with middle bits. The specimens with nonstandard widths (including the group that actually have the standard width) are given a second bit with a prefix "W" followed by a number indicating the nominal width in millimeters.

The specimens with the implanted delaminations are given two middle bits. The first has a prefix "D" followed by a number indicating the nominal intrusion of the implanted delamination from the free edge. The second has a prefix "A" followed by a number indicating the nominal intrusion of the implanted angle ply split from the free edge. The facts that the delamination was at the +15°/-15° interface and that the implanted angle ply splits were in the $[-15_6]$ sublaminate were not encoded in the specimen designations.

The final bit is the specimen number. This differentiates the data from nominally identical specimens. This bit is a simple integer. In most cases, it ranged from one to five. It was convenient to manufacture six each of the specimens with implanted delaminations. An extra two specimens each of the 10 mm and 30 mm wide $[\pm 15_3]_s$ specimens were made to determine delamination initiation stress. Thus, the final bit had values as high as seven.

APPENDIX A
DELAMINATION GROWTH DATA FOR $[\pm15_3]_s$ SPECIMENS OF NONSTANDARD WIDTH

Specimen	Stress [MPa]	Associated Strain [μstrain]	Number of Delaminations	Maximum Intrusion [mm]	Delaminated Area [mm²]
315A0-W30-3	449	3978	0	0	0
	468	4164	1	6	90
	487	4356	1	16	575
	426	3936	3	16	785
	441	4081	F[a]	F	3000
315A0-W50-1	451	4116	0	0	0
	459	4176	0	0	0
	467	4254	0	0	0
	477	4368	1	3	15
	490	4452	1	3	20
	497	4536	F	F	4300
315A0-W50-2	448	4086	0	0	0
	459	4170	0	0	0
	468	4266	0	0	0
	477	4350	0	0	0
	489	4452	0	0	0
	498	4524	0	0	0
	508	4626	1	17	300
	460	4284	F	F	5700
315A0-W50-3	450	4080	1	4	30
	460	4164	2	4	45
	467	4206	2	4	45
	480	4332	2	4	45
	488	4392	2	5	48
	486	4386	F	F	5765
315A0-W50-4	447	3972	0	0	0
	459	4044	0	0	0
	467	4152	0	0	0
	478	4236	0	0	0
	487	4308	0	0	0
	497	4404	0	0	0
	509	4506	1	1	3
	517	4590	1	2	10
	526	4656	F	F	7390

[a] "F" denotes failure.

APPENDIX A (Continued)
DELAMINATION GROWTH DATA FOR $[\pm15_3]_s$ SPECIMENS OF NONSTANDARD WIDTH

Specimen	Stress [MPa]	Associated Strain [μstrain]	Number of Delaminations	Maximum Intrusion [mm]	Delaminated Area [mm²]
315A0-W50-5	449	4116	0	0	0
	459	4182	0	0	0
	468	4362	2	14	352
	480	4458	2	14	412
	487	4536	2	14	412
	498	4680	3	14	540
	508	4788	F[a]	F	6366
315A0-W70-1	452	4020	0	0	0
	445	4698	1	28	2225
	444	4690	F	F	5210
315A0-W70-2	449	4080	0	0	0
	460	4188	0	0	0
	471	4284	0	0	0
	479	4386	0	0	0
	489	4470	0	0	0
	500	4566	0	0	0
	509	4572	1	45	4272
	433	3888	F	F	9273
315A0-W70-3	450	4272	0	0	0
	460	4404	0	0	0
	469	4470	1	5	53
	480	4572	1	5	60
	489	4806	1	10	225
	501	5004	2	28	1283
	491	5796	F	F	11792
315A0-W70-4	450	4236	1	29	2480
	422	3971	F	F	12350
315A0-W70-5	450	3852	0	0	0
	460	3870	0	0	0
	471	3936	0	0	0
	479	4002	0	0	0
	490	4056	0	0	0
	500	4134	0	0	0
	509	4242	0	0	0
	519	4308	0	0	0
	529	4368	0	0	0
	536	4488	3	27	1998
	529	4430	F	F	12895

[a] "F" denotes failure.

APPENDIX B
DELAMINATION GROWTH DATA FOR $[\pm15_n/0_n]_s$ SPECIMENS

Specimen	Stress [MPa]	Associated Strain [μstrain]	Number of Delaminations	Maximum Intrusion [mm]	Delaminated Area [mm²]
15A1-0-4	760	5718	0	0	0
	809	7032	0	0	0
	861	6558	1	1	2
	928	7032	8	3	84
	965	7344	11	8	320
	1033	8058	F[a]	F	F
15A1-0-5	761	6246	0	0	0
	812	6624	2	2	16
	857	6966	4	2	40
	911	7350	10	3	112
	954	7848	F	F	F
215A1-0-4	556	4140	0	0	0
	593	4422	0	0	0
	631	4662	0	0	0
	667	4950	0	0	0
	701	5190	1	2	9
	740	5466	4	6	158
	777	5784	6	26	2564
	793	6516	F	F	F
215A1-0-5	553	4476	0	0	0
	591	4794	0	0	0
	630	5118	3	4	51
	674	5400	4	4	77
	700	5598	5	4	88
	732	5892	F	F	F
315A1-0-4	494	3834	0	0	0
	526	4056	1	1	1
	558	4302	2	6	8
	591	4866	3	26	1395
	622	5112	3	26	2867
	610	7206	F	F	F
315A1-0-5	492	4086	0	0	0
	529	4380	0	0	0
	556	4614	1	3	41
	593	4908	2	5	88
	624	5154	3	42	3310
	595	5874	F	F	F

[a] "F" denotes failure.

APPENDIX B (Continued)
DELAMINATION GROWTH DATA FOR $[\pm 15_n/0_n]_s$ SPECIMENS

Specimen	Stress [MPa]	Associated Strain [μstrain]	Number of Delaminations	Maximum Intrusion [mm]	Delaminated Area [mm²]
515A1-0-4	497	4458	1	1	2
	525	4404	1	2	4
	558	4650	1	22	1045
	592	5568	2	28	2620
	599	5832	F[a]	F	F
515A1-0-5	493	4134	1	2	2
	528	4680	1	2	3
	516	5238	F	F	F
815A1-0-4	412	3522	1	2	5
	442	4032	1	2	5
	470	4026	1	2	5
	495	4392	2	32	3408
	523	5286	2	32	3408
	535	6090	F	F	F
815A1-0-5	415	3744	2	3	16
	440	3918	3	12	382
	469	4758	3	12	387
	495	4476	4	13	1696
	522	5010	3	32	2878
	512	4734	F	F	F

[a] "F" denotes failure.

APPENDIX C
DELAMINATION GROWTH DATA FOR $[0_n/\pm15_n]_s$ SPECIMENS

Specimen	Stress [MPa]	Associated Strain [μstrain]	Number of Delaminations	Maximum Intrusion [mm]	Delaminated Area [mm²]
15B1-0-4	881	7134	0	0	0
	940	7314	0	0	0
	1000	7728	0	0	0
	1059	8190	1	2	10
	1033	8550	F[a]	F	F
15B1-0-5	882	6960	0	0	0
	942	7368	0	0	0
	1001	7776	0	0	0
	1059	8196	1	1	3
	1119	8604	4	2	11
	1176	9108	F	F	F
215B1-0-4	646	4926	0	0	0
	693	5214	0	0	0
	735	5544	0	0	0
	773	5862	1	2	7
	813	6930	4	30	2241
	857	7914	2	30	4000
	891	8484	F	F	F
215B1-0-5	646	5118	0	0	0
	690	5472	0	0	0
	730	5766	0	0	0
	771	6078	1	1	2
	813	6408	4	2	31
	859	6828	5	9	311
	857	6990	F	F	F
315B1-0-4	541	4350	5	2	22
	575	4614	5	2	27
	609	4866	5	3	34
	646	5178	6	3	55
	681	5436	7	23	1049
	717	6588	6	24	2231
	752	6858	5	24	2248
	789	7182	5	24	2261
	792	7302	F	F	F

[a] "F" denotes failure.

APPENDIX C (Continued)
DELAMINATION GROWTH DATA FOR
$[0_n/\pm15_n]_s$ SPECIMENS

Specimen	Stress [MPa]	Associated Strain [μstrain]	Number of Delaminations	Maximum Intrusion [mm]	Delaminated Area [mm²]
315B1-0-5	539	4542	1	3	23
	575	4854	1	3	23
	611	5184	3	3	42
	647	5436	3	3	53
	684	5742	4	4	100
	719	6144	5	9	249
	753	7158	6	25	2407
	788	7470	6	25	2407
	824	7866	6	25	2411
	860	8244	F[a]	F	F
515B1-0-4	502	4554	1	1	1
	534	4836	1	1	1
	567	5136	2	4	36
	603	5550	2	4	36
	642	5832	4	19	655
	668	6726	5	19	1437
	702	7098	F	F	F
515B1-0-5	502	4932	1	1	1
	534	5226	2	1	4
	568	5550	2	1	4
	602	5874	2	1	4
	635	6216	5	6	116
	643	6306	F	F	F
815B1-0-4	485	4596	3	1	5
	516	4890	4	2	14
	549	5274	6	13	372
	581	5592	8	13	435
	565	6786	F	F	F
815B1-0-5	483	4914	6	1	7
	517	5232	7	3	19
	547	5532	7	4	50
	577	5844	F	F	F

[a] "F" denotes failure.

APPENDIX D
GROWTH-TO-TAB STRESSES FOR $[\pm 15_n 0_n]_s$ AND $[0_n/+15_n]_s$ SPECIMENS

Specimen	Growth-to-Tab Stress [MPa]	Growth-to-Tab Strain [μstrain]	Specimen	Growth-to-Tab Stress [MPa]	Growth-to-Tab Strain [μstrain]
215A1-0-1	618	7248	215B1-0-1	908	7560
215A1-0-2	706	5880	215B1-0-2	747	6954
215A1-0-3	717	6240	215B1-0-3	823	6090
215A1-0-4	793	6516	215B1-0-4	813	6930
215A1-0-5	732	5892	215B1-0-5	857	6990
	713	6355		830	6905
	(8.8%)	(8.9%)		(7.2%)	(7.6%)
315A1-0-1	556	b	315B1-0-1	725	6228
315A1-0-2	647	5646	315B1-0-2	727	6144
315A1-0-3	619	4722	315B1-0-3	694	4932
315A1-0-4	568	4494	315B1-0-4	681	5436
315A1-0-5	624	5154	315B1-0-5	723	6450
	603	5004		710	5838
	(6.5%)	(10.1%)		(2.9%)	(10.8%)
515A1-0-1	616	4962	515B1-0-1	687	5292
515A1-0-2	591	5250	515B1-0-2	650	5268
515A1-0-3	565	4362	515B1-0-3	600	4668
515A1-0-4	558	4650	515B1-0-4	702	7098
515A1-0-5	503	4896	515B1-0-5	643	6306
	567	4824		656	5726
	(7.5%)	(6.9%)		(6.1%)	(16.9%)
815A1-0-1	544	4710	815B1-0-1	659	4998
815A1-0-2	545	5256	815B1-0-2	584	6582
815A1-0-3	558	4620	815B1-0-3	640	5220
815A1-0-4	485	4194	815B1-0-4	549	5274
815A1-0-5	495	4476	815B1-0-5	577	5844
	525	4651		602	5584
	(6.3%)	(8.4%)		(7.6%)	(11.5%)

[a] Numbers in parentheses are coefficients of variation.
[b] Broken gage.

APPENDIX E
DELAMINATION GROWTH DATA FOR $[\pm 20_F]_s$ FABRIC SPECIMENS

Specimen	Stress [MPa]	Associated Strain [μstrain]	Number of Delaminations	Maximum Intrusion [mm]	Delaminated Area [mm²]
F20F-0-4	357	6348	0	0	0
	381	6768	11	2	46
	406	7236	16	4	149
	429	7680	19	4	235
	452	8436	F[a]	F	F
F20F-0-5	357	6474	3	2	9
	381	6966	11	3	45
	404	7440	13	3	86
	429	8148	20	4	299
	453	8760	20	6	515
	473	9294	F	F	F
F20W-0-4	411	7638	0	0	0
	437	8100	1	1	2
	465	8766	8	3	54
	492	9438	15	3	116
	513	9954	F	F	F
F20W-0-5	410	7344	0	0	0
	438	7758	8	2	22
	465	8604	23	3	142
	492	9174	23	4	251
	502	9348	F	F	F

[a] "F" denotes failure, including at least one delamination across the entire width.

APPENDIX F
DELAMINATION AND ANGLE PLY SPLIT FORMATION DATA FOR $[0_3/\pm15_3]_s$ SPECIMENS WITH IMPLANTED DELAMINATIONS

Specimen	Delamination Formation[a]		Angle Ply Split Formation[b]	
	Stress [MPa]	Strain [μstrain]	Stress [MPa]	Strain [μstrain]
315B1-D10-A0-1	148	1218	362	3024
315B1-D10-A0-2	150	1266	314	2874
315B1-D10-A0-3	128	1110	315	2778
315B1-D10-A0-4	123	1020	123	1020
315B1-D10-A0-5	144	1266	263	2226
315B1-D10-A0-6	148	1236	431	3636
	140	1186	301	2593
	(8.3%)	(8.4%)	(34.5%)	(34.5%)
315B1-D10-A20-1	148	1266	148	1266
315B1-D10-A20-2	188	1716	188	1716
315B1-D10-A20-3	146	1338	146	1338
315B1-D10-A20-4	146	1344	146	1344
315B1-D10-A20-5	121	1206	121	1206
315B1-D10-A20-6	162	1362	162	1362
	152	1372	152	1372
	(14.6%)	(13.0%)	(14.6%)	(13.0%)

[a] The point at which the implanted teflon debonded from neighboring plies.

[b] The point at which an angle ply split was first visible on an X-radiograph.

[c] Numbers in parentheses are coefficients of variation.

APPENDIX G

GROWTH OF THE DELAMINATION TO THE END OF THE IMPLANTED ANGLE PLY SPLIT IN $[0_3/\pm15_3]_s$ SPECIMENS WITH IMPLANTED DELAMINATIONS AND ANGLE PLY SPLITS

Specimen	Stress [MPa]	Strain [μstrain]	Same as Failure?
315B1-D10-A20-1	698	5970	Yes
315B1-D10-A20-2	674	5766	Yes
315B1-D10-A20-3	719	6372	Yes
315B1-D10-A20-4	663	5652	No
315B1-D10-A20-5	707	6648	No
315B1-D10-A20-6	680	5808	No
	690	6036	
	(3.1%)	(6.5%)	

[a] Numbers in parentheses are coefficients of variation.

APPENDIX H
SIZING OF THE ELEMENTS IN THE FINITE ELEMENT MESH

The finite element mesh used in this investigation is a two-dimensional model of the cross-section of the specimen perpendicular to the loading direction. For the purposes of calculation, all models used an effective ply thickness of 0.134 mm, the nominal value for a ply of AS4/3501-6. The values were scaled appropriately for other effective ply thicknesses.

From symmetry considerations, only one quarter of the cross-section needed to be modeled. Thus, the width of the the modeled cross-section was one half the width of the specimen and the thickness of the modeled cross-section was one half the thickness of the specimen.

The actual specimen width was not used in most cases. A full-sized model would have been inappropriate because the change in internal energy would be small compared to the internal energy in the entire model. The roundoff error involved in the numerical solution would then become unacceptably large. The accuracy of this approach was verified using full-sized models without the constraints on the x_2 face which represent the symmetry conditions at the center of the test section. It was found that the accuracy was sufficient (i.e. that the asymptotic value of strain energy release rate did not differ by more than 1% between the two versions) as long as the delamination did not extend to within two boundary region widths of the far free edge.

Since the calculated internal energy per unit length is a function of model width, the widths of the model had to be consistent for similarly sized delaminations. Relatively small widths were used. The model widths used for various delamination sizes are shown for the various specimen types in Table H.1.

The thickness of each element in the model was one quarter of the nominal ply thickness as was illustrated in Figure 7.1. The width of the model was divided into three regions. There was a four element wide region over the delamination surface, a three element wide region which extended 0.1 mm in front of the delamination tip, and a five element wide region extending the rest of the way to the centerline of the specimen. The elements in each region were skewed toward the delamination tip, as shown in Figure 7.1, with a "skewing factor" for each region of 1.9. This means that the boundaries of the elements in a region of width w containing n elements are at the following distances from the boundary of the region:

$$d_i = w\left(\frac{i}{n}\right)^{1.9} \qquad i = 1,2,3,\ldots,n \tag{H.1}$$

The boundaries of the twelve elements in the model used in this investigation are given in terms of the delamination size, a, and the halfwidth of the specimen, b, in Table H.2.

TABLE H.1

FINITE ELEMENT MODEL WIDTHS USED FOR VARIOUS DELAMINATION SIZES

Specimen Type	Model Width [mm]	Range of Delamination Sizes [mm]
$[\pm 15]_s$	1.0	0.001-0.100
	2.5	0.100-0.500
	5.0	0.500-2.500
	16.7	2.50-15.0
$[\pm 15/0]_s$	2.3	0.001-0.200
	5.7	0.200-1.000
	11.4	1.000-3.000
	50.0	3.00-40.0
$[0/\pm 15]_s$	2.78	0.001-0.200
	6.94	0.200-1.000
	13.88	1.000-3.000
	50.0	3.00-40.0

TABLE H.2

POSITION OF BOUNDARIES OF FINITE ELEMENTS ACROSS MODEL WIDTH

Element Number	Position of Boundaries* Inside Boundary	Outside Boundary
1	0	0.346(b-a-0.1 mm)**
2	0.346(b-a-0.1 mm)	0.621(b-a-0.1 mm)
3	0.621(b-a-0.1 mm)	0.825(b-a-0.1 mm)
4	0.825(b-a-0.1 mm)	0.953(b-a-0.1 mm)
5	0.953(b-a-0.1 mm)	b-a-0.1 mm
6	b-a-0.1 mm	b-a-0.463 mm
7	b-a-0.463 mm	b-a-0.124 mm
8	b-a-0.124 mm	b-a
9	b-a	b-0.928a
10	b-0.928a	b-0.732a
11	b-0.732a	b-0.421a
12	b-0.421a	b

* Position given in distance from the centerline of the specimen

** a = width of delamination
b = width of the model = halfwidth of specimen being modeled

The elements are numbered one through twelve starting at the centerline of the specimen.

APPENDIX I
STRAIN ENERGY RELEASE RATE CALCULATIONS FOR $[\pm15_3]_s$ SPECIMENS OF NONSTANDARD WIDTH

Specimen	Stress [MPa]	Associated Intrusion [mm]	Strain Energy Release Rate Calculations[a]			
			A [J/m²]	B [J/m²]	C [J/m²]	D [J/m²]
315A0-W30-3	487	6	797	796	1177	1585
	441	16	654	653	967	2265
315A0-W50-1	497	3	830	829	1220	1332
315A0-W50-2	460	17	711	710	1051	1704
315A0-W50-3	488	4	801	800	1180	1323
	486	5	794	793	1174	1353
315A0-W50-4	517	1	899	898	1303	1341
	526	2	930	929	1362	1445
315A0-W50-5	508	14	868	867	1283	1908
315A0-W70-1	444	28	663	662	980	1639
315A0-W70-2	433	45	630	629	931	2061
315A0-W70-3	489	5	804	803	1187	1312
	501	10	844	843	1248	1575
	491	28	811	810	1199	2268
315A0-W70-4	422	29	599	598	885	1506
315A0-W70-5	529	27	941	940	1391	2288

[a] Key: A - O'Brien's Method
B - Finite Element Method
C - Geometrically Integrated Finite Element Method
D - Geometrically Integrated Finite Element Method with Finite Dimension Effects

APPENDIX J
STRAIN ENERGY RELEASE RATE CALCULATIONS FOR $[\pm 15_n/0_n]_s$ SPECIMENS

Specimen	Stress [MPa]	Associated Intrusion [mm]	Strain Energy Release Rate Calculations[a]			
			A [J/m^2]	B [J/m^2]	C [J/m^2]	D [J/m^2]
15A1-0-4	928	1	711	709	1110	1128
	965	3	768	767	1197	1257
	1033	8	880	878	1366	1552
15A1-0-5	911	2	685	682	1066	1101
	954	3	751	749	1168	1228
215A1-0-4	740	2	904	900	1412	1459
	777	6	996	993	1547	1709
	793	26	1038	1035	1611	2318
215A1-0-5	732	4	884	881	1377	1467
315A1-0-4	558	1	771	780	1112	1236
	591	6	865	863	1346	1481
	610	26	921	918	1429	2057
315A1-0-5	593	3	870	868	1359	1426
	624	5	964	960	1500	1624
	595	42	876	873	1355	2307
515A1-0-4	525	1	1137	1173	1569	1825
	558	2	1284	1292	1880	2088
	592	22	1446	1441	2243	3150
	599	28	1480	1475	2297	3379
515A1-0-5	516	2	1098	1105	1608	1786
815A1-0-4	495	2	1617	1657	2275	2637
	535	32	1889	1883	2932	4504
815A1-0-5	440	3	1278	1286	1862	2114
	495	12	1617	1612	2521	3028
	522	13	1799	1793	2802	3412
	512	32	1730	1724	2685	4127

[a] Key: A - O'Brien's Method
B - Finite Element Method
C - Geometrically Integrated Finite Element Method
D - Geometrically Integrated Finite Element Method with Finite Dimension Effects

APPENDIX K
STRAIN ENERGY RELEASE RATE CALCULATIONS FOR $[0_n/\pm15_n]_s$ SPECIMENS

Specimen	Stress [MPa]	Associated Intrusion [mm]	Strain Energy Release Rate Calculations[a] A [J/m²]	B [J/m²]	C [J/m²]	D [J/m²]
15B1-0-4	1106	2	1009	1007	1574	1625
15B1-0-5	1119	1	1033	1031	1618	1643
	1176	2	1141	1139	1779	1838
215B1-0-4	813	2	1091	1089	1709	1764
	891	30	1310	1308	1969	3070
215B1-0-5	813	1	1091	1094	1720	1748
	859	2	1218	1213	1908	1970
	857	9	1212	1210	1881	2172
315B1-0-4	609	2	918	917	1442	1490
	681	3	1148	1145	1798	1887
	717	23	1273	1271	1975	2747
	792	24	1553	1550	2410	3393
315B1-0-5	684	3	1158	1156	1813	1903
	719	4	1280	1277	2000	2130
	753	9	1403	1401	2187	2526
	860	25	1831	1828	2842	4046
515B1-0-4	567	1	1326	1374	2109	2143
	642	4	1700	1700	2667	2844
	702	19	2033	2030	3155	4176
515B1-0-5	635	1	1663	1723	2645	2688
	643	6	1706	1702	2666	2931
815B1-0-4	516	1	1757	1863	2775	2821
	549	2	1989	2034	3158	3264
	565	13	2107	2103	3289	4004
815B1-0-5	517	1	1764	1870	2785	2831
	547	3	1975	1989	3124	3280
	577	4	2198	2204	3465	3696

[a] Key: A - O'Brien's Method
B - Finite Element Method
C - Geometrically Integrated Finite Element Method
D - Geometrically Integrated Finite Element Method with Finite Dimension Effects

MITLibraries
Document Services

Room 14-0551
77 Massachusetts Avenue
Cambridge, MA 02139
Ph: 617.253.5668 Fax: 617.253.1690
Email: docs@mit.edu
http://libraries.mit.edu/docs

DISCLAIMER OF QUALITY

Due to the condition of the original material, there are unavoidable flaws in this reproduction. We have made every effort possible to provide you with the best copy available. If you are dissatisfied with this product and find it unusable, please contact Document Services as soon as possible.

Thank you.

Some pages in the original document contain pictures or graphics that will not scan or reproduce well.